In Situ Deformation Studies of HCP Metal Alloys with Neutron Diffraction, X-Ray Diffraction, and High Resolution Digital Image Correlation

Thèse N° 7262

Présentée le 30 juillet 2019

à la Faculté des sciences et techniques de l'ingénieur
Neutrons et rayons X en mécanique des matériaux
Programme doctoral en science et génie des matériaux

pour l'obtention du grade de Docteur ès Sciences

par

Karl Alan SOFINOWSKI

Acceptée sur proposition du jury

Prof. P. Muralt, président du jury
Prof. H. Van Swygenhoven, directrice de thèse
Prof. K. Máthis, rapporteur
Prof. M. Seefeldt, rapporteur
Prof. R. Logé, rapporteur

2019

EPFL
ÉCOLE POLYTECHNIQUE
FÉDÉRALE DE LAUSANNE

Acknowledgements

Abstract

Mg and Ti alloys are attractive materials for structural applications in the transportation and biomedical industries due to their high strength-to-weight ratios. However, due to their hexagonally close-packed (HCP) lattice structure, they exhibit poor formability at room temperature and strong plastic anisotropy. The anisotropy often results in non-intuitive deformation behaviors. *In situ* test methods such as x-ray diffraction (XRD), neutron diffraction (ND), and high-resolution digital image correlation (HRDIC) are powerful tools that make it possible to examine the evolution of the microstructure during deformation. In this thesis, the plastic deformation behavior of three HCP metals is examined using various *in situ* mechanical test techniques. Each study focuses on a particular aspect of the plastic deformation: the effect of strain path changes on Mg AZ31B, the high work hardening of a Ti-6Al-4V alloy, and the three-stage work hardening and springback of a Grade 2 Ti.

First, the mechanical behavior of cold-rolled Mg AZ31B is studied during in-plane multiaxial loading and tension-tension strain path changes using *in situ* ND and EBSD. The results are compared with uniaxial tensile loading of dogbone-shaped samples measured with *in situ* ND and acoustic emission. The relative activity of slip and twinning mechanisms and the active twin variants are discussed for the different strain paths. It is shown that initial strains of 4-5% cause a hardening effect during the reload for strain path change angles of 90 and 135 degrees. The strengthening is primarily due to twin and dislocation accumulation during the prestrain that impedes dislocation motion during the reload. The twinning observed during the prestrain activates complex multivariant secondary twinning which may also contribute to the strengthening.

Second, a multi-phase Ti-6Al-4V prepared by electron beam melting and thermal post-treatments is studied using *in situ* XRD and HRDIC. The material exhibits both increased strength and ductility over standard wrought or HIP'ed Ti-6Al-4V. The mechanical improvements are due to a prolonged, continuous work hardening effect not commonly observed in Ti alloys. *In situ* XRD and HRDIC are used to examine the strain partitioning between the phases during tensile loading. Specimens annealed between 850 and 980°C were tested and the effect of annealing temperature on the micromechanical response is discussed. It is shown that the work hardening is the result of a composite load-sharing behavior between three mechanically distinct microstructures: large α lamellae and a martensitic region of fine acicular α' and a third phase not previously reported in this material.

Finally, the three-stage work hardening and springback in a commercially pure, cold-rolled α-phase titanium (CP-Ti Grade 2) is examined. Interrupted tensile load tests with *in situ* XRD, HRDIC, and quasi-*in situ* EBSD show that twinning plays a minor role in both of these phenomena. The work hardening plateau is shown to be the result of the sudden activation and multiplication of $\langle c + a \rangle$ slip and the subsequent redistribution of load between grain families. The springback can be attributed to backwards motion and annihilation of dislocations, driven by backstresses from dislocations accumulated during loading. The peak broadening behavior suggests that the internal stress state is highest in the rolling direction, resulting in consistently higher springback along that direction.

Keywords

Résumé

Les alliages de Mg et de Ti ont des applications structurelles dans les industries du transport et biomédicales en raison de leur rapport résistance / poids élevé. Cependant, à cause de leur structure hexagonale compacte (HC), ils présentent une faible aptitude au formage à température ambiante et une forte anisotropie plastique. L'anisotropie entraîne souvent des comportements de déformation non prédictibles. Les méthodes de mesure *in situ* telles que la diffractométrie de rayons X (DRX), la diffraction des neutrons (DN) et la corrélation d'images numériques à haute résolution (HRDIC) sont des outils puissants qui permettent d'examiner l'évolution de la microstructure au cours de la déformation. Dans cette thèse, le comportement en matière de déformation plastique de trois métaux HC est examiné à l'aide de différentes techniques d'essais mécaniques *in situ*. Chaque étude est centrée sur un aspect particulier de la déformation plastique: l'effet des changements de trajectoire de déformation sur le Mg AZ31B, le fort écrouissage d'un alliage Ti-6Al-4V, l'écrouissage en trois étapes et le retour élastique d'un Grade 2 Ti.

Premièrement, le comportement mécanique multiaxial du Mg AZ31B laminé à froid est étudié lors de changements de trajectoire ou en tension grâce à la diffraction de neutrons et la diffraction d'électrons rétrodiffusés (EBSD) *in situ*. Les résultats sont comparés à la charge en tension d'éprouvettes de traction mesurée par diffraction de neutrons *in situ* et émission acoustique. L'activité relatives des mécanismes de glissement et de maclage et des variantes de macles activées sont discutées pour les différents chemins de contrainte. Il est démontré que des déformations initiales de 4-5% provoquent une contrainte élastique accrue lors du rechargement pour des angles de changement de trajectoire de déformation de 90 et 135 degrés. Le renforcement est principalement dû à l'accumulation de dislocations lors du mouvement initial de dislocations gênant la charge lors du rechargement. Le maclage observé lors de la précontrainte active un maclage secondaire à variantes multiples et complexe qui peut également contribuer au renforcement lors de la recharge.

Deuxièmement, un Ti-6Al-4V multi-phases préparé par fusion par faisceau d'électrons et post-traitements thermiques est étudié in-situ sous DRX et HRDIC. Le matériau présente à la fois une résistance et une ductilité accrues par rapport au Ti-6Al-4V corroyé ou en compression isostatique à chaud (HIP). Les améliorations mécaniques sont dues à un effet de durcissement continu prolongé, non observé dans les alliages de Ti. La DRX et la HRDIC *in situ* sont utilisées pour examiner le partage des contraintes entre les phases lors du chargement en traction. Les échantillons traités thermiquement entre 850 et 980 ° C ont été testé et l'effet de la température de recuit sur la réponse micromécanique est discuté. Il est montré que l'écrouissage est le résultat d'un comportement composite de partage de charge entre trois microstructures mécaniquement distinctes: les grandes lamelles α et une région martensitique de fine aciculaire α 'et une troisième phase non signalée précédemment dans ce matériau.

Finalement, l'écrouissage en trois étapes et le retour élastique d'un titane en phase α laminé à froid (CP-Ti Grade 2) sont examinés. Des essais de charge de traction interrompus avec des mesures de DRX *in situ*, HRDIC et EBSD quasi *in situ* montrent que le maclage joue un rôle mineur…

Mots-clés

Alliages HC, *in situ* x-ray diffraction, *in situ* neutron diffraction, high resolution digital image correlation, multiaxial deformation

Contents

List of Figures

List of Tables

Chapter 1   Introduction

Sheet metal forming is ubiquitous in the automotive and aerospace industries. Modern forming processes such as stamping subject metals to multiaxial stresses and strain path changes that can cause undesired stress concentrations and deviations from desired dimensions. Additionally, formed parts like the exterior aircraft plating can experience extreme multiaxial loading during use. It is therefore critical for both efficency and safety that the plastic deformation and development of internal stresses during sheet metal forming is accurately understood.

In particular, there is significant interest in light metal alloys such as magnesium and titanium alloys due to their high strength-to-weight ratio. The widespread application of these metals is hindered in part by their poor formability at room temperature in comparison to aluminum alloys and steels. This is a result of their hexagonal close-packed (HCP) lattice structure, which only allows easy deformation along the crystallographic a-axes. Deformation along the crystallographic c-axis must be accomodated by $\langle c + a \rangle$ slip mechanisms with a high activation stress or deformation twinning, leading to an inherent plastic anisotropy within single crystallites. The anisotropy often leads to the development of signifcant stress inhomogeneity and texture during deformation that depends strongly on the initial microstructure of the material (texture, grain size distribution, and crystallographic axes c/a ratio) and loading conditions (loading mode, strain rate, and strain path).

In order to optimize forming processes, constitutive mathematical models are often employed to predict deformation behavior. Crystal plasticity models are particularly appealing because they can simulate the texture and internal stress evolution during forming [1]. While powerful, these models require significant experimental validation to get accurate results. This is reflected in the wide range of CRSS values reported in HCP metals and the failure of models based on uniaxial experiments to predict various plastic effects during multiaxial and multi-step loads. This latter point is, for instance, particularly important in magnesium alloys, which activate different twinning mechanisms and variants based on the loading mode [2–4]. During strain-path changes, these alloys exhibit significant detwinning that has only recently been incorporated in models using results from multi-step loading experiments [5–7]. Another example is titanium, which shows a strong, directionally-dependent springback during unload. Existing models for springback are validated only against macroscopic tests and do not address the underlying microstructural causes [8,9]. Thus, it is evident that more experimental data specifically addressing these unexpected plastic effects is needed.

A variety of methods are available to collect data for constitutive models, but *in situ* techniques are particularly valuable. Post-mortem techniques, such as scanning or transmission electron microscopy (SEM or TEM), directly measure the deformed microstructure but lose temporal information about how the microstructure formed. By contrast, *in situ* mechanical test techniques examine the plastic behavior during deformation. *In situ* TEM methods can directly observe defect formation and interaction, map strains, and follow grain rotation in metals during deformation [10]. However, these techniques are limited to a statistically small volume of the sample and thus preclude studies on coarse-grained metals. For bulk material properties, *in situ* x-ray and neutron diffraction (XRD and ND) are more appropriate. These techniques can probe much larger volumes to identify internal strain development and texture evolution of the bulk material not accessible to other techniques [11,12]. *In situ* high resolution digital image correlation (HRDIC) is also useful to examine strain partitioning and slip behavior with a resolution from 100s to 10s of nm [13–15].

These methods, complemented by *ex situ* techniques, give invaluable information on the texture and internal stress evolution that can be compared directly with simulated results.

Within the European Research Council (ERC) Advanced Grant MULTIAX (see http://www.psi.ch/erc-multiax), the works presented here will examine plastic effects in three polycrystalline HCP metals: deformation plasticity and twinning in Mg AZ31, multi-phase load sharing in Ti-6Al-4V prepared by electron-beam melting, and non-linear plastic springback in commercially pure Ti (CP-Ti). *In situ* diffraction is used to capture the internal strain evolution and twinning behavior of the bulk material. *In situ* high resolution digital image correlation is used to observe the mactrostrain evolution and slip behavior during deformation. It is expected that the findings of these studies will be useful to validate improved crystal plasticity finite element models. Additionally, novel machines were designed for miniaturized multiaxial mechanical testing within the scope of the MULTIAX grant. This work also presents a bottom-up preparation method for miniaturized cruciforms that can be used for multiaxial testing of a wide range of previously innaccesible materials.

1.1   Deformation Mechanisms in HCP Metals

The hexagonal close-packed (HCP) crystal structure is one of the two highest-density systems of atomic packing, along with face-centered cubic. The HCP unit cell has a six-fold rotational symmetry about the longer *c*-axis. Three equivalent axes a_1, a_2, and a_3 are perpendicular to the *c*-axis, each at an angle of 120° to one another and each with the same unit length *a*. The structure leads to close-packed "basal" planes perpendicular to the *c*-axis. Pure HCP metals are typically described by the ratio of their lattice parameters *c/a*, which affects the relative activity of deformation slip and twinning modes during deformation. Mg has a nearly ideal *c/a* ratio of 1.623 and deforms primarily by $\langle a \rangle$ slip on basal planes, while deformation twinning is prevalent as a mechanism for accommodating deformation along the *c*-axis. By comparison, Ti has a *c/a* ratio of 1.588 and deforms preferentially by $\langle a \rangle$ slip on prismatic planes. Twinning is active in Ti but contributes much less to the overall plastic strain than in Mg [16].
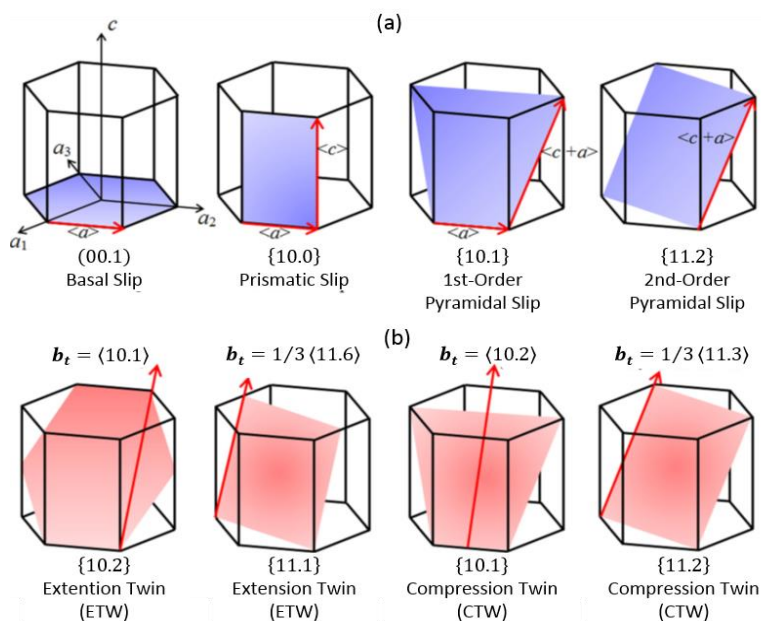
Figure 1-1 Deformation mechanisms in HCP metals. Figure adapted from [17].

The asymmetry of the HCP unit cell leads to significant plastic anisotropy. Dislocation slip occurs by the movement of dislocations. Slip is activated on a given slip plane when the stress felt by a dislocation overcomes a certain stress necessary to move the dislocation, the critical resolved shear stress (CRSS). CRSS values vary significantly for different deformation mechanisms depending on the c/a ratio and chemical composition of the alloy. The addition of alloying elements has been shown to change the relative activity of different deformation mechanisms. For example, Al and Zn decrease the basal stacking fault energy (SFE) in Mg [18] and Al is known to both decrease the basal SFE and increase prismatic SFE in Ti [19], promoting basal slip. Additionally, alloying elements can act as solid solution strengtheners or cause the formation of additional phases, thereby further changing the plastic behavior of the metal.

Slip System	Slip Plane	Slip Direction	Number of slip systems	
			Total	Independent
$Ba\langle a\rangle$	(00.1)	$\langle 11.0\rangle$	3	2
$Pri\langle a\rangle$	$\{10.0\}$	$\langle 11.0\rangle$	3	2
$Pyr\langle a\rangle$	$\{10.1\}$	$\langle 11.0\rangle$	6	4
$Pyr_{1st}\langle c+a\rangle$	$\{10.1\}$	$\langle 11.3\rangle$	6	5
$Pyr_{2nd}\langle c+a\rangle$	$\{11.2\}$	$\langle 11.3\rangle$	6	5
$Pri\langle c\rangle$	$\{10.0\}$	$\langle 00.1\rangle$	3	2

Table 1-1 Common slip mechanisms for HCP metals.

Two types of dislocation slip are commonly observed in HCP alloys: $\langle a\rangle$ slip, with Burgers vector $\mathbf{b} = \langle 11.0\rangle$ along one of the a axes, and $\langle c+a\rangle$ slip, for which $\mathbf{b}$ has a component along the c-axis. A third type of slip, $\langle c\rangle$ slip with $\mathbf{b} = \langle 00.1\rangle$, is possible on prismatic $\{10.0\}$ planes; however, it is rarely observed experimentally and often ignored in crystal plasticity simulations. The dislocation-based deformation mechanisms for HCP metals are listed in Table 1-1 and are shown schematically on the top row in Figure 1-1. For all HCP materials, $\langle a\rangle$ slip can occur on basal (00.1) planes ($Ba\langle a\rangle$ slip), prismatic $\{10.0\}$ planes ($Pri\langle a\rangle$ slip), and first-order pyramidal $\{10.1\}$ planes ($Pyr\langle a\rangle$ slip). $Ba\langle a\rangle$ and $Pri\langle a\rangle$ slip can at most provide four independent slip systems and $Pyr\langle a\rangle$ slip is simply the combination of $Ba\langle a\rangle$ and $Pri\langle a\rangle$ slip. Thus, $\langle a\rangle$ slip alone cannot provide the five independent slip systems necessary for homogeneous slip [20] as it cannot accomodate strain along the c-axis. C-axis strain can be accomodated by $\langle c+a\rangle$ slip on first-order pyramidal $\{10.1\}$ and second-order pyramidal $\{11.2\}$ planes ($Pyr_{1st}\langle c+a\rangle$ and $Pyr_{2nd}\langle c+a\rangle$ slip). However, the CRSS for both $\langle c+a\rangle$ modes is considerably higher than for $\langle a\rangle$ slip at ambient temperatures due to the larger Burgers vector.

Each dislocation distorts the crystal lattice locally and generates a stress field. Thus, dislocations act as barriers to the motion of other dislocations. As deformation proceeds, the accumulation of dislocations within a polycrystal progressively reduces the mean free path length of mobile dislocations and more stress is required to move dislocations through the crystal. This process is called work hardening. Dislocations on different slip systems entangle and form dislocation "forests" that significantly harden the polycrystal. In the case of single slip, where only one slip system is active, the polycrystal is also hardened by dislocations piling up at grain boundaries, but the hardening is much less than from forest hardening.

Deformation twinning is another mechanism that can accomodate strain along the c-axis. Deformation twinning occurs when the crystal lattice shears to produce a mirror reflection across a defined twin plane. The original lattice is called the "parent" and the twinned lattice is called the "daughter". The parent and daughter have the same lattice structure but different orientations. Unlike dislocation-based plasticity, which generally causes a gradual rotation of the crystal lattice as dislocations accumulate, twinning causes a sudden

reorientation of the crystal lattice. Deformation twinning in HCP metals is polar by nature. If twinning is caused by a shear stress in one direction, a shear stress in the opposite direction will not cause twinning. Deformation twins are thus classified as either extension or compression twinning. Extension twins (ETW) result in an elongation along the *c*-axis in the parent polycrystal, while compression twins (CTW) cause a contraction along the *c*-axis.

Four main twinning modes are observed in HCP metals, shown in the bottom row of Figure 1-1: {10.1}⟨10.2⟩ CTW, {10.2}⟨10.1⟩ ETW, {11.2}1/3⟨11.3⟩ CTW, and {11.1}1/3⟨11.6⟩ ETW. The twinning shear of the four modes is shown in Figure 1-2 as a function of the *c/a* ratio. In general, twinning modes which require a lower twinning shear *g* will be favored. Twinning affects deformation behavior in several ways. The onset of twinning often causes a strain burst with low work hardening, e.g. observed as a stress plateau during compression of HCP alloys. The shear results in twin boundaries with large misorientation angles between the parent and daughter grains which can act as impediments to dislocation motion. Additionally, the reoriented lattice can be more or less favorably oriented for slip than the parent grain.
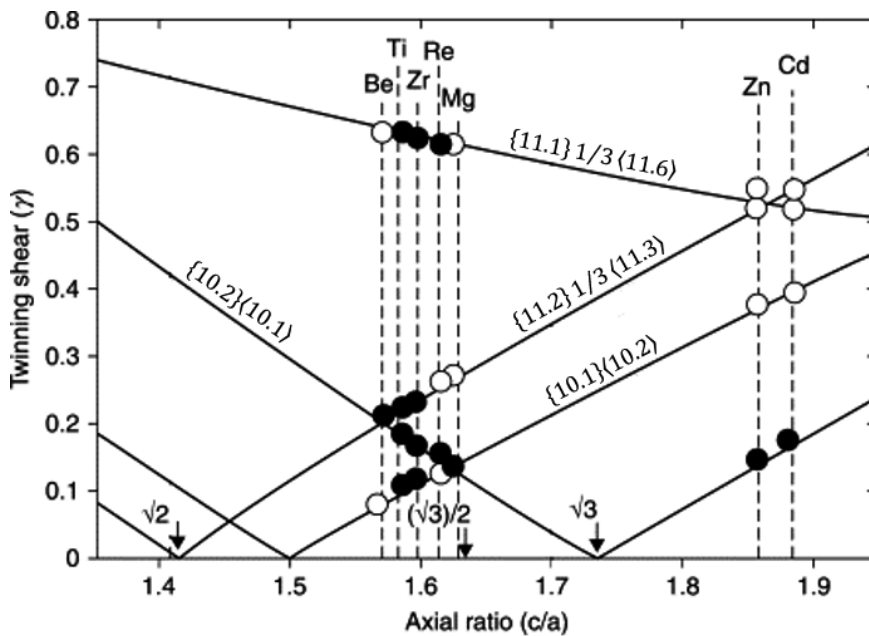
Figure 1-2 Twinning shear versus c/a ratio for common twinning modes in HCP metals. Closed circles indicate active twinning systems. Figure adapted from [21].

The probability that a specific slip or twinning mode is activated depends on the CRSS of the mechanism and on the orientation of the slip Burgers vector and slip plane (shear direction and twin plane for twinning) with respect to the stress on a crystallite. The orientation dependence can be represented by a generalized Schmid Law:

$$\mathrm{m} = \mathbf{b}^{\mathrm{T}} \cdot (\mathbf{g}^{\mathrm{T}} \cdot \mathbf{S} \cdot \mathbf{g}) \cdot \mathbf{n} \qquad (1\text{-}1)$$

where $\mathbf{b}$ is the slip Burgers vector, $\mathbf{n}$ is the slip-plane normal, $\mathbf{g}$ is a rotation matrix between the sample basis and the crystallite basis, and $\mathbf{g}^{\mathrm{T}}\mathbf{S}\mathbf{g}$ is the normalized stress tensor $\mathbf{S}$ in three dimensions expressed in the crystal orientation. For the twinning modes, $\mathbf{b}$ is the twinning shear direction and $\mathbf{n}$ is the twin-plane normal. When the loading is perfectly uniaxial, Eq. $\mathrm{m} = \mathbf{b}^{\mathrm{T}} \cdot (\mathbf{g}^{\mathrm{T}} \cdot \mathbf{S} \cdot \mathbf{g}) \cdot \mathbf{n}$ (1-1) yields the Schmid Factor (SF). For multi-slip cases, we will call this value the normalized resolved shear stress. When the stress tensor only

contains positive elements, i.e. the crystallite is under tensile loads only, the value of m ranges from 0 to 0.5. A value of m = 0.5 means the crystallite is well-oriented for the deformation mechanism, while a value of m = 0 means the mechanism is not possible. When the stress tensor contains negative elements, i.e. when the crystallite is under a combination of tensile and compressive loads, the value of m ranges between 0 and 1.0, with 1.0 representing the case of pure shear. The full derivation of this value is shown in Section 4.8.

The SF has been shown to be an accurate predictor for active mechanisms in single crystals. In polycrystals, however, the local stress state on an individual crystallite may be significantly different than the applied stress tensor. For example, Abdolvand et al. [22] recently showed that grains in Zr and Ti exhibit strong neighbour effects, to the point that the stress along the loading direction could even decrease during tensile plastic flow. This local heterogeneity can result in deformation behaviors in individual grains that are inconsistent with other grains of the same orientation. However, given a statistically large number of grains in a polycrystal, the average behavior of the grains is expected to follow Schmid's Law. By observing the relative plastic hardness of different grain families, the relative activity of different deformation mechanisms in the grain family can then be predicted by their CRSS and SF (NRSS in the case of multiple slip). This forms the basis for interpreting *in situ* diffraction experiments.

1.1.1   Deformation Mechanisms in Magnesium AZ31

Magnesium AZ31 is one of the most commonly used wrought alloys of Mg. The addition of alloying elements Al and Zn has been shown to increase the strength of Mg by strengthening and softening the slip on basal and prismatic planes, respectively [23–25]. Yasi et al. [26,27] confirm the behavior with first-principles modelling. The addition of the alloying elements also slightly increases the *c/a* ratio [28], but the effect on the deformation is minimal in comparison to the solid solution strengthening effect.

	CRSS (MPa)	Relative CRSS ($\mathrm{CRSS}_X/\mathrm{CRSS}_{Ba\langle a\rangle}$)				
Model [Ref.]	$Ba\langle a\rangle$	$Pri\langle a\rangle$	$Pyr\langle a\rangle$	$Pyr_{2nd}\langle c+a\rangle$	ETW	CTW
TEM [29]	--	2-2.5	--	--	--	--
EPSC [30]	10	5.5	--	6	3	--
VPSC [31]	25	3.2	--	5	1.5	--
EPSC [32]	12	5	--	8.3	4.5	--
EPSC [33]	30	2.7-3	2.7	3.2-3.3	1.2	--
VPSC [34]	2	30	--	25	27.5	--
NVPSC [35]	17	6.4	--	17.1	9.7	20
VPSC [36]	28	3.9	--	3.4	0.1	--
EVPSC [37]	17	5	--	5.9	1.2	--
EVPSC [38]	12	6.5	--	8.3	2.9	--
MS-EPSC [39]	49	2.8	--	5.1	6.5	--
EPSC [2]	4	4.8	--	18.8	1	--
EVPSC [40]	25	3.9	--	12.6	1.4	--
EVPSC-TDT [6]	12	6.3	--	8.3	2.5	14.2

Table 1-2 Literature data for relative CRSS values of Mg AZ31 at room temperature.

A non-exhaustive list of the CRSS values reported in literature for dislocation slip and twinning at room temperature are shown in Table 1-2. It is generally agreed upon that $Ba\langle a\rangle$ slip is the easiest slip mechanism at room temperature, followed by $Pri\langle a\rangle$ and $Pyr\langle a\rangle$ slip. There is not good agreement on the role of $Pyr\langle a\rangle$ slip, which is difficult to distinguish in post-mortem tests because the same deformation can be achieved by cross-slip between basal and prismatic planes. Thus, models generally omit $Pyr\langle a\rangle$ slip completely (Table

1-2). However, *in situ* neutron diffraction by Muránsky et al. [33] given evidence that it is active although not as much relative to the other $\langle a \rangle$ slip mechanisms.

Deformation involving $\langle c + a \rangle$ slip have the highest CRSS of all slip mechanisms. TEM studies on pure Mg by Stohr and Poirier [41] and Agnew et al. [42] separately observed their presence, but their role in the deformation was difficult to understand due to their tendency to dissociate and the small probe size of TEM. *In situ* XRD experiments by Máthis et al. [43] showed that the activity of $\langle c + a \rangle$ slip increases with increasing deformation temperature, but is relatively low at room temperature. The relative activity of non-basal slip has been shown to depend strongly on texture and loading path [5,44,45]. Steglich et al. [36] even reported that $Pyr_{2nd}\langle c + a \rangle$ slip was the second most active mechanism after $Ba\langle a \rangle$ slip. However, the model uses $\mathrm{CRSS}_{Pyr_{2nd}\langle c+a \rangle} < \mathrm{CRSS}_{Pri\langle a \rangle}$, which has not been reported elsewhere, and is validated only with *ex situ* measurements.

Due to the difficult activation of $\langle c + a \rangle$ slip mechanisms, $\{10.2\}\langle 10.1 \rangle$ extension twinning is readily observed in Mg alloys. The CRSS for extension twinning is generally considered to be between that of $Ba\langle a \rangle$ and $Pri\langle a \rangle$ slip (Table 1-2). The twin reorients the crystal lattice by 86.3°, resulting in a significant texture change and introduces highly misoriented grain boundaries into the parent grain. In this way, twinning can reduce the mean free path of dislocation slip as dislocations interact strongly with the twin boundaries. Serra and Bacon [46–49] showed that dislocations annihilate at extension twin boundaries and can activate twinning dislocation sources within the twins. More recent studies have investigated the transmutation of dislocations crossing twin boundaries [50–54]. The process results in multiplication of different types of dislocations in the twin that cause latent hardening [52]. On the other hand, the presence of twins can result in the easy accomodation of strain by detwinning when the direction of the shear stress is reversed. Crystal plasticity models of Mg AZ31 incorporating detwinning consider the CRSS of detwinning to be roughly the same as [55,56] or lower than [34,57] the CRSS of twinning. It has been shown to cause hysteresis in tension-compression studies of Mg alloys [2,34,58–60].

Generally, twinning in Mg alloys follows Schmid's Law. However, EBSD studies by Beyerlein et al. [61,62] and others [63,64] have shown that the active twin variant does not necessarily correspond with the lowest SF. Instead, the selected variant depends strongly on the ability of the neighbouring grains to accomodate the twin deformation by prismatic glide [63,65]. Other types of twinning such as $\{10.3\}$ CTW and $\{30.4\}$ CTW [66,67] and $\{10.2\} - \{10.1\}$ double twinning can result from the local accomodation effects [63,68–71]. However, the strain accomodated by these mechanisms is minor compared to the main modes.

1.1.2   Deformation in multi-phase Ti-6Al-4V
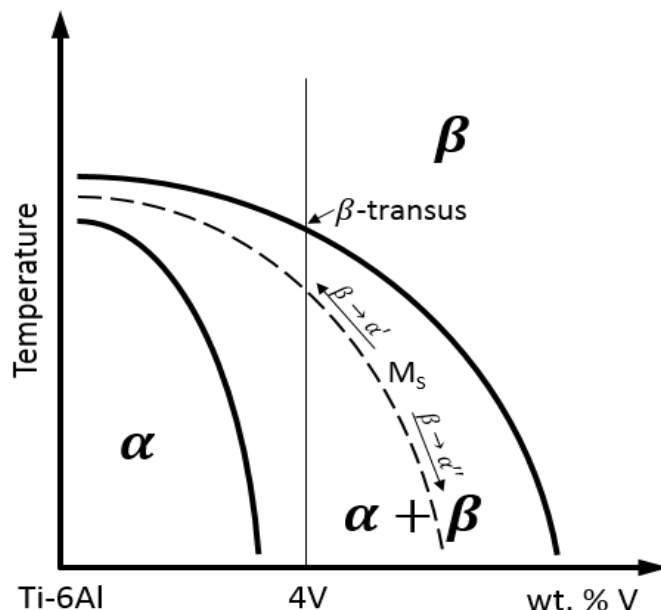
Figure 1-3 Schematic phase diagram of Ti-6Al-(X)V. M_S is the martensite start temperature.

Ti-6Al-4V is the most commonly used Ti alloy, accounting for an estimated 50% of Ti usage in the world. Pure Ti can exist as two main crystallographic phases: below a transus temperature of 882°C [72] it is α phase (HCP) and above the transus it is β (BCC). The addition of alloying elements changes the β transus temperature such that multiple phases can exist in tandem. Al is an α stabilizer and raises the β transus, while V is a β stabilizer that lowers the transus. A schematic phase diagram for Ti-6Al is shown in Figure 1-3. By heat treating at temperatures below the β transus, a dual-phase microstructure with different volume fractions of α and β phase is formed. At high cooling rates, β undergoes a martensitic transformation. At 4 wt.% V, the β tranforms to HCP α' martensite. The martensite is enriched in β stabilizers and thus has slightly smaller lattice parameters than the α phase.

The mechanical properties of multi-phase Ti-6Al-4V result from the load-sharing between the mechanically distinct phases. The β phase is plastically soft compared to the two HCP phases due to its cubic crystal structure, while the α phase is strong because of its limited number of low-CRSS independent slip systems. The mechanical behavior of α' martensite, on the other hand, is less certain. Traditionally, the martensite is considered a strong, brittle phase due to several studies of dual-phase $\alpha + \alpha'$ alloys that exhibited increased yield strength and low elongation to failure [73–77]. Thus, the phase has mainly been used as an intermediate decomposition phase for producing bimodal α-phase microstructures. However, work by Matsumoto et al. [78,79] achieved high ductility in $\alpha + \alpha'$ Ti-6Al-4V, citing cross-slip between the two phases. Zafari et al. [80] were able to achieve elongation before failure of 14-15% in a fully α' martensite, albeit with significant necking. De Formanoir et al. [81,82] achieved a high-work hardening and ductility in a dual-phase $\alpha + \alpha'$ Ti-6Al-4V, with the work hardening at low stresses suspected to come from early plasticity in the martensite. Thus, significant evidence exists that martensite can be an effective strengthening phase in Ti-6Al-4V without sacrificing ductility.

Other metastable crystallographic phases have been observed in Ti alloys: α'', isothermal and athermal ω, and β'. The β' phase forms only in solute-rich β alloys and has not been reported in Ti-6Al-4V. Athermal

ω forms in alloys with high concentrations of β-stabilizers and has only been observed in Ti-V alloys with V concentrations greater than 15 wt.% V. Additionally, Al suppresses the formation of ω. Thus, this phase has only been reported as thin planar interface complexions in Ti-6Al-4V, where local concentrations of V can become very high close to martensite phase boundaries [83]. The α'' phase, on the other hand, is an orthorhombic (OR) martensitic phase that has been reported in Ti-6Al-4V when quenching from below 900°C [84]. The $\beta \rightarrow \alpha''$ transformation is favored over α' at higher β-stabilizer solute contents (Figure 1-3), which can occur by partitioning of V to the β phase during annealing. The OR structure comes from a distortion of HCP structure due to the high β-stabilizer solute content. The phase is often referred to as "soft" martensite due to an OR→HCP transformation under strain [85].

1.1.3   Deformation Mechanisms in Commercially Pure Ti (Grade 2)

Commercially pure Grade 2 Ti (CP-Ti) sheet is used extensively for structural components in the medical, aerospace, and chemical processing industries. Pure Ti is an α-phase alloy with a c/a ratio around 1.588. Recently, several groups have reported a three-stage work hardening during tensile loading [86–88]. Previously, this behavior has only been reported in CP-Ti for compressive loading as the result of low-CRSS twinning and subsequent work hardening by twin boundary-dislocation interaction [89–93]. Additionally, the material has been shown to exhibit a strong, non-linear plastic recovery during unloading that results in considerable springback [8,94]. The effect has been proposed to be the result of microstrain due to a Bauschinger behavior [9] but no prior literature exists with experimental evidence of these theories.

Model [Ref.]	CRSS (MPa) $Pri\langle a \rangle$	Relative CRSS ($\mathrm{CRSS}_X/\mathrm{CRSS}_{Ba\langle a \rangle}$)			
		$Ba\langle a \rangle$	$Pyr\langle a \rangle$	$Pyr_{1st}\langle c+a \rangle$	$Pyr_{2nd}\langle c+a \rangle$
TEM + Slip trace analysis [95]	120	1.5	1.2	2.0	--
CPFE single crystal [96]	181	1.2	--	2.6	--
CPFE single crystal [97]	150	2.3	--	7.4	--
Taylor-type modelling [98]	--	6.0	--	9.0	--
VPSC [99]	90	2.5	--	9.4	--
EPSC [100]	80	1.1	1.4	3.3	--
VPSC [101]	57	4.8	2.9	5.4	4.1
EPSC [102]	68	2.6	1.8	3.7	--
EVPSC [88]	141	1.8	1.4	2.4	2.5
EVPSC [103]	50	2.4	1.8	1.3	3.0

Table 1-3 Literature data for relative CRSS values of CP-Ti at room temperature.

A non-exhaustive list of the CRSS values reported in literature for dislocation slip and twinning at room temperature are shown in Table 1-3. Unlike Mg, $Pri\langle a \rangle$ slip is the easiest slip mechanism at room temperature, followed closely by $Pyr\langle a \rangle$ slip. $Ba\langle a \rangle$ slip is also commonly observed, although the reported CRSS values can range from 1.25 to 1.65 times higher than $\mathrm{CRSS}_{Pyr\langle a \rangle}$. An XRD study by Warwick et al. [104] even suggests that $Ba\langle a \rangle$ slip could have a lower CRSS than $Pyr\langle a \rangle$ slip. As in Mg, $\langle c+a \rangle$ slip is harder than the $\langle a \rangle$ slip mechanisms but is much more active during tensile deformation of Ti. This can be explained by the smaller c/a ratio and higher twinning shear for extension twinning (Figure 1-2).

The relative activity of twinning in CP-Ti during tensile deformation is extremely sensitive to the chemical composition. For example, small impurities of oxygen (0.11+ wt.%) can significantly suppress deformation twinning [105]. Thus, reports of twinning in CP-Ti vary significantly. Becker et al. [87] observed $\{11.2\}\langle \bar{1}\bar{1}.3 \rangle$ CTW and $\{10.2\}\langle 10.1 \rangle$ ETW of up to 18.3% and 2.8% area percent, respectively, and thus

concluded that the three stage work hardening was due to twinning. Conversely, Roth et al. [86] and Amouzou et al. [88] observed that the three-stage hardening was still present despite almost no twinning (<0.5% and 5.7% vol. fraction for rolling and transverse direction samples, respectively) at the same strain rates. The deformation behavior should therefore be considered for each specific composition.

The twinning mode is also very sensitive to the loading direction with respect to the texture. The main twinning system during tensile loading transverse to the rolling direction is $\{10.2\}\langle10.1\rangle$ extension twinning, which causes an 84.8° rotation of the parent lattice structure [86,87]. Along the rolling direction, compression twinning has been observed even during tensile loading. Roth et al. [86] observed primarily $\{10.2\}\langle11.\overline{3}\rangle$ compression twins with some $\{10.2\}\langle10.1\rangle$ extension twins during loading of a CP-Ti along the rolling direction.

The large CRSS differences in α-Ti (Table 1-3) give rise to an initial period in which plasticity is dominated by single slip on low-CRSS slip systems. Dislocation generation and glide is relatively easy during this period as there is no secondary system of dislocations to act as obstacles to slip. The result is the formation of long, planar dislocation pile-ups, for example by Han et al. [106]. A significant stress inhomogeneity is expected to develop at low strains between plastically soft grains which can deform by $\langle a \rangle$ slip and hard orientations which require $\langle c + a \rangle$ slip.

1.1.4 Research outline

In this thesis, the plastic deformation mechanisms of various HCP alloys are examined using state-of-the-art *in situ* mechanical test techniques. This is presented as a collection of published articles and unpublished work, outlined below:

Chapter 2: The experimental methods and technical details of the experiments are presented. These are elaborations from the experimental methods presented in each chapter, with a focus on sample preparation and the fundamental principles of *in situ* test techniques used in this thesis.

Chapter 3: The results of a finite element analysis study to examine the idea of a composite, bottom-up approach to cruciform design are presented.

Chapter 4: The plastic deformation mechanisms of cold-rolled Mg AZ31B during tension-tension strain path changes are examined with *in situ* neutron diffraction and acoustic emission. The full work is published in Acta Materialia: https://doi.org/10.1016/j.actamat.2018.10.033.

Chapter 5: The enhanced work-hardening behavior of a Ti-6Al-4V alloy prepared by electron beam melting and a novel thermal post-treatment is examined with *in situ* x-ray diffraction and high resolution digital image correlation. The results from *in situ* uniaxial tension tests are submitted to Acta Materialia: Under Review.

Chapter 6: The work-hardening and springback behavior of commercially pure Ti sheet is examined with *in situ* x-ray diffraction. The results from *in situ* uniaxial tension tests are submitted to Acta Materialia: Under Review.

Chapter 7: A summary of the most important findings in this thesis is presented. This chapter also gives suggestions on the future development of *in situ* test techniques for studying multiaxial plastic deformation in polycrytalline metals.

Chapter 2   Experimental Methods

2.1   Sample Preparation

2.1.1   Cruciform Design

Significant effort has been invested into optimizing cruciform-shaped samples over the last two decades. Qualities of the ideal cruciform shape were outlined by Deng at el. [107] and the most important points can be summarized below:

(1) The stress and strain distribution in the gauge section should be spatially uniform over the entire deformation. Only in-plane stresses should develop in the gauge section during loading.
(2) Large strains should be able to be achieved in the test section before failure. Failure should initiate in the gauge section.
(3) The influence of the arms on one another (called "cross talk" or the "ring effect") should be minimized.

Point (1) defines the most important consideration of cruciform testing: namely, the development of the desired uniform in-plane stress state within the gauge section. Consider a three-dimensional Cartesian basis with axes 1 and 2 along the arms of a cruciform sample and axis 3 out-of-plane with the cruciform sheet. The stress state at the center of the cruciform can be described by the equivalent (von Mises) stress σ_v [108]:

$$\sigma_v^2 = \frac{1}{2}[(\sigma_{11} - \sigma_{22})^2 + (\sigma_{22} - \sigma_{33})^2 + (\sigma_{33} - \sigma_{11})^2 + 6(\sigma_{23}^2 + \sigma_{31}^2 + \sigma_{12}^2)] \tag{2-1}$$

where σ_{11}, σ_{22}, and σ_{33} are the resolved stress components and σ_{23}, σ_{31}, and σ_{12} are the resolved shear stress components of the Cauchy stress tensor. The von Mises stress is a scalar value of stress that can be used to predict the yield of ductile materials, such as metals, under complex load states. A uniform stress state is particularly important for *in situ* diffraction testing, as stress inhomogeneity in the coherent scattering volume can cause artificial peak broadening or asymmetry due to the cruciform shape. Shear and rotation in the gauge section should be avoided to ensure that the forces measured at the arms are the same forces applied to gauge section. In this ideal case, the shear components $\sigma_{23} = \sigma_{31} = \sigma_{12} = 0$, the out-of-plane stress component $\sigma_{33} = 0$, and in-plane stress components σ_{11} and σ_{22} at the center could then be well-approximated by dividing the applied force by the cross section of the arms.

Points (2) and (3) arise as inherent complications of the cruciform-shaped geometry. Point (2) simply states that the cruciform should be able to reach enough strain to examine the desired mechanical phenomena before failure. The cruciform geometry necessarily results in stress concentrations at the corners of the gauge section or in the arms. This is particularly important for low-work hardening materials, as stress concentrations outside of the gauge section can quickly lead to unstable plastic flow and premature failure of the specimen.

Point (3) refers to the development of an additional compressive stress that forms on the transverse axis while loading uniaxially on one axis. Dubbed "cross talk" or the "ring effect", it can be thought of as an additional geometric Poisson contraction due to a linear deformation along a non-uniform cross-section [11,109,110], as if pulling on a rubber ring. *In situ* experiments by Van Petegem et al. [11] showed that significant in-plane compressive stresses developed during unixial loading of cruciform-shaped specimens, which resulted in different elastic lattices strain evolutions between the cruciform and dogbone samples under uniaxial load. In other words, a uniaxial load on a cruciform sample results in a multiaxial stress state

at the center of the sample. Assuming that the stress state is planar, the effect can be measured as the ratio of the strain along the principal axes: $\varepsilon_{11}/\varepsilon_{22}$. Theoretically, the effect could be compensated for by applying a load along the transverse direction; practically, however, this would be difficult as the ring effect has been shown to vary non-linearly with the applied load depending on the cruciform geometry and elastic-plastic properties of the material [111]. Thus, in practice, the strain evolution at the cruciform center must always be measured to account for this effect.

Points (1), (2), and (3) can be addressed by parametric finite element analysis (FEA) studies. FEA is a computational technique to approximate the continuous evolution of variables over a complex shape. The shape is subdivided into small, simple elements, such as an 8-node "brick" or 4-node tetragon, the equations are solved at each node, and the result is propagated as the starting conditions for the nodes on the next element. For cruciform design, FEA is used to study the effect of various geometric features on the stress and strain evolution in the sample during deformation. The main geometric features are discussed below with respect to the effect they have on the stress and strain evolution in the gauge section as well as implications on *in situ* diffraction studies.

Three-fold symmetry of the cruciform: The cruciform should be symmetric along the three principle directions to ensure the development of uniform stresses at the center of the cruciform. Symmetry out-of-plane with the loading directions is necessary to avoid bending moments. This precludes sample designs that have a thinned test section only on one side.

Arm length: The length of each arm, defined loosely as the distance between the grip and gauge section, should be chosen such that it is long enough to result in a uniform stress distribution where the arm meets the gauge section. Additional arm length does not significantly affect the stress and strain distribution in the gauge section.

Type of grip: In principle, the type of grip does not affect the deformation if the arm length is long enough. The grip design should be chosen based on the available tensile loading machine and the desired stress levels.

Arm width: Wider arms allow for a larger gauge section, which is beneficial for the formation of a spatially uniform stress field at the center of the sample. A larger area of uniform thickness leads to a larger area with uniform stress distribution in the center. However, increasing the width of the gauge section means that higher loads are necessary to reach the same stresses at the center, so the load limits of the machine must be considered.

Radius of curvature between the arms: A fillet is used to reduce the stress concentration at the intersections of the arms. A larger fillet radius reduces the stress concentration. However, a larger fillet radius also increases the stress in the arms versus the gauge section and the ring effect. Thus, the radius should be chosen as small as possible such that the stress concentration at the intersection of the arms is minimized.

Slots in the arms: Slots are introduced in the arms to improve the spatial homogeneity of stresses at the center of the gauge section (Point (1)). In the ideal case, the stress could be calculated as the force divided by the area of the gauge section. Slots also have a secondary beneficial effect in that they can deflect out-of-plane, which can mitigate out-of-plane moments and shear due to imperfections in sample alignment or shape [111,112].

Reduced gauge section: Reducing the thickness of the gauge section with respect to the arms is the primary way to localize the deformation towards the center of the cruciform sample (Point (2)). An area of uniform reduced cross section should be maintained at the center to ensure a uniform stress distribution within the gauge volume. A fillet or chamfer should be introduced wherever the gauge section is thinned to eliminate stress concentrations from the change in thickness.
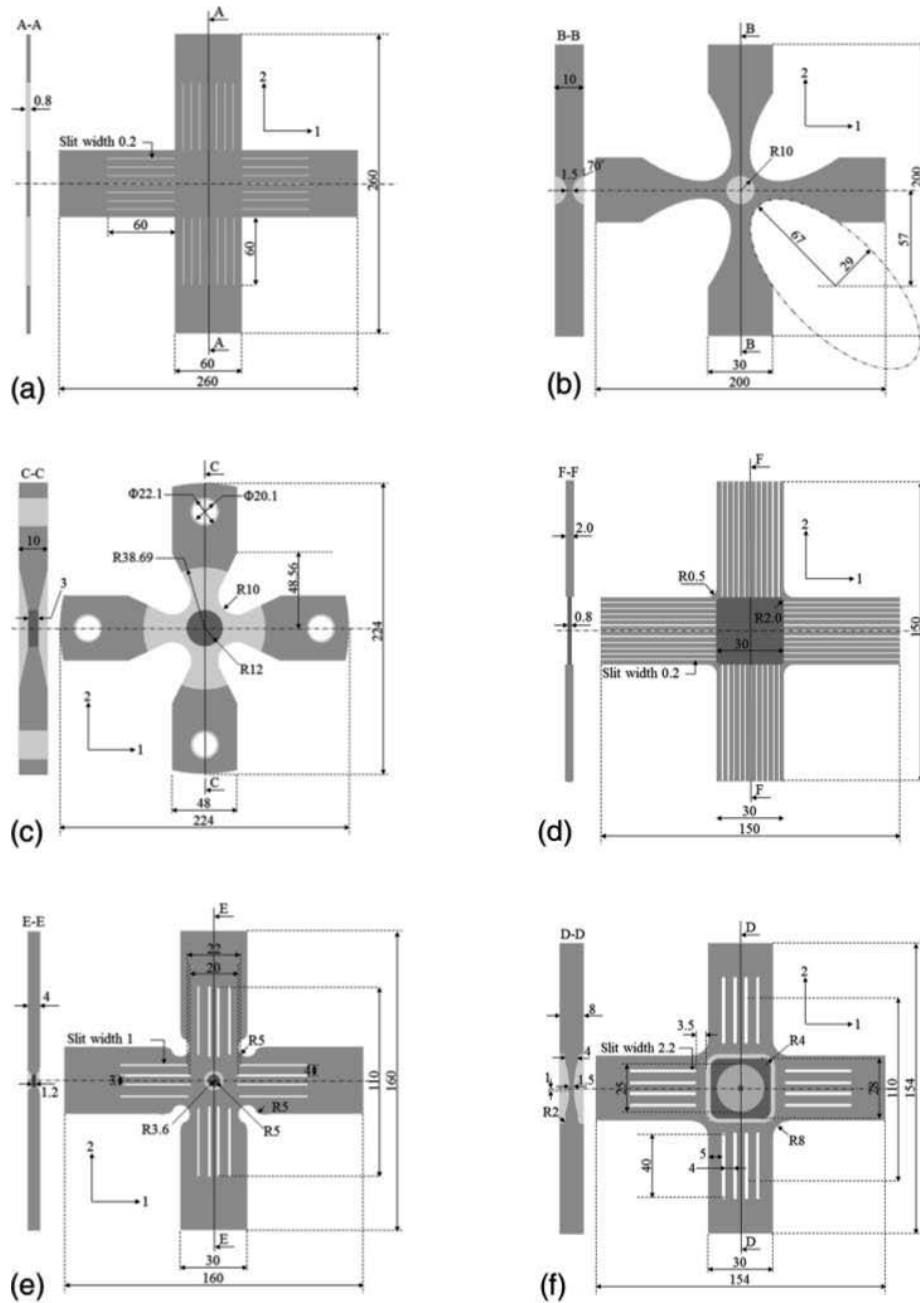
Figure 2-1 Various cruciform designs found in literature. Figure adapted from [111].

A variety of cruciform designs from literature are shown in Figure 2-1. Flat cruciforms (with no reduced gauge section) are the simplest and most cost-effective cruciform designs. However, they will necessarily develop stress concentrations outside of the gauge section and thus can only be used for applications where high strains are not necessary. Müller and Pöhlandt [113] used a flat cruciform without slots to determine the yield loci over of unalloyed steel and Al alloy AlMgSi. Slots can be added to improve the gauge stress

distribution, as is done in the current ISO standard for cruciform biaxial tensile testing, Figure 2-1a [114]. Kuwabara et al. [115] employed a similar flat design with slots in the arms to study the evolution of plastic work contours in low-carbon steel over equivalent plastic strains of $\varepsilon_0^p \leq 0.03$. Huh et al. [116] used the same design to study the strain rate effect on the yield loci of a TRIP steel. The slotted arms and wide square test section result in a homogeneous plastic strain evolution over the gauge section but develop highly localized stresses at the tips of the slots.

Higher plastic strains can be realized in cruciforms with a thinned gauge section. Several groups [109,110,117] developed cruciforms with a continuously thinned gauge section to ensure crack initiation at the center during fatigue testing. One such cruciform, produced by Baptista et al. [117], is shown in Figure 2-1b. However, the continuous variation in gauge cross-section necessarily causes an inhomogeneous stress distribution at the center, as previously noted by Wilson and White [118]. This is particularly detrimental for *in situ* diffraction studies, where it can cause artificial peak broadening unrelated to the material. Thus, designs have been developed with a uniform reduced gauge section [119,120], as in Figure 2-1c. Such designs have been used successfully for multiaxial *in situ* diffraction studies of 316L steel [11] and Mg AZ31 [4]. However, the design is not ideal, as it has a large ring effect due to the large corner radius between the arms and develops the highest stress concentrations at the corners.

The best cruciform designs use a combination of slots in the arms and a reduced gauge section. Deng et al. [107] designed a cruciform with slots all the way to the edge of the gauge section and a sharp transition from the gauge section (Figure 2-1d). They suggest that the sharp transition to the gauge section reduces the area which is affected by the stress concentrations at the slot tips, and show by FEA that the stress distribution should be very uniform over 80% of the gauge section. However, DIC measurements show that strain localizes at one of the corner slot tips, which will lead to premature failure of the sample. To mitigate this problem, the slots are typically offset from the reduced gauge section to reinforce the slot tips by the thickness of the arm. Liu et al. [121] use a 4-slot design with the slots offset different distances from the reduced gauge section (Figure 2-1e). Additional spacing between the outer slots and the arms edge shifts the highest stress concentrations to the tips of the interior slots. They also show that the larger the ratio between the arm and gauge section thickness, the higher the stress concentrations will be in the gauge section, using a thickness ratio of at least $t_{\mathrm{arm}}/t_{\mathrm{gauge}} = 3.33$.

The most optimized modern cruciform designs follow the shape in Figure 2-1f. This cruciform employs straight arms with a filleted corner, a rounded-square, two-step reduced gauge section, and slots in the arms offset from the gauge section. The design is based on work from Hayhurst et al. [122] and Kelly et al. [112], who proposed a similar design with a single-step reduced gauge section. However, the thickness ratio $t_{\mathrm{arm}}/t_{\mathrm{gauge}}$ was only 1.31 and 1.5 for the respective studies, too low to effectively shift the stress to the center, and both studies used notches very close to the reduced gauge section. Makinde et al. [123] attempted to optimize this design for several geometric parameters, notably saying that $4 \leq t_{\mathrm{arm}}/t_{\mathrm{gauge}} \leq 6$. The spacing of the slots and distance to the gauge section was not, however, studied. Zidane et al. [124] shifted the slots away from the gauge section and added an additional thinning step to the gauge section ($t_{\mathrm{arm}}/t_{\mathrm{gauge}} = 4$). Fracture consistently occurred in the center of the sample, regardless of load path. Upadhyay et al. [111] further optimized the design by increasing the distance between the outer slots and the arm edge, resulting in a cruciform with the highest stress and strain in the gauge section of the samples.

Regardless of design, it is now generally accepted that the stress state in the gauge section cannot be easily estimated from the applied forces. Upadhyay et al. [111] performed a FEA study of the gauge stress

and strain evolution in the six cruciform geometries shown in Figure 2-1. The simulations show that the gauge stresses in the elastic regime can be related as a linear combination of the applied forces, as previously proposed by Hoferlin et al. [125] and Bonnand et al. [126]. After plastic deformation begins, however, the stress evolution becomes very non-linear. Upadhyay showed that the stress evolution is always non-linear with a linear load or displacement control, and thus emphasized the use of FEA to evaluate the stress evolution with measured strain and applied load data. He also presented a design where the ring effect was significantly mitigated (but not completely eliminated) versus existing samples. Thus, the design addresses Points (1), (2), and (3). The downside of the design is that it contains many complex features that make it very difficult and expensive to produce.

2.1.2   Ultrashort-Pulsed Laser Ablation

In some cases, materials are not available in large quantitites due to cost or the specific techniques required to produce them. For example, in this thesis, an additive-manufactured Ti-6Al-4V alloy is annealed within quartz tubes which restricts two of the dimensions of the material to <15 mm. This makes it difficult to produce complex cruciform designs. For example, directly scaling the Upadhyay cruciform design to test this Ti-6Al-4V requires features on the scale of 10s of μm with tolerances <10 μm. Various micromachining techniques exist for metals, including lithography, micro-electro discharge machining (micro-EDM), micromilling, and laser ablation [127]. Lithographic techniques are restricted to building moulds for metal deposition or electroplating rather than operating on existing bulk material. Micro-EDM is excellent for producing complex profiles, but degradation of the workpiece during machining and precision motion control make it a very expensive process. Micromilling with ultra-high precision tools is promising, but suffers from similar problems to micro-EDM. Laser ablation offers an attractive solution some of the problems faced by the other techniques: high precision control, easily adjustable ablation rates, and high design flexibility for creating 3D profiles.

Traditional laser ablation can lead to significant photothermal effects such as melting, phase transformation, and thermal stress gradients built up in a large heat affected zone (HAZ). However, by pulsing the laser below the thermalization time (10^{-10}-10^{-12} seconds for metals), ablation can occur by photochemical processes without inducing a significant rise in material temperature. Such techniques are collectively called ultrashort-pulsed laser ablation. High energy densities expel material rapidly so less energy is transmitted to the lattice, resulting in a significantly reduced HAZ as compared to laser ablation with longer pulse times [128–130]. Therefore, ultrashort-pulsed laser ablation is an effective technique for milling cruciforms with minimal thermal damage to the material being studied.

In this study, small-scale cruciform shapes were manufactured using a frequency-tripled Nd:YAG picosecond pulsed laser at the Swiss Federal Laboratories for Materials Science and Technology (EMPA). The laser was operated with a pulse width of 10 picoseconds and wavelength $\lambda = 355$ nm. The 10 ps pulse duration is in the range of the thermalization time of metals [131,132], so both thermal and athermal ablation mechanisms are expected. However, by proper control of fluence, pulse frequency, and laser scanning parameters, microstructure damage can be minimized and kept within 100s of nanometers of the surface [133–135]. Molecular dynamics simulations have even shown that the larger heat affected zone created by picosecond pulsed laser ablation (versus femtosecond pulses) may anneal defects and fill voids created during ablation [136]. Using the same laser as in this research, Guitton et al. [137] showed with Laue microdiffraction that damage to the initial microstructure of Cu sheet did not affect bulk diffraction

properties. Thus, ultrashort-pulsed picosecond laser ablation was chosen as an appropriate method for preparing small-scale samples shown in this thesis.

2.1.3 High Resolution Digital Image Correlation Patterning
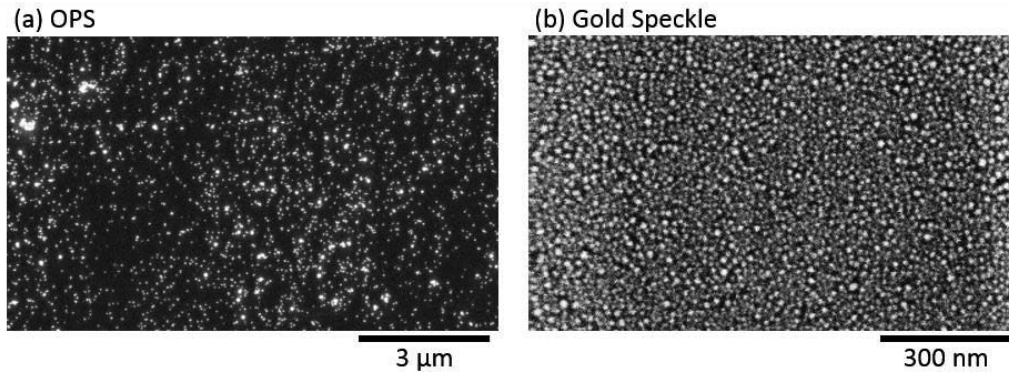
Figure 2-2 BSE micrographs comparing the length scale of HRDIC patterns on Ti-6Al-4V. (a) OPS pattern at 1,800x magnification and (b) gold speckle pattern at 12,000x magnification.

For the Ti-6Al-4V, two different patterning techniques were applied to study the material deformation at two different length scales. The two resulting patterns are shown in Figure 2-2. Colloidal silica polishing suspension (OPS) was applied using a technique developed by Yan et al. [13] to achieve 2,000-4,000× magnification. Sputtered gold particles were applied using a technique developed by Gioacchino et al. [14] to achieve 12,000-14,000× magnification. The exact procedures were modified for the Ti-6Al-4V used in this study and are presented below.

Samples were first polished to achieve a mirror-like surface for EBSD imaging. The pre-cut dogbones were mechanically ground using SiC sandpaper with decreasing grit size (320, 600, 800, and 1200 grit) and then polished with 3 µm and 1 µm diamond paste to remove surface roughness. Final polishing was performed for 45 minutes using 0.1 µm OPS to achieve a mirror-like surface. Samples were vibration polished for 12 h in a Buehler Vibro-met2 with Buehler Mastermet2 polishing suspension to relieve residual surface stresses.

Colloidal Silica Polishing Suspension (OPS) Pattern

The OPS pattern was applied manually using a dedicated 0.05 µm OPS solution. The quality of the solution is important, as the same procedure did not work with a three-year old solution in which the OPS had agglomerated. The procedure is outlined below:

1. Flush a dedicated polishing cloth with distilled water. Remove the excess water when the cloth is visibly clean—the cloth should be damp.
2. Using a pipette, apply 20-30 drops of 0.05 µm OPS solution to the cloth in a ring.
3. Applying light pressure, just enough that the sample does not move under your finger, hold the sample in the ring of OPS solution for 30 seconds at 50 RPM
4. Dip the sample in ethanol for 1 second.
5. Dip the sample in distilled water for 1 second.
6. Allow the sample to dry completely in air. Do not wipe or blow dry the sample as it may cause agglomeration of the particles.

7. Repeat steps 1-5, adjusting the patterning time (Step 3) to achieve thicker or sparser pattern densitites.
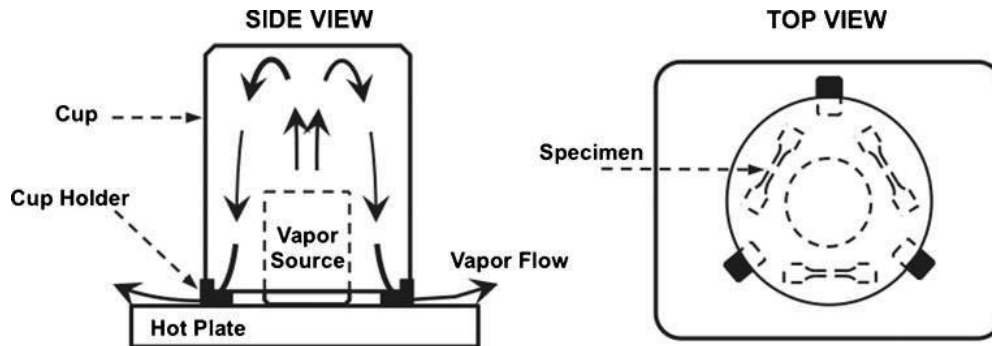
Gold Speckles

Figure 2-3 Setup for remodelling the gold sputter layer. Figure from [14].

The gold speckle pattern is made by remodelling sputtered gold. Gold is first sputtered on the sample for 30 seconds. The sputtering time may be adjusted according to the desired thickness of the Au layer. Remodelling is performed using the setup in Figure 2-3. The sample is placed on a hot plate with a beaker of distilled water and covered by a larger beaker. Spacers between the large beaker and hot plate allow air flow between the remodelling environment and external atmosphere. The water vapour prevents the clustering of the gold particles during remodeling above 240°C. The optimum remodelling conditions for this Ti-6Al-4V were 300°C for 60 minutes. However, the temperature and time should be adjusted to optimize the Au pattern density and morphology of the speckles. Due to the warm, wet environment, there is a risk of oxidation during remodelling. Oxidation of the sample surface can lead to brittle cracking at the surface. This should be considered when selecting optimum parameters for remodelling.

2.2   *In Situ* Mechanical Testing

2.2.1   *In Situ* SEM Techniques

Quasi-in situ EBSD

Two *in situ* SEM techniques were used in this work: quasi-*in situ* electron backscatter diffraction (EBSD) and high resolution digital image correlation (HRDIC). EBSD is a kinematic technique which measures electrons scattered back out of the material from an incident electron bream. Electrons diffracted in Bragg condition form Kikuchi bands which can be used to determine the orientation and phase of the diffracting volume. The beam is scanned across the surface, thereby providing a map of the crystallographic structure and phase across the surface of the sample. Taken at different points during deformation, the evolution of the EBSD pattern can show grain rotations (e.g. caused by dislocation activity), twinning and twin modes, and changes in grain size distribution and texture. The sample can be loaded incrementally *ex situ* and EBSD patterns are taken between loads, i.e. a "quasi-*in situ*" EBSD test. Transmission EBSD (also known as transmission Kikuchi diffraction, or TKD) follows the same principles as EBSD, but in this case the Kikuchi patterns are measured from electrons passing through the sample. This technique has been successfully applied for *in situ* mechanical testing [138]. However, the technique requires electron-transparent samples (maximum thickness about 3 µm for a light metal such as aluminum) and therefore is limited to ultra-fine grained or nanocrystalline metals to avoid sample size effects.

High Resolution Digital Image Correlation (HRDIC)
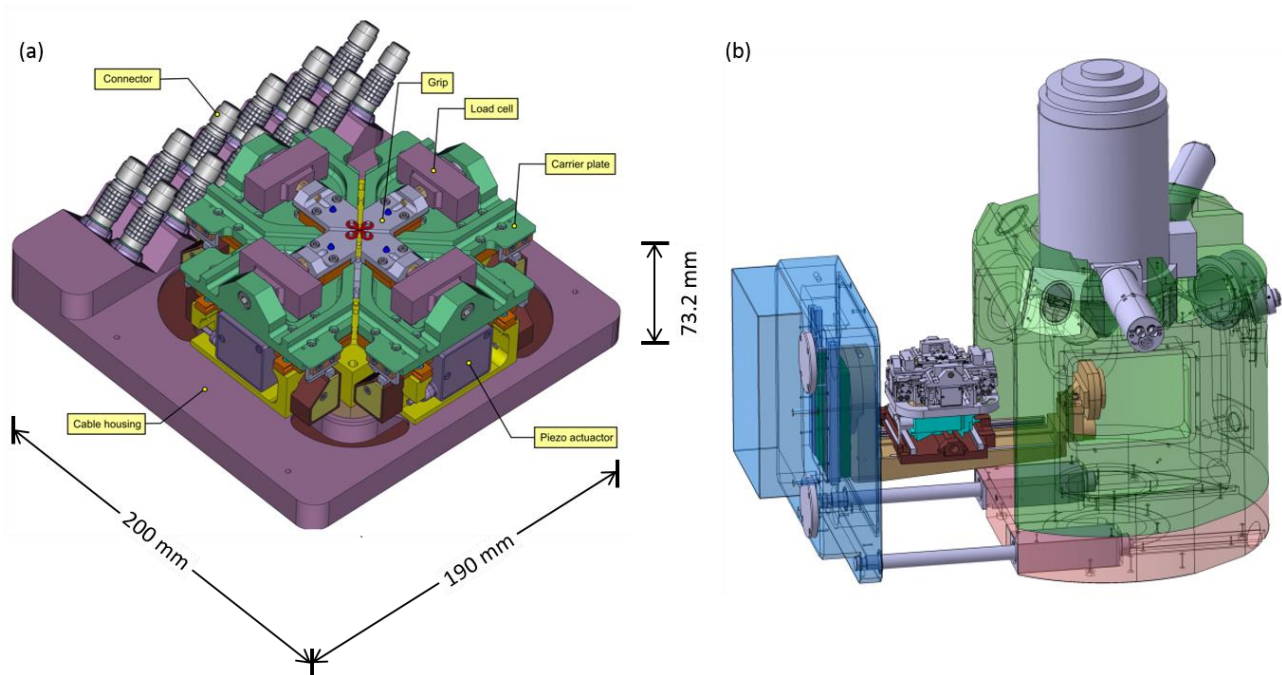
Figure 2-4 (a) Miniaturized multiaxial tensile machine for *in situ* XRD and SEM mechanical testing; (b) Model of the machine mounted inside an SEM chamber

High resolution digital image correlation (HRDIC) was performed using a miniaturized multiaxial tensile machine was designed for *in situ* XRD and SEM mechanical testing, shown in Figure 2-4. The dimensions of the machine ($190 \times 200 \times 73.2$ mm^3) are small enough that it fits within a standard SEM chamber. Four independent piezo-controlled arms can apply a load up to 44 N on each axis. Cruciform samples are mounted on pins at the end of each arm. A separate sensor array can be mounted on the machine to measure the actual displacement of each arm with a resolution of 1 nm. This array cannot be mounted inside of the SEM chamber. The machine can be run in piezo control, force control, or sensor-control. The small size of the machine makes it possible to test materials too expensive or not available in bulk, e.g. ultra-fine grained metals.

HRDIC follows the same principles as DIC but is performed at higher magnifications. DIC is an optical technique in which a surface pattern on a material is tracked as the material is deformed. The changes in the pattern can be used to measure full-field displacements and strains at the surface of the material. In HRDIC, the spatial resolution of the pattern can reach tens of nanometers over relatively large areas. The patterning techniques are described above in Section 2.1.3.

2.2.2 Fundamental Principle of *In Situ* Diffraction

In situ diffraction techniques allow for non-destructive measurements of the microstructure evolution during deformation. A sample is irradiated with a beam of x-rays or neutrons that pass through the sample and create a diffraction pattern based on the microstructure of the material. Multiple patterns are taken during loading and their evolution gives information about the evolution of internal strains, relative load sharing between families of similarly-oriented grains, changes in dislocation density and grain size, and twinning.
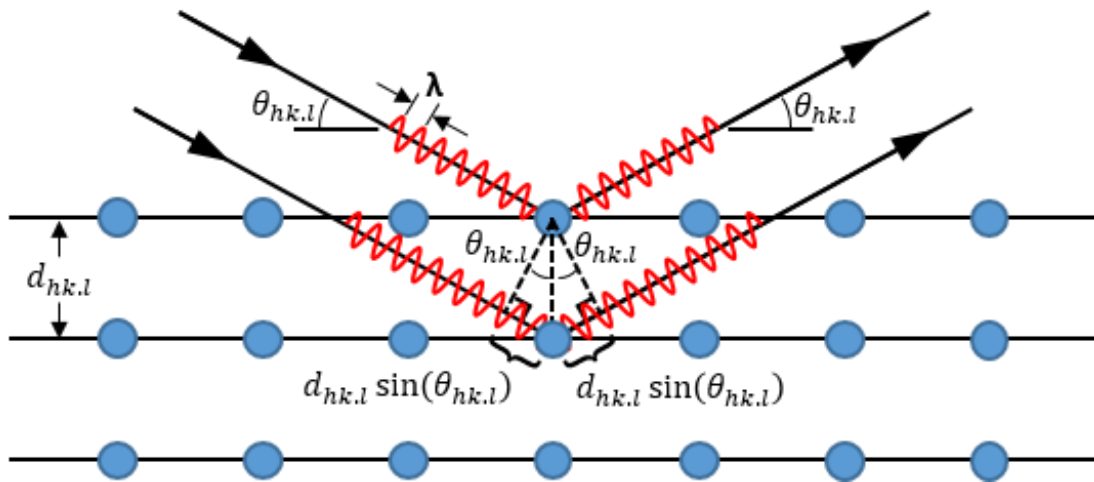
Figure 2-5 Schematic of coherent scattering according to Bragg's Law.

The basic principle behind both x-ray and neutron diffraction is the same: constructive interference of incoming x-ray or neutron beams interacting with a crystalline structure results in strong scattering at preferred angles. The angles are described by Bragg's Law:

$$n\lambda = 2d_{hk.l}\sin(\theta_{hk.l}) \tag{2-2}$$

where n is the order of the reflection, λ is the wavelength of the incoming beam, $d_{hk.l}$ is the lattice spacing for grain family $\{hk.l\}$, and $\theta_{hk.l}$ is half of the diffraction angle 2θ for the grain family. Bragg's Law is shown schematically in Figure 2-5. Each $\{hk.l\}$ grain family describes a set of grains oriented such that they fulfill Bragg condition. Scattering is measured either in reflection, where the beam does not pass through the sample, or in transmission, where it does. In this thesis, all samples were measured in transmission.

2.2.3 Single Peak Profile Fitting

For each diffraction pattern, the instrumental background is measured and subtracted and reflections are fit individually. Peak profiles are fit with an split Pearson VII function to capture the peak position 2θ, peak width (measured as full-width at half-maximum, FWHM), and peak shape of each $\{hk.l\}$ reflection. The function fits the peak on either side of the peak maximum independently, described by the equations:

$$P(\theta) = I_{\max}\left[1 + \left(2^{1/M_R} - 1\right)\left(10^{-\beta} + 1\right)^2 \left(\frac{\theta - \theta_0}{w}\right)\right]^{-M_R} \quad for\ \theta \geq \theta_0 \tag{2-3}$$

$$P(\theta) = I_{\max}\left[1 + \left(2^{1/M_L} - 1\right)\left(10^{-\beta} + 1\right)^2 \left(\frac{\theta - \theta_0}{w}\right)\right]^{-M_L} \quad for\ \theta < \theta_0 \tag{2-4}$$

where θ is the diffraciton angle, θ_0 is the angle at the peak maximum, $I_{\max}$ is the intensity of the peak, w is the peak width (FWHM), β is an asymmetry parameter, and M_L and M_R describe the shape of the decay to the left and right of the peak position, respectively. For M_L or $M_R = 1$, the peak profile is perfectly Cauchy (or Lorentzian); as M_L or $M_R \to \infty$, the peak profile becomes increasingly Gaussian.

The Pearson VII function was chosen as a versatile fitting method to capture both strain and size broadening measured by XRD. Experiments have shown that crystallite strain broadening can be approximated by a Gaussian function, while size broadening results in a Cauchy distribution [139–142]. Experimentally measured XRD peak profiles, then, can be better described by a convolution of these two functions than either one alone. The Pearson VII function can capture this dual behavior by varying the M

parameter. This could also be captured by a Voigt function [143], which is a convolution of the Gaussian and Cauchy functions, or a Pseudo-Voigt function, which approximates the Voigt function as a linear combination of the two [144]. The theoretical advantage of a Voigt function is the ability to deconvolute the size and strain broadening components. However, whole-powder-pattern modelling experiments by Scardi and Leoni [145,146] have shown that while line profile analysis for single peaks is effective for comparing relative microstructural changes, quantitative data about the size and strain is inaccurate. This is due to an *a priori* assumption of the line broadening sources, i.e. only a strain and size component in the Voigt function. The Pearon VII function avoids these assumptions and was thus chosen because it can fit a wider variety of peak shapes.

A split function was chosen to capture peak asymmetry which may arise during deformation. One source of peak asymmetry is peak overlap from mechanically different microstructures. For example, asymmetry was observed by Mughrabi et al. [147] due to composite behavior between cells and dislocation walls and Vidal et al. [148] as the result of a bimodal Cu grain distribution. In that case, the profile is fit with two separate peaks describing each distinct domain. However, a phase could have compositional gradients which result in a range of lattice parameters which can't be individually fit. Certain defects have also been shown to contribute to peak asymmetry, as has been extensively studied for planar faults (stacking faults and twin faults) in FCC metals [142,145,149–151]. In the materials examined in this study, the XRD peak profiles are generally symmetric and the split Pearson VII is able to capture that well by setting $M_L \approx M_R$. However, a split function was still used to avoid any *a priori* assumptions about the materials being studied.

Evolution of elastic lattice strains

Elastic lattice strains $\varepsilon_{hk.l}$ for a given $\{hk.l\}$ grain family can be calculated from the change in lattice spacing during deformation:

$$\varepsilon_{hk.l} = \left(d_{hk.l} - d_{hk.l}^0\right)/d_{hk.l}^0 \qquad (2\text{-}5)$$

where $d_{hk.l}$ is the lattice spacing at a certain applied stress and $d_{hk.l}^0$ is the initial lattice spacing. In the elastic regime, the elastic lattice strains evolve linearly with the applied stress. As a grain family plastifies, the elastic lattice strains will deviate from linearity. The relative behavior of $\varepsilon_{hk.l}$ describes how load is shared between different grain families and phases. The relative plasticity of different grain families can give evidence of which deformation mechanisms are active within a grain family (e.g. [33,152]).
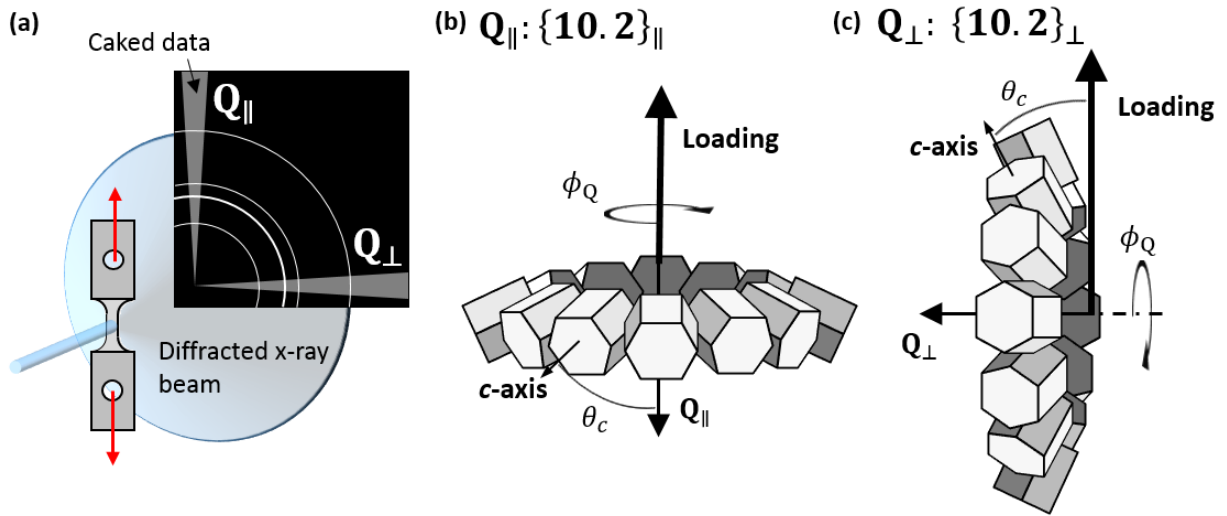
Figure 2-6 Schematic of a representative reflection ({10.2}) showing possible grain orientations contributing to a diffraction ring. (a) schematic of a diffraction setup measuring one quarter of the diffraction rings. Pale gray triangles show the angular range over which each diffraction ring is integrated to get the $\mathbf{Q}_\parallel$ and $\mathbf{Q}_\perp$ signals; (b) grain orientations contributing to the{10.2}$_\parallel$ peak; (c) grain orientations contributing to the{10.2}$_\perp$ peak.

The physical interpretation of the lattice strain depends on whether the axial ($\mathbf{Q}_\parallel$) or radial ($\mathbf{Q}_\perp$) lattice strains are measured. A schematic of grain families measured in $\mathbf{Q}_\parallel$ and $\mathbf{Q}_\perp$ is shown in Figure 2-6. For a 2D detector setup, the 2D diffraction pattern is "caked", i.e. radially integrated over a predefined angle, to determine the axial and radial signal. This is diagrammed in Figure 2-6a. The signals measured along $\mathbf{Q}_\parallel$ and $\mathbf{Q}_\perp$ refer to two completely different sets of grains, shown in Figure 2-6b and Figure 2-6c for the {10.2} reflection. The axial lattice strains directly measure the elongation along the loading direction; thus an increase in axial lattice strain with applied stress corresponds to the $\{hk.l\}$ grain family going in tension along the tensile axis. Conversely, the radial lattice strains measure the elongation perpendicular to the loading direction (i.e. the Poisson contraction); an increase in radial lattice strain implies that the $\{hk.l\}$ grain family is going into compression along the loading direction. The axial lattice strain evolution is particularly valuable as all of the grains which contribute to the diffraction signal have the same orientation with respect to the loading direction.

Peak Broadening: Evolution of FWHM

The peak broadening for a given $\{hk.l\}$ grain family can be calculated from the change in FWHM during deformation. The peak broadening, $\delta FWHM_{hk.l}$, can be calculated from the peak width as:

$$\delta FWHM_{hk.l} = \frac{2\pi \cos\theta}{\lambda}\left(FWHM_{hk.l} - FWHM_{hk.l}^0\right) \tag{2-6}$$

where $FWHM_{hk.l}$ is the peak width at a certain applied stress and $FWHM_{hk.l}^0$ is the initial peak width, in degrees, and the first term is to convert to q-space. The FWHM for a given peak is the convolution of microstrain and grain size contributions and can be expressed as [153]:

$$FWHM_{hk.l} = \frac{K_{Sch}}{D} + f_m g \sqrt{\rho_{\text{disl}}\overline{C_{hk.l}}} \tag{2-7}$$

where D is the average crystallite size, K_{Sch} is the Scherrer constant describing the grain shape, f_m is a function related to the type and arrangement of dislocations, g is $1/d_{hk.l}$, ρ_{disl} is the dislocation density, and $\overline{C_{hk.l}}$ is the average contrast factor. Thus, it can be seen that peak broadening is related to three factors: (i) a change in coherent scattering length (change in average grain size e.g. by twinning or cell formation), (ii) incoherent strain in the diffracting volume (e.g. from changes in the dislocation density), or (iii) intergranular strain inhomogeneity (i.e. different grains in the same grain family under different strains).
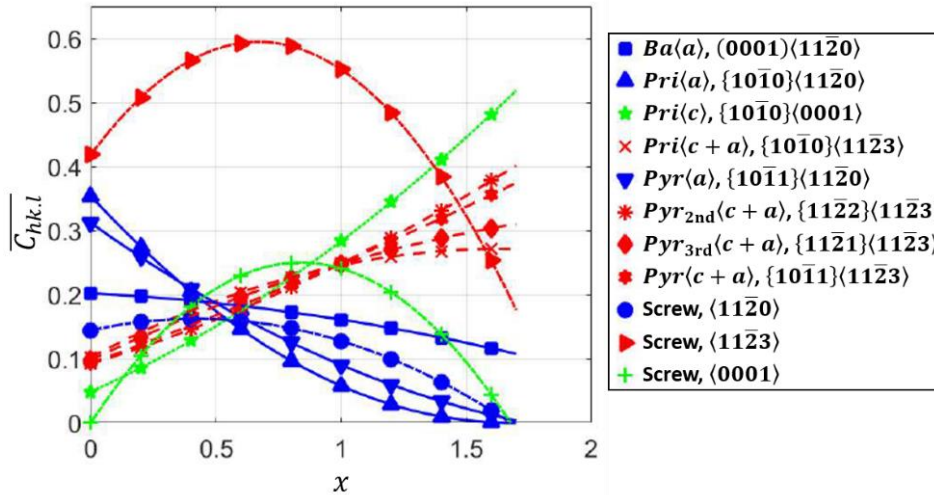
Figure 2-7 Contrast factor for common deformation mechanisms in Ti, adapted from [154]. "Screw" refers to screw dislocations, all other entries refer to edge dislocations.

Dragomir and Ungar [155] have shown that the average contrast factor $\overline{C_{hk.l}}$ for HCP metals varies as a quadratic function of x:

$$\overline{C_{hk.l}} = \overline{C_{hk.0}}(1 + q_1 x + q_2 x^2) \tag{2-8}$$

where $x = (2/3)(l/ga)^2$, l is the fourth index of the reflection, g is $1/d_{hk.l}$, a is the lattice parameter, and $\overline{C_{hk.0}}$, q_1, and q_2 are fitting constants related to the elastic constants of the metal. A more complete description of the derivation and physical meaning of the fitting constants is given in [155]. The average contrast factor is shown as a function of x in Figure 2-7 for the most common deformation mechanisms in Ti. It is clear that the magnitude of $\overline{C_{hk.l}}$ varies significantly depending on the deformation mechanism. Therefore, the determination of $\overline{C_{hk.l}}$ requires significant assumptions about the relative activity of deformation mechanisms and f_m about the type (edge or screw) and arrangement of dislocations within the grain families. Thus, only the relative peak broadening behavior is considered rather than the absolute magnitude.

2.2.4   *In Situ* X-Ray vs. Neutron Diffraction

Whereas characterization techniques such as TEM and EBSD investigate a small volume of the material, diffraction techniques can be used to examine the bulk behavior of the material. Each diffraction pattern contains information on the crystallographic structure, phases, and internal strains in the sample. The high flux and brilliance of synchrotron sources makes it possible to collect XRD patterns from small volumes at high speeds, up to thousands of patterns per second. Thus, mechanical tests can be performed *in situ* to study the evolution of the microstructure, taken from changes in the collected XRD patterns, during loading.
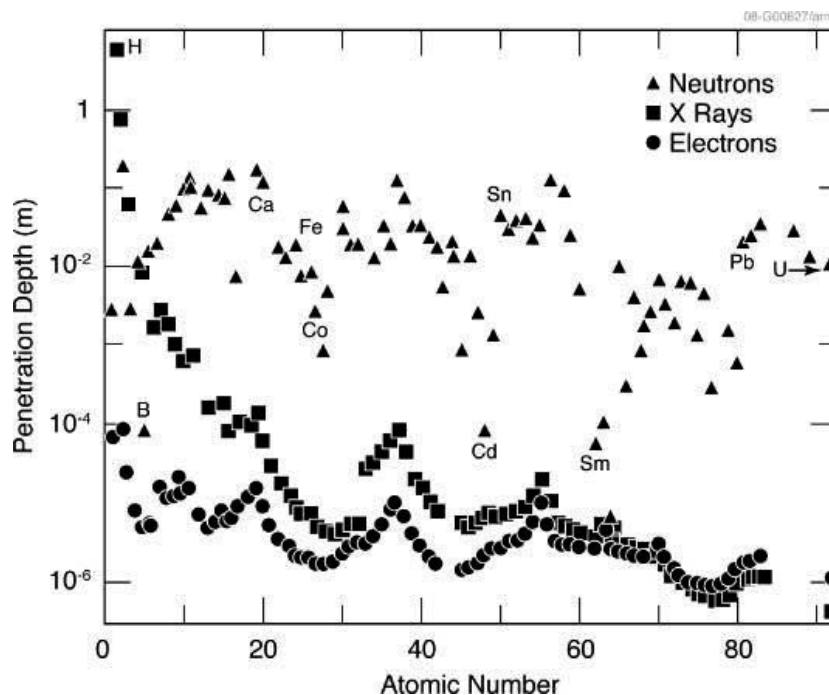
Figure 2-8 Penetration depth of neutrons, x-rays, and electrons by element. Penetration depth defined as depth where beam intensity is reduced by a factor of 1/e. Neutron wavelength taken as 0.14 nm for these calculations. Figure adapted from [156].

Neutron diffraction (ND) follows the same basic principles as XRD, but the different scattering characteristics of neutrons and x-rays can make them complementary techniques. Thermal neutrons have no electronic charge. These particles interact with the nuclei of atoms rather than the electron cloud and thus have a much smaller effective scattering cross-section than x-rays. Thus, the penetration depth of a neutron does not show a strong correlation with atomic number, as shown inFigure 2-8, whereas x-ray penetration depth generally decreases with increasing atomic number. This can be valuable for example in the field of tomography, where neutrons may be able to distinguish between elements with similar atomic numbers better than x-rays. Neutrons can also be used to detect light elements such as Hydrogen, which interact poorly with x-rays.

For elements beyond the first two rows of the periodic table, it is clear that the penetration depth of neutrons is generally one or two orders of magnitude higher than x-rays. Thus, for *in situ* mechanical testing, it is possible to penetrate samples several centimeters thick with neutrons. Therefore, even metals with grain sizes in the high 10s of μms can be measured with good counting statistics. Additionally, the scattering power is strong at high angles, so higher-order grain families can be measured with good statistics. The disadvantage of the high attenuation length is that measurement time for neutrons are much longer than for x-rays. Acquisition times at modern spallation sources are in the range of 10-90 minutes. This requires that the deformation be paused during the measurements, which can result in stress relaxation and creep.

Neutron measurements can either be performed using the "white beam" or "time-of-flight" (ToF) method. In the white beam method, a monochromator is used to fix the wavelength and the intensity of the scattered beam is measure as a function of the diffraction angle. In the ToF method, a full polychromatic beam is used and the intensity is measured as a function of the wavelength. This requires the energy of each neutron to be known, which is calculated from the time it takes to reach the detector from an initial point. All of the neutron experiments presented here were ToF experiments.

2.2.5   POLDI Beamline: *In Situ* Neutron Diffraction
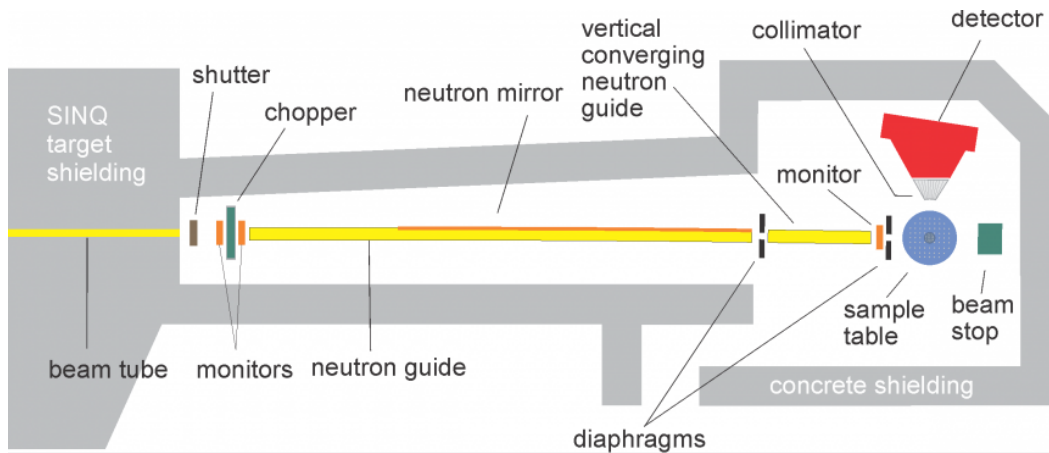
Figure 2-9 Schematic of the experimental setup at the POLDI beamline (SINQ). *Source:*
https://www.psi.ch/en/sinq/poldi/

The mechanical behavior of Mg AZ31B was investigated with *in situ* ND at the POLDI beamline at the Swiss Spallation Neutron Source (SINQ). A schematic of the beamline setup is shown in Figure 2-9. POLDI stands for Pulse OverLap DIffractometer and is a ToF diffractometer. Because SINQ is a continuous source, the neutron beam must be "chopped" into pulses using a multi-slit rotating disc. The start time for each pulse is thereby known and can be used to calculate the ToF to the detector. The pulsed neutrons are directed at the sample by a curved neutron mirror, shaped by two diaphragms and a radial collimator, and diffracted to a one-dimensional ^{3}He detector. The detector measures scattering within a horizontal angular range of 30° and vertical tolerance of ± 2.5°.

Each neutron pulse contains neutrons at a range of energies. Thus, to obtain ToF information, the fast neutrons from one pulse should be restricted from catching the previous pulse. This can be achieved by reducing the chopper speed but goes at the cost of intensity. At POLDI, the standard restriction that pulses cannot overlap is dropped to maximize the duty cycle of the chopper disc and the arrival time of the neutrons is measured with respect to the scattering angle. The time of flight can then be directly calculated from the rate of change in arrival time with respect to scattering angle. A more detailed description of the beamline setup and pulse overlap ToF technique is given in [157,158].

Figure 2-10 Large-scale multiaxial deformation rig at POLDI beamline (SINQ, Paul Scherrer Institute).

In situ multiaxial tests were performed on a large-scale deformation rig at the POLDI beamline (Figure 2-10). The machine was designed in conjunction with the Competence Centre for Materials Science and Technology (CCMX) and Zwick/Roell Group (Ulm, Germany). Each arm is piezo-controlled and can move independently from one another. The horizontal axis can produce loads up to 50 kN, while the vertical axis can reach 100 kN. Two 5 megapixel CMOS cameras are mounted at 15 degrees to the test section normal to take images for digital image correlation. More information on the technical details of the machine can be found in [11]. The machine is mounted such that the cruciform is 45 degrees to the incoming beam and the detector is mounted at 90 degrees to the beam. Thus, the diffraction vector **Q** is along the horizontal loading axis.

2.2.6   MS Beamline Experiments: *In Situ* Powder XRD

The work hardening behavior of a Ti-6Al-4V alloy was investigated at the Materials Science (MS) beamline X04SA at the Swiss Light Source (SLS). The MS beamline allows for powder diffraction studies at energy ranges of 5-38 keV. The diffracted signal is collected with a one-dimensional Mythen II strip detector with a resolution of 3.7 mdeg over an angular range of 120 degrees. The tests were performed in transmission with a monochromatic beam at a power of 20 keV. For more technical information about the MS beamline, please refer to [159].
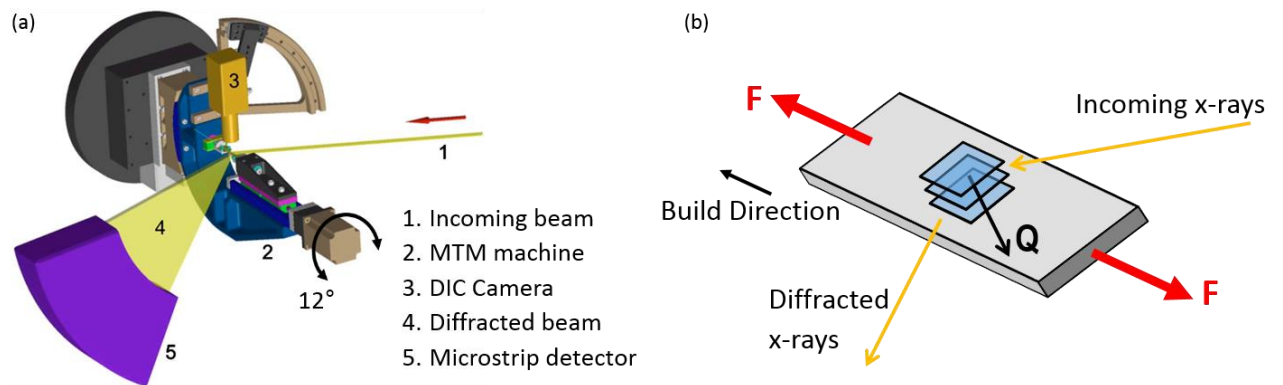
Figure 2-11 Schematic of the experimental setup at the MS beamline. (a) MTM machine mounted on the beamline; (b) Schematic of the dogbone with incoming beam, showing the diffraction vector with respect to the loading direction.

Uniaxial tensile tests were performed using a Micro-Tensile Machine (MTM) mounted on the MS beamline. A schematic of the experimental setup is shown in Figure 2-11a. For a more detailed description of the setup and machine, please refer to the work of Van Swygenhoven et al. [160]. A camera was mounted above the sample to take images for DIC. Dogbones were measured in transmission with the diffraction vector **Q** perpendicular to the loading direction (Figure 2-11b). To increase counting statistics, the machine was rocked along the tensile axis over an angular range of 12 degrees.

2.2.7   I12 JEEP Beamline: *In Situ* Powder XRD
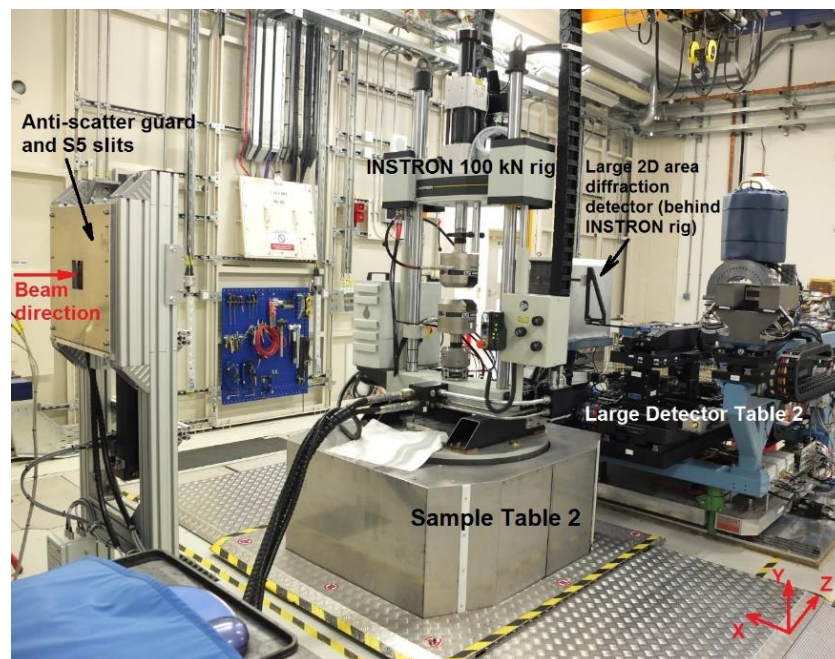
Figure 2-12 Instron 100kN servo-hydraulic tensile test machine mounted on the I12 beamline. Figure from I12 JEEP beamline webpage.

The work hardening and springback of CP-Ti was investigated at the I12 Joint Engineering, Environmental, and Processing (JEEP) beamline at Diamond Light Source in the UK. The beamline is designed for time-resolved *in situ* measurements at energies of 53-150 keV. Due to the low attentuation of pure Ti, the measurements were performed at 53 keV with a monochromatic beam. Patterns are collected with a

two-dimensional Pilatus 2M CdTe detector with a pixel size of 172 × 172 μm^2. Uniaxial tensile tests were performed on an Instron 100kN tensile test rig, shown in Figure 2-12. For more technical information about the JEEP beamline, please refer to [161].

2.2.8   Acoustic Emission

Acoustic emission (AE) refers to the release of transient elastic waves from localized sources such as dislocation generation and motion and twinning [162,163]. The waves propogate through the metal and can be detected at the surface by piezoelectric sensors. AE can detect surface vibrations as small as 10^{-14} m at a frequency of 10 kHz and thus is capable of detecting small events with a high time resolution [162]. Different plastic events produce waveforms with distinct frequency and intensity signatures [3,162–164]. Thus, the raw signal can be separated into components from different types of plastic events during post-processing. The generation and motion of dislocations is a gradual process, with each event contributing a low intensity to the signal. Twinning, on the other hand, involves the rapid shear of many atoms and thus produces a sudden, strong burst of energy.
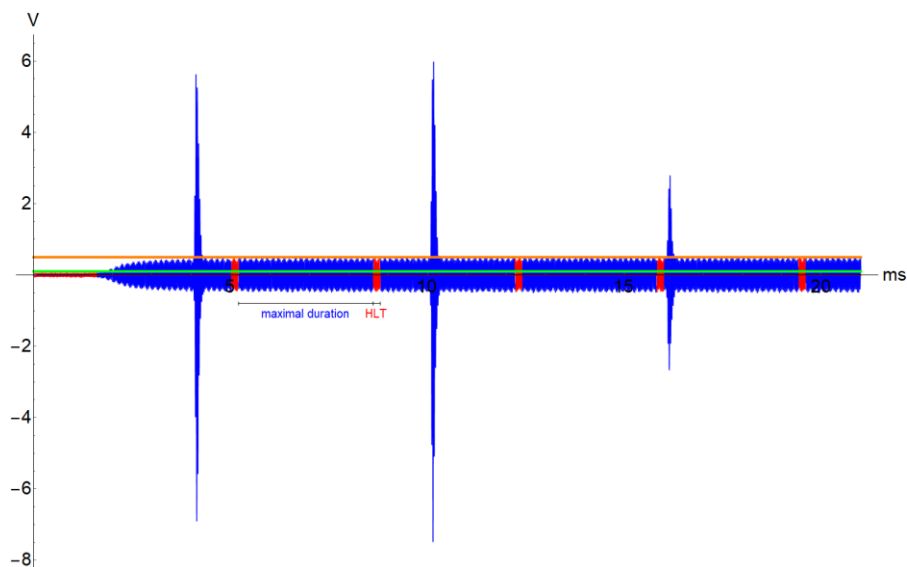
Figure 2-12 Idealized acoustic emission signal showing both burst and continuous emission. The green line delineates the noise threshold, the red line delineates the burst signal threshold. Figure taken from [165].

In Mg alloys, the signal can generally be separated into a continuous contribution from dislocation slip and a burst contribution from twinning [2–4,43]. An idealized acoustic emission signal is shown inFigure 2-12. A threshold intensity is used to distinguish between plastic events and background noise (green line inFigure 2-12), and a second threshold is used to distinguish between the two mechanisms (red line inFigure 2-12). In this thesis, the data is post-processed according to an adaptive sequential k-means (ASK) procedure which statistically groups signals based on their energy and frequency. In general, AE signals from dislocation-based plasticity have a lower energy signature than twinning. However, the distinction between different clusters is not uniquely defined and thus requires verification by complementary experimental methods. The AE post-processing procedure in this thesis follows the same process outlined in [165].

Chapter 3 — A Composite Cruciform Design for Multiaxial Metal Testing

As described in Section 2.1.1, a key component of modern cruciform design is the reducing the test section thickness to increase the plastic deformation in the center of the cruciform. In general, this is achieved by removing material from a sheet, e.g. by machining. However, there are disadvantages to thinning the test section. In particular, sheet metals often have a microstructure gradient from the surface to the center and thus measurements of thinned samples only capture the microstructures in the center of the sheet. Furthermore, many interesting new materials are difficult to obtain in thick sheets, e.g. nanocrystalline and ultrafine-grained materials prepared by severe plastic deformation techniques. Therefore, a bottom-up technique that reinforces the arms of a cruciform instead of thinning the center section would be advantageous. The choice of reinforcement material is of key importance, and its mechanical properties should be chosen to optimize the multiaxial test.

A few examples of reinforced cruciform experiments already exist. Shiratori et al. [166] first introduced the idea by bolting additional brass plates to the arms of cruciform samples. More recently, Green et al. [167] created aluminum cruciforms similar to the design in Figure 2-1d (but with a one-step test section reduction) by bonding additional plates of aluminum on the arms with adhesive. In all published experiments, the reinforcement material has been the same as the tested material. In this chapter, FEA is used to explore the idea of using a mechanically different material to reinforce the cruciform arms. Three different materials are compared: material that is stronger than, weaker than, and equivalent to the substrate (material being tested). The results of a composite cruciform of aluminum reinforced with polymer are shown as a proof of concept and the strain is compared to the FEA results.

3.1 Experimental Procedure

3.1.1 Sample Preparation

The base material used in this study was rolled aluminum foil (Goodfellow, ID: AL000441), hard tempered, chemical composition 99.0% aluminum (Cu <1000, Fe <7000, Mn <1000, Si <5000, Zn <1000 ppm). The foil thickness was measured to be 50 ± 1 μm. The reinforcement was a bi-layer composite of polyethylene terephthalate (PET) on ethylene-vinyl acetate (EVA), commercially available as office lamination pouches (Fellowes "Enhance 80" Lamination Pouches). The laminate was measured by SEM to be 75 ± 2 μm thick. Foils of aluminum are placed as-received in the lamination pouches and pressed at 110 °C to bond the EVA to the aluminum. The surface of the aluminum was left unpolished so that surface roughness could be tracked using digital image correlation (DIC).
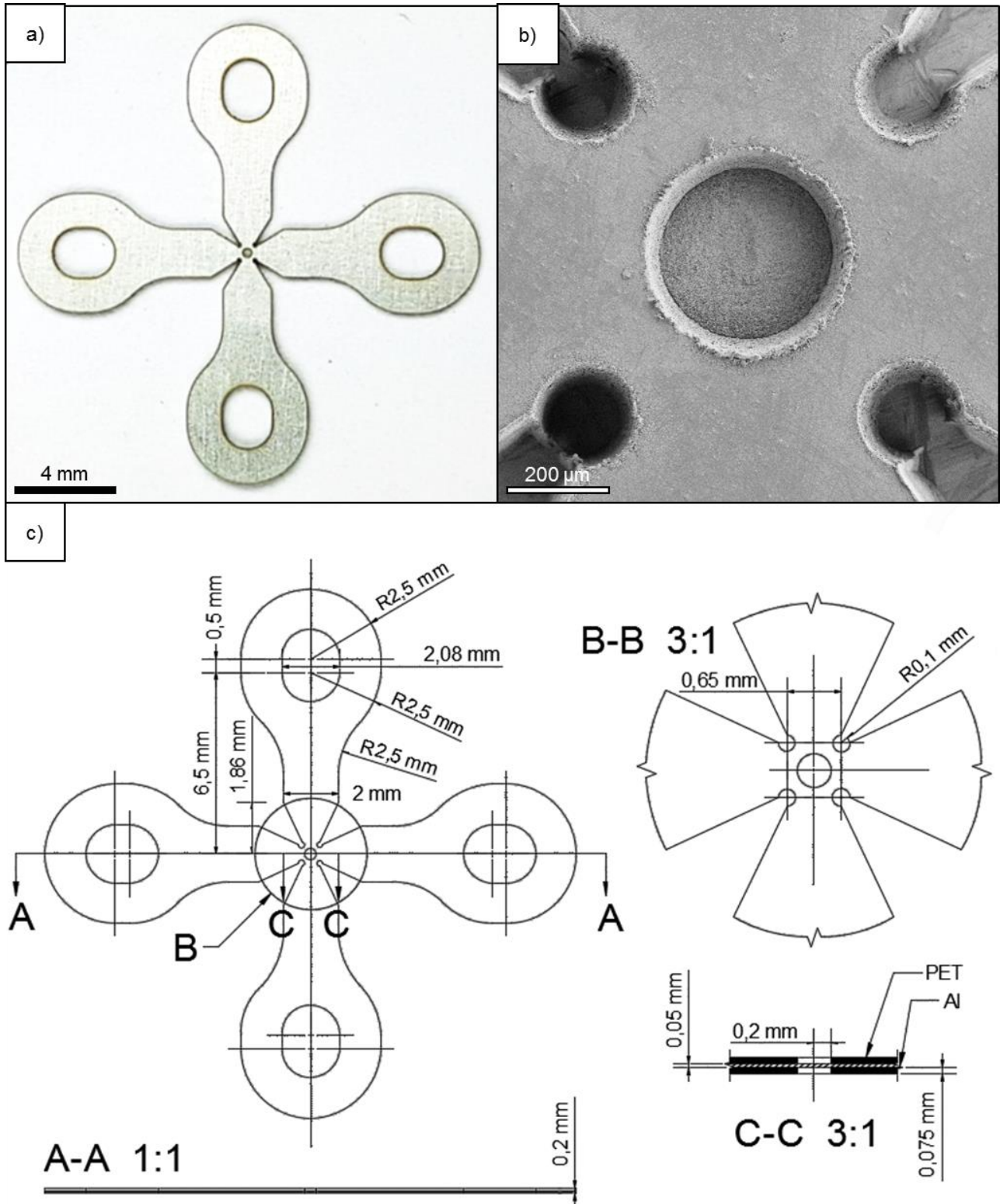
Figure 3-1 Cruciform design used in experiments. (a) Image of full cruciform; (b) SEM micrograph of cruciform test section, coated in carbon to prevent charging; (c) Cruciform dimensions.

The cruciform geometry used in these experiments is shown in Figure 3-1. The cruciform was cut and milled using a frequency tripled Nd:YAG picosecond pulsed laser at the Swiss Federal Laboratories for Materials Science and Technology (EMPA). The laser was operated at a pulse width of 10 picoseconds and

wavelength $\lambda = 355$ nm. First, the test section is milled on both sides by scanning the laser to completely remove the polymer laminate from the test section, stopping when the laser hits the aluminum surface. The ablation threshold, i.e. the minimum single-pulse fluence required to ablate a material, for PET is $\phi_{Th,PET} \approx 800$ J/m^2 [168]; there are several reported values for aluminum, ranging from $\phi_{Th,Al}$ = 350 J/m^2 [169] to 1200 J/m^2 [170]. The laser power was adjusted during ablation so that the fluence per pulse was just above the ablation threshold of PET to minimize damage to the aluminum. This picolaser has been used previously to mill miniaturized metal cruciform samples without introducing significant microstructural damage [137].

Because the fluence used to mill the polymer is also near $\phi_{Th,Al}$, very little damage is expected to occur on the surface due to initial ablation events like direct vaporization of the metal, which occurs at higher energy densities. It should be noted, however, that some heat accumulation is still expected to occur during the milling due to the high pulse frequency (240 kHz). Work by König et. al. [171] suggests that ablation events occur up to 2 ms after each pulse, during which time several hundred pulses would be applied during the scan. Despite this, the pulse frequency was still kept high to reduce sample preparation times. In future work, the pulse frequency and speed can be adjusted to eliminate long-term heat accumulation altogether.

After milling the test section, the cruciform is cut from the sheet. The cruciform geometry used in this experiment is based on work by Hommer et. al. [172]. The cruciform specimen consists of three-quarter circle fillets at the arm intersections and a circular, reduced-thickness test section at the center. A parametric study in Abaqus Standard 6.14 [173] using finite element modelling (FEM) was conducted to determine the fillet radius and position for the aluminum-polymer samples. The design was chosen because it produces large stress concentrations at the narrow points of the arms. Therefore, the test should show if the reinforcement material can produce significant plasticity in the gauge section before failure.

3.1.2   Mechanical Tests

Cruciform samples were tested *ex situ* with the miniaturized multiaxial deformation machine described in Section 2.2.1. A PixelLink camera (P-DL729MU) with inline 2× telecentric lens (Edmund Optics, model #67313) mounted above the sample was used to capture images for DIC analysis. A custom-written LabVIEW® program is used to control the machine and camera. DIC was performed using the Matlab™ program *ncorr* to extract strain data in the test section. All DIC strains shown in this paper are calculated in *ncorr* using the Lagrangian finite strain tensor. Two types of tests were performed: uniaxial loading along one axis and equibiaxial (1:1 load ratio) loading. Additional equibiaxial and uniaxial tests were run on cruciform samples without polymer as a control.

3.1.3 Finite Element Analysis
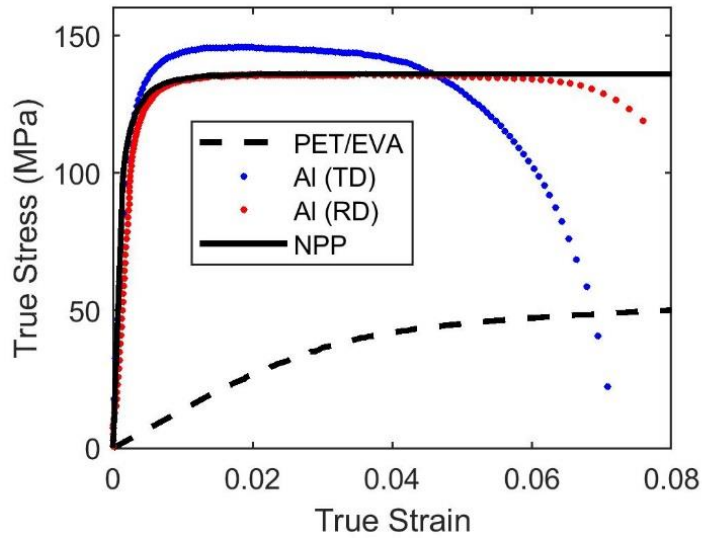
Figure 3-2 True stress-true strain curves for aluminum (rolling direction "RD" and transverse direction "TD") and PET/EVA polymer composite from mechanical tests and the nearly perfect plastic ("NPP") curve used for the simulations.

Following the procedure outlined in [174], finite element analysis (FEA) was performed in Abaqus Standard 6.14 for comparison with the DIC measurements. Dogbones of aluminum (rolling and transverse direction) and composite PET/EVA were deformed to obtain mechanical data for the model. The measured and input material curves are shown in Figure 3-2. The aluminum reaches ultimate tensile strength (σ_{UTS}) at 1.5% strain, past which localized shear banding is observed, typical of highly ductile materials. The appropriate shear damage model in Abaqus would require inputs from specialized notch tests which are not possible considering the dimensions of the available sheet. Instead, the material is approximated as nearly perfect plastic (NPP).

The polymer laminate was treated as a single composite material. It was modelled as an isotropic material with modulus $E_{\mathrm{Poly}} = 1396$ MPa and Poisson's ratio $v_{\mathrm{Poly}} = 0.4$, using the measured true stress vs. true strain curve as inputs to define the plastic response. The elastic response of the aluminum was modelled as isotropic with $E_{\mathrm{Al}} = 69000$ MPa and $v_{\mathrm{Al}} = 0.33$. The anisotropic plastic response was defined using a built-in Abaqus material model based on the quadratic Hill 48 yield criterion and associated flow rule [175]. The true stress vs. true strain curve for the rolling direction was input as the reference plastic flow data with a rate-independent, isotropic hardening law. A yield stress of 95 MPa was used instead of the 0.2% yield stress of 123 MPa to account for microplasticity. The six anisotropic yield stress ratios were calculated to be $R_{11} = 1$, $R_{22} = 1.163$, $R_{33} = 0.96$, $R_{12} = 1.0815$, $R_{13} = 0.98$, and $R_{23} = 1.0615$. Because the aluminum is available as a thin sheet, it was not possible to measure the yield stress in the out-of-plane direction with a simple dogbone test. Instead, the R_{33} value was adjusted to give the best fit between the force-strain curves of the simulations and the force-strain curves for a cruciform under equibiaxial load. The determination of the shear stress ratio R_{12} requires knowledge of the Lankford coefficients for the dogbone tests (see [173]). Considering that this material already exhibits localized necking around 1.5% plastic strain, accurate calculation of the coefficients would require measurements of the out-of-plane contraction on the order of 10s of nanometers. Shear stress ratios R_{13} and R_{23} require both the out-of-plane dogbone tests and determination of the Lankford coefficients.

However, it was observed that the response of the simulations is insensitive to small variations in the shear stress ratios. Therefore, the shear stress ratios R_{12}, R_{13}, and R_{23} were instead approximated as:

$$R_{ij} = \frac{(\sigma_{ii}+\sigma_{jj})/2}{\sigma_{11}/\sqrt{3}}, \text{ where } i = 1-3, j = 1-3 \text{ and } i \neq j \tag{3-1}$$
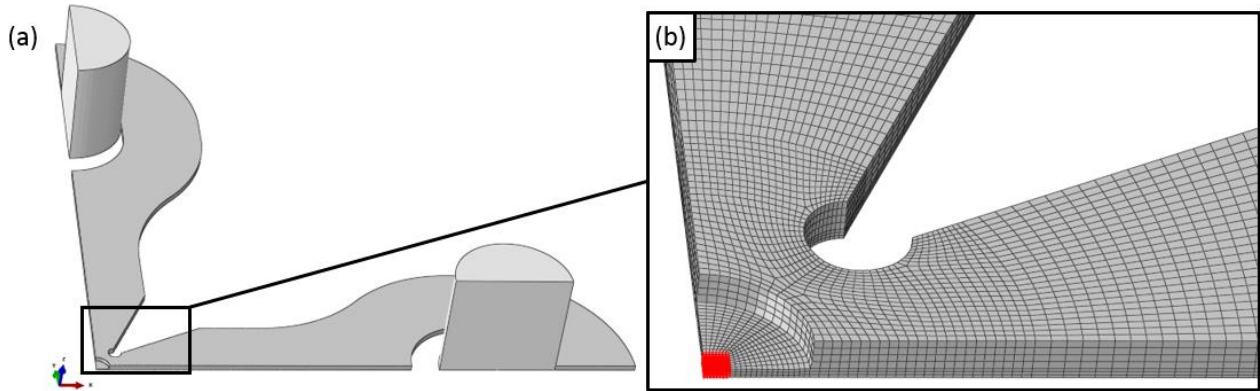
Figure 3-3 (a) Abaqus assembly of 1/8th cruciform geometry with two discrete rigid body pins; (b) Magnified view of the mesh in the test section. The 192 elements used to calculate simulation strain data are highlighted in red.

To improve computational efficiency, only 1/8th of the cruciform geometry was modeled. Symmetric boundary conditions were applied on the XZ-, YZ-, and XY-planes (Figure 3-3a). To mimic the experimental loading, two rigid pins were modeled and used to apply forces inside the holes in the cruciform arms. A structured hexahedron mesh with linear 8-node elements (C3D8 elements) is used to approximate the geometry. A 50×50 μm^2 area at the center of the test section was partitioned using $8 \times 8 \times 3$ elements, for a total of 192 elements (Figure 3-3b). This area was chosen because it is a typical x-ray beam cross-section used during *in situ* multiaxial measurements, as in [176]. All strain values from the simulations presented in this paper are the result of averaging over the integration points of these 192 elements. The two pins were modeled using discrete rigid body shell elements, with one semi-circular face constrained to lay flat in the XY plane. A concentrated force is applied to a reference point, defined at the center of the semi-circle face in the XY-plane, to mimic the force-control of the experiments. The pins are constrained to move only in X or Y (cross arm pin) respectively, and they are not allowed to rotate. Contact interaction between the pins and cruciform is approximated as frictionless. In these simulations, delamination of the polymer from the aluminum was not considered.

3.2 Results of Mechanical Tests
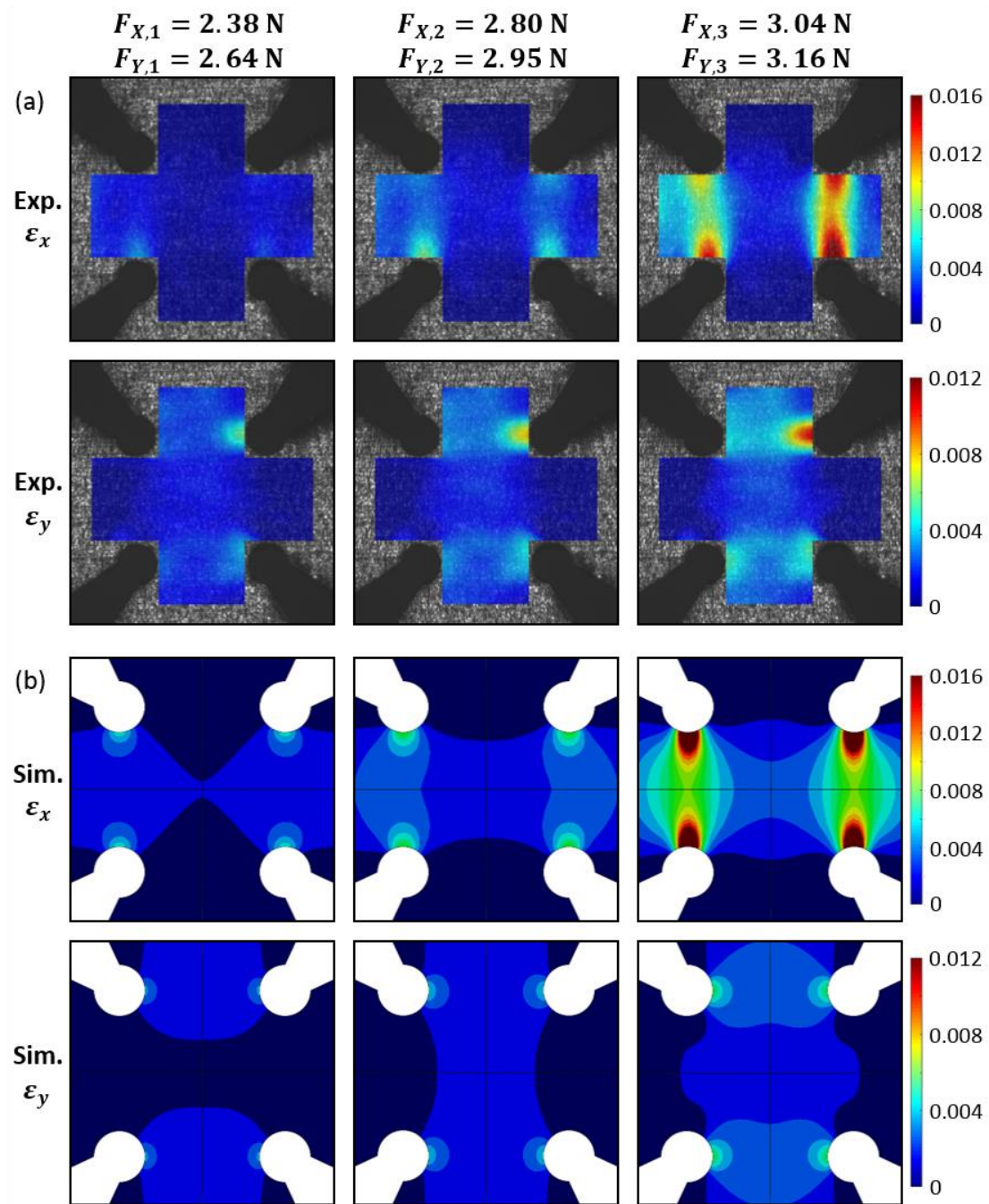
Figure 3-4 Strain evolution during equibiaxial loading of a cruciform without reinforcement. (a) Experimentally measured DIC strain maps and (b) Abaqus simulations.

The strain evolution for equibiaxial tensile loading of a cruciform without reinforcement is shown in Figure 3-4. Due to the cruciform geometry, two stress concentrations form in the fillets between the arms that lead to strain localizations at the narrowest points of the arms. Upon reaching σ_{UTS}, instable plastic flow begins at the strain localizations and the Al necks, preventing the test section from reaching significant plastic strain. The simulations accurately predict the strain localizations in the arms. The strain at the center of the cruciform reaches $\varepsilon_x = 0.00218$ and $\varepsilon_y = 0.00232$ before necking and failure in the arms.
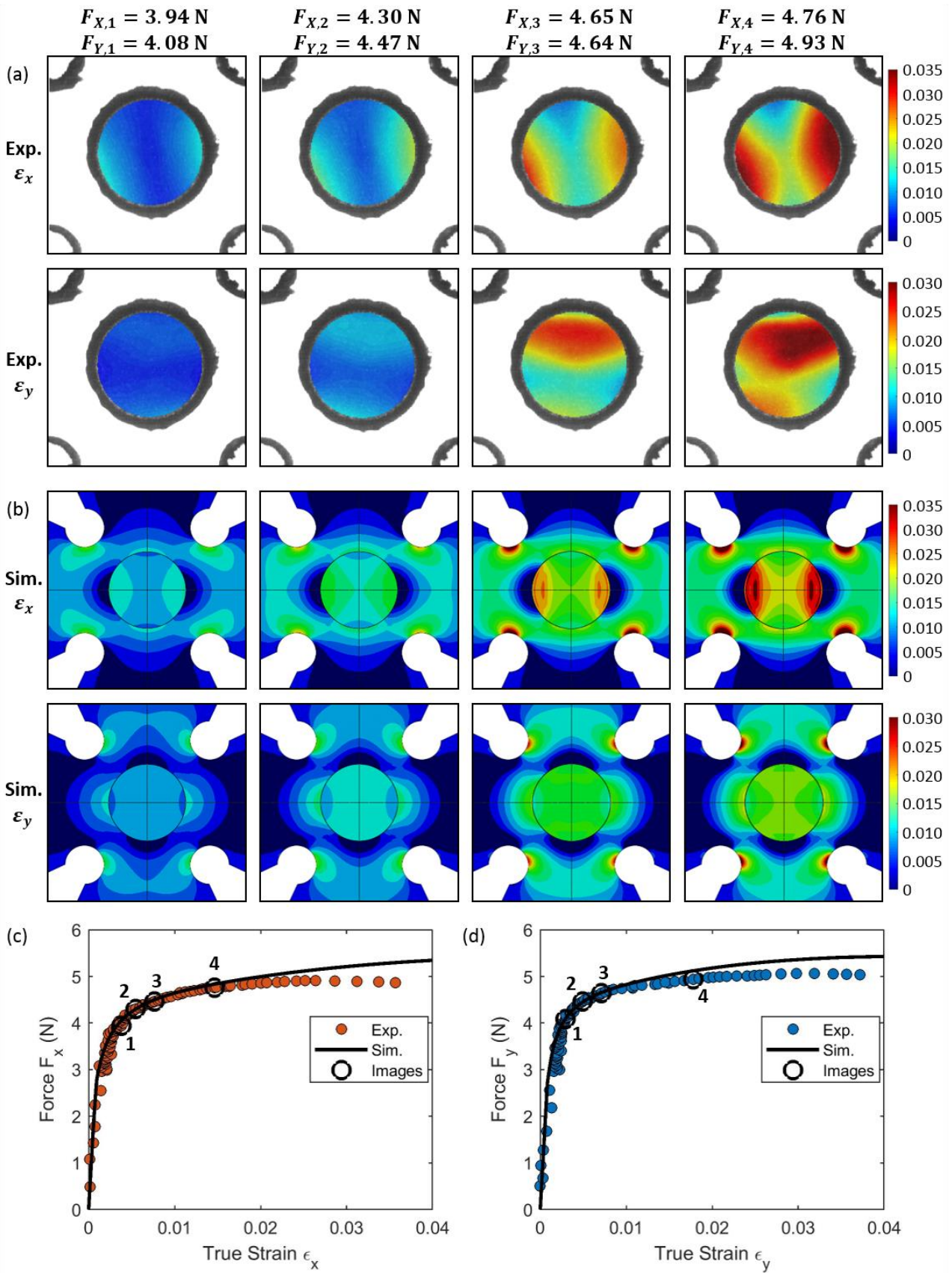
Figure 3-5 Strain evolution during equibiaxial loading of a reinforced cruciform. (a) Experimentally measured DIC strain maps and (b) Abaqus simulations. True strain vs. applied force curves are shown in the (c) x- and (d) y-directions, with circles indicating where the displayed DIC strain maps were taken.
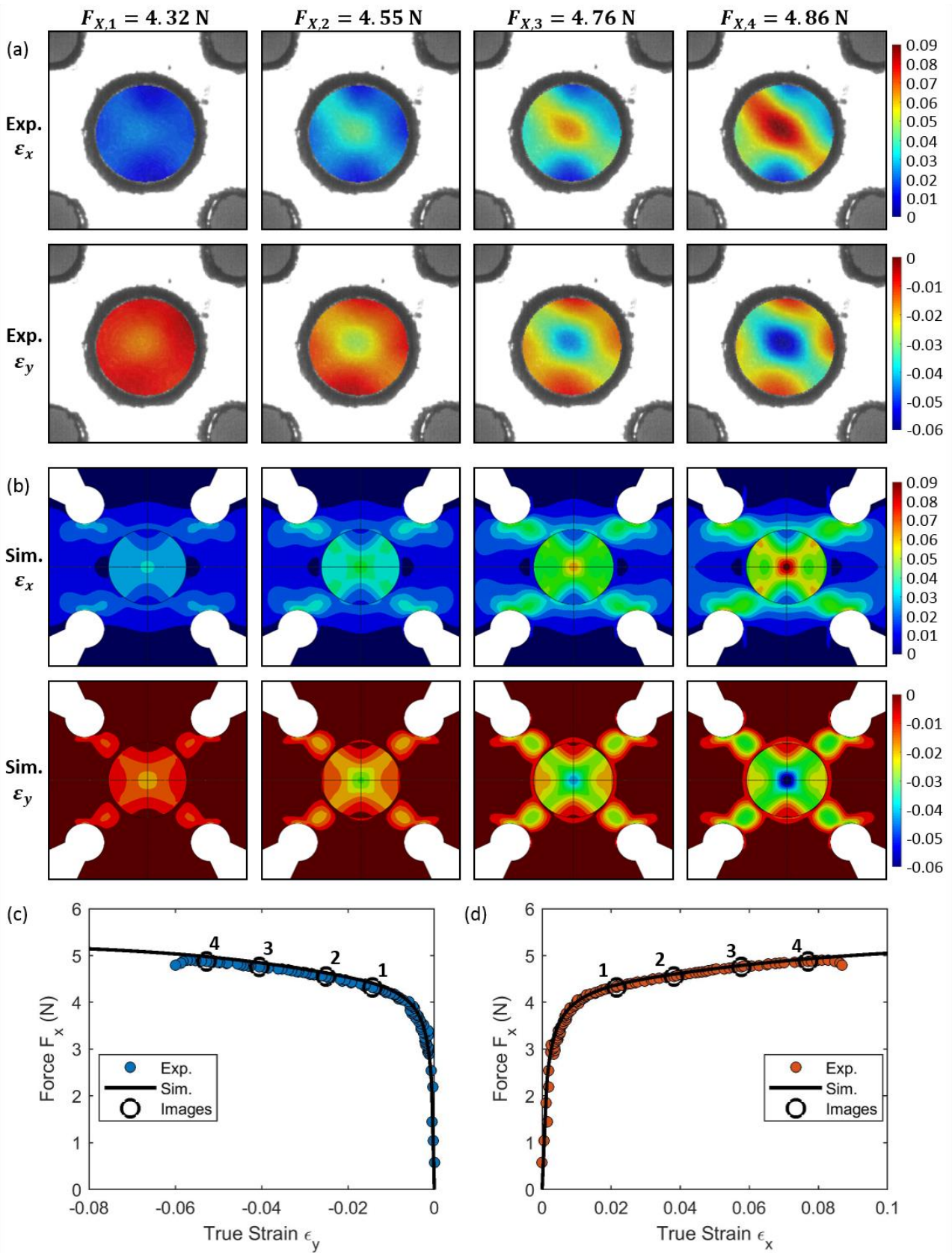
Figure 3-6 Strain evolution during uniaxial loading of a reinforced cruciform. (a) Experimentally measured DIC strain maps and (b) Abaqus simulations. True strain vs. applied force curves are shown in the (c) x- and (d) y-directions, with circles indicating where the displayed DIC strain maps were taken.

The strain evolution for equibiaxial tensile loading of a reinforced cruciform is shown in Figure 3-5. The true strain versus applied force in the rolling and transverse directions are shown in Figure 3-5c and d. The stress and strain evolution in the gauge section is distinctly different than the non-reinforced cruciform. The simulations show that stress concentrations still develop at the the fillets between the arms, but the polymer reinforcement shares the loading and delays the onset of strain, allowing the gauge section to reach higher strains. The strain at the center of test section reaches $\varepsilon_x = 0.0252$ and $\varepsilon_y = 0.0298$ before necking, an order of magnitude higher than the non-reinforced sample.

The DIC strain maps show that the strain distribution in the gauge section already differs from the simulations just after plastic yield in the gauge section begins. At this point, the simulations show that the circular fillets between the arms have already begun to yield (Figure 3-5b). Thus, the differences between the experiments and simulations are attributed to a small misorientation between the loading axes that results in one of the fillets plastifying before the others. The corners initially work harden, allowing the strain at the center of the gauge section to increase. Around point 3, however, the measured strains at the center of the sample begin to deviate noticeably from the simulations (Figure 3-5c and d). The strain distribution is heavily asymmetric at this point, and the stress state at the center is no longer approximately equibiaxial. Due to the low work hardening of the Al and polymer reinforcement, the strain localization grows rapidly and ultimately causes the material to neck prematurely.

A uniaxial tension test was also performed as uniaxial and equibiaxial loading represent the two extreme loading cases for cruciform-shaped samples. The strain evolution for uniaxial tensile loading of a reinforced cruciform is shown in Figure 3-6. The true strains versus applied force in the rolling direction are shown in Figure 3-6b and c. The strain along the transverse direction ε_y is plotted against F_x because $F_y = 0$. For the case of uniaxial loading, the simulations capture the strain evolution in the gauge section very well. The strain components form an X shape connecting the four fillets typical of uniaxial tension of cruciform samples. The ring effect, introduced in Section 2.1.1, results in a compressive stress along the transverse direction, shown by the compressive ε_y strain.

3.3 Parametric FEA study of theoretical reinforcement materials

Reinforcement Materials	K (MPa), n				
	37, 0.1	69, 0.2	129, 0.3	240, 0.4	447, 0.5
40	A1	A2	A3	A4	A5
80	B1	B2	B3	B4	B5
120	C1	C2	C3	C4	C5
160	D1	D2	D3	D4	D5
200	E1	E2	E3	E4	E5

Table 3-1 $R_{p0.2}$ and work hardening variables used to define the plastic strain evolution of theoretical reinforcement materials (indicated by the corresponding letter-numer pairing).

The simulations of equibiaxial loading were repeated with various theoretical materials to determine criteria for choosing an ideal reinforcement material. The mechanical properties considered were: elastic modulus, 0.2% yield stress ($R_{p0.2}$), and work hardening capability (given by K and n for the exponential hardening law $\sigma = K\varepsilon^n$). Three elastic moduli were considered: E = 10 GPa, E = 69 GPa (the same as the aluminum base materials), and E = 140 GPa. A theoretical plastic response was generated for each material using the yield stress and the work hardening variables shown in Table 3-1. The names of each theoretical

plastic response are shown in Table 3-1. All theoretical materials were modelled as mechanically isotropic. The simulations used the same base material, Al, and cruciform geometry used for the DIC experiments. Delamination of the reinforcement and base material was not considered in this study, as there are a variety of potential joining methods,such as adhesive bonding, electroplating (for metals), and sputtering. The simulations were compared based on the evolution of equivalent plastic strain (PEEQ) in the center of the gauge section before failure. Because both the reinforcement and base materials are defined such that they can take load indefinitely, a criterion must be established to determine when the cruciform has "failed." Failure was defined as the point where the maximum Von Mises stress in the base material stops increasing. This point can be conceptualized as the initiation of instable plastic flow.
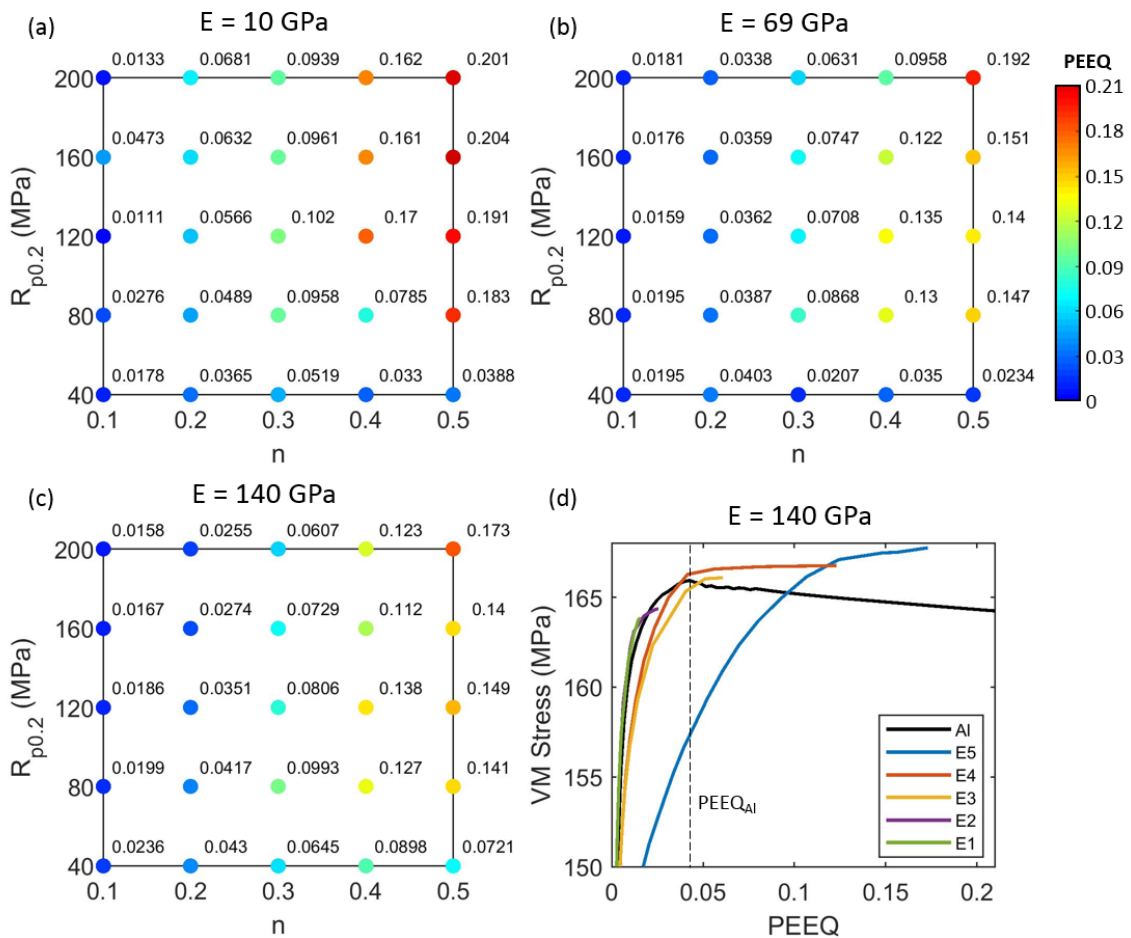
Figure 3-7 PEEQ at the center of the gauge section at failure for reinforcement materials with (a) E = 10 GPa, (b) E = 69 GPa, and (c) E = 140 GPa. The values are

The PEEQ at the center of the gauge section at failure is shown in Figure 3-7 as a function of yield stress and hardening exponenet n. One chart is given for each elastic response: Figure 3-7a for reinforcement materials with E = 10 GPa, Figure 3-7b for reinforcement materials with E = E_{Al} = 69 GPa, and Figure 3-7c for reinforcement materials with E = 140 GPa. The PEEQ values are assigned a color based on their magnitude to make trends more visible. Because both the reinforcement and base materials are defined such that they can take load indefinitely, the values of PEEQ at failure will be artificially inflated. However, their relative magnitudes can be compared to draw conclusions about the effect of varying mechanical properties on the cruciform performance. A simulation with the reinforcement material the same as the base material, i.e. as

if the cruciform were made by machining from a block, was performed for comparison. The value of PEEQ at failure for this test, PEEQ$_{Al}$ = 0.0366, is marked on the color bar for comparison.
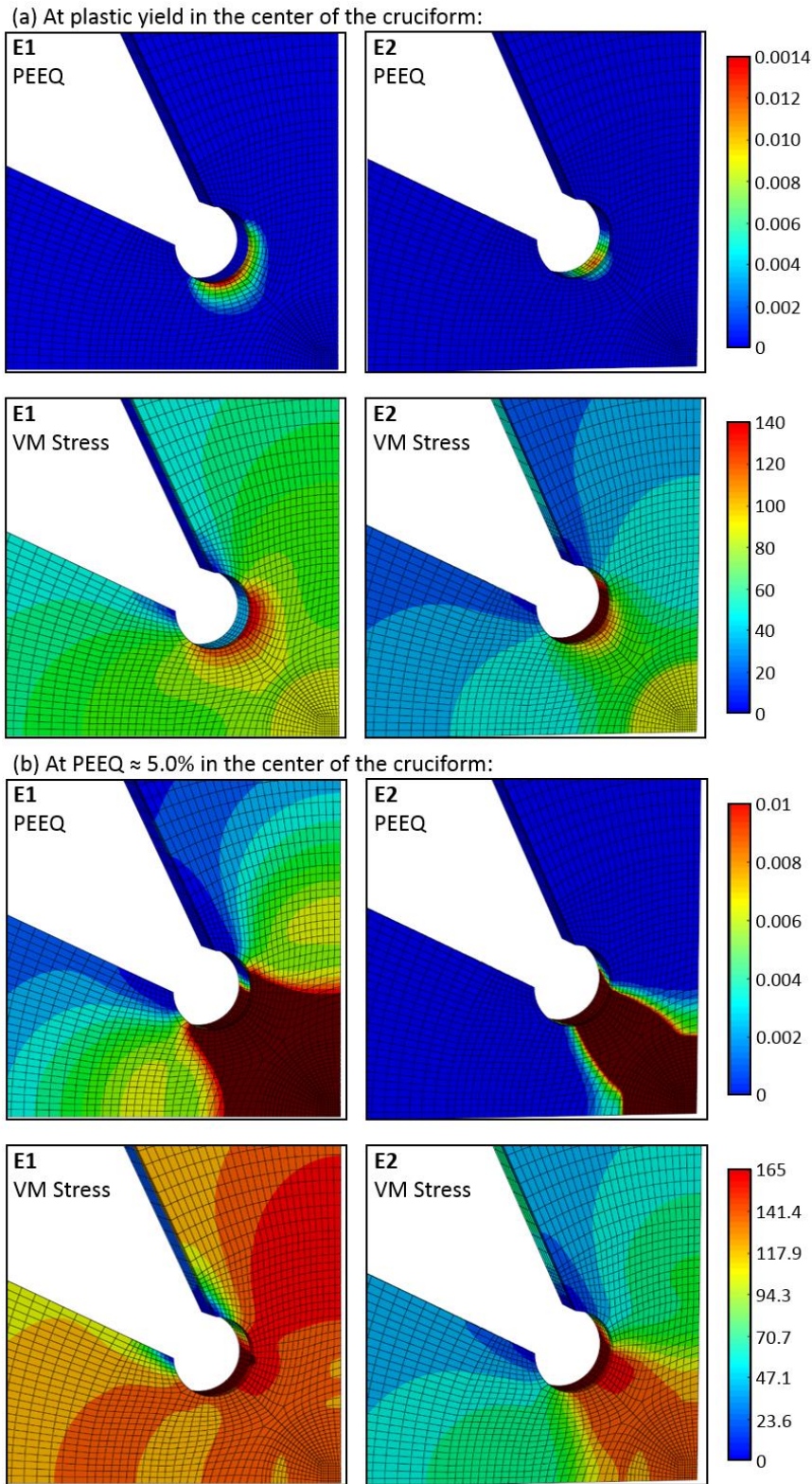
Figure 3-8 Von Mises stress and PEEQ distributions for two simulations (a) at plastic yield in the center of the cruciform and (b) at PEEQ ≈ 5.0% in the center of the cruciform. The reinforcement materials have the same yield stress and work hardening but different elastic moduli: *E* = 10 GPa for E1 and *E* = 140 GPa for E2.

Figure 3-8 shows the Von Mises stress and PEEQ distributions for two cruciform simulations. The reinforcement materials in both simulations have the same yield stress and work hardening behavior, but one has E = 10 GPa (simulation "E1")and the other has E = 140 GPa (simulation "E2"). The cruciforms are shown in 1/8th view from behind. Figure 3-8a is taken at the onset of plastic yield in the center of the cruciform. Figure 3-8b is taken when the PEEQ at the center of the cruciform reaches ~5.0%. The color limits are set to highlight the plasticity in the arms. In simulation E1, plasticity initiates in the base material. The reinforcement distributes the stress along the fillet. As loading proceeds, significant plasticity occurs in the arms that allows the gauge section to reach high strains. By contrast, plasticity initiates in the reinforcement in simulation E2. The stress is concentrated at the fillet, causing localized deformation. The cruciform is still able to reach decent plastic strain in the center due to the high work hardening of the reinforcement that delays failure.

The findings of the parametric study are summarized below:

- Increasing the yield strength when the material has low work hardening does not significantly improve the plasticity in the gauge section. This can be explained because the gauge section is constrained to deform with the reinforcement material. Thus, even though stronger reinforcement materials can reach higher stresses, the gauge section can't deform unless the reinforcement also deforms. When the reinforcement material yields, the low work hardening leads to rapid plasticity and failure.
- The ideal material has a high yield stress and work hardening. This is expected. The role of the reinforcement is to share the load with the base material. A material with higher work hardening can deform while still taking load, reducing the stress concentration in the fillets of the base material. This is shown in Figure 3-7d.
- Interestingly, among reinforcement materials with higher yield stress (>80 MPa) and good work hardening ($n > 2$), the ones with the low (10 GPa) elastic modulus appear to outperform the others. This trend can be explained by observing the Von Mises stress distribution during loading (Figure 3-8). By initiating plasticity in the base material, the stress is more homogeneously distributed throughout the sample during deformation, allowing the samples with low elastic modulus to reach higher strains. Thus, the ideal reinforcement material for this cruciform shape and base material should be a low modulus, high yield strength, high work hardening material.

3.4   Discussion

In this study, an Al sheet was reinforced by a PET/EVA composite and loaded under both uniaxial and biaxial tension. With the reinforcement, the Al successfully reached biaxial plastic strains in the center of the gauge section an order of magnitude higher than without the reinforcement. FEM was able to capture the magnitude of the strain at the gauge center and the general trends of the strain distribution. However, due to plastic instability of the Al it was difficult to reproduce the strain distribution in the gauge section. It is expected that a more advanced FE model including plastic-damage mechanisms could more accurately describe the deformation. Nevertheless, the test successfully demonstrates that a layered composite cruciform design can effectively increase deformation in the test section of the sample.

The PET/EVA laminate reinforcement technique presented here is limited to soft metals due to the low yield strength and work hardening of the polymers. However, by using methods such as electroplating, stronger materials could be used to reinforce cruciform arms, making this layered composite technique available to a wide range of materials. The expected performance of different reinforcement materials can

then be predicted using FEA. Based on a parametric FEA study, the ideal reinforcement material is elastically soft, stronger than the base material, and has a high work hardening. Of course, such an ideal material does not exist in the real world. However, the FEA also implies that any stronger reinforcement material with good work hardening can greatly enhance plasticity. In the case of the low-work hardening Al considered in this study, this applies to most metals: steels, copper, and even most Al alloys.

It is important to consider that the mechanical differences between the reinforcement and base material can change the residual stress state of a sample. If the reinforcement is softer than the base material, it will plastify more during load, resulting in a tensile residual stress from the reinforcement in the unloaded state. Conversely, a harder reinforcement material would result in a compressive residual stress. For a simple exploration of the yield space, this factor is irrelevant. However, for experiments that involve strain path changes additional stresses during the unloads could potentially alter the initial state for subsequent loads. More mechanically distinct materials will increase this effect, as well as increasing the shear between the layers. The ultimate choice of reinforcement should thus be a compromise between the ideal mechanical properties and the parameters of the experiment.

It is also important to note that the success or failure of a reinforcement material for one cruciform geometry does not imply the same results for a different geometry. An ineffective reinforcement material might be made effective by, for example, increasing the thickness of the reinforcement layer. A superior cruciform design, such as the one proposed by Upadhyay et al. [174], would also reduce the load shared by the reinforcement. Separate parametric studies are therefore recommended to optimize reinforcement materials for other geometries.

3.5   Conclusions

In this work, a simple technique to produce cruciform shaped samples for multiaxial tensile testing is presented. It is based on a bottom-up approach in which the arms of the cruciform are reinforced by a mechanically distinct material to create a "reduced thickness" gauge section without introducing mechanical damage to the test material. Equibiaxial loading of Al sheet reinforced by a PET/EVA polymer laminate was able to achieve plastic strains of 2-3% at the center of the cruciform, whereas only 0.2-0.3% was observed for the same cruciform geometry without reinforcement. FE modelling was able to capture the general trends of the strain evolution in the gauge section during loading. A parametric FEA study of elastic modulus, yield stress, and work hardening was also performed to develop criteria for optimizing the reinforcement material. The results demonstrate that a layered composite cruciform with reinforced arms is an effective way to improve plasticity for sheet metal testing, extending the range of potential materials that can be observed under multiaxial loading conditions.

Chapter 4   *In situ* tension-tension strain path changes of cold-rolled Mg AZ31B

The work presented in this chapter is a published article by the same name. It has been reformatted to integrate with this thesis. The article is published and available as open source material in Acta Materialia. A full bibliographic reference is given below:

K. Sofinowski, T. Panzner, M. Kubenova, J. Čapek, S. Van Petegem, H. Van Swygenhoven, *In situ* tension-tension strain path changes of cold-rolled Mg AZ31B, Acta Materialia. 164 (2019) 135–152. doi:10.1016/j.actamat.2018.10.033.

This is a first author paper written in entirety by the PhD candidate (K. Sofinowski). *In situ* neutron experiments were performed by him in conjunction with Dr. T. Panzner, the head beamline scientist at POLDI at the time, and Dr. J. Čapek. All data analysis and figures for the *in situ* tests were prepared by him with the exception of the acoustic emission analysis, which was completed by Dr. Čapek. Post-mortem EBSD was performed by Dr. M. Kubenova. EBSD analysis and figures were prepared by the PhD candidate in conjunction with Dr. M. Kubenova.

4.1   Introduction

The widespread use of magnesium and its alloys in lightweight structural elements for the transportation industry has been limited because of their poor formability at room temperature as compared to other ductile metals[177–179]. In particular, the out-of-plane basal texture of cold-rolled sheet greatly limits $\{10.2\}\langle10.1\rangle$ extension twinning for in-plane tensile loading, the most easily activated mode that can accommodate c-axis strain. Instead, high-CRSS $\langle c + a \rangle$ slip on pyramidal planes and non-basal slip of $\langle a \rangle$ dislocations must be activated to provide enough independent slip systems to accommodate strain[29,180,181]. The result is a highly anisotropic deformation behavior that depends heavily on the loading mode and direction.

In situ neutron diffraction has been used extensively to investigate the evolution of intergranular strain during loading to provide insight on the relative behavior of different magnesium alloy deformation modes. The results have been compared with various crystal plasticity models [6,37,152,182–187]. Muránsky et al. [33] demonstrated the effectiveness of using Schmid Factor (SF) analysis to evaluate the activity of deformation mechanisms in an AZ31B dogbone under uniaxial tension. Čapek et al. [188] used SF analysis to determine the susceptibility of grain orientations to twinning under tensile and compressive loading.

Various other techniques have been used to study, in particular, the interaction between twins and dislocations. *In situ* acoustic emission (AE) has been used in several studies as a complementary technique to monitor the relative activity of dislocation slip and twinning with a high time resolution [3,59,189]. Electron back-scatter diffraction (EBSD) and transmission electron microscopy (TEM) studies have revealed the influence of texture on dislocation slip [190,191], twin-twin interactions [192], and the interactions between twinning and dislocations [50,51,193–198]. Notably, Lou et al. [199] used AE and EBSD to show that the activation stress for nucleation of twins is less than that of de-twinning in AZ31B. Wagoner et al. [200] showed that the hardening contribution of extension twinning can be ascribed more to textural hardening rather than the twins acting as barriers for dislocation slip.

Although it is widely accepted that deformation mechanisms depend heavily on load path, all of the aforementioned works have been restricted to uniaxial tension and compression. Little attention has been given to tension-tension load path changes or multiaxial loads that occur in cold-forming operations of AZ31 sheet. Chino et al. [201] examined uniaxial and biaxial tensile loading using EBSD and TEM. They observed an increased stretch formability for larger grain sizes which was attributed to enhanced basal slip due to lattice rotation by twinning. Steglich et al. [36] used the mechanical behavior of an in-plane equibiaxial tensile test to modify the VPSC model of Lebensohn and Tomé [202,203]. Their results suggest that for this loading mode the CRSS of prismatic $\langle a \rangle$ slip is actually higher than that of pyramidal $\langle c + a \rangle$ slip, whereas all uniaxial studies have suggested the opposite. Zhang et al. [44] performed a deep drawing experiment and used EBSD analysis to study the effect of texture on the limiting drawing ratio. The groups of Wen et al. [45] and Hama et al. [5] performed the first tension-tension strain path studies by loading a dogbone specimen, cutting smaller dogbones at various angles relative to the previous loading direction, then loading those smaller dogbones uniaxially again. Their results show that back-stresses from dislocation motion in the initial load cause lower yield stresses with increasing strain path change angle. All of these studies, however, were performed *ex situ*, so only the macroscopic stress-strain and texture can be compared. No experimental validation of the specific mechanisms responsible for the deformation are presented.

In this work, the relative activity of deformation modes under in-plane multiaxial tension and strain path changes in Mg AZ31B sheet were studied. Six load paths were performed on cruciform-shaped specimens: three monotonic loads with force ratio (F1:F2) between axis 1 and 2 of 1:0 (uniaxial along the rolling direction), 7:10, and 1:1, and three load path changes in which samples were preloaded along the rolling direction, unloaded, and followed by a second load of 1:0, 7:10, and 1:1. Uniaxial tensile deformation of a dogbone sample was performed for comparison. Samples were measured *in situ* using simultaneous neutron diffraction, digital image correlation (DIC), and (AE). Post-mortem EBSD imaging was used to confirm the results of the neutron diffraction and identify the active twin variants.

4.2   Material and Experimental Procedure

4.2.1   Material and Sample geometry

Cold-rolled Mg AZ31B sheet (chemical composition 3.13Al-1.12Zn-0.44Mn-0.025Si wt. %, trace amounts of Fe, Cu, and Ni, balance Mg) was purchased from Concept Métal. EBSD analysis was performed using a Zeiss ULTRA 55 field emission gun scanning electron microscope equipped with an EDAX Hikari Camera and operated at 20kV in high current mode with an aperture of 120 μm. The EBSD data was analyzed using OIM Analysis 7.3 software. Samples were ground using silicon carbide grinding paper to 1200 grit, then polished with 6, 3 and 1-μm oil-based diamond paste, and finished by polishing with 0.05-μm high purity alumina and colloidal silica. EBSD maps were collected using a step size of 0.3 μm and with field of view of 716 μm × 287 μm.
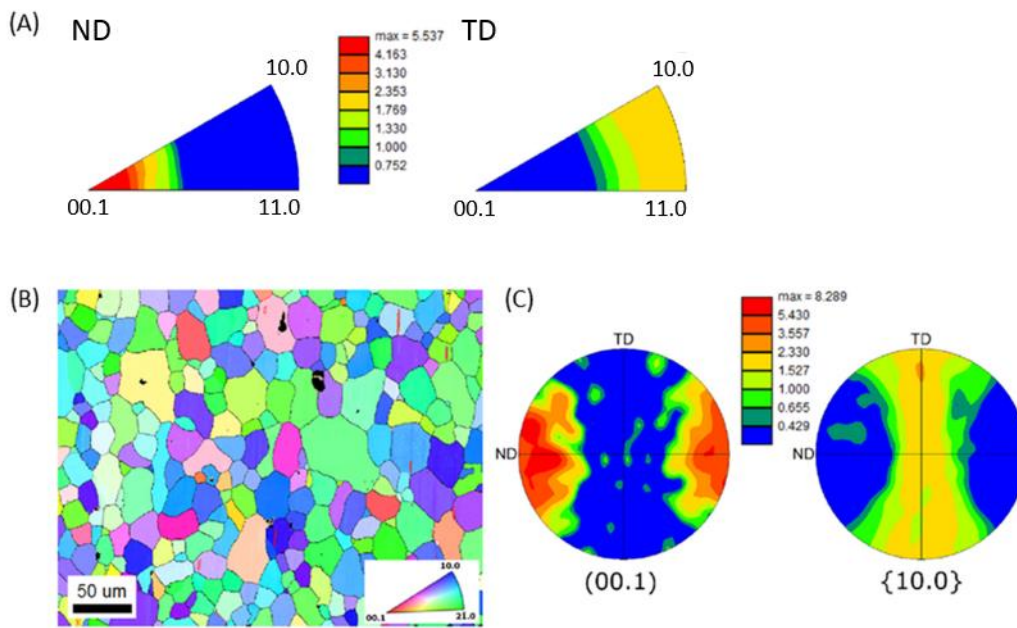
Figure 4-1 (A) IPFs, (B) IPF map, and (C) corresponding pole figures of the initial microstructure. The grain orientations in the IPF map are colored with respect to the diffraction vector **Q**.

Figure 4-1 shows the (A) ND and TD inverse pole figures (IPF), (B) IPF map, and (C) (00.1) and {10.0} pole figures for the initial microstructure. The IPF map is taken in the out-of-plane direction, but the orientations are colored with respect to the diffraction vector **Q**, i.e. the neutrons "see" the grain orientations in Figure 4-1B. The grains are roughly equiaxed with an average grain size of 27 ± 17 μm and there is a strong (00.1) out-of-plane basal texture.

For the mechanical tests, cruciform and dogbone specimens were cut from a 10 mm thick sheet using water jet cutting as in [11]. The test section was reduced by mechanical grinding to a thickness of 2.5 +/- 0.02 mm. Sample dimensions are the same as in [11].

4.2.2 Mechanical Testing and Neutron Diffraction
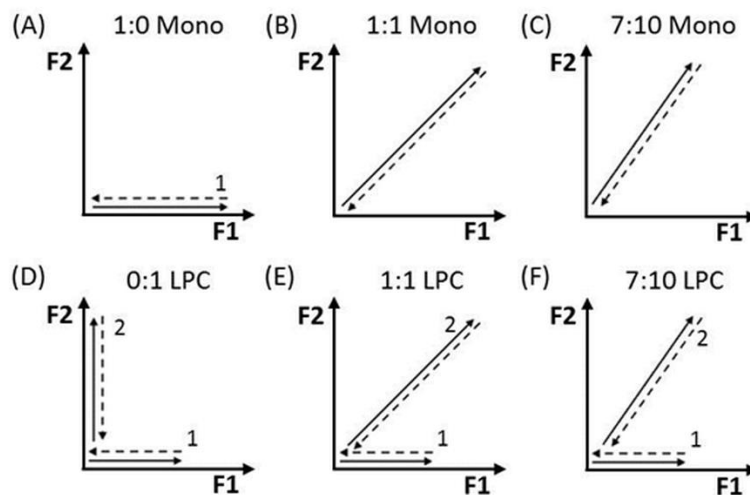
Figure 4-2 Diagrams of the load paths. The preload-unload (force ratio F1:F2 = 1:0) is labeled as "1", and the second load-unloads are labeled as "2".

Samples were tested using the multiaxial deformation rig at the POLDI beamline of the Swiss Spallation Source (SINQ). The rig is used to apply proportional and non-proportional loads for in-plane tensile testing of cruciform samples. For more information on the machine specifications and capabilities, see [11].

Six different load paths were performed with the cruciform samples as shown in Figure 4-2. Load paths A-C describe monotonic load paths with no preload, with load ratios F1:F2 between the axes of 1:0 (uniaxial), 1:1 (equibiaxial), and 7:10, respectively. Load paths D-F describe load path changes (LPCs). For all three LPCs, specimens were first loaded and unloaded uniaxially on axis 1 (1:0 load-unload), then reloaded to force values up to 20 kN with load ratios of 0:1, 1:1, and 7:10, respectively. During the uniaxial loads, the "unloaded" axis was held at constant force F = 300 N.

The macroscopic strain is measured using the 3D DIC system Gom Aramis® as described in [11]. The system uses two 5 megapixel CMOS cameras angled at 15° to the normal of the center of the sample. The cameras measure a 20 ×20 mm2 field of view. A random speckle pattern is created on each sample by spraying with a fine mist of paint. Images are taken during loading at a frequency of 1 Hz. The macroscopic strain tensor is calculated over a 3.8×3.8 mm^2 gauge area at the center of the test section corresponding to the area intersected by the neutron beam. All strain values reported in this work are averaged over this area. From the macroscopic strain tensor ε the equivalent (Von Mises) strain is calculated by:

$$\varepsilon_{\text{Eq}} = \frac{1}{1+v'}\sqrt{\frac{1}{2}[(\varepsilon_1 - \varepsilon_2)^2 + (\varepsilon_2 - \varepsilon_3)^2 + (\varepsilon_3 - \varepsilon_1)^2]} \qquad (4\text{-}1)$$

where v' is the effective Poisson's ratio and ε_1, ε_2, and ε_3 are the principle strains.

Due to the complex cruciform geometry, the stress state at the center of the cruciform samples cannot be directly calculated from the applied load. The circular thickness reduction in the center causes additional stresses due to the geometry of the sample itself, termed the "ring effect" or "cross-talk" between the arms [107,111]. The ring effect can be thought of as adding an additional "geometrical" Poisson contraction to the deformation [11]. Assuming the test section is in a plane stress state, the effect can be measured as the ratio between the strain components along the two principle axes $\varepsilon_2/\varepsilon_1$ for a uniaxial deformation along axis 1. For this cruciform shape and material, this ratio is $\varepsilon_2/\varepsilon_1 = -0.51$ in the elastic regime and in the plastic regime the difference increases to $\varepsilon_2/\varepsilon_1 = -0.80$. For comparison, the Poisson contraction of the dogbone is $v = -0.31$ in the elastic regime and $v = -0.58$ in the plastic regime. The development of the ring effect with respect to the elastic and plastic regimes is discussed more in depth in [111].

Neutron diffraction was performed at the POLDI beamline at SINQ (Paul Scherrer Institute, Switzerland) [157,158]. The principles and setup of the beamline are the same as in [11]. A schematic of the setup and the peak fitting equations using Mantid data analysis software [204] are provided as supplementary material online. The samples are oriented such that the scattering vector **Q** is in-plane with the sample, along horizontal axis 1. Thus, if the cruciform is strained along axis 1, the loading direction is parallel with **Q**. If it is strained along axis 2, the loading direction is perpendicular to **Q**.

All samples were loaded using force control at a rate of 40N/s. For each load-unload, nine (in some cases eight) points were measured: one initial point, two (or one) points in the elastic regime, five points in the plastic regime and one point in the completely unloaded state. Each point was measured for 75 minutes. For measurements in the elastic regime, the sample was held at constant force. For measurements in the plastic regime, the sample was held at constant displacement so as to minimize plastic deformation during

the measurements. To mitigate the effect of stress relaxation during measurements, a pause of 300 s was taken at each point before neutron data was collected.

4.2.3   Acoustic Emission

Acoustic emission was measured simultaneously for all samples, dogbone and cruciform, with the neutron diffraction. However, due to the development of stress concentrations in the corner of the cruciform arms, the corners are always at a later stage of deformation than the gauge section. Consequently, it is difficult to separate the signal caused by the corner of the arms from the signal being measured by the neutrons. Therefore, only the acoustic emission measurements from the dogbone are discussed in this paper. For more details on the acoustic emission setup and data analysis techniques we refer to [3,205].

4.2.4   Normalized Resolved Shear Stress Analysis

The normalized resolved shear stresses (NRSS) were calculated for 1:0, 7:10, and 1:1 loading for all potentially active slip and twinning deformation modes. NRSSs were calculated for all grain families with a lattice plane normal parallel to $\mathbf{Q}$ (i.e. grains in diffraction condition) using a generalized resolved shear stress law similar to the one described by Muránsky et al. [33]:

$$\mathrm{m} = \mathbf{b}^{\mathrm{T}} \cdot (\mathbf{g}^{\mathrm{T}} \cdot \mathbf{S} \cdot \mathbf{g}) \cdot \mathbf{n} \tag{4-2}$$

where $\mathbf{b}$ is the slip Burgers vector, $\mathbf{n}$ is the slip-plane normal, and $\mathbf{g^T S g}$ is the normalized stress tensor $\mathbf{S}$ in three dimensions expressed in the crystal orientation by rotation matrix $\mathbf{g}$. For the twinning modes, $\mathbf{b}$ is the twinning shear direction and $\mathbf{n}$ is the twin-plane normal. In the special case of uniaxial tension on a dogbone, Eq. $\mathrm{m} = \mathbf{b}^{\mathrm{T}} \cdot (\mathbf{g}^{\mathrm{T}} \cdot \mathbf{S} \cdot \mathbf{g}) \cdot \mathbf{n}$ (4-2) yields the Schmid Factor. For multi-slip cases, we will call this value the normalized resolved shear stress. For multiaxial tensile stress states, the maximum value is 0.5. For a stress state with both positive and negative stress components, the maximum value can be up to 1.0 (in the case of pure shear).
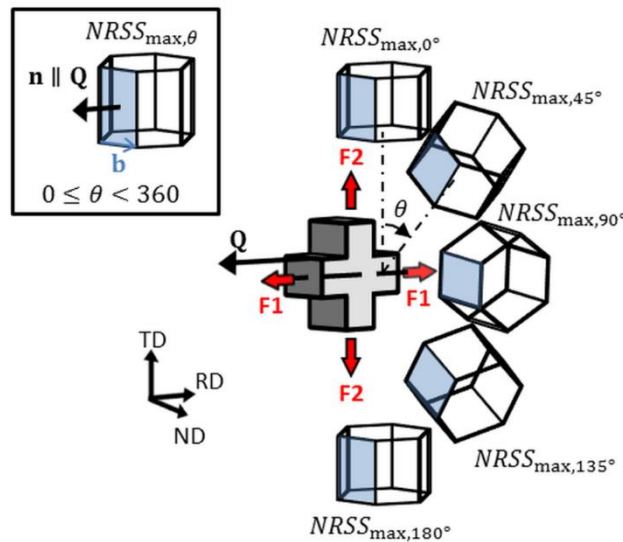
Figure 4-3 Schematic showing how the NRSS is calculated for a given slip mechanism and diffracting grain family. (A) The maximum NRSS for a given grain orientation and deformation mode is calculated from all possible slip systems. (B) The process is repeated for each grain contributing to the diffraction peak and the results are weighted by the texture.

Model	CRSS (MPa)				
	$Ba\langle a\rangle$	$Pri\langle a\rangle$	$Pyr\langle a\rangle$	$Pyr_{2nd}\langle c+a\rangle$	ETW
EPSC-TDT, VPSC-TDT [6]	12	75	--	100	30
T-CPFE [206]	17	108	--	290	12.8
EVPSC [40]	25	98	--	315	35
CPFE [5]	25	95	--	100	40
VPSC [36][a]	28	110	--	96	2
EVPSC [37]	17	85	--	100	20
VPSC (various) [207]	9-21	73-90	--	100-148	31-38
EPSC [33]	30	85-90	80	95-100	35
VPSC [199]	24	88	--	160	--
EPSC [152]	10	55	--	60	30
EPSC [152][b]	20	90	65	95	30

[a]1:1 proportional loading
[b]Extrusion

Table 4-1 CRSS values from crystal plasticity simulations of AZ31.

NRSS values were calculated for both the initial and prestrained texture. For a given deformation mode and grain family, the maximum NRSS for each slip system of each possible grain orientation contributing to the diffraction was calculated as described schematically in Figure 4-3. The NRSS values for each grain family were weighted based on the area fraction of grains in the IPF maps for the initial and prestrained microstructure. A full description of the calculations is provided in Appendix 4B at the end of this chapter.

The distribution of NRSS values shows how well a grain family is oriented for each possible deformation mechanism. However, whether or not a given mechanism is active also depends on the critical resolved shear stress (CRSS). A selection of reported CRSS values for AZ31 is shown in Table 4-1. On average, $\mathrm{CRSS}_{Ba\langle a\rangle} \approx \mathrm{CRSS}_{TTW}$, $\mathrm{CRSS}_{Pri\langle a\rangle} \approx \mathrm{CRSS}_{Pyr\langle a\rangle}$ and they are 3-4 times higher than $\mathrm{CRSS}_{Ba\langle a\rangle}$, and $\mathrm{CRSS}_{Pyr_{2nd}\langle c+a\rangle}$ is 5-6 times higher than $\mathrm{CRSS}_{Ba\langle a\rangle}$. Thus, for a higher CRSS mechanism to be activated first, its NRSS values must must be significantly higher.

The NRSS distributions for each grain family are used to interpret the lattice strain and integrated intensity obtained by neutron diffraction. This data is measured from a large ensemble of grains. The possibility that different slip systems may be active in individual grains in a grain family is not excluded, but the peak behavior represents the collective response of the ensemble of grains.

4.3 Results

4.3.1 Uniaxial Deformation (Dogbone)
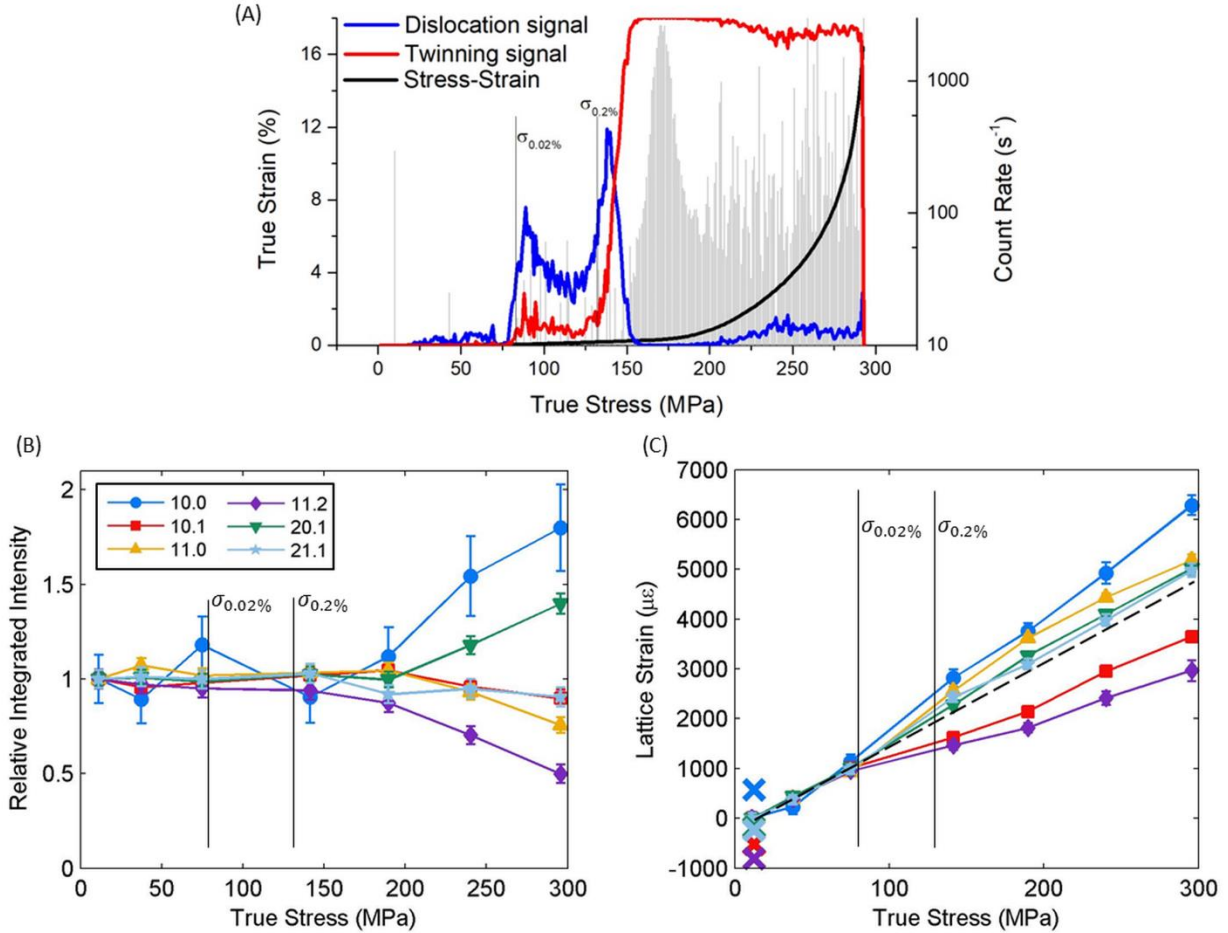
Figure 4-4 (A) Acoustic emission results, (B) relative integrated intensity evolution, and (C) lattice strain evolution for a dogbone under tensile load (crosses mark the lattice strains after unload).

Def. mode	$\{10.1\}$	$\{20.1\}$	$\{10.0\}$	$\{21.1\}$	$\{11.0\}$	$\{11.2\}$
Ba$\langle a \rangle$	0.360	0.216	0	0.190	0	0.446
Pri$\langle a \rangle$	0.337	0.404	0.433	0.476	0.433	0.314
Pyr$\langle a \rangle$	0.467	0.458	0.382	0.479	0.382	0.382
Pyr$^{2nd}\langle c + a \rangle$	0.324	0.380	0.335	0.482	0.446	0.402
ETW	0.027	0	0	0.005	0	0.137

Table 4-2 NRSS values for the dogbone test.

Figure 4-4A shows the evolution of the acoustic emission signal as a function of the true stress-true strain curve (black curve). The count rate of the total acoustic emission signal is shown on a logarithmic scale as light grey bars. The relative contributions of the twinning and dislocations to the total acoustic emission signal are shown in red and blue, respectively. At stresses below 150 MPa, the twinning and dislocation contributions do not add up to 100% due to the presence of noise in the signal. Figure 4-4B and C displays the peak evolution of six diffracting grain families as a function of the applied stress. The integrated intensity

evolution is shown in Figure 4-4B, with values normalized to the initial intensity for each peak. The lattice strain evolution is shown in Figure 4-4C. The crosses indicate the residual lattice strain for the grain families after unloading. The vertical lines indicate the 0.02% and 0.2% yield offset.

Table 4-2 shows the NRSS values for the dogbone for all possible deformation mechanisms. For the dogbone, the direction of the applied stress is parallel to the diffraction vector within the angular range of the detector, so all of the grains that contribute to a given diffraction peak have nearly the same NRSS.

Between 0 and 75 MPa, in the elastic regime, the lattice strain evolution of all grain families is very similar. This is expected given that single crystal pure Mg is elastically isotropic, with an anisotropy factor S_{66}/S_{44} of 0.97 [33]. In this region, the acoustic emission shows that there is no twinning signal and the dislocation signal is small. The integrated intensities of all peaks are relatively stable; however, the $\{10.0\}$ intensity varies noticeably at stresses before 0.02% yield. Such large variations over a small strain range could be related to twinning, but it is unlikely because the grain family has an NRSS = 0 for ETW. Additionally, the acoustic emission registers no twinning signal in this regime. Therefore the intensity variations are more likely due to poor counting statistics.

Between 75 and 140 MPa, the AE dislocation signal suddenly increases and the lattice strains diverge. This stress range corresponds to a microplastic regime dominated by dislocation generation. The $\{10.1\}$ and $\{11.2\}$ grain families shed load well below macroscopic yield, implying that these families are already undergoing plastic deformation. These families have a high NRSS for $Ba\langle a \rangle$ slip, the slip system with the lowest CRSS (Table 4-1), and are thus plastically softer than the surrounding grains. The load they shed is redistributed to the plastically harder grain families. Due to the strong basal texture, these soft grain families represent only a small fraction of the total grains in the dogbone. This explains why the onset of plasticity in these grains is not visible in the macroscopic mechanical response.

Just after 0.2% yield (132 MPa), there is a sudden increase in the AE count rate and twinning signal (Figure 4-4A). The energy released by a single twinning event is much higher than that of a single dislocation moving. Thus, although Figure 4-4A shows that the twinning plays a large role in this plastic regime, dislocation-based deformation is still active—the signal is just dwarfed by the twinning signal. At this point, the integrated intensity of the $\{10.0\}$ grain family increases significantly, while the $\{11.2\}$ intensity decreases significantly. The particularly strong decrease in $\{11.2\}$ and simultaneous increase in $\{10.0\}$ reflection intensities can be attributed to $\{10.2\}$-type ETW, also observed in [33]. Although the NRSS for ETW of the $\{11.2\}$ grain family is low (NRSS = 0.137), it is the highest NRSS for grain orientations that we measure that are present in the initial texture. The newly-oriented $\{10.0\}$ twins have NRSS = 0 for basal slip and so they are expected to become plastically harder with twinning, which is reflected in their increasing lattice strain (Figure 4-4B).

With further plastic deformation (>200MPa) the AE dislocation signal becomes stronger and the integrated intensity of the $\{20.1\}$ grain family increases while the intensity of $\{11.0\}$ grain family decreases. Simultaneously, the $\{11.0\}$ grain family appears to shed load while the $\{10.1\}$ and $\{11.2\}$ grain families take more load again. The strong intensity increase of the $\{20.1\}$ peak is likely related to twinning. The parent grains related to ETW for this family are in the $\{4\bar{1}.4\}$ grain family, which diffracts out of range of our detector. The NRSS is 0.107 for this grain family, which is higher than all of the measured grain families except for $\{11.2\}$.

NRSS analysis suggests that the moderate intensity drop of the {11.0} grain family, on the other hand, is due to dislocation-related grain rotation. The load-shedding of the {11.0} grain family suggests the activation of $Pyr_{2nd}\langle c+a \rangle$ slip in these grains because pyramidal slip is the only deformation mode for which the {11.0} family has a higher NRSS than {10.0} family, which does not shed load. This was also observed by Muránsky et al. [33]. The activation of $\langle c+a \rangle$ slip directly implies that $Pri\langle a \rangle$ slip is already active, because the two deformation modes have similar NRSSs but $Pri\langle a \rangle$ slip has a lower CRSS for uniaxial loading (Table 4-1). Thus the dogbone deformation must initially be dominated by $Ba\langle a \rangle$ and simultaneous ETW, with $Pri\langle a \rangle$ and then $Pyr_{2nd}\langle c+a \rangle$ slip at later stages of deformation.

4.3.2 Multiaxial Monotonic Loading (cruciform)
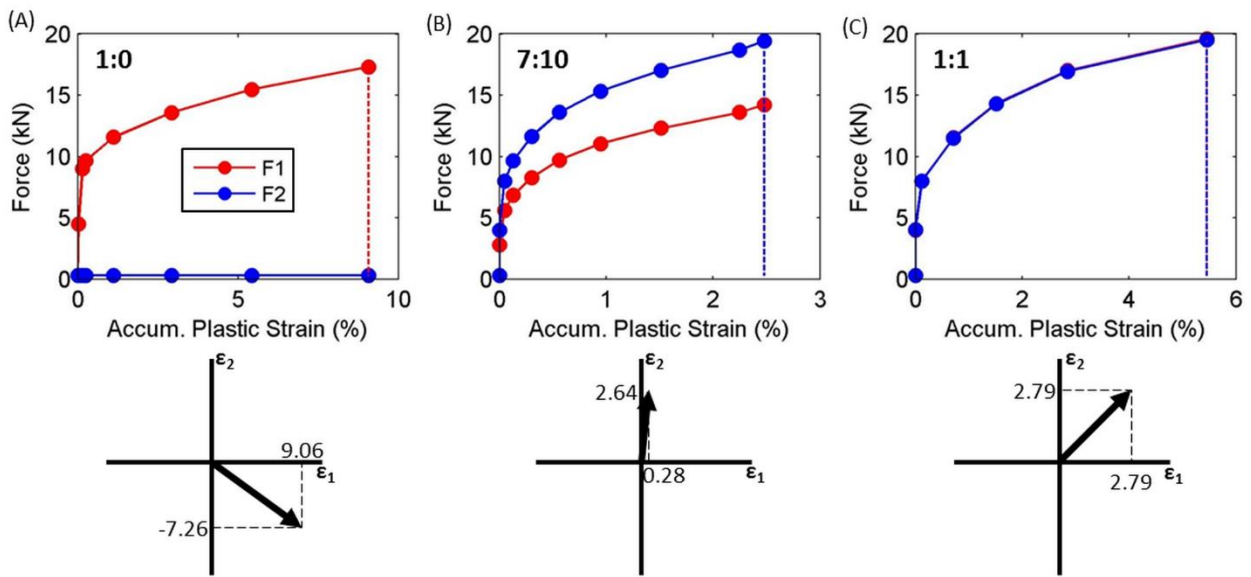
Figure 4-5 Force-accumulated plastic strain plots for the (A) 1:0, (B) 7:10, and (C) 1:1 monotonic loads. The corresponding strain paths are shown below each load path.

Figure 4-5 displays the mechanical response for the three monotonic load paths that have been performed. The applied forces are plotted against the plastic component of the von Mises strain. Due to the ring effect, the force ratios of the 1:0 and 7:10 monotonic loads do not correspond to the same strain ratios. The measured strain ratios are shown below. Because of the complex shape of the cruciform it is not possible to directly convert applied force in the arms into stress at the gauge volume. Therefore these force-accumulated plastic strain curves cannot be directly compared with one another.
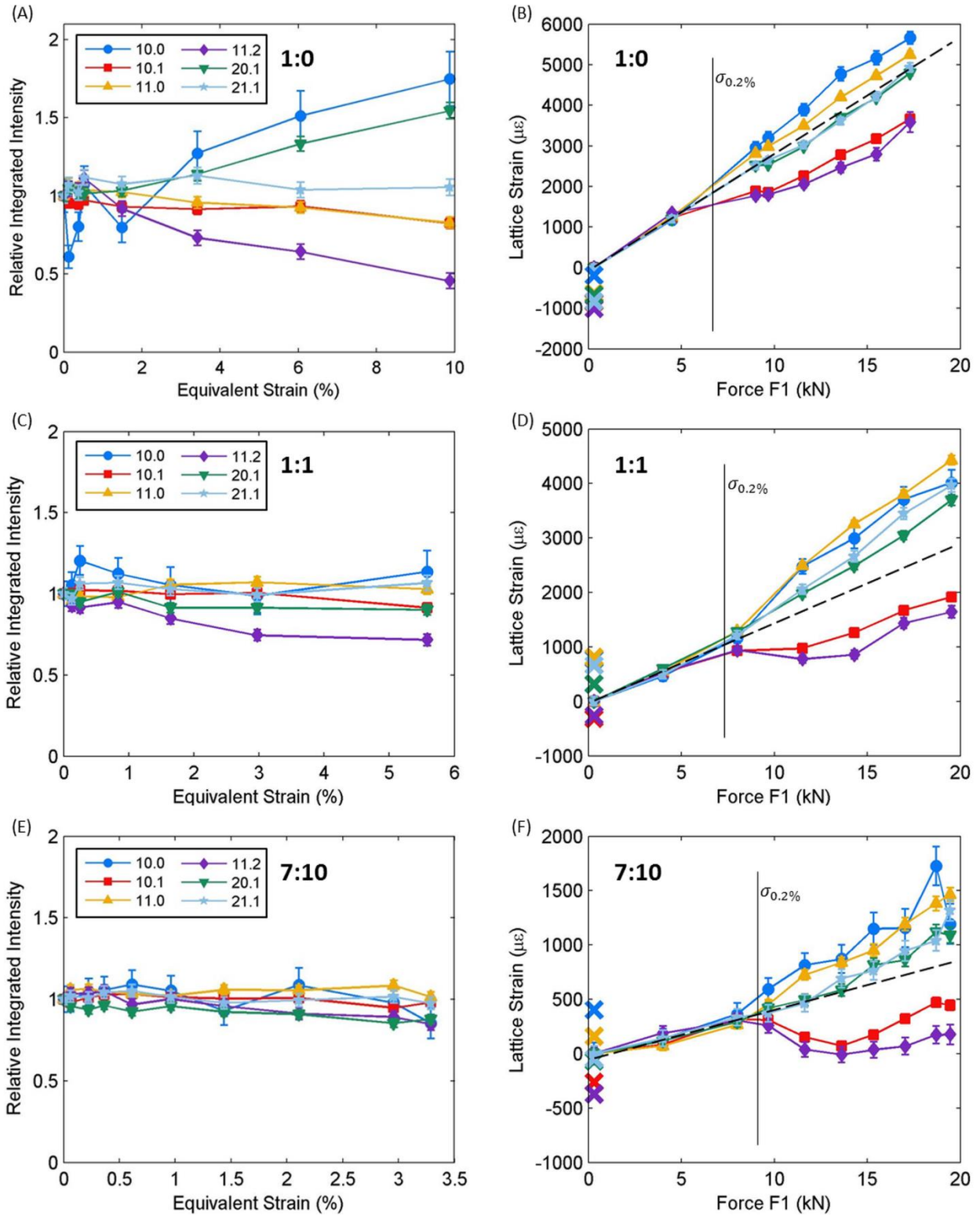
Figure 4-6 Integrated intensity and lattice strain evolution from *in situ* neutron diffraction of cruciforms during (A,B) 1:0, (C,D) 1:1, and (E,F) 7:10 monotonic loads.
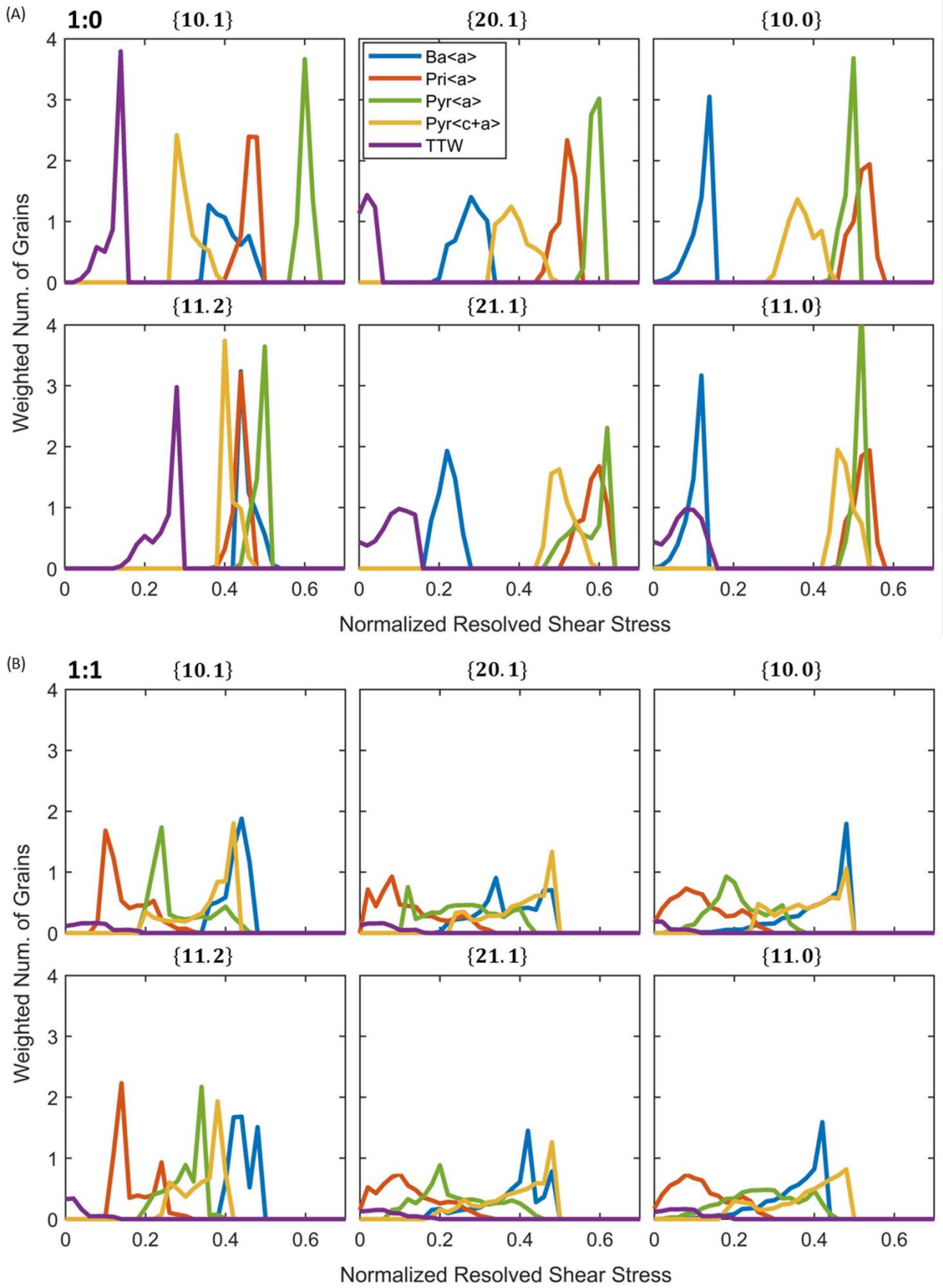
Figure 4-7 NRSS distributions for the 1:0 and 1:1 monotonic loads.

Figure 4-8 Post-mortem IPF map, grain boundary map with highlighted twin boundaries, and (00.1) pole figure for the (A,B,C) 1:0 monotonic load and (D,E,F) 1:1 monotonic load.

Figure 4-9 (A) IPF map and (B) grain boundary map of a twinned grain after the 1:1 monotonic load. (C) Pole figure with the orientations of the parent grain and six {10.2} twin variants. (D) Calculated NRSS values for the six twin variants.

Figure 4-6 displays the peak evolution for 1:0, 1:1, and 7:10 monotonic loading of the cruciform-shaped samples. The relative integrated intensity is shown as a function of the equivalent strain for each loading mode (Figure 4-6A,C,E), and the corresponding lattice strain is shown as a function of the force on axis 1 (Figure 4-6B,D,F). The integrated intensity of each peak is normalized by dividing by the initial value. In the lattice strain evolutions, the crosses show the lattice strain in the unloaded state due to residual stresses. The lower magnitude of the residual lattice strains for the 1:1 and 7:10 loads is due to the increasing Poisson contraction on axis 1 caused by the increasing relative strain component on the transverse axis [176]. NRSS

grain distributions for the 1:0 and 1:1 monotonic loads are shown in Figure 4-7. The NRSS distribution for 7:10 monotonic loading is available online as supplementary material.

Figure 4-8 shows the EBSD analysis for the 1:0 (Figure 4-8A-C) and 1:1 (Figure 4-8D-F) monotonic loads. The IPF maps are shown on the left, the grain boundary maps with highlighted twin boundaries in the middle, and pole figures on the right. EBSD images for the 7:10 monotonic load are not shown because its behavior was similar to the 1:1 load. Note: the EBSD sample for the 1:0 montonic load is *not* the same sample that was tested *in situ*. The sample was deformed *ex situ* to an equivalent strain of 4.88%. Thus, the microstructure in Figure 4-8A-C is representative of the starting microstructure for all of the LPC reloads.

During the 1:0 monotonic load, the evolution of the integrated intensity is very similar to that of the dogbone, despite the presence of the ring effect. ETW from the $\{11.2\}$ grain family into the $\{10.0\}$ family results in a decrease in intensity of the former and an increase in the latter (Figure 4-6A). This twinning system is seen in the IPF map (Figure 4-8A) as yellow-green parent grains with blue twins and appears as the presence of intensity around the TD poles of the pole figure (Figure 4-8C). The IPF map also shows several grains with dark purple twins which contribute to the intensity increase of the $\{20.1\}$ grain family (green curve, Figure 4-6A). Different twinning systems are visible in several other grain orientations. These grain orientations, however, are diffracting outside of the angular range of the detector and are therefore not seen in the neutron diffraction pattern.

Despite the similarities of the intensity evolution with the dogbone sample, the ring effect has a noticeable influence on the lattice strains of the measured grain families (Figure 4-6B). The $\{10.1\}$ and $\{11.2\}$ grain families are the most plastically soft for low-CRSS $Ba\langle a\rangle$ slip (Figure 4-7A) and they plastify early in the microplastic regime (Figure 4-6A). The $\{20.1\}$ and $\{21.1\}$ families plastify at higher stresses, which causes the relaxation in the lattice strain at 9kN. The plasticity is likely due to $Ba\langle a\rangle$ slip, as the NRSS distributions for $\{21.1\}$ and $\{20.1\}$ have lower values than those of the $\{10.1\}$ and $\{11.2\}$ (see Figure 4-7A). One could argue that $Pri\langle a\rangle$ or $Pyr\langle a\rangle$ slip could be responsible for the load shedding, but the NRSS distributions are similar for all diffraction peaks so load shedding should then be observed in all families if that were the case. The $\{10.0\}$ and $\{11.0\}$ families are poorly oriented for $Ba\langle a\rangle$ slip and thus remain plastically hard. It is likely that $Pri\langle a\rangle$ or $Pyr\langle a\rangle$ slip are activated in these grains around the same time as $Ba\langle a\rangle$ slip, because the NRSS values for $Pri\langle a\rangle$ or $Pyr\langle a\rangle$ slip are 3-4 times larger than $Ba\langle a\rangle$ slip, enough to counter the differences in CRSS. Dislocation-based grain rotation for these grain families is seen as a "smearing" of the basal texture in the pole figure (Figure 4-8C). After unloading, the ring effect results in a compressive residual stress in the unloaded state that pushes all of the measured grain families into compression (marked "x" in Figure 4-6B).

During the 1:1 monotonic load, the intensities are relatively stable (Figure 4-6C). This suggests that the role of twinning is minimal, at least for $\varepsilon_{Eq} < 5.5\%$. A small amount of ETW and $\{10.1\} - \{10.2\}$ double twinning is observed in the IPF maps (Figure 4-8D,E). The pole figure in Figure 4-8F shows a slightly stronger basal texture than the initial microstructure, and the $\{11.2\}$ - $\{10.0\}$ twinning system is not activated in this load path, evident from the lack of intensity at the TD poles of the pole figure (Figure 4-8F). There is, however, still a gradual decrease in integrated intensity of the $\{11.2\}$ peak (Figure 4-6C). The intensity change is likely due primarily to grain rotation from dislocation activity because there are only a few $\{11.2\}$ grains that are capable of twinning. Note, however, that the IPF map (Figure 4-8D) shows that there are some narrow extension twins in a few $\{11.2\}$ grains which also contribute to the intensity decrease.

The NRSS values for ETW were calculated for several twinned grains in the 1:1 load. One such grain is shown in Figure 4-9. The selected variants V6 and V5 have NRSS values of 0.155 and 0.073, respectively, the first and third highest NRSS values (Figure 4-9D). V3, which has the second highest NRSS value (0.099) is not observed. Non-Schmid twinning and twin variant selection has been previously observed in AZ31 [63,65] and is discussed further in Section 4. In many twinned grains it appears that nucleation is preferred to growth of existing twins.

For 1:1 biaxial loading, NRSS analysis shows that all grain families have grains well-oriented for low-CRSS $Ba\langle a\rangle$ slip. However, the $\{10.1\}$ and $\{11.2\}$ grain families have nearly all grains with high NRSS, whereas the other families have a much wider distribution. The $\{10.1\}$ and $\{11.2\}$ grain families plastify early in the microplastic regime as $Ba\langle a\rangle$ slip is activated in a majority of the grains (Figure 4-6D). It is likely that the grains with high NRSS values in the other families plastify early as well, but the response measured by diffraction averaged out with the harder grains and the family as a whole takes more load. As the $\{10.1\}$ and $\{11.2\}$ grain families harden, load is redistributed to the other grain families, resulting in the load shedding that is seen in the $\{10.0\}$ and $\{11.0\}$ grain families at F1 = 11.5 kN.

From the lattice strain evolution (Figure 4-6D), the $\{10.0\}$ and $\{11.0\}$ grain families seem to take always more load. The $\{11.0\}$ family does not have any grains with NRSS > 0.44 and is therefore indeed plastically hard compared to the other grain families. The $\{10.0\}$ family, however, has many grains with high NRSS values for $Ba\langle a\rangle$ slip which are plastically soft. Load shedding is not observed because $\{10.0\}$ grains are oriented such that one $Ba\langle a\rangle$ slip system with a Burgers vector perpendicular to the diffraction vector **Q** is significantly preferred over the other two. Thus, the $\{10.0\}$ family is plastically soft in some directions perpendicular to **Q**, but hard along **Q**. The other five grain families in this study deform along several slip systems, so the lattice strain evolution can be interpreted as a result of plasticity.

During the 7:10 monotonic load, the intensities are very stable for $\varepsilon_{\text{Eq,7:10}} < 3.5\%$ (Figure 4-6E) and the lattice strain behaviors generally follow the same trends as in the 1:1 load (Figure 4-6F). It is expected that the deformation behavior is dominated by $Ba\langle a\rangle$ slip with reduced twinning, as observed for the 1:1 load.

4.3.3   Load Path Changes (cruciform)

During the LPC experiments the cruciform samples are first preloaded uniaxially (force ratio 1:0) along the rolling direction to a total plastic strain of 3.7-4.7%. After the applied force is released a second load is applied, with load ratios of 0:1, 7:10 and 1:1 as described in Figure 2. Due to the ring effect, the strain path change angle is not the same as the angle between the applied loads. This is shown in Figure 10 for the three LPCs. The angles between the directions of the plastic strain during the strain path change are 170°, 135° and 90° for the 0:1, 7:10, and 1:1 LPCs, respectively, as calculated from the macroscopic strain measurements.
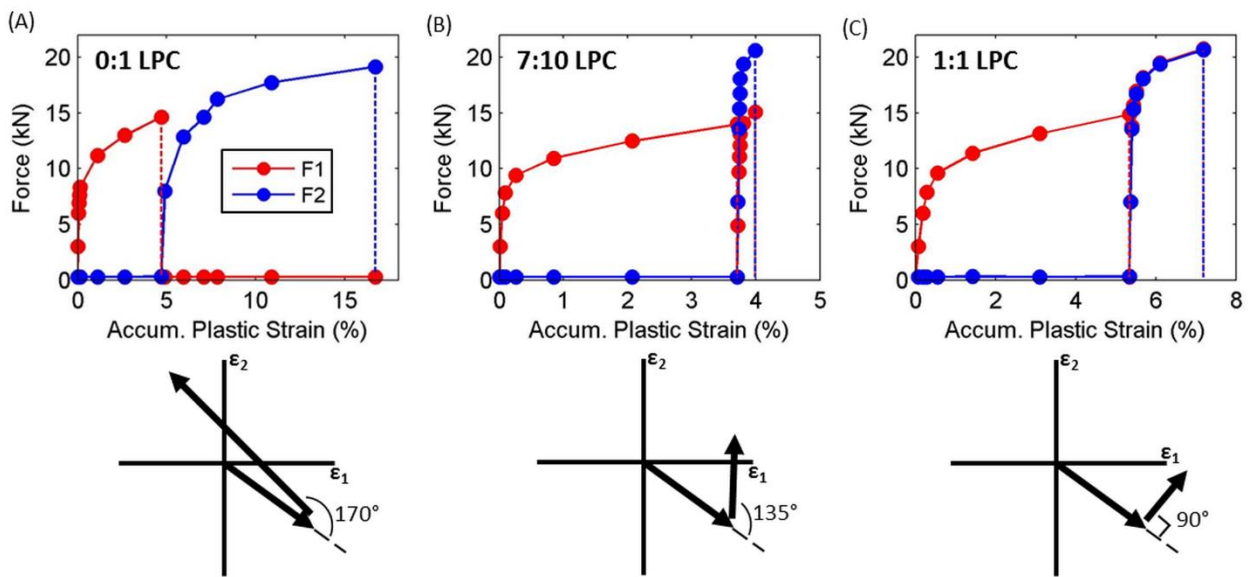
Figure 4-10 Force-accumulated plastic strain plots for the (A) 0:1, (B) 7:10, and (C) 1:1 load path changes. The corresponding strain path changes are shown below each load path.

The mechanical response of the LPCs is shown in Figure 4-10, with the corresponding strain path change shown below each LPC. As with the monotonic multiaxial loads, it is not possible to directly compute the stress state in the center of the cruciform from the force in the arms, so applied force is shown instead. The slight variations in prestrain were caused by differences in the thickness of the samples due to machining tolerances. However, the observed diffraction data suggests that the microstructure evolution during prestrain was very similar for each sample. In both the 7:10 and 1:1 reloads, there is a significant overshoot in force-accumulated plastic strain curve, whereas in the 0:1 reload there is an undershoot. This suggests a higher yield stress for the 7:10 and 1:1 LPCs and a lower yield stress in the 0:1 LPC upon reloading.

Neutron Diffraction and EBSD analysis
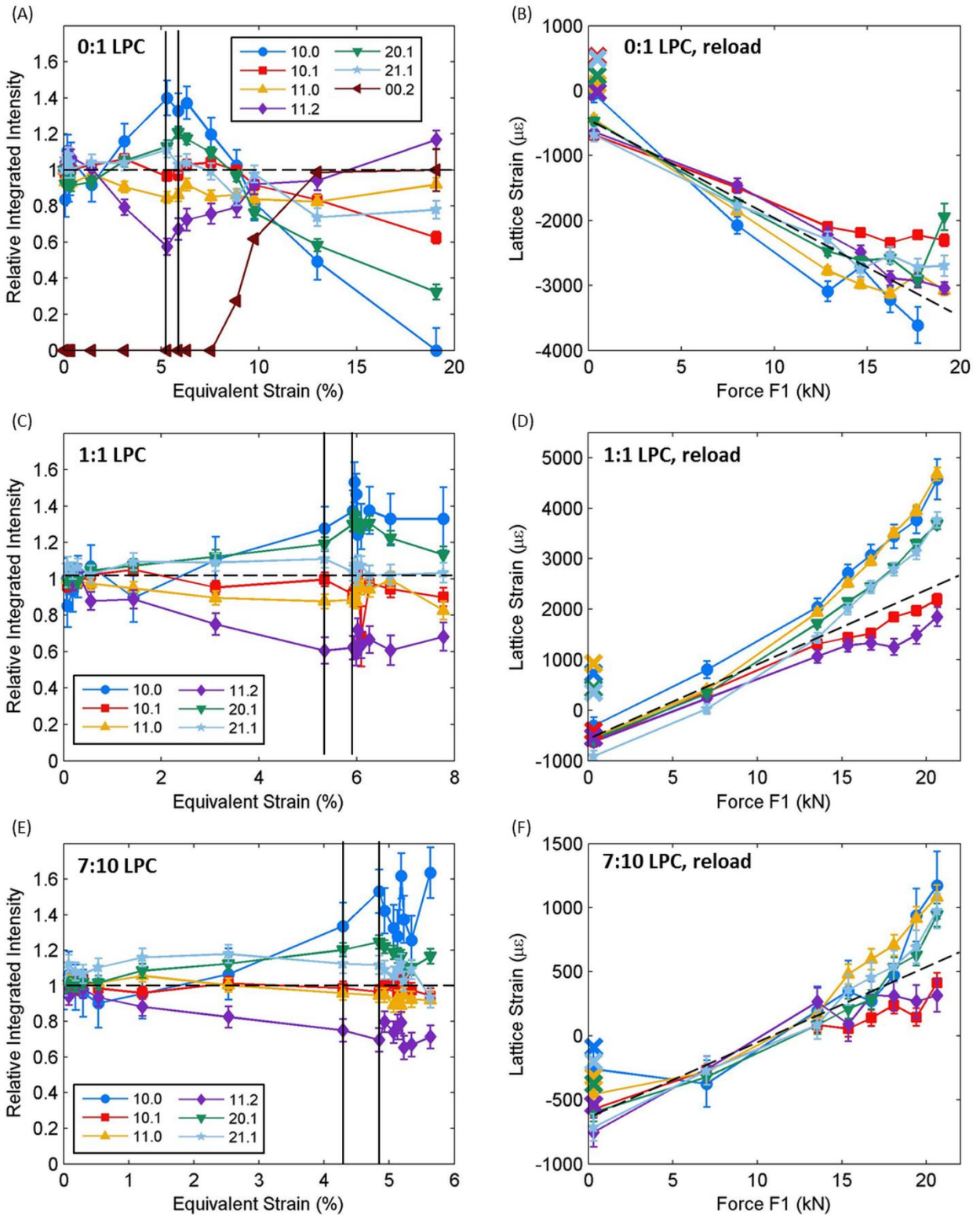
Figure 4-11 Integrated intensity and lattice strain evolution from *in situ* neutron diffraction of cruciforms during (A,B) 0:1, (C,D) 1:1, and (E,F) 7:10 LPCs. Black vertical lines on the integrated intensity plots demarcate the unload: to the left is the 1:0 preload, in between is the unload, and to the right is the reload. Lattice strains are shown only for the reload. NRSS grain distributions for the 0:1 and 1:1 LPCs are shown in Figure 4-12. The NRSS distribution for 7:10 LPC is available online.
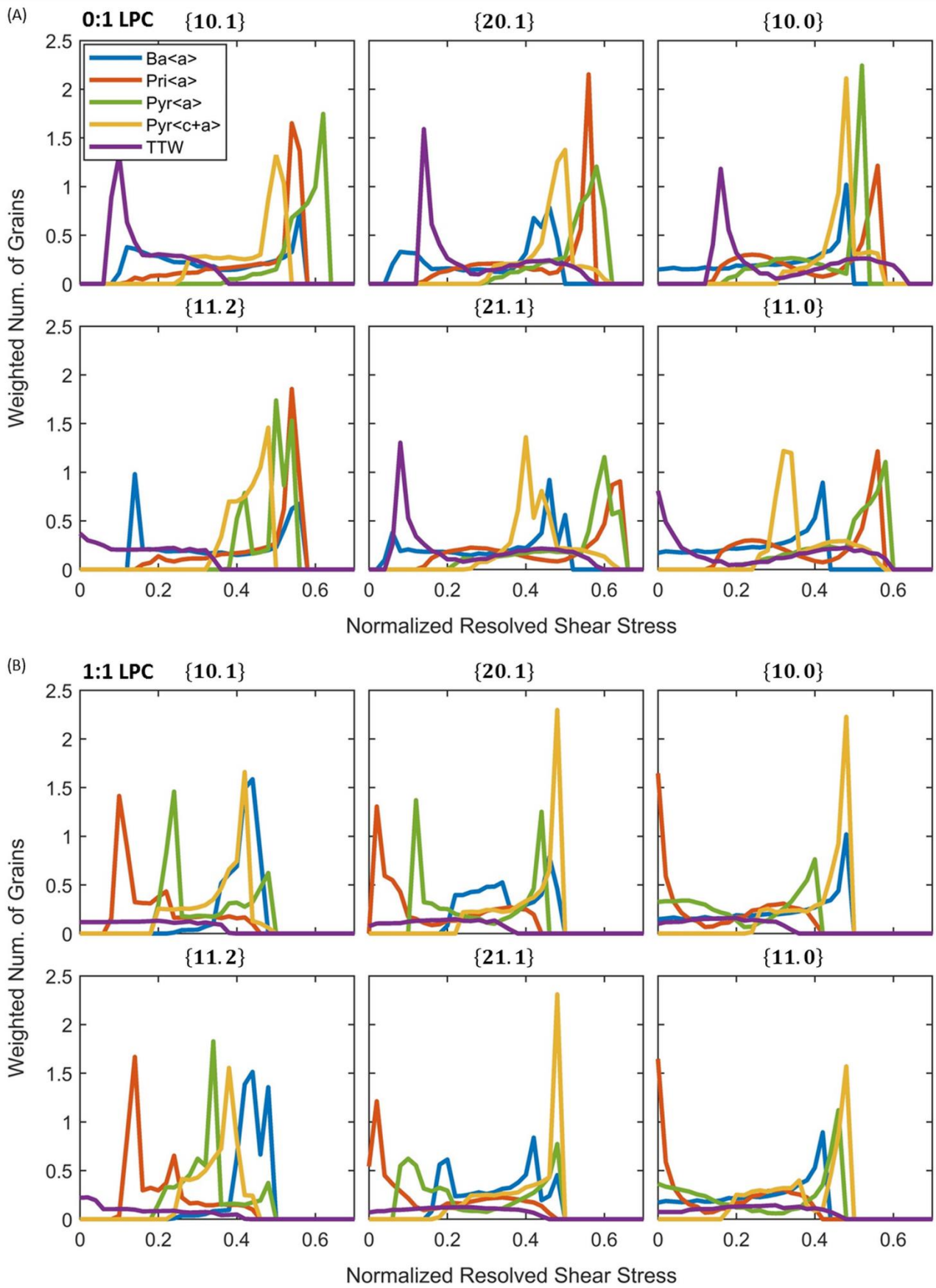
Figure 4-12 NRSS distributions for the reloads of the 0:1 and 1:1 LPCs.

TTW {101$\bar{2}$}86±4°⟨12$\bar{1}$0⟩
CTW {101$\bar{1}$}56±4°⟨12$\bar{1}$0⟩
DTW{101$\bar{1}$}–{101$\bar{2}$}38±4°⟨12$\bar{1}$0⟩
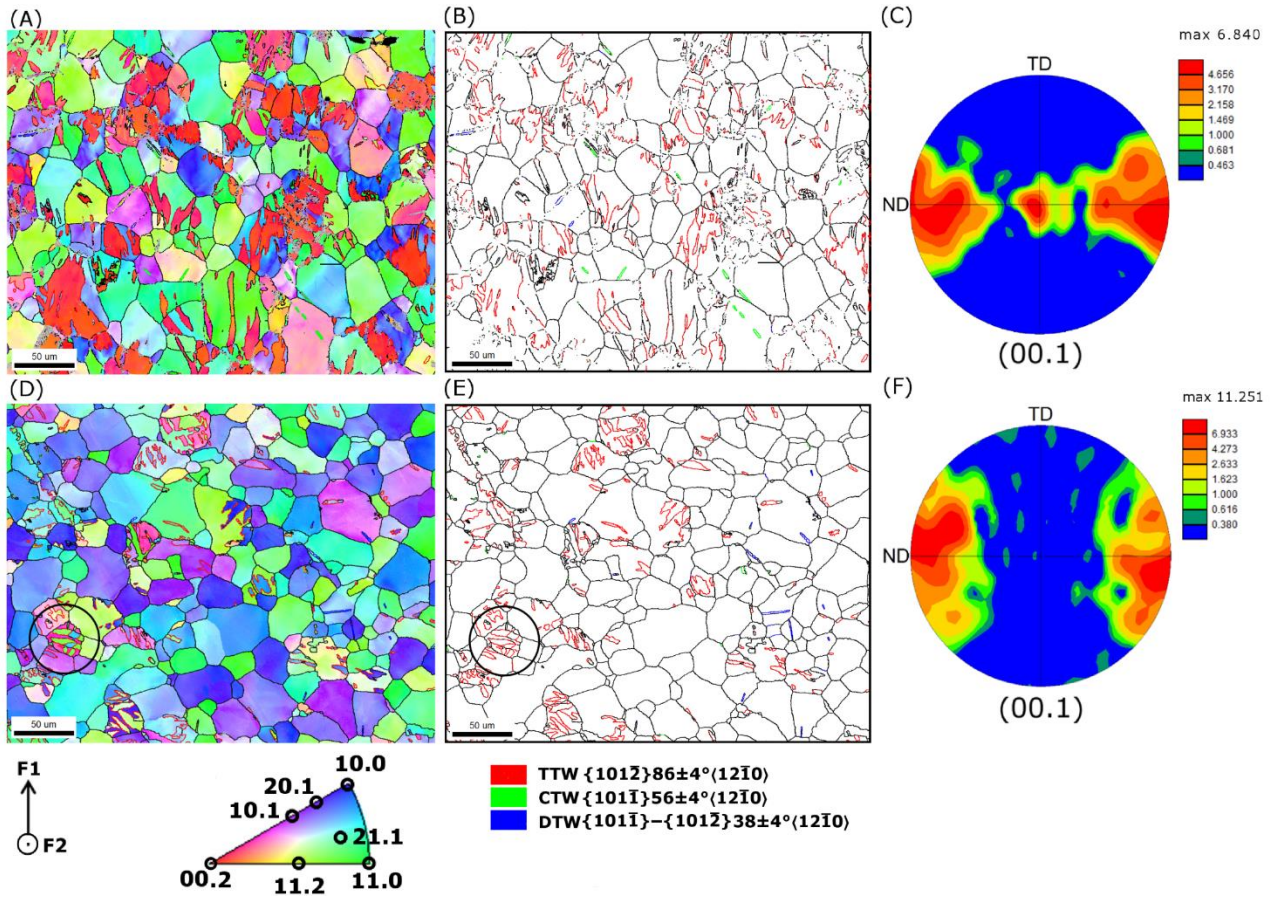
Figure 4-13 Post-mortem IPF map, grain boundary map with highlighted twin boundaries, and (00.1) pole figure for the (A,B,C) 0:1 LPC and (D,E,F) 1:1 LPC.

TTW	NRSS		
	1:0 (uniaxial)	1:1 (equibiaxial)$_I$	1:1 (equibiaxial)$_{II}$
v1	0.369	-0.083	0.455
v2	0.141	0.072	0.111
v3	0.255	0.283	0.067
v4	0.322	-0.065	0.425
v5	0.069	0.037	0.095
v6	0.231	0.231	0.081

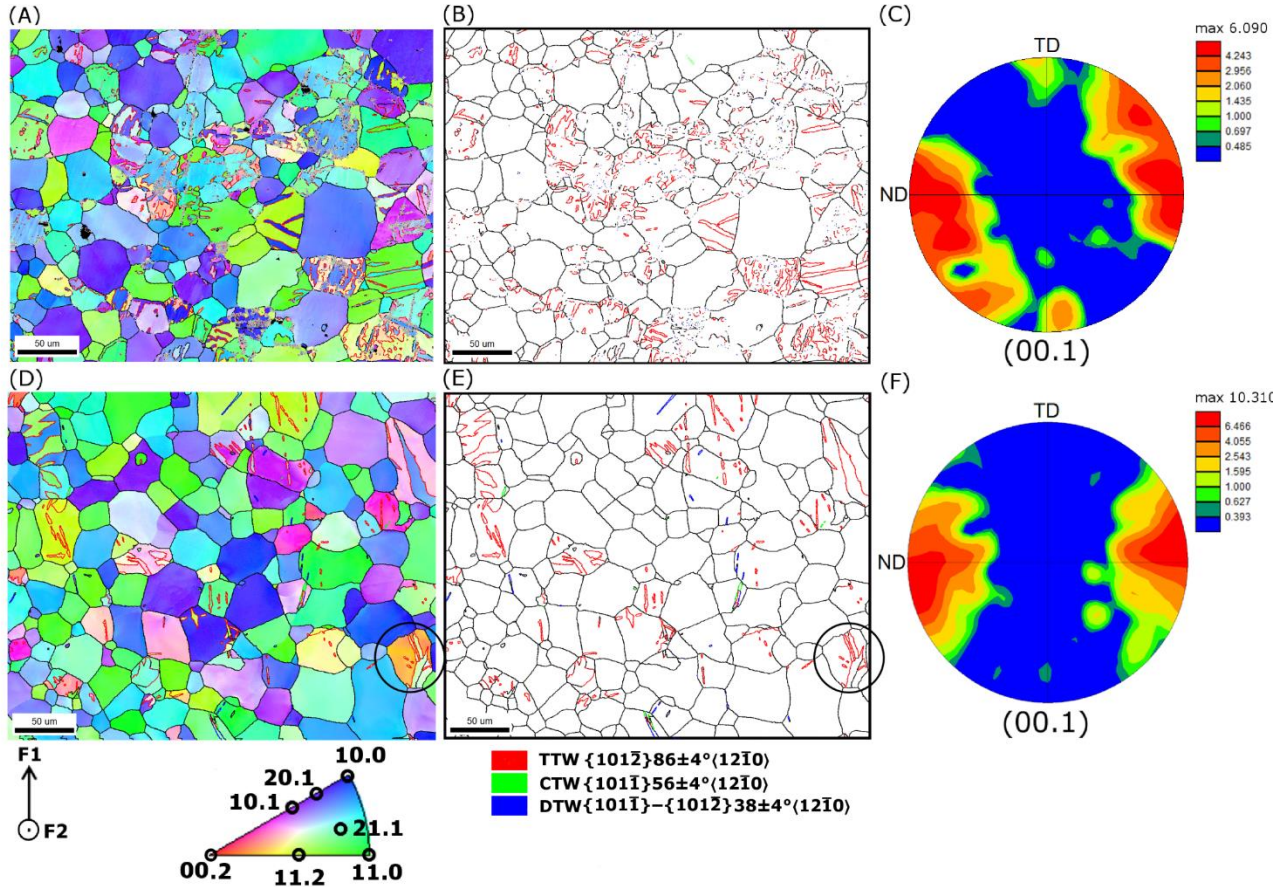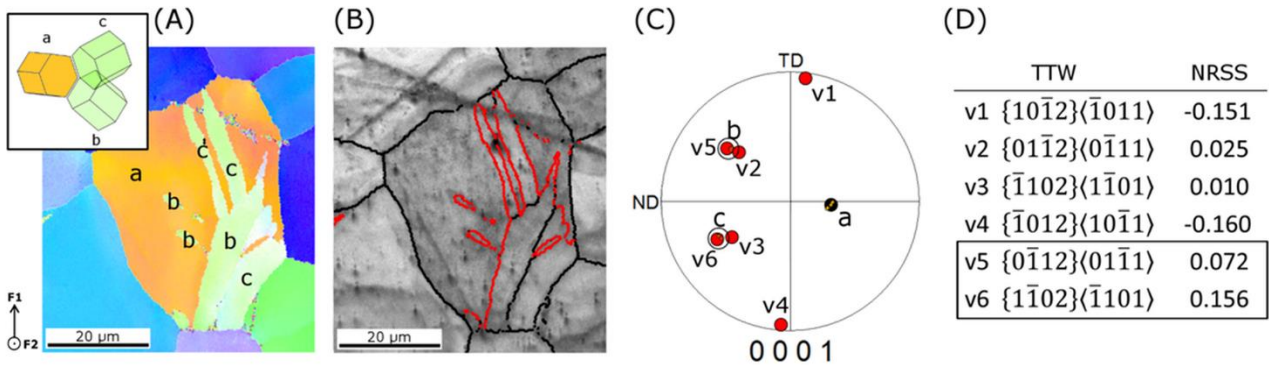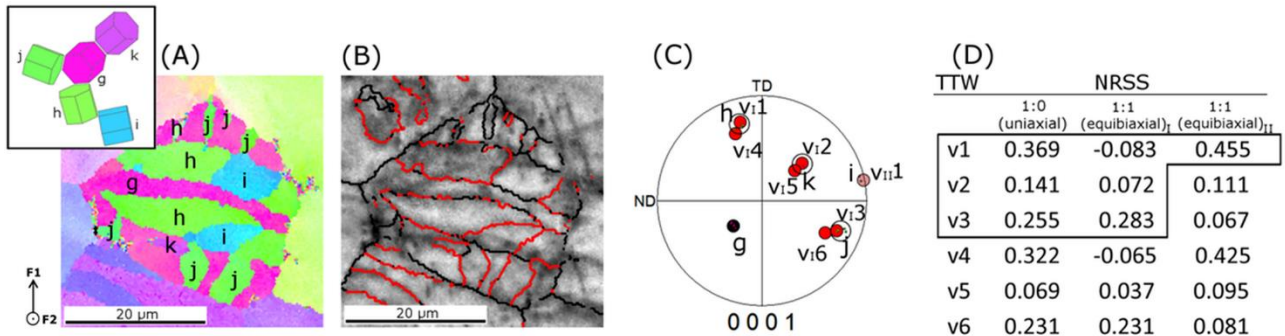Figure 4-14 (A) IPF map and (B) grain boundary map of a heavily-twinned grain after the 1:1 LPC. (C) Pole figure with the orientations of the parent grain and six {10.2} twin variants. Variant twin plane and shear direction are the same as in Figure 4-9. (D) Calculated NRSS values for the six twin variants.

Figure 4-11 shows the diffraction peak evolution for the 0:1, 7:10, and 1:1 LPCs. The two vertical lines on the integrated intensity graphs show where the load path changed: the left line indicates the end of the preload, the right the beginning of the second load, and in between the unload. During the preload, the peaks behave as expected from the 1:0 monotonic load test (Figure 4-6A). Equivalent strain was used instead of accumulated plastic strain to capture the behavior during the unload. The magnitudes of the integrated intensity changes are lower because the samples are only strained to 3.7-4.7%. In the 0:1 LPC, the (00.2) intensity is normalized with respect to the final value because the peak is not visible in the preload due to

the texture. Due to the cruciform geometry, it was only possible to achieve 2% and 1.2% equivalent strain in the gauge section for the reloads of the 1:1 and 7:10 LPCs, respectively.

Figure 4-13 shows the EBSD analysis for the 0:1 LPC (Figure 4-13A-C) and 1:1 LPC (Figure 4-13D-F). The IPF maps are shown on the left, the grain boundary maps with highlighted twin boundaries in the middle, and pole figures on the right. EBSD images for the 7:10 LPC are not shown because its behavior was similar to the 1:1 LPC.

During the reload of the 0:1 LPC, the lattice strain differs considerably between the first and second measurement points. This apparent "anisotropy" in the elastic strain behavior must be ascribed to very early microplastic deformation during the reload. It is also evident in the mechanical response in Figure 4-10, which already shows a slight increase in plastic strain between the unloaded state and the first point of the reload. In this microplastic regime, the plastically soft {10.1} and {11.2} grain families are already shedding load. It is anticipated that if an intermediate measurement point was taken, the lattice strain behavior would be isotropic in the elastic regime and then deviate at the onset of microplastic yield.

As the sample plastifies, the integrated intensity of the {10.0} grain family decreases while the {11.2} and (00.2) grain family intensities increase significantly (Figure 4-11A). These behaviors are a result of primary twinning combined with de-twinning and secondary twinning. During the preload, ETW of {11.2} grains create twins in the {10.0} orientation. During the 0:1 reload the {10.0} grain family, including the twins, are oriented well for ETW into the (00.2) orientation. This results in de-twinning back into the {11.2} orientation and secondary ETW into the (00.2) orientation. The extensive twinning into the (00.2) orientation is seen in the IPF map in Figure 4-13A. The blue parent grains with red twins are the {10.0} - (00.2) ETW system. Several of the grains have been completely swallowed up by the (00.2) twins.

For the last 7% of strain, the integrated intensity of the (00.2) grain family stays constant, suggesting that twinning into this orientation has mostly stopped. However, the integrated intensity of the {10.0} grain family continues to decrease until almost no grains remain in diffraction condition. This is due to twinning of {10.0} grains into orientations *near* the (00.2) peak but just outside of the ±2.5° detector tolerance. In this strain range, the integrated intensity of the {11.2} family increases past the initial intensity. No twinning is observed into the orientation (Figure 4-13A,C) and the intensity changes gradually compared to the twinning families, so it is likely that the intensity changes are due to grain rotation from dislocation activity.

The {10.1}, {20.1}, and {21.1} grain families also show a decrease in integrated intensity in the plastic regime (Figure 4-11A). A large fraction of the grains in the {21.1} and {20.1} families are well-oriented for ETW, with NRSS values greater than 0.4. ETW is visible in the IPF map (Figure 4-13A) in both the green {21.1} and the dark purple {20.1} grains. The {10.1} grain family, on the other hand, has the majority of its grains with a low NRSS for ETW. Twinning is hardly active in these grains (Figure 4-13A). Thus, the intensity drop is more likely related to dislocation-related grain rotation.

Both the {10.1} and {11.2} grain families shed load in the microplastic regime (Figure 4-11B) because they are well-oriented for $Ba\langle a \rangle$ slip. However, immediately after macroplastic yield, the {11.2} grain family begins to take more load while the {10.1}, {20.1}, and {21.1} families all shed load. As discussed previously, the {20.1} and {21.1} families have begun twinning and thus are able to accommodate strain with little hardening. The {10.1} family, however, is not twinning significantly. The only deformation mode for which the {11.2} family is harder than the {10.1} family is $Pyr\langle a \rangle$ slip, implying that this mechanism may be active. The activity of this mechanism is often ignored in crystal plasticity models, but several studies have shown

that the inclusion of this mechanism can improve predictions of the lattice strain evolution of various loading modes [33,152].

During the second load of the 1:1 LPC (Figure 4-11C), the integrated intensities for all peaks stay relatively stable over $\varepsilon_{\text{Eq}} < 2\%$. This suggests that twinning activity is limited, and the twins from the preload are not de-twinning. The pole figure shows a strengthening of basal texture like the 1:1 monotonic load (Figure 4-13F). As in the 1:1 monotonic load, some $\{10.1\} - \{10.2\}$ double twinning is observed in the IPF map (Figure 4-13D). Yellow-green grains with blue extension twins are visible that are similar to those in the preload, confirming the absence of de-twinning. The presence of these twins from the preload causes intensities at the TD poles of the pole figure which are not obvious due to the high values at other orientations.

A few grains show very complex twinning after the 1:1 LPC. The twinning in the reload was dominated by the nucleation of new twins rather than the growth of existing ones. Figure 4-14 examines the twin variant selection in one heavily-twinned grain (circled in Figure 4-13D). The grain in Figure 4-14A has three primary twin variants V$_\text{I}$1, V$_\text{I}$2, and V$_\text{I}$3, along with one secondary twin orientation, V$_\text{II}$1, which twinned from V$_\text{I}$1. The "h" and "j" twins (NRSS 0.369 and 0.255, respectively) are suspected to have formed during the 1:0 preload. However, it is possible that the "j" twins formed during the 1:1 reload, as they have a very high NRSS of 0.283. During the reload, the "i" twins form as secondary twins within the "h" primary twins. The "k" twin is then nucleated at the triple junction of the "h", "j" and "i" twins. As in the 1:1 monotonic load, the selected variants do not necessarily correspond with the highest NRSS value, which is discussed in Section 4. This activation of multiple twin variants in one grain is not seen in any of the other LPCs.

The lattice strain evolution during the reload shows that the $\{10.1\}$ and $\{11.2\}$ grain families shed load early (Figure 4-11D) as they have a large fraction of grains well-oriented for low-CRSS $Ba\langle a \rangle$ slip. However, they quickly harden and begin to take load again after very little strain. All grain families are plastically hard during the reload, despite having grains well-oriented for $Ba\langle a \rangle$ slip. This suggests that there is significant plastic hardening from dislocations generated during the preload in all grains.

During the second load of the 7:10 LPC, the integrated intensities also do not change significantly (Figure 4-11E), suggesting there is no twinning activity (at least for $\varepsilon_{\text{Eq}} < 1.2\%$). The large intensity fluctuations of the $\{10.0\}$ family are due to low counting statistics—such behavior over small strain ranges during a continuous load are not physical.

As in the 7:10 monotonic load, the $\{10.1\}$ and $\{11.2\}$ grain families shed load first while the $\{10.0\}$ and $\{10.1\}$ families take the most load (Figure 4-11F). This behavior is expected from NRSS analysis (available online as supplementary material). Unfortunately, the sample reached such low strains that it is hard to draw further conclusions from the lattice strain evolution.
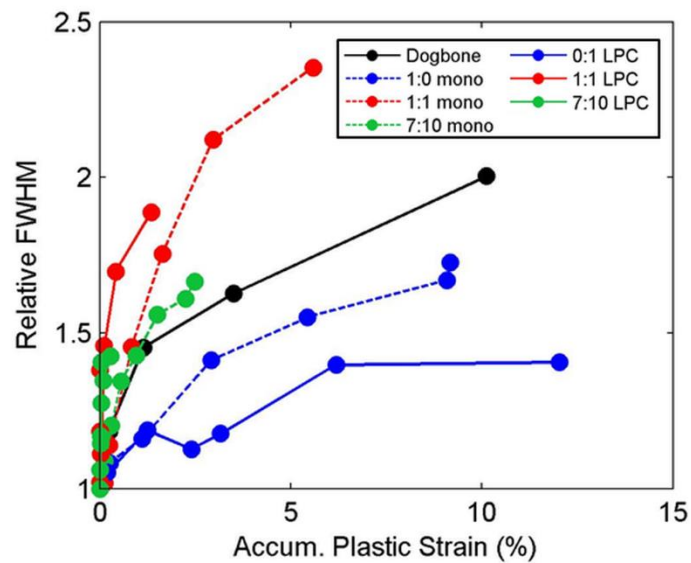
Figure 4-15 Peak broadening of the {10.1} grain family. For the LPCs, only the reloads are shown.

The effect of the preload is also seen in the behavior of the peak broadening. Figure 4-15 shows the peak broadening of the {10.1} peak for the monotonic loads and LPC reloads. Monotonic loads are shown as dashed lines, and the corresponding LPC reloads are shown as solid lines of the same color. The peak broadening during deformation of the dogbone is shown in black. Only the {10.1} reflection is shown as the peak broadening in the other reflections shows the same trends. EBSD analysis shows that the average grain size does not change significantly, despite the observed twinning, so the peak broadening behavior is attributed to changes in dislocation density during the tests.

The 1:0 monotonic load has lower peak broadening than the dogbone while the broadening of the 7:10 and 1:1 monotonic loads is increased. After a 1:0 preload, the 0:1 reload shows even lower peak broadening than the 1:0 load. The 7:10 and 1:1 reloads show increased broadening compared to the corresponding monotonic loads. Interpretations of these observations are discussed below.

4.4   Discussion

The combination of *in situ* neutron diffraction, acoustic emission, and EBSD is a powerful tool to identify active deformation mechanisms during multiaxial loading of AZ31. The interpretation of the diffraction data relies on NRSS analysis. Obviously, such an analysis has its limitations, because it does not take into account the effects of elastic and plastic anisotropy or texture evolution. However, since AZ31 is nearly elastically isotropic, NRSS analysis at the onset of plasticity can be justified. At later stages of deformation, plastic anisotropy becomes more important and the true behavior can only be captured by crystal plasticity models. In literature there exists large variations for the reported CRSS values of the various deformation mechanisms in AZ31 (see Table 4-1). It is anticipated that the findings of this study would be useful for the validation of improved crystal plasticity finite element (CPFE) models.

Monotonic loads

The results from the dogbone confirm the findings of crystal plasticity simulations of uniaxial tension [33,38,187]: at the onset of plasticity $Ba\langle a \rangle$ slip is activated in a subset of grains with their c-axis away from the sheet normal followed by ETW-induced plasticity and, later, $Pri\langle a \rangle$ slip. At larger plastic strains, $\langle c + a \rangle$

slip on $\{11.2\}$ 2nd order pyramidal planes is activated, in agreement with the findings of Muránsky et al. [33]. AE measurements give evidence that there should be very little twinning activity in the elastic regime (<75MPa), despite large intensity variations in the $\{10.0\}$ grain family. This finding is in contrast to the study of Muránsky, who proposed that the variations were due to deformation twinning in a few well-oriented grains.

In the 1:0 monotonic load $Ba\langle a\rangle$ is again activated in the microplastic regime in the $\{10.1\}$ and $\{11.2\}$ grain families, followed by ETW, then $Pri\langle a\rangle$ and $Pyr_{2nd}\langle c+a\rangle$ slip. The separation between the NRSS values for $Ba\langle a\rangle$ slip imply that grain families will begin to plastify one after another. The compressive transverse stress effectively improves the orientation of all measured grain families for slip and ETW as compared to the dogbone.

The lower peak broadening observed in the cruciform versus the dogbone is a direct result of the ring effect. It has been shown that the out-of-plane texture is favourable for ETW when subjected to in-plane compression [3,181,197,199,208]. This is evident from the higher NRSS values for ETW in the cruciform for every grain family except the $\{10.0\}$. The additional compressive stress of the ring effect activates more ETW in the cruciform than in the dogbone, so fewer dislocations are needed to accommodate strain, explaining the lower peak broadening observed in the cruciform.

In the 1:1 monotonic load, every grain family observed in this study has grains which are well-oriented for low-CRSS $Ba\langle a\rangle$ slip (Figure 4-7B). $Pri\langle a\rangle$ slip is likely limited under this stress state, as few grains have values of NRSS > 0.2 for the mechanism. Conversely, $Pyr_{2nd}\langle c+a\rangle$ is promoted for this loading mode (Figure 4-7B). Considering CRSS values reported by Ma [6], Wang [37,207] , Hama [5], and Agnew [152], the NRSS distribution implies that in many grains $Pyr_{2nd}\langle c+a\rangle$ slip may be activated before $Pri\langle a\rangle$ slip. NRSS analysis also predicts that there should be very few grains that can twin, which is confirmed in both the integrated intensity evolution and EBSD results. Thus, $Pyr_{2nd}\langle c+a\rangle$ slip becomes particularly important as a way of accommodating through-thickness reduction.

VPSC modeling of 1:1 loading by Steglich et al. [36] support this idea, suggesting that 1) $Pyr_{2nd}\langle c+a\rangle$ slip is the dominant non-basal slip mechanism and 2) both twinning and $Pri\langle a\rangle$ slip are suppressed. However, their model suggests $\mathrm{CRSS}_{Pyr_{2nd}\langle c+a\rangle} < \mathrm{CRSS}_{Pri\langle a\rangle}$, which is different than most literature (Table 4-1). Our analysis suggests that $Pri\langle a\rangle$ slip is still likely, just reduced compared to uniaxial loading. On the other hand, TEM observations by Chino et al. [201] show hardly any dislocations with a *c*-axis component over a nominal biaxial strain of 20%. However, they also saw more twinning, particularly contraction twinning, which could accommodate through-thickness strain in lieu of $Pyr_{2nd}\langle c+a\rangle$ slip. The stronger basal texture of the AZ31 used by Chino can account for these differences, as it should simultaneously lower the NRSS for $Ba\langle a\rangle$ slip and increase the NRSS values for contraction twinning.

Despite the basal texture, twin nucleation and growth is observed in several grains (Figs. 8, 9). As also seen in [201], $\{10.2\}$-type ETW is the predominant twin mechanism, but double twinning is also present which can accommodate strain in the through-thickness direction. NRSS analysis of the twinned grains shows that the selected twin variants do not necessarily correspond to the highest NRSSs. One example is shown in Figure 4-9. The selected variants have the first and third highest NRSS values. Non-Schmid twin variant selection has been previously described in Mg alloys as a result of short-range internal stresses at localized strain inhomogeneities between the parent grain and neighboring grains [63,65,209,210].

A 7:10 monotonic load showed similar behavior to the 1:1 load and the NRSS distributions are very similar for the grain families examined in this study. This suggests that applying a tensile load that opposes in-plane can limit twinning and promote slip. This can be understood by considering that extension twinning is a volume-conserving process—to accommodate extension along the *c*-axis, the grains must contract perpendicular to the *c*-axis. Hama et. al. [5] have previously suggested that the Poisson contraction in the transverse direction is important for twinning in a dogbone with a strong basal texture. Further tests at various load ratios should be performed to strengthen this assumption.

Load Path Changes

During the preload of the LPCs, both twinning and dislocations are generated. The mechanical response of the reload depends strongly on the angle of the LPC.

The reload of the 0:1 LPC shows a significant undershoot in the force-strain curve. This is suspected to be related to three mechanisms: 1) backwards motion of existing dislocations due to the Bauschinger effect, 2) de-twinning, and 3) primary and secondary ETW in the reload. All three mechanisms accommodate strain without increasing the dislocation density, which explains why the peak broadening is the lowest in this load path.

The 0:1 LPC corresponds to a 170° strain path change, nearly a reverse loading. Dislocations formed during the preload glide easily in the reverse direction aided by back stresses built up during the preload, i.e. the Bauschinger effect. The load reversal also promotes de-twinning, which is active almost immediately after loading begins. This is evident from the intensity changes in the {11.2} - {10.0} twin system. De-twinning is active before the appearance of the (00.2) peak, which implies that de-twinning has a lower CRSS than ETW. Reverse loading experiments performed on ZK60A [211] and AZ31 [34,199,212] have suggested that de-twinning has a lower CRSS than twinning as 1) there is no need for nucleation and 2) localized back-stresses formed between the twin and the matrix can be supportive. This can explain why some of the {10.0} twins de-twin rather than secondary twin, despite many grains having high NRSS values for ETW (Figure 4-12). As the de-twinning mechanism is exhausted, basal slip initially dominates and non-basal slip increases as strain increases. This was also observed by Lou et. al. [199] and Wu et. al. [212].

In addition to de-twinning, there are many {10.0} and near-{10.0} grains well-oriented for primary and secondary ETW into the (00.2) orientation. In all twinned grains, one- or two-variant ETW is observed, and the twin variants with the highest NRSS are activated. In grains with two variants, both produce strain along the same direction. It is clear from the IPF map (Figure 4-13A) that twin growth is preferred to nucleation, as many of the twins have nearly consumed the {10.0} parent grains. This is typical of metals with high plastic anisotropy [213]. Twin transmission is seen across a few grains, but growth and intersection of existing twins was responsible for the majority of the twinning activity. Twin thickening is associated with low work hardening [214,215].

The growth of these twins causes a significant texture change, which is evident from the pole figure (Figure 4-13C). The (00.2) orientation is poorly oriented for both basal and prismatic $\langle a \rangle$ slip, so these grains become plastically hard. However, even after high NRSS ETW in the {10.0} grains is exhausted, twin nucleation and growth is observed in other grain families and the textural hardening seems to have little effect on the bulk mechanical response over the observed strain.

Both the 7:10 and 1:1 LPCs show a significant overshoot in the force-strain curve upon reloading. No significant twinning is observed except in a few grains, which show multivariant secondary twinning. The lack of low-CRSS twinning and hardening due to dislocations from the preload result in a rapid increase in dislocation density and thus the rapid peak broadening compared to the corresponding monotonic loads.

The results of the 1:1 LPC show that the basal texture is broken during the preload, but returns to a strengthened basal texture during the reload. The deformation primarily occurs by $Ba\langle a \rangle$ slip and twinning is limited to a few grains, which suggests that $Pyr_{2nd}\langle c + a \rangle$ slip is active early in the deformation. Unlike the initial texture, the prestrained texture has a significant number of grains with high NRSS for $Pri\langle a \rangle$ slip, which is expected to be more active than in the 1:1 monotonic load. These findings generally match the results of 90° strain path changes performed by two-step loading of cut dogbones [5,45]. Both groups found that the experimental yield stress systematically decreases with increasing strain path change angle, attributed to back-stresses and texture softening for $Ba\langle a \rangle$ slip [45], twinning in the reload and de-twinning [5]. Our experiments show, however, a significant strengthening in the reload, and twinning is limited. Although the strain path in the 1:1 LPC corresponds to a 90° load strain path change, the different reloading paths result in different deformation behaviors. In our tests the 1:1 proportional load has a forward force component that competes with the back-stresses from the dislocation structure. Thus, dislocations are not free to run backwards and instead act as barriers to forward dislocation motion. The differences in the tests show what advantages cruciforms have over dogbones for approximating real cold-forming processes for sheet metals.

Although most grains are poorly oriented for twinning, some $\{10.1\} - \{10.2\}$ double twinning and extension twinning is observed. The double twinning is limited to a few grains and is not expected to contribute significantly to the bulk strain. Complex twinning is seen in several grains, such as the one in Figure 4-14. In general, the twin variants are selected according to the highest NRSS values. However, some twins, such as the "k" twin in Figure 4-14A, nucleate despite having a low NRSS. It is suspected that the nucleation of the "k" twin was aided by high local stresses at the triple junction between the "h", "j", and "i" twins which can overcome the low NRSS [65]. Twin growth is restricted by the high misorientation angles of ~56° at the twin boundaries, which limits the contribution of twinning to the deformation [210,214,216]. Additionally, the twin boundaries act as strong barriers to dislocation due to the high misorientation angles. Dislocations piled up at twin boundaries can act as a hardening mechanism to further slip and twin growth [50,192,217], making these grains plastically hard. However, there are very few of these grains, so it is expected that the majority of the strengthening is due to dislocation-based hardening in the grains from the preload.

4.5   Conclusion

For the first time, in-plane tension-tension strain path changes on cold-rolled Mg AZ31B sheet have been investigated *in situ* using neutron diffraction. Post-mortem EBSD was performed to quantify the twinned volume fraction and twin variant selection of the deformation. The findings are summarized below:

1. Acoustic emission during *in situ* deformation of a dogbone sample shows that very little twinning occurs before microplastic yield (at ~75 MPa for this alloy), as was proposed in [33].
2. Dogbone and 1:0 monotonic load: Strain is initially accommodated by $Ba\langle a \rangle$ slip and {10.2}-type ETW. At higher strains, $Pri\langle a \rangle$ and $Pyr_{2nd}\langle c + a \rangle$ are also active.
3. 7:10 and 1:1 monotonic load: Strain is initially accommodated by $Ba\langle a \rangle$ slip. Twinning is limited to a few grains, implying that $Pyr_{2nd}\langle c + a \rangle$ slip is more active than in the uniaxial loads to

accommodate c-axis strain. NRSS analysis also suggests that $Pri\langle a \rangle$ slip is limited. When twins are observed, twinning is primarily one- or two-variant {10.2}-type ETW and some {10.1} − {10.2} double twinning is observed.

4. The dislocation and twin network built up during the 1:0 preload affects the 0:1, 7:10, and 1:1 LPC in different ways:

    a. 0:1 LPC (170° strain path change): Back-stresses from the prestrain, de-twinning, and low-CRSS extension twinning and growth result in an undershoot of the force-strain curve. Deformation is dominated by $Ba\langle a \rangle$ slip and high-Schmid variant extension twinning and growth.

    b. 7:10 and 1:1 LPC (90° and 135° strain path change): The dislocation network and high-angle twin boundaries from the preload plastically harden the grains, resulting in an overshoot of the force-strain curve. As in the monotonic loads, $Pyr_{2nd}\langle c + a \rangle$ slip is active to accommodate c-axis strain in non-twinned grains. NRSS analysis suggests that $Pri\langle a \rangle$ slip is also active in well-oriented grains. Twin nucleation is only observed in a few grains and growth is suppressed by the high angle twin boundaries between different variants.

5. The similar behavior of the 7:10 and 1:1 monotonic load suggest any tensile load that at least prevents contraction in-plane can suppress twinning and promote slip for a strong basal texture. Further multiaxial load experiments should be performed to confirm this behavior.

4.6   Acknowledgements

4.7   Appendix 4A: Sample Geometry and Experimental Setup
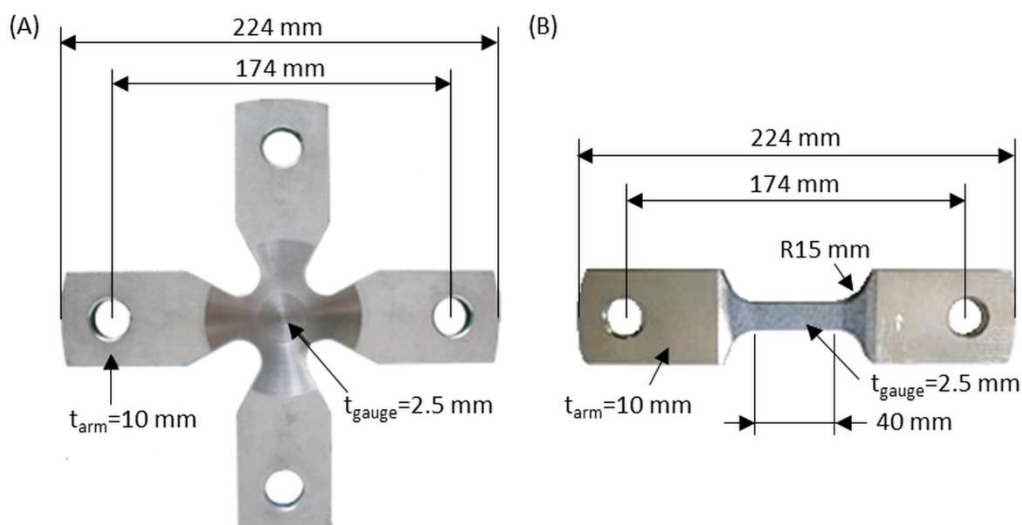
Figure 4-16 Dimensions of (A) cruciform-shaped sample and (B) dogbone sample.
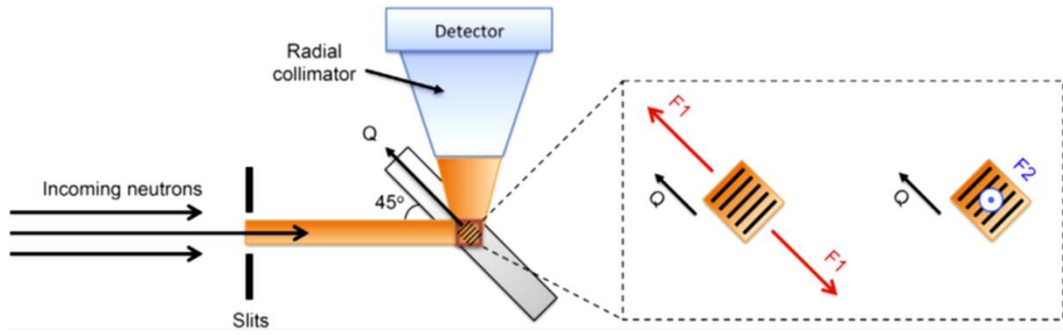
Figure 4-17 Orientation of the sample within the beamline showing the direction of the diffraction vector **Q** with respect to the loading. Image taken from [11].

Figure 4-16 shows the dimensions of the cruciform and dogbone samples. The samples are loaded into a multiaxial mechanical test rig at the POLDI beamline, a time-of-flight diffractometer for measuring thermal neutron scattering at the Swiss Light Source. The setup is displayed schematically in Figure 4-17. The size of the incoming neutron beam was cut to 3.8×3.8 mm^2 using horizontal and parallel slits. The outgoing beam is collimated using a radial collimator with an aperture of 3.8 mm.

Diffraction peaks were fitted using the single-peak fitting Mantid data analysis software [204]. The peaks are described by a Gaussian shape with a mean position, width, and intensity. The elastic lattice strain ε_{hkl} at a point can be calculated by taking the relative change in interplanar spacing d_{hkl} between the point and the initial value prior to deformation d_{hkl}^0:

$$\varepsilon_{hkl} = \frac{d_{hkl} - d_{hkl}^0}{d_{hkl}^0} \tag{4-3}$$

The peak broadening can be similarly described as the relative change in peak width:

$$w_{hkl} = \frac{\Delta q_{hkl}}{q_{hkl}} \tag{4-4}$$

where Δq_{hkl} is the full-width at half-maximum (FWHM) of the hkl diffraction peak. The integrated intensity I_{hkl} of the peak is calculated as the area under the diffraction peak:

$$I_{hkl} = \int I(q) dq \tag{4-5}$$

where $I(q)$ is the count intensity of a given scattering vector. All integrated intensities shown in this work are normalized with respect to the initial integrated intensities of the diffraction peaks prior to deformation:

$$I_{hkl}^n = \frac{I_{hkl}}{I_{hkl}^0} \tag{4-6}$$

4.8   Appendix 4B: Calculation of Normalized Resolved Shear Stress

4.8.1   Abaqus Finite Element Analysis

Following the procedure outlined in [111], finite element analysis (FEA) was performed in Abaqus Standard 6.14 to approximate the stress tensor for the 1:0, 7:10, and 1:1 monotonic loads. The elastic response of the AZ31 was modelled as isotropic with $E = 42.9$ MPa and $\nu = -0.31$. The plastic response was defined using the true stress vs. true strain curve for the rolling direction (Figure 4-5A, Section 4.3.2) as

the reference plastic flow data with a rate-independent, isotropic hardening law. A yield stress of 108.07 MPa was used instead of the 0.2% yield stress of 132 MPa to account for microplasticity.
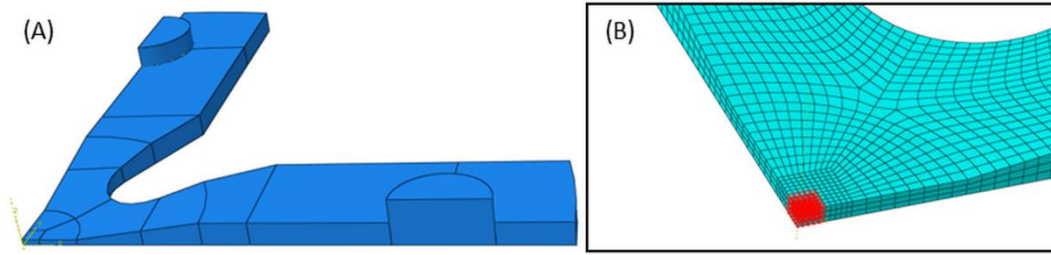
Figure 4-18 (A) Abaqus assembly of 1/8th cruciform geometry with pins. (B) Mesh in the test section. The 75 elements used to determine the stress tensor are highlighted in red.

To improve computational efficiency, only 1/8th of the cruciform geometry was modeled. Symmetric boundary conditions were applied on the XZ-, YZ-, and XY-planes (Figure 4-18). To mimic the experimental loading, two rigid pins were modeled and used to apply forces inside the holes in the cruciform arms. The pins were modeled using discrete rigid body shell elements, with one semi-circular face constrained to lay flat in the XY plane. A concentrated force is applied to a reference point, defined at the center of the semi-circle face in the XY-plane, to mimic the force-control of the experiments. The pins are constrained to move only in X or Y (cross arm pin) respectively, and they are not allowed to rotate. Contact interaction between the pins and cruciform is approximated as frictionless.

A structured hexahedron mesh with linear 8-node elements (C3D8 elements) is used to approximate the geometry. A 3.8×3.8 mm^2 area at the center of the test section was partitioned using $5 \times 5 \times 3$ elements, for a total of 75 elements (Figure 4-18B). This area was chosen because it is the cross-section of the x-ray beam used during *in situ* multiaxial measurements. The stress tensors from the simulations are the result of averaging over the integration points of the elements. Due to the complex cruciform geometry, the stress state in the test section varies with time. The values used in this study were taken when the equivalent plastic strain reached 0.2%.
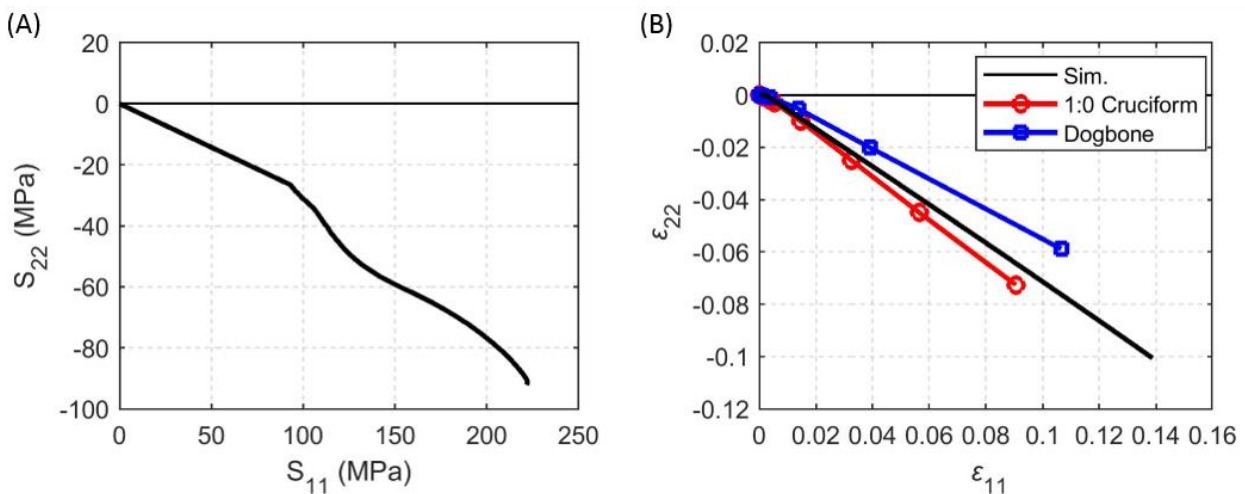
Figure 4-19 FEA prediction of the ring effect during a uniaxial load on the horizontal axis. (A) S_{11} and S_{22} components of the Cauchy stress tensor and (B) ε_{11} and ε_{22} components of the resulting strain tensor, plotted against the values measured by DIC of the 1:0 monotonic load and dogbone for comparison.

Figure 4-19 shows the development of the ring effect in the test section predicted by FEA. Due to the cruciform-shaped geometry, a compressive stress develops along the transverse axis. In the elastic regime, the stresses develop linearly with a ratio $S_{22}/S_{11} = -0.285$. At the elastic-plastic transition, a kink is observed, resulting in a non-linear development of S_{22}/S_{11} in the plastic regime. By the end of the simulation, $S_{22}/S_{11} = -0.406$. The resulting strain ratio predicted by FEA is $\varepsilon_{22}/\varepsilon_{11} = -0.725$, close to the measured value of -0.80. It is suspected that the difference in predicted and measured strains is the result of the isotropic hardening law used for the FEA, whereas in reality the sheet texture would result in anisotropic plastic behavior. The non-linear stress evolution in the plastic regime is the result of plastic yield in the cruciform outside of the test section.

Chapter 5   *In Situ* Characterization of a High Work Hardening Ti-6Al-4V Prepared by Electron Beam Melting

The work presented in this chapter is a written article by the same name. It has been reformatted to integrate with this thesis. The article has been submitted to Acta Materialia and is currently under review. The version in this thesis is as-submitted to the reviewers. A full bibliographic reference is given below:

K. Sofinowski, M. Šmíd, I. Kuběna, S. Vivés, N. Casati, S. Godet, H. Van Swygenhoven, *In situ* characterization of a high work hardening Ti-6Al-4V prepared by electron beam melting. Acta Materialia: *Under Review*

This is a first author paper written in entirety by the PhD candidate (K. Sofinowski). The material was prepared by Dr. S. Vivés in the 4Mat group of Dr. S. Godet. *In situ* XRD experiments were performed by K. Sofinowski in conjunction with Dr. S. Van Petegem. *In situ* HRDIC was performed by K. Sofinowski in conjunction with Dr. M. Šmíd. All data analysis and figures for the *in situ* tests were prepared by K. Sofinowski. Transmission electron microscopy and transmission kikuchi diffraction was performed by Dr. I. Kuběna.

5.1   Introduction

Titanium alloys, Ti-6Al-4V in particular, have found widespread use in the aerospace and biomedical fields due to their excellent strength-to-weight ratio, corrosion resistance, and biocompatibility [218–224]. However, the relatively low work hardening and ductility of the alloys in comparison to other metals like steels still restricts their usage [82,225]. The desire for Ti alloys with increasingly optimized combinations of strength and ductility has led to the development of alloys with increasingly complex multi-phase microstructures [220,226]. By tailoring the phase volume fractions and morphologies, different balances of strength, ductility, and work-hardening can be achieved.

Generally, a combination of thermo-mechanical processes is used to optimize the microstructure. For example, various thermal forming and annealing techniques have been applied to dual-phase $\alpha + \beta$ Ti-6Al-4V to create bi-modal grain distributions that balance strength and ductility [227–231]. Post post-processing routes for additive manufactured (AM) parts, however, cannot use mechanical processes to control grain size or morphology because the printed parts are already near their final shape. Thus, thermal-only post-processing routes are being explored to tailor new microstructures in AM parts [232,233].

Recently, de Formanoir et. al. applied a novel heat treatment to generate a dual-phase $\alpha + \alpha'$ microstructure in a Ti-6Al-4V prepared by electron beam melting (EBM) [81]. The alloy showed both higher ultimate tensile strength (UTS) and ductility as-compared to standard wrought or hot-isostatic pressed (HIP'ed) samples. The improved mechanical properties were attributed to a composite work-hardening behavior between the α and α' phases. The α' phase is generally considered to be an unwanted brittle phase and is usually decomposed to $\alpha + \beta$ [73–77]. However, recent studies were able to achieve high ductilities in a fully α'-martensitic [80] and $\alpha + \alpha'$ dual-phase [78,79] Ti-6Al-4V, challenging the conventional idea that the martensite is inherently brittle.

In this study, the source of the work hardening behavior of a Ti-6Al-4V alloy prepared by EBM and post heat treatments similar to those performed by de Formanoir et al. [81] is determined during uniaxial tensile loading. It is shown that the high work hardening is due to the composite behavior of three mechanically distinct phases: α lamellae and martensitic regions containing acicular laths of α' and a third phase which has not been identified in literature. The load sharing between the three phases is investigated *in situ* with x-ray diffraction (XRD) and high resolution digital image correlation (HRDIC) and the implications on hardening mechanisms within the phases are discussed.

5.2   Experimental Procedure

5.2.1   Material

	Al	V	C	Fe	O	N	H	Ti
Arcam Ti-6Al-4V	6	4	0.03	0.10	0.15	0.01	0.003	Balance

Table 5-1 Chemical composition (wt. %) of the Arcam Ti-6Al-4V powder used in the EBM process (from [81]).

Blocks of Ti-6Al-4V were prepared by EBM using an Arcam AB® A2 machine with the standard ARCAM melting parameters. The chemical composition of the powder used is shown in Table 5-1. To reduce the number of macroscopic defects inherent to the EBM process, the blocks were subjected to hot isostatic pressing (HIP) for 2h at a pressure of 1000 bar and temperature 920°C followed by slow cooling in a furnace. After HIP, 300 µm thick sheets were cut from the block. The sheets were encapsulated in quartz tubes under an argon atmosphere, to avoid oxidation, and annealed for 2h at four different sub-transus temperatures (850, 900, 950 and 980°C) to produce different proportions of α/β. Immediately after annealing, the sheets were water quenched (WQ) to transform the β phase into martensite. For more details on the EBM process and subsequent post-treatments we refer to [81].

For *in situ* XRD, flat dogbone specimens were cut from the sheets by wire electro-discharge erosion and then polished by mechanical grinding to remove surface defects. After polishing, the gauge section dimensions were 1.25 mm wide and between 270-290 µm thick. It should be noted that shallow notches developed at the edges of the gauge section of the XRD samples during polishing. Strain concentrations developed at these notches and resulted in the premature failure of the 850C, 900C, and 950C heat-treated samples.

In situ HRDIC dogbones were cut using picosecond-pulsed laser ablation at the Swiss Federal Laboratories for Materials Science and Technology (EMPA). The samples were then mechanically ground using SiC sandpaper with decreasing roughness (320, 600, 800, and 1200 grit) then polished with 3 µm and 1 µm diamond paste. The final gauge sections were 300 µm wide and between 67-80 µm thick. Final polishing was performed using an OPS suspension for 45 minutes to achieve a mirror-like surface.

5.2.2   *In situ* X-ray Diffraction

XRD spectra were recorded *in situ* during continuous tensile loading (initial strain rate 0.0001 s^{-1}) using a miniaturized tensile machine mounted at the Materials Science beam line at the Swiss Light Source [159]. Samples were measured in transmission using a 20 keV beam of 200 × 500 µm^2. Diffraction patterns were acquired every 20 s with a Mythen II microstrip detector with the diffraction vector **Q** perpendicular to the loading direction. During each diffraction pattern, the machine was rotated +/- 6° about the loading axis to increase grain statistics. A PixelLink camera (P-DL729MU) with inline 2× telecentric lens (Edmund Optics,

model #67313) mounted above the sample was used to capture images for DIC analysis. The strain values reported in this study are averaged over the irradiated section of $200 \times 500 \ \mu m^2$.

Diffraction peaks are fit using a split Pearson VII function and the peak position, peak width (full-width at half-maximum – FWHM), and peak intensity are extracted. The evolution of the elastic lattice strains is calculated from the change in peak position of a given $\{hk.l\}$ reflection ($\varepsilon_{hk.l} = \left(d_{hk.l} - d_{hk.l}^0\right)/d_{hk.l}^0$) and can be used to examine load sharing between different grain families [33]. A positive change in slope of $\varepsilon_{hk.l}$ vs. applied stress implies that grain family $\{hk.l\}$ is taking more load, whereas a negative change in slope implies that it is taking less load ("shedding load"). Changes in the FWHM correlate to changes in the dislocation density within grains or intergranular stress inhomogeneity within a grain family.

5.2.3 *In situ* High Resolution Digital Image Correlation

Dogbones were prepared with one of two types of speckle patterns to perform HRDIC at different magnifications: colloidal silica – OPS (low magnification) or gold speckles (high magnification). The OPS pattern was prepared by dispersing dilute OPS polishing suspension on the surface of the dogbone using the methods in [13]. The gold speckle pattern was prepared by remodelling a thin layer of gold deposited on the surface of the dogbone as in [14,15]. After patterning, EBSD micrographs were collected using a Zeiss ULTRA 55 FEG scanning electron microscope (SEM). Maps were taken with step sizes between 80-120 nm (20kV, high current mode, 120 μm aperture). Raw data was post-processed using OIM Analysis 7.3 software.

Interrupted tensile load tests were performed using one axis of a miniaturized biaxial machine (described in [176]) mounted inside of a FEG Zeiss ULTRA 55 SEM. Dogbones were loaded in tension at a constant total strain rate $\dot{\varepsilon}_{tot} = 0.00014 \ s^{-1}$ to five predetermined force levels. At each level, the dogbone was held under load for ~45 minutes at a constant displacement to take a series of four SEM images. The images were stitched together to form a 2 × 2 grid with dimensions of 108 μm × 81 μm (OPS sample) or 16 μm × 12 μm (gold-patterned sample). High contrast images were obtained using conditions described by Yan et al. [13]: an in-lens detector was used at a working distance of 7 mm with acceleration voltage of 3kV and an aperture size of 30 μm. Strain maps were calculated from the images using the open source 2D DIC Matlab software Ncorr [234] with a subset radius of 15 pixels, a subset spacing of 3 pixels, and a strain radius of 3.

A dogbone was strained *ex situ* to correlate macrostrain values with the piezo motor steps because the displacement of the arms could not be directly measured *in situ* due to the size constraints of the SEM chamber. Unlike the *in situ* tests, the *ex situ* test was continuous. Thus, it is expected that the actual macrostrain values of the *in situ* tests are slightly higher than shown due to creep during the HRDIC imaging.

5.2.4 Electron Microscopy Techniques

Pre- and post-mortem SEM and TEM was performed to characterize the microstructure of the material. TEM lamellae were prepared by focused ion beam (FIB) milling using a Zeiss NVision-40 FEG-SEM. TEM and selective area electron diffraction (SAED) were performed using a JEOL JEM-2100F TEM (Institute of Physics of Materials, Brno) and a JEOL JEM 2010 TEM (Paul Scherrer Institue). Transmission Kikuchi diffraction (TKD) was performed using a Tescan LYRA 3 XMU FEG-SEM (IPM, Brno) and the patterns were indexed using Oxford Instruments Aztec software.

5.3   Results

5.3.1   Material Characterization

Microstructure
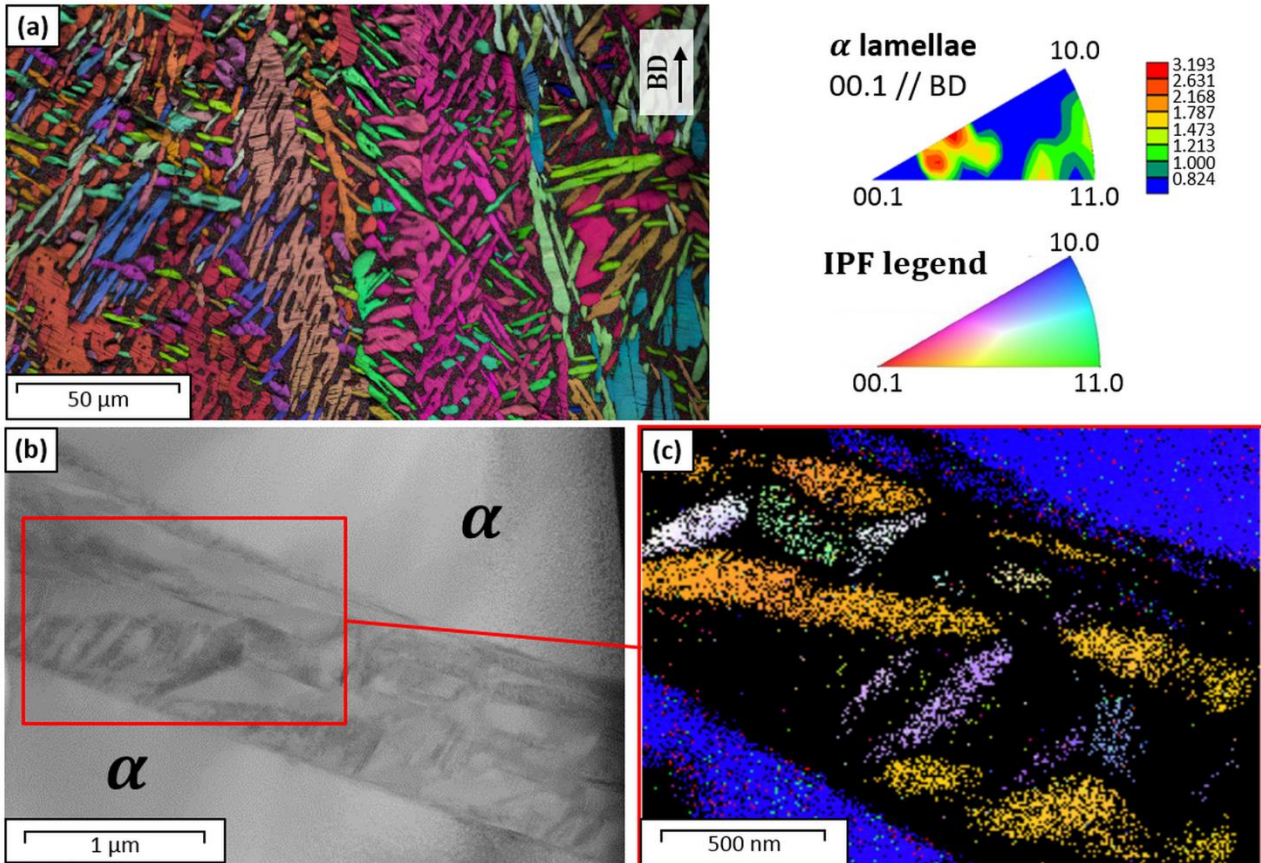
Figure 5-1 Microstructure of the 900C sample: (a) IPF and IPF map (w.r.t the build direction) of the α lamellae surrounded by dark grey martensite; (b) TEM dark-field contrast micrograph of the martensite region between α lamellae; (c) IPF map from transmission kikuchi diffraction of the martensite region.

The microstructure of all heat treated samples consists of large α lamellae surrounded by regions of martensite. The volume fraction of these martensite regions was measured by analysis of BSE micrographs as in [81] to be: 850°C − 25 ± 4%, 900°C − 34 ± 4%, 950°C − 48 ± 4%, and 980°C − 58 ± 4%. The values observed here are systematically lower than those reported by de Formanoir et al. [81]. This can be attributed to faster cooling rates during the transfer to the water quench because the samples were thinner.

The α lamellae are approximately 2-4 µm wide and 10-20 µm long and form a "basket-weave" microstructure typically seen in α/β alloys [235,236]. Individual lamellae are either single grain or several grains with low misorientation angle grain boundaries. An inverse pole figure (IPF) map for the 900C sample is shown in Figure 5-1a. The IPF is generated from an area three times larger than the map. In some areas large colonies of grains with the same orientation have formed due to a preferred orientation relationship with the parent β grain [231,235].

TEM micrograph and IPF map obtained by TKD (Figure 5-1b-c) show that the martensite regions contain fine acicular α' approximately one order of magnitude smaller than the α lamellae. The α' laths exhibit a heavily twinned/faulted microstructure typical of Ti-6Al-4V martensite [73]. The laths appear to have no preferred crystallographic orientation (Figure 5-1c), but are known to have a specific Burgers relationship to the parent β grains with 12 possible variants [237]. The seemingly "random" texture is likely due to the absence of preferred variant selection during the martensitic transformation. A large distribution of α' lath sizes is observed in all samples, but larger laths are observed in samples annealed at higher temperatures.
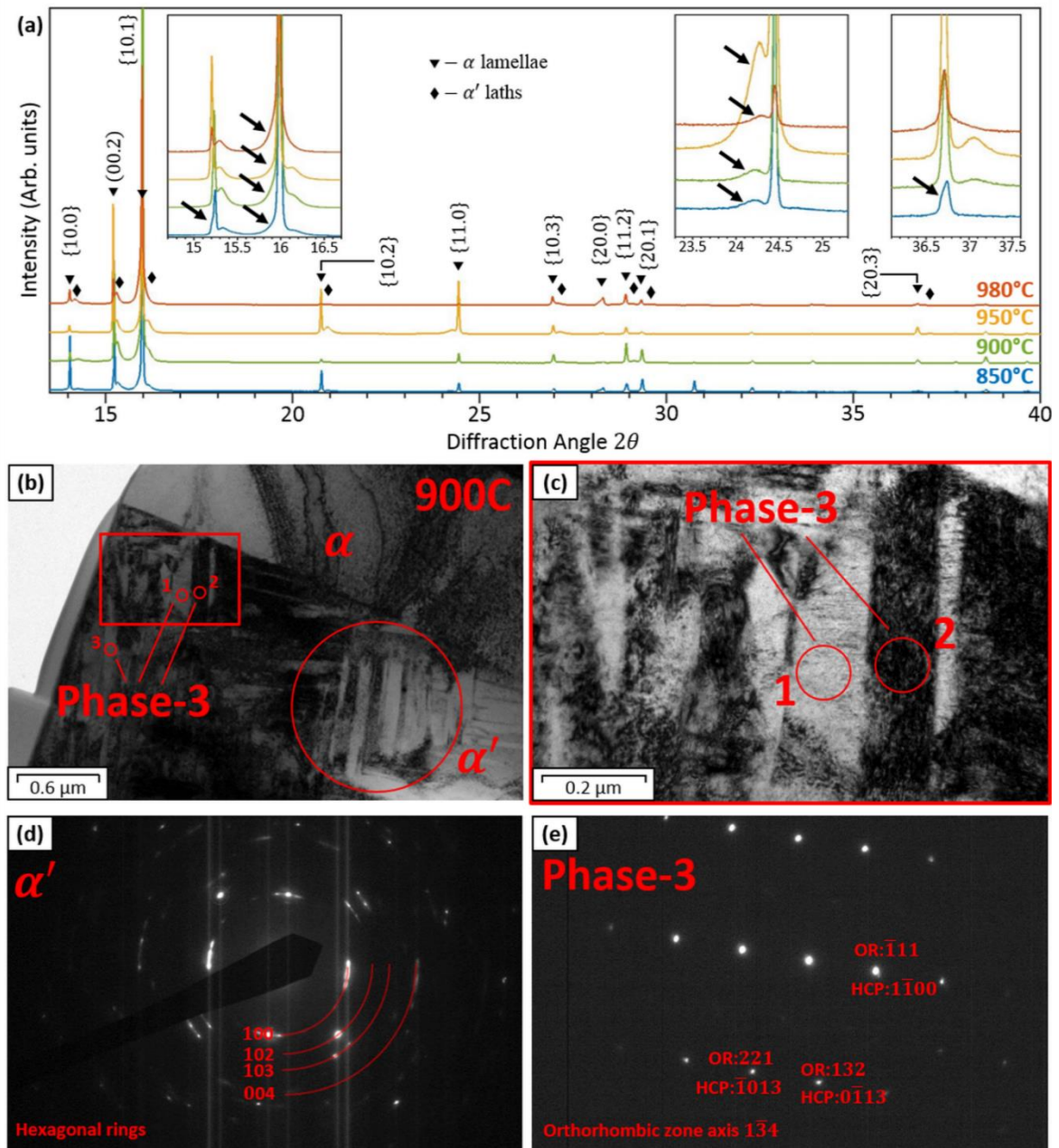
Figure 5-2 (a) XRD profiles of the un-strained heat treated samples. Insets highlight scattering angles where Phase-3 peaks were observed; (b) TEM bright-field micrograph of martensite region showing the location of α, α', and Phase-3 identified by SAED; (c) Magnified view of suspected Phase-3 laths; (d) SADP of α' showing hexagonal rings; (e) SAED pattern of Phase-3 lath 1 from Figure 5-2c, which can be indexed by either OR or HCP lattice parameters calculated from XRD.

Sample	α lamellae		α' laths	
	a (Å)	c (Å)	a (Å)	c (Å)
850C-2h-WQ	2.928 ± 7e-6	4.675 ± 5e-3	2.881 ± 7e-4	4.647 ± 4e-2
900C-2h-WQ	2.928 ± 6e-6	4.678 ± 8e-6	2.883 ± 3e-4	4.654 ± 1e-4
950C-2h-WQ	2.929 ± 3e-6	4.686 ± 1e-5	2.894 ± 3e-3	4.659 ± 3e-4
980C-2h-WQ	2.927 ± 5e-5	4.686 ± 8e-5	2.899 ± 4e-4	4.659 ± 4e-4

Table 5-2 Lattice parameters of the α and α' phases measured by synchrotron XRD.

The lattice parameters of the α and α' HCP phases shown in Table 5-2 were calculated from the XRD patterns (Figure 5-2a). During the anneal, Al and V partition to the α and β phase, respectively. The solute atoms are then trapped during the water quench, resulting in Al-enriched α lamellae and V-enriched martensite regions. The lattice parameters of the α' phase are systematically smaller than the α phase due to the larger mismatch between the size of the Al solute atoms and Ti. The effect of partitioning is visible in the increasing a and c lattice parameters of the α' and the c parameter of the α phase as the annealing temperature increases. The variation in initial peak intensities between the different heat treatments is suspected to be due to the limited number of diffracting grains as the crystallographic textures should be similar for all samples.

A third phase in the martensite region

Additional XRD reflections, marked by arrows in Figure 5-2a, were observed in all un-strained samples indicating the presence of a third phase not previously identified in this material (henceforth, "Phase-3"). Two distinct peaks were observed for all heat treatments near $2\theta_{hk.l} = 24.22°$ and $2\theta_{hk.l} = 15.97°$. Additional peaks were observed as "shoulders" on α peaks in the 850C sample (shown in insets in Figure 5-2a). The Phase-3 peaks can be indexed with either orthorhombic (OR) or HCP lattice parameters. Indexing as HCP yields lattice parameters that decrease with increasing annealing temperature between a = 2.956 ± 1e-4 Å and c = 4.684 ± 3e-4 Å (850C sample) and a = 2.945 ± 4e-4 Å and c = 4.64 ± 3e-2 Å (980C sample). The error on the c parameter of the 980C sample is large compared to the 850C sample because there is significant uncertainty in the peak position due to the overlap between the peaks. Indexing Phase-3 as OR yields lattice parameters of a = 2.956 ± 9e-4 Å, b = 5.05 ± 7e-4 Å, and c = 4.61 ± 3e-2 Å for the 850C sample. The OR parameters could not be calculated for the other heat-treated samples because the additional peaks are not distinctly visible in the un-strained XRD patterns.

To further characterize Phase-3, selected area electron diffraction (SAED) was performed on laths within the martensite region, i.e. regions which are not primary α lamellae (Figure 5-2b,c). Circles show the size of the SAED apertures used to produce the diffraction pattern in Figure 5-2d and e. The SAED pattern in Figure 5-2d can be clearly indexed using the α' lattice parameters calculated from XRD, shown in Table 5-2. However, using smaller apertures, several laths were identified which could not be well-indexed by the α or α' lattice parameters. These laths are suspected to belong to Phase-3. The SAED pattern in Figure 5-2e comes from the circled area marked "1" in Figure 5-2c. Using the lattice parameters calculated from XRD, the spots can be indexed as either OR or HCP with a 3% and 30% indexing error, respectively.

In other words, XRD and SAED show the presence of a third phase, but cannot definitively determine its crystallographic structure. Considering Phase-3 to be HCP implies that two chemically distinct α' martensites are formed during quenching, which has never been reported in literature, or that a secondary α forms in the martensite regions. Since Phase-3 diffracts at lower angles than the primary α and α' peaks,

there must be differences in chemical composition and/or residual stresses. A secondary α phase, so-called α_m, has been observed in Ti-6Al-4V martensite as the result of a massive transformation at near-quench cooling rates [238]. However, the observed α_m had nearly identical chemistry and lattice structure to the α' martensite, so it is difficult to explain the large difference in XRD peak positions. Secondary α has also been previously observed as planar interface complexions in martensite [83], but such phenomena are known to be related to diffusion-controlled processes [239–241] and should not have occurred during a quench.

The small indexing error of the SAED spots, on the other hand, suggests that Phase-3 is OR α'' martensite. The lattice parameters are indeed similar to the α'' phase observed in Ti-6Al-6V-2Sn (a=2.95 Å, b=5.00 Å, and c=4.63 Å). The phase forms as a distorted HCP structure at high β-stabilizer solute content, which explains its location in the martensite. This martensite has been reported in Ti-6Al-4V when quenching from starting temperatures of 800°C-900°C [84], a temperature range through which all of the heat treatments in this study pass during the water quench. However, it has never been reported in combination with α' martensite.

In summary, more advanced methods are required to characterize the crystallography of Phase-3. It is suggested that atom probe tomography could potentially identify short-range chemical differences in the martensite regions that could not be identified by standard energy dispersive methods. Our study, however, focuses on explaining the enhanced work hardening observed in this Ti-6Al-4V due to the load sharing between the α, α', and Phase-3.

Mechanical behavior
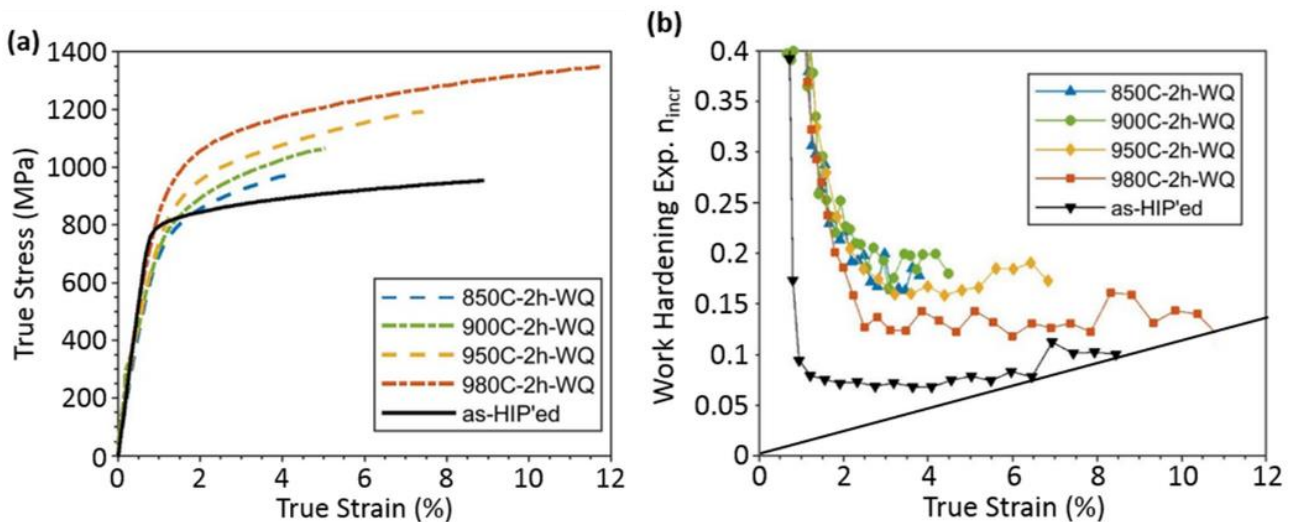
Figure 5-3 (a) True stress, true strain curves until necking or fracture and (b) work hardening exponent n_incr as a function of the strain for the samples tested with *in situ* XRD. The cutoff line in (b) is Considere's criterion for necking.

The true stress-strain curves until necking or fracture and the evolution of the work hardening exponent $n_\mathrm{incr} = \mathrm{d}\ln\sigma/\mathrm{d}\ln\varepsilon$ are shown in Figure 5-3. As in the study of de Formanoir et al. [81], the annealed samples show significant increases in work hardening and ultimate tensile strength as compared to the as-HIP'ed sample. The trends are also the same: as annealing temperature (and thus martensite region volume fraction) increases, 0.2% yield strength ($R_\mathrm{p0.2}$) and ultimate tensile strength also increase. Unfortunately, stress concentrations outside of the gauge section caused the premature fracture of the 850C,

900C, and 950C samples at 4%, 5%, and 7%, respectively. Nevertheless, we believe that it is unlikely that new work hardening mechanisms will appear beyond 4-5% strain so the behaviors observed here represent a complete picture of the work hardening in the material.

5.3.2   Deformation of the 900C Sample

Load Sharing Between Phases: In situ XRD
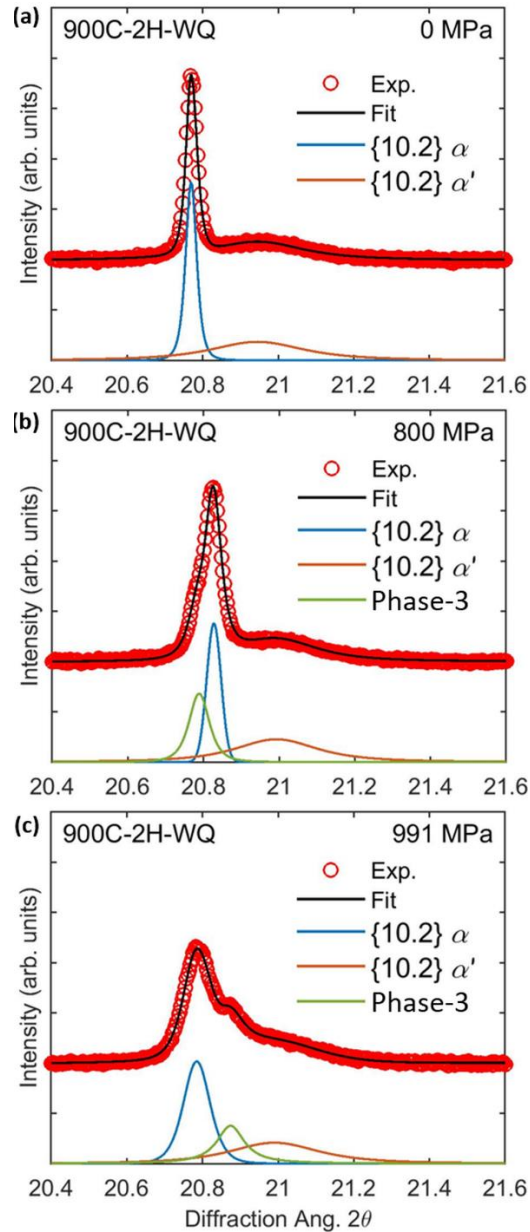
Figure 5-4 Peak evolution of the 900C sample near the $\{10.2\}$ HCP reflection (a) in the initial (unloaded) state, (b) just after macroplastic yield, and (c) at the end of loading.

As the samples were deformed *in situ*, additional reflections of Phase-3 were observed near the $\{10.2\}$ and $\{20.3\}$ HCP reflections, as shown in Figure 5-4. Initially, the Phase-3 peak is hidden by the $\{10.2\}$ α peak (Figure 5-4a). As the deformation proceeds the peaks shift relative to one another due to the mechanical differences between the phases (Figure 5-4b,c). The full video of the evolution of the $\{10.2\}$ and $\{11.0\}$ reflections is available as supplementary material online.
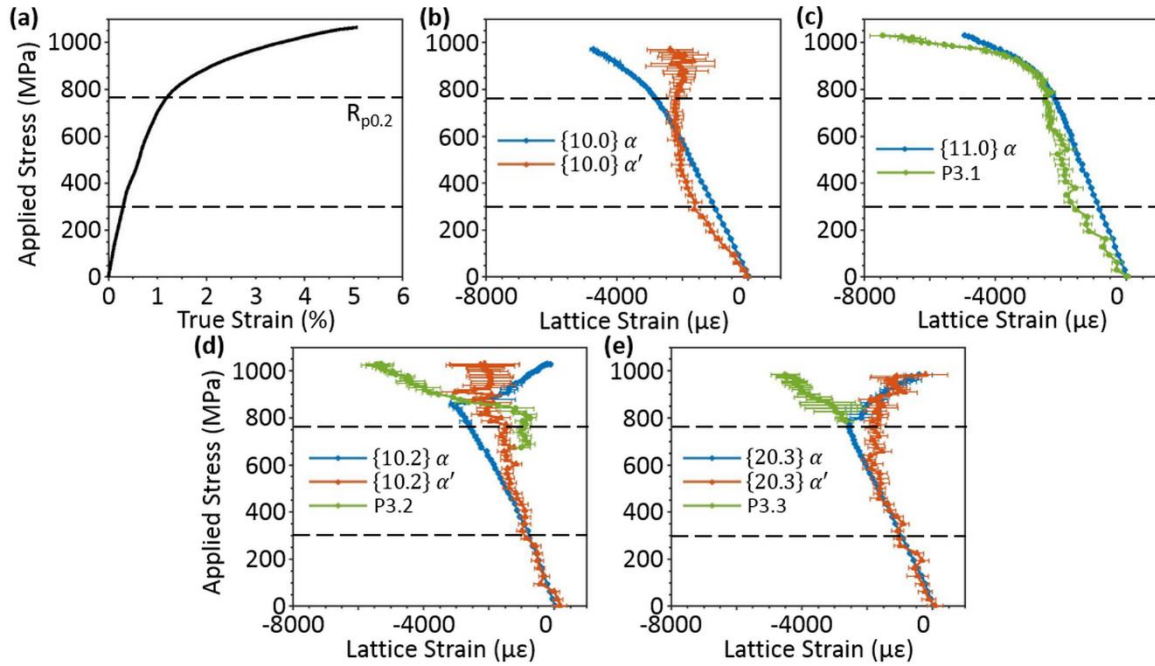
Figure 5-5 (a) Applied stress, true strain curve and (b-e) lattice strain evolution of several grain families for the 900C sample. The same stresses are marked on each graph for comparison.
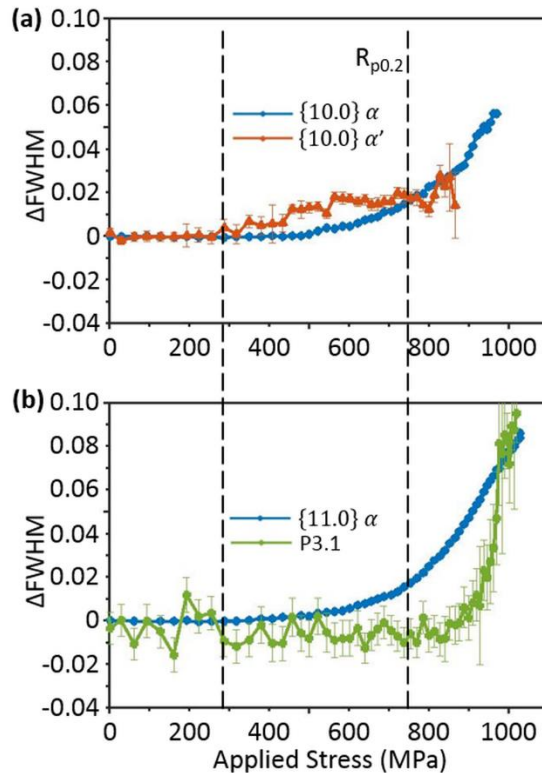
Figure 5-6 Peak broadening of the (a) $\{11.0\}$ and (b) $\{10.0\}$ grain families in the 900C sample. The same stresses as in Figure 5-5 are marked for comparison.

The evolution of the elastic lattice strains ($\varepsilon_{hk.l}$) as a function of applied stress are shown in Figure 5-5 for a few $\{hk.l\}$ grain families of the three phases. Grain families having a peak position in a similar 2ϑ range are plotted together. As it is uncertain whether Phase-3 is OR or HCP, the Phase-3 grain families will be named

as follows: P3.1, which could be either $\{11.0\}$ secondary α or $\{200\}$ α''; P3.2, which could be either $\{10.2\}$ secondary α or $\{112\}$ α''; and P3.3, which could be either $\{20.3\}$ secondary α or $\{300\}$ α''. The $\{10.1\}$, $\{20.0\}$, $\{11.2\}$, and $\{20.1\}$ HCP reflections show significant overlap between α, α', and Phase-3 peaks in the initial microstructure so it is difficult to uniquely fit the peaks. The peak broadening (ΔFWHM) of the $\{10.0\}$ α, $\{10.0\}$ α', $\{11.0\}$ α, and P3.1 grain families is shown in Figure 5-6. The error bars for $\{11.0\}$ α are too small to be shown ($\delta(\Delta FWHM) < \pm 0.001$). The elastic lattice strain and FWHM evolution in Figs. 5 and 6 are only shown as far as the diffraction peaks could be uniquely fit; i.e. depending on the reflection, they are not necessarily shown for the full loading.

The following can be deduced from the development of the elastic lattice strains and peak broadening of the three phases:

Elastic regime: Below applied stresses of ~300 MPa, $\varepsilon_{hk.l}$ changes linearly for all phases (Figure 5-5), suggesting that all phases behave elastically.

Microplastic regime: Between ~300 MPa and R$_{p0.2}$=760 MPa, α' and Phase-3 both seem to shed load, however with important differences: peak broadening is observed for the α' peaks (Figure 5-6a) but not for Phase-3 peak P3.1 (Figure 5-6b). This behavior can be explained by load sharing within the martensite region. As stress is applied, intergranular stresses are redistributed between the Phase-3 laths and some α' laths plastify. The lattice strain of some α reflections starts deviating before reaching R$_{p0.2}$, suggesting early plastification of some well-oriented grains. This is confirmed by the peak broadening e.g. in the $\{10.0\}$ and $\{11.0\}$ grain families in Figure 5-6b.

Plastic regime: Above R$_{p0.2}$=760 MPa, the α phase plastifies: some grain families shed load strongly, e.g. $\{10.2\}$ and $\{20.3\}$ (Figure 5-5d,e), while other grain families continue to take load, e.g. $\{11.0\}$ and $\{10.0\}$ (Figure 5-5b,c). Within the martensitic regions, the α' laths do not take more load. Instead, the load is rapidly taken by Phase-3 (Figure 5-5) accompanied by a rapid peak broadening (Figure 5-6).

The α grain families that shed load in the plastic regime depends on which families are plastically "soft," i.e. which have the most grains deforming by low critical resolved shear stress (*CRSS*) slip mechanisms. Crystal plasticity simulations of Ti-6Al-4V have estimated that $\langle a \rangle$ slip on prismatic planes ($Pri\langle a \rangle$) is the easiest, followed closely by basal $\langle a \rangle$ slip ($Ba\langle a \rangle$), first-order pyramidal $\langle a \rangle$ slip ($Pyr_{1st}\langle a \rangle$), and finally second-order pyramidal $\langle c + a \rangle$ slip ($Pyr_{2nd}\langle c + a \rangle$) [242,243]. Thus, families with many grains well-oriented for low-*CRSS* $Pri\langle a \rangle$ or $Ba\langle a \rangle$ will be plastically "softer" than other families.
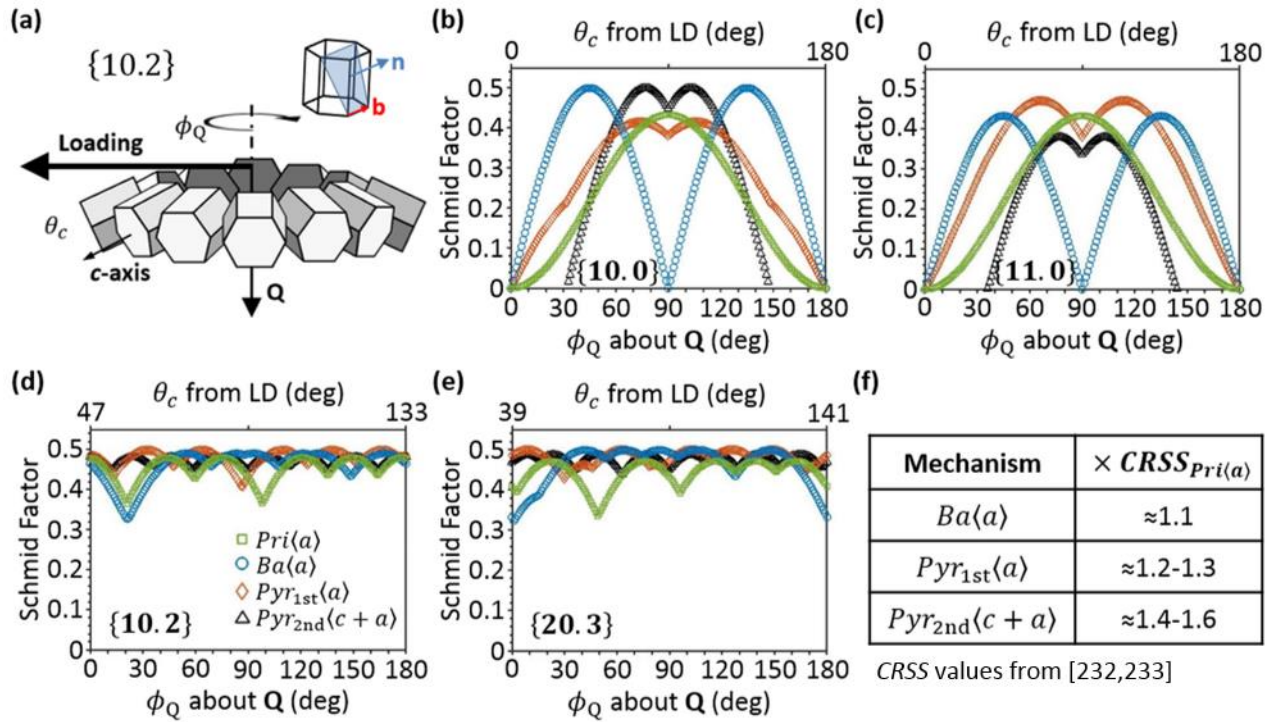
Figure 5-7 (a) Schematic of possible crystallite orientations that contribute to the $\{10.2\}$ grain family and their relationship to the loading direction and **Q**; (b-e) Maximum SF distributions for $Ba\langle a\rangle$, $Pri\langle a\rangle$, and $Pyr_{1st}\langle a\rangle$ slip for all possible grain orientations contributing to each grain family.

The Schmid Factor (SF) has been shown to be a relevant predictor of slip activity in a single Ti-6Al-4V crystallite once it has plastified [244]. However, each grain family consists of a wide range of crystallite orientations with respect to the loading direction. This is diagrammed for the $\{10.2\}$ grain family as an example in Figure 5-7a. Thus, the SF distribution for potentially active slip mechanisms is calculated for all possible orientations contributing to each grain family (Figure 5-7b-e). The *CRSS* of each slip mechanism relative to $CRSS_{Pri\langle a\rangle}$ from crystal plasticity simulations [242,243] is shown in Figure 5-7f. Only the highest SF from all possible slip systems is shown for each slip mechanism.

From Figure 5-7, the $\{10.0\}$ and $\{11.0\}$ grain families likely contain a mix of plastically "soft" and "hard" grains. Grains with $\theta_{c-\text{axis}} < 25$ deg. are plastically hard, with SFs below 0.35 for all $\langle a\rangle$-type slip mechanisms, and only grains with $\theta_{c-\text{axis}} > 45$ deg. (>60 deg. for $\{11.0\}$) deform by the slip mode with the lowest *CRSS*, $Pri\langle a\rangle$ slip. The change in the XRD peak shows that the ensemble behavior of these grains takes load. Conversely, all grain orientations possibly contributing to the $\{20.3\}$ and $\{10.2\}$ (Figure 5-6h,i) reflections are plastically soft (SF>0.35 for either $Pri\langle a\rangle$ or $Ba\langle a\rangle$ slip in every grain), explaining the significant load-shedding observed in the families.

The load transfer trends observed between α, α', and Phase-3 for the 900C sample are also occurring in samples that underwent different heat treatments. The effect of the heat treatment on the mechanical properties will be described later, in Section 3.3.

Strain Partitioning Between Phases: In situ HRDIC
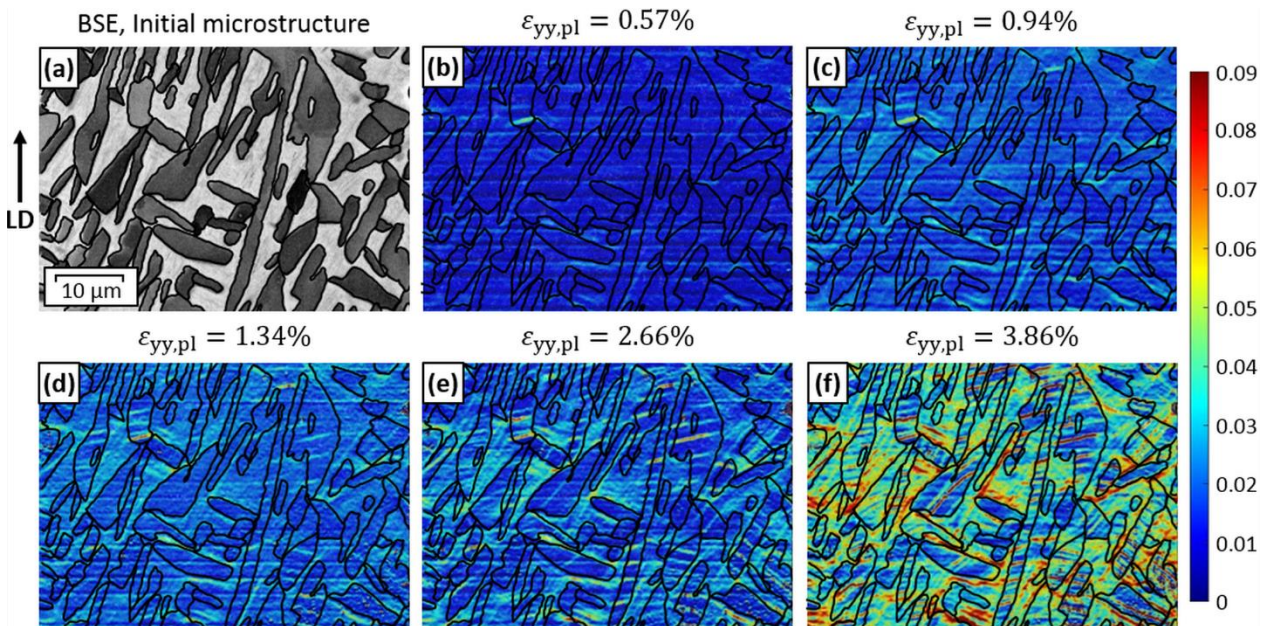
Figure 5-8 Strain maps from an OPS-speckled sample: (a) BSE micrograph of the initial microstructure with α lamellae (dark grey) surrounded by martensite regions (light grey); (b)-(f) HRDIC strain maps at various stages of loading. Grain boundaries have been highlighted in black.
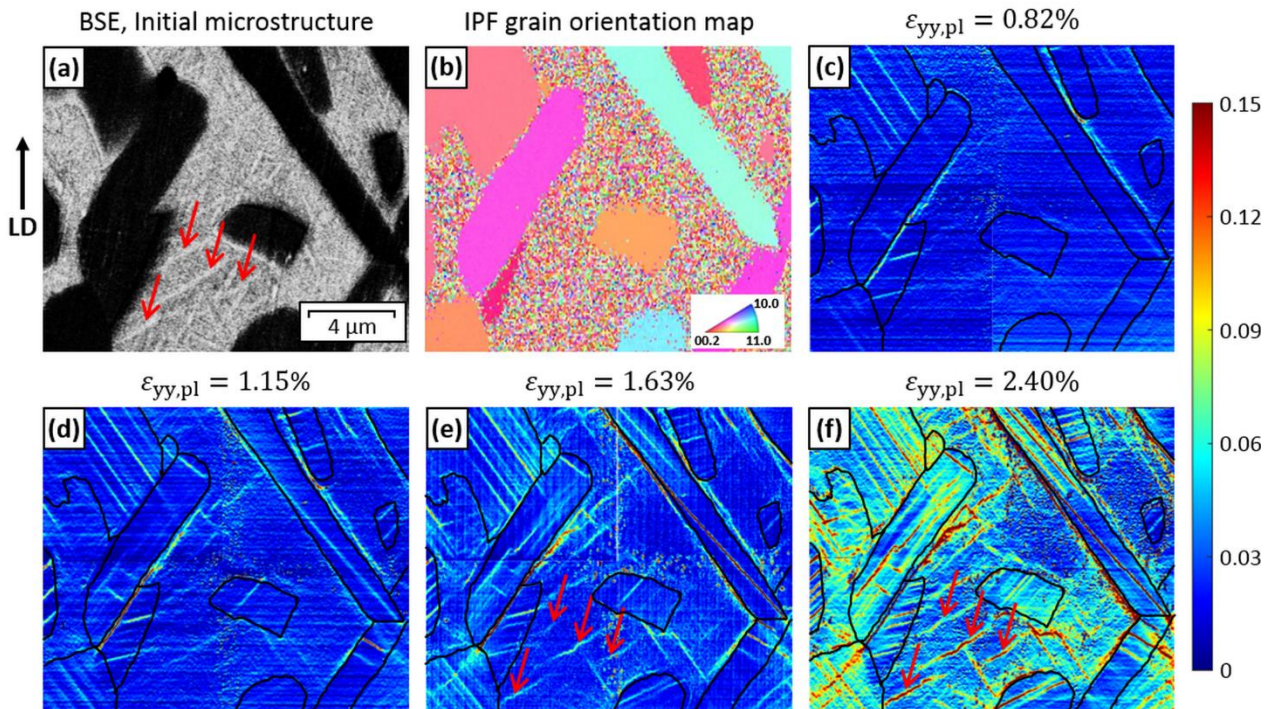
Figure 5-9 Strain maps from an Au-speckled sample: (a) BSE micrograph of the initial microstructure with α lamellae (dark grey) surrounded by martensite regions (light grey); (b) IPF map of the examined region; (c)-(f) HRDIC strain maps at various stages of loading.

In situ HRDIC was performed during interrupted tensile loading of dogbones treated at 900C to further understand the strain partitioning between the phases. The strain maps from an OPS-speckled sample are shown in Figure 5-8. The boundaries between the α lamellae and martensite regions have been highlighted in black. The maps show that strain is accommodated primarily by the martensite regions early in the deformation (Figure 5-8b-d), as expected from the XRD (Figure 5-8b-f). The strain in the martensite is distributed throughout the regions. However, it is not homogeneous but instead localized at the interfaces between the α lamellae and martensite regions. By contrast, strain within a single α lamella is not homogeneously distributed but instead localized in planar slip bands.

In situ HRDIC was also performed on a gold-speckled sample to capture more details on the deformation behavior at a higher magnification. In Figure 5-9, four adjacent strain maps have been stitched together to show a larger area. Arrows in the BSE micrograph (Figure 5-9a) indicate four particularly large laths in the martensite region. The local strain evolution in the martensite regions described in Figure 5-9 appears much less homogeneous than what was observed in the OPS-speckled map. High strain concentrations are observed at α grain boundaries because of the strain mismatch between the α lamellae and martensite regions. Strain appears to accumulate preferentially at lamellae oriented near 45 degrees to the loading direction.

By $\varepsilon_{\mathrm{pl}} = 0.82\%$, slip bands appear already in several α lamellae (Figure 5-9c). Between $\varepsilon_{\mathrm{pl}} = 01.63\%$ (Figure 5-9e) and $\varepsilon_{\mathrm{pl}} = 2.40\%$ (Figure 5-9f), very few new slip bands are forming. Instead, existing slip bands grow and intensify, as in grain 9. This implies that dislocations are nucleating and gliding on slip planes which are already active. The single slip-dominated behavior of the α phase has been previously documented in Ti alloys and the active slip mechanism is shown to be well-predicted by SF analysis [244–246]. Slip trace analysis of the strain maps confirms that low-CRSS $Pri\langle a \rangle$ and $Ba\langle a \rangle$ slip account for the majority of the slip traces.

Within the martensite region, strain localizations appear along interfaces of several martensite laths (marked by arrows in Figure 5-9e). Strain accumulates preferentially at the larger laths, in particular with their major axis oriented near 45 degrees to the loading direction. The intensity of these concentrations increases rapidly with increasing load and can be a source for the nucleation and growth of microcracks within the martensite regions.

3.2.3 Post-mortem Electron Microscopy Characterization
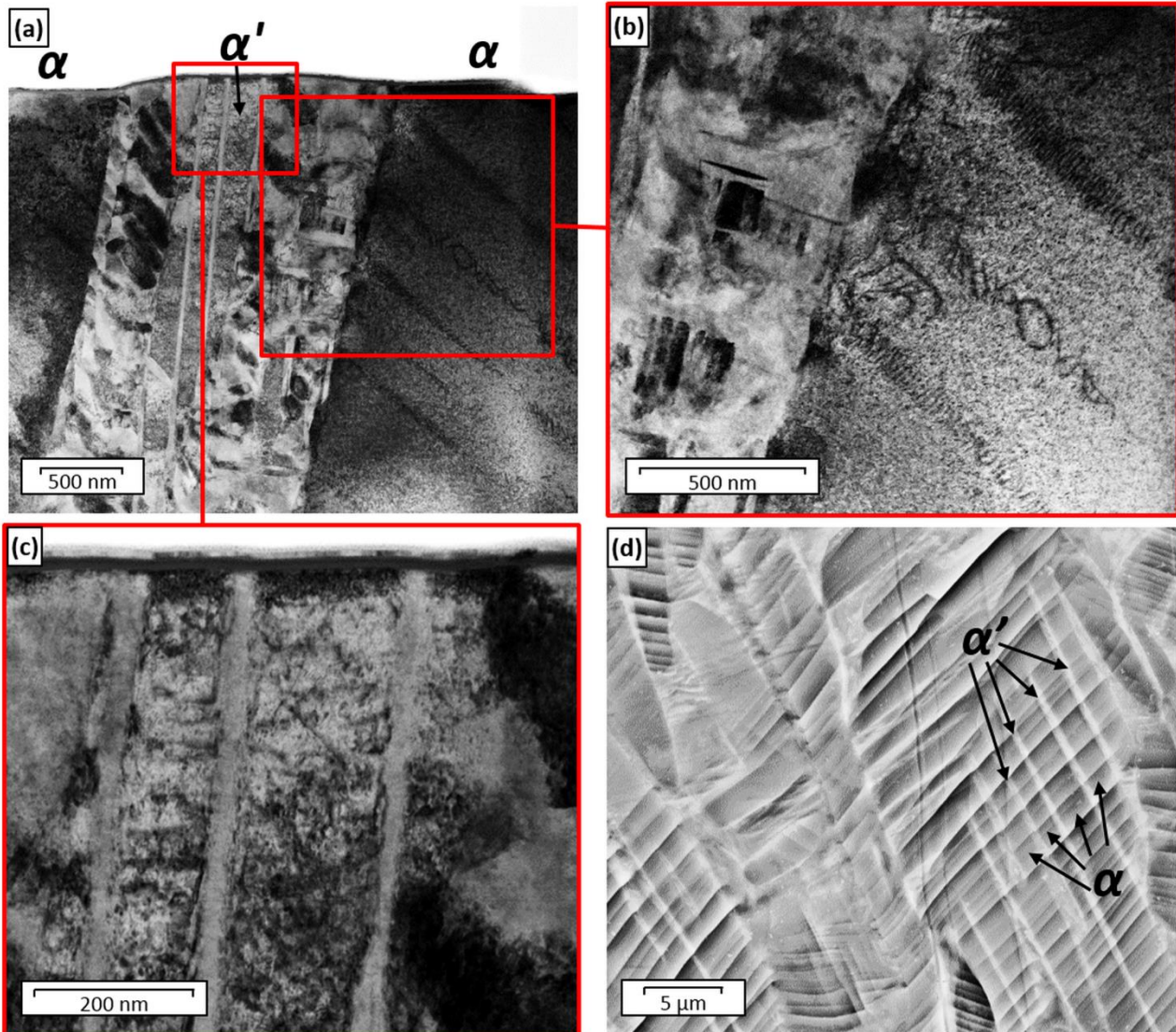
Figure 5-10 (a) TEM micrograph of the 980C sample after 12% strain; (b) Magnified view of forest dislocation structure in a large α' lath; (c) Magnified view of dislocation pileups on single slip systems at the interfaces of an α lamella; (d) ECCI image of the 900C sample after 5% strain.

TEM micrographs of the deformed 980C sample are shown in Figure 5-10a-c. The 980C sample is shown because it had particularly large α' laths that could be examined for the dislocation structure. Only a single active slip system is observed in the α lamellae, shown in Figure 5-10b. The dislocations are more densely packed at the grain boundary than at the center of the grain, suggesting that they are nucleating from the interface and travelling into the grain [106]. The pile-up of these dislocations are responsible for the very localized strain bands observed in the HRDIC (Figure 5-8 and Figure 5-10). By contrast, a forest of dislocations is observed in the α' lath (Figure 5-10c) typical of high work hardening materials. The α' lath contains several twins which are suspected to have formed during the $\beta \rightarrow \alpha'$ martensite transformation [73].

The TEM observations in Figure 5-10a-c suggest that slip transmission between the martensite regions and the α lamellae hardly occurs. Only in cases where 1) the width of the martensite region between adjacent α lamellae is narrow and 2) these lamellae have the same crystallographic orientation, shearing can occur

across the martensite regions. This is seen in electron contrast channelling imaging (ECCI) micrograph of the deformed 900C sample in Figure 5-10d.

5.3.3 The Role of Heat Treatment Temperature
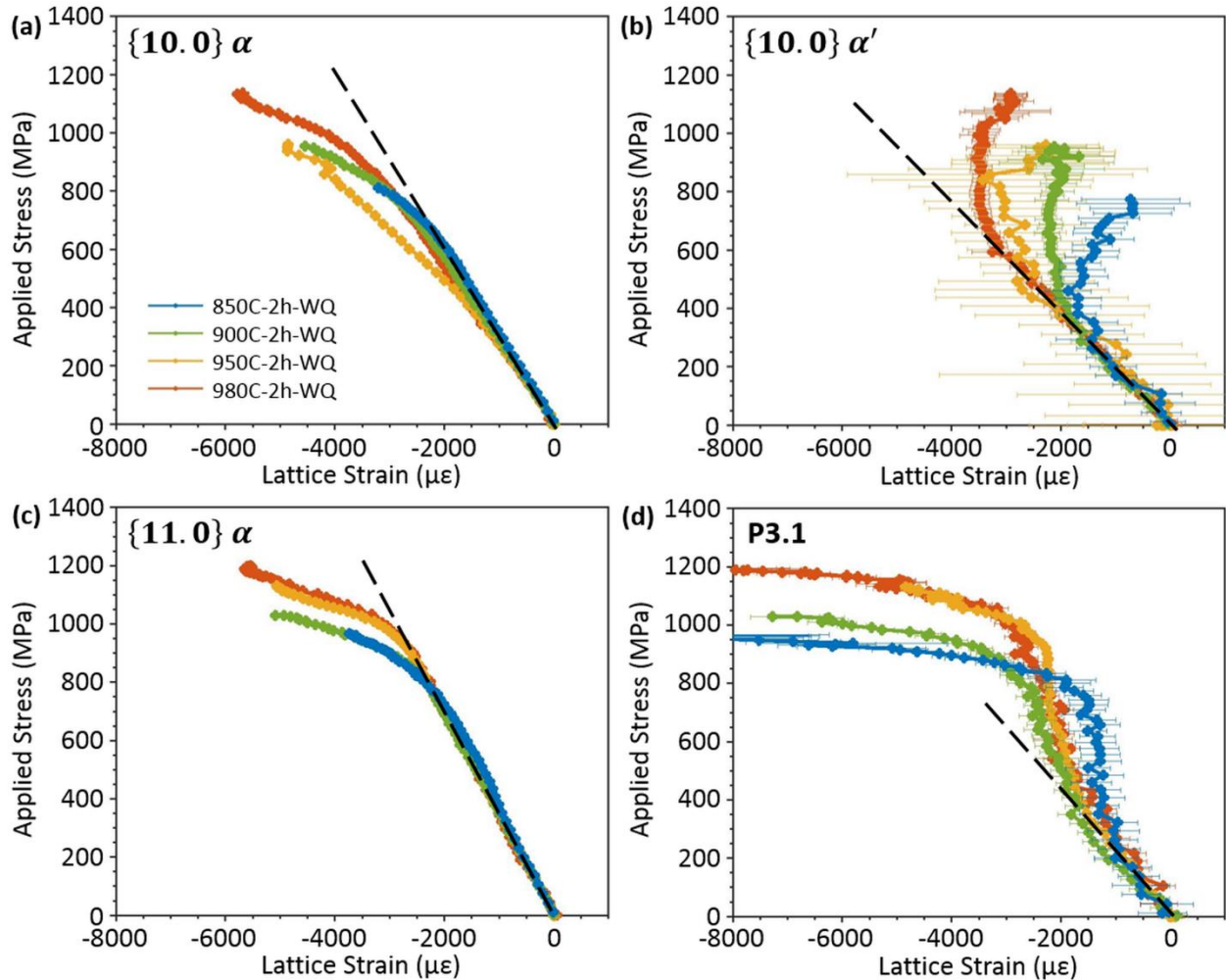
Figure 5-11 Elastic lattice strain evolution of the (a) {11.0} and (b) {10.0} grain families for all heat treated samples. The dashed black lines serve as a guide for the eye.

The qualitative trends presented for the 900C sample are consistent for all heat treatments. However, the yield stress and work hardening of the grain families varies with heat treatment (Figure 5-3). The elastic lattice strain evolutions of the $\{10.0\}\,\alpha$ and α' and the $\{11.0\}\,\alpha$ and P3.1 grain families for all heat treatments are shown in Figure 5-11. The slightly different behavior of the $\{10.0\}\,\alpha$ peak in the 950C sample compared to the other heat treatments is probably a fitting artefact due to the overlap of a low intensity Phase-3 peak with $\{10.0\}\,\alpha$. As the annealing temperature and thus martensite region volume fraction increases, the following trends can be observed:

1. The yield strength of all phases increases. For every 5% increase in martensite (α' + Phase-3) vol. fract., the yield strength of the α lamellae increases ~30 MPa and that of the α' laths increases ~60 MPa.
2. The macroscopic applied stress at which Phase-3 sheds load seems to be independent of heat treatment. The width of the P3.1 peak stays relatively constant up to $R_{p0.2}$, implying that the phase

is not plastifying but instead shedding load due to delamination between the martensite regions and the α lamellae.

The primary effect of annealing at different sub-β transus temperatures is to change the volume fraction and chemical composition of the phases. Chemical partitioning of solute elements Al and V decreases with annealing temperature. Thus, after the quench, there is a higher concentration of Al in α' at higher annealing temperatures [247]. Al is the primary solid solution strengthening element for Ti-6Al-4V [19,248] and causes the observed increase in the yield strength of the α' phase. The higher annealing temperatures also result in a larger volume fraction of the martensite regions. The combination of these two effects result in more load being taken by the martensite regions and less load being felt by the α lamellae. Thus, it takes a higher applied stress to cause yield in the α lamellae. The result is that the macroscopic yield stress increases as the annealing temperature is increased.

5.4   Discussion

The mechanical properties of the EBM + heat-treated Ti-6Al-4V come from the synergistic behavior between three mechanically distinct phases: α lamellae and a composite martensite region consisting of laths of α' and a third hard phase. The enhanced work hardening can be attributed to a progressive load sharing and plasticity of the phases. The findings are summarized below:

1. **Below 300 MPa**, the linear evolution of the elastic lattice strains suggest all phases deform elastically.
2. **Between 300 MPa ($\sim$0.4$R_{p0.2}$) and $R_{p0.2}$=760 MPa**, the elastic lattice strains show that the martensite composite takes less load compared to the elastic region. HRDIC shows that strain is inhomogeneously accommodated in the martensite regions and large strain mismatches develop at the interfaces of α lamellae and martensite regions (α' + Phase-3), suggesting local delamination. The α' laths begin to plastify, resulting in peak broadening, while the P3.1 peak width stays relatively constant, suggesting that the phase has not begun to plastify yet. The lattice strain evolution of the α lamellae deviates slightly from linearity suggesting that a few well-oriented grains begin to plastify. This also results in a slight peak broadening. The collective behavior of the three phases results in high work hardening rates at low strains.
3. **Above $R_{p0.2}$=760 MPa**, the elastic lattice strains show that plastically soft α grain families begin shedding load, which is redistributed to the harder α grain families and Phase-3. The latter behaves as the hardest phase and takes significant load as shown in Figure 5-11. Work hardening in the sample comes from the pile-up of dislocations in the α lamellae. The sudden increase in FWHM of P3.1 (Figure 5-6) suggests Phase-3 deforms or comes under a huge intergranular stress. In this regime, strain localizations develop within the martensite at the interfaces of the larger laths. These strain localizations can eventually lead to crack propagation and failure.
4. As annealing temperature increases, the macroscopic yield stress and UTS increase, which can be explained by the higher volume fractions of martensite (α' +Phase-3) which takes more load and delays the onset of plasticity in the α lamellae.
5. For every 5% increase in martensite region volume fraction, the yield strength of the α lamellae and α' laths increases $\sim$30 MPa and $\sim$60 MPa, respectively.

The 850C and 900C samples have yield strengths lower than that of the as-HIP'ed (Figure 5-3a). This was also noted in [81] where it was proposed to be due to the presence of soft α'' martensite, although the

phase was not observed. Our findings suggest that the yield strength is related to the plastic yield of the α lamellae that results from the early load shedding of the martensite regions ($\alpha' +$ Phase-3), where the α' martensite behaves plastically soft. At lower annealing temperatures, the martensite regions transfer load earlier to the α lamellae, causing the lower yield stress of the α phase and thus macroscopic yield stress.

Mechanically hard behavior of Phase-3

As mentioned earlier, Phase-3 can be indexed as either OR or HCP. The SAED from selected laths shows a better fit for OR, suggesting that Phase-3 is α'' martensite. However, α'' martensite is conventionally considered a "soft" phase with low yield strength and high ductility [84]. XRD observations of Ti-7%Mo (wt.) by Ivasishin et al. [85] showed that α'' peaks merged into a single peak after deformation, suggesting that soft behavior of the martensite is due to the transformation of the OR structure to an HCP structure. Our *in situ* XRD observations, however, show distinct Phase-3 peaks throughout the deformation so there is no evidence for such a transformation. OR phases in other materials have been shown to be plastically hard, such as cementite particles in bainitic steel [249], but such behavior has never been reported for α'' martensite in Ti alloys.

Conversely, considering Phase-3 as a third HCP phase, then the hard mechanical behavior could then be explained by the large lattice parameters and the small size of the laths. Compared to the α and α' phases, Phase-3 would have the largest a lattice parameter. The low-CRSS deformation mechanisms of Ti-6Al-4V involve $\langle a \rangle$ slip on basal and prismatic planes, which would be hindered by the larger a lattice parameter. Additionally, the Phase-3 laths are approximately one order of magnitude smaller than the α lamellae, which would lead to an additional Hall-Petch hardening effect compared to the primary α phase.

Regardless of its structure, the presence of an additional hard phase plays a key role in the enhanced ductility in the 980C sample and in the materials prepared by de Formanoir et al. [81]. Previously, Matsumoto et al. [78] were able to achieve UTS > 1200 MPa and elongation before failure of ~14% in a dual-phase $\alpha + \alpha'$ Ti-6AL-4V. They attribute the enhanced ductility to the reduced strain incompatibility and increased slip transmission between two HCP phases, which allows the sample to strain without a significant work hardening after 1-2% plastic strain. Conversely, the work hardening in this study and observed by de Formanoir et al. in [81] remains relatively high over the entire deformation and there is no evidence that slip transfer occurs between the martensite and α grains. In this regime the lattice strains show that Phase-3 shares load with the α grains, which allows the α lamellae to continue to deform and work harden.

5.5　Conclusion

The origin of a high work hardening in Ti-6Al-4V alloys prepared by EBM was characterized using *in situ* XRD and HRDIC. Samples were post-treated with a sub-β transus anneal followed by water quenching (described in [81]) to produce a microstructure of α lamellae surrounded by regions of martensite. The martensite regions are shown to have a composite structure due to the presence of a third, hard phase previously unidentified in this material. The enhanced work hardening and extended plasticity is explained by a gradual load transfer between the three phases: load transfer from the α lamellae to the martensitic regions and load transfer between the two phases present in the martensitic region. Strain partitioning is inhomogeneous at the micro scale and delamination between the three phases is observed which will eventually lead to failure.

5.6   Acknowledgements

Chapter 6   *In Situ* Characterization of Work Hardening and Springback in Grade 2 α-Titanium Under Tensile Load

The work presented in this chapter is a written article by the same name. It has been reformatted to integrate with this thesis. The article has been submitted to Acta Materialia and is currently under review. The version in this thesis is as-submitted to the reviewers. A full bibliographic reference is given below:

K. Sofinowski, M. Šmíd, S. Van Petegem, S. Rahimi, T. Connoley, H. Van Swygenhoven, *In situ* characterization of work hardening and springback in grade 2 α-titanium under tensile load. Acta Materialia: *Under Review*

This is a first author paper written in entirety by the PhD candidate (K. Sofinowski). The material was prepared by Dr. S. Rahimi in the Advanced Forming Research Centre at the University of Strathclyde, Wales. *In situ* XRD experiments were performed by K. Sofinowski in conjunction with Dr. S. Van Petegem. *In situ* HRDIC was performed by K. Sofinowski in conjunction with Dr. M. Šmid. All data analysis and figures for the *in situ* tests were prepared by K. Sofinowski.

6.1   Introduction

Springback, the strain recovery in a product following a forming process, is a major challenge faced by manufacturers during modern sheet metal forming, especially during cold stamping. Springback causes a processed part dimensions to deviate from their desired profile and can result in higher-than-predicted residual stresses following the final deformation [250]. Information on the microstructural mechanisms underpinning the springback is thus crucial for the development of alloys and forming processes to mitigate the effect.

Recently, Khayatzadeh et al. [8,94] reported that the springback in Grade 2 commercially pure α titanium (CP-Ti) shows a non-linear anelastic recovery during unload. Similar non-linear unloading behaviors have been previously observed in a wide range of steels [250–259] and is known to vary with the alloy composition. However, most of the existing studies are focused on fitting constitutive models, and only a few attempts have been made to explain the underlying microstructural sources of the effect. Luo and Ghosh [250] suggest that the bowback of pinned dislocations and disintegration of dislocation cell structures generated during deformation contribute to the non-linear springback in DQSK steel. Post-mortem TEM observations in pure Fe by Benito et al. [253] support this description.

As compared to steel and other FCC alloys, characterization of springback in HCP alloys is considerably less developed. Due to the inherent anisotropy of the HCP unit cell, additional deformation behaviors must be taken into account. It has been observed, for example, that deformation in α-phase Ti polycrystals is dominated by single slip [106,260] and do not form dislocation cells, implying that different mechanisms than those described above for steel [250] must be active. Without five easily-activated independent slip systems, deformation twinning is often observed in HCP metals. Cáceres et al. [261] attributed the anelastic springback in AZ91 magnesium to partial reversal of extension twins formed during loading. Additionally, {10.2}⟨10.1⟩ extension twinning in CP-Ti causes an 84.8° rotation of the unit cell [86,87], resulting in significant texture

changes during loading. Hama et al. [5] showed in a magnesium alloy that plastically hard grains twinned into plastically soft orientations, leading to increased easy glide of dislocations during unloading that contributed to the additional strain recovery. Even in the absence of twinning, Abdolvand et al. [22] observed that intergranular stresses on certain grains in CP-Ti could decrease during continuous tensile loading depending on their grain neighborhood. Thus, the microstructural sources of springback in CP-Ti warrant further investigation.

Additionally, the stress-strain behavior of the CP-Ti studied by Khayatzadeh et al. [8,94] showed distinct three-stage work hardening. This behavior is often described during compression for CP-Ti [89–93] and other HCP materials [262–265] as the result of $\{10.2\}\langle10.1\rangle$ extension twinning and the subsequent hardening as dislocation glide is hindered by the new twin boundaries. More recently, the three-stage work hardening has been reported for tension tests in CP-Ti [86–88]. Becker and Pantleon [87] reported that the three stages A, B, and C correspond to easy dislocation slip, the activation of $\{11.2\}\langle\overline{1}\overline{1}.3\rangle$ compression twinning, and the saturation of this twinning system and subsequent activation of $\{10.2\}\langle10.1\rangle$ extension twinning. On the other hand, Roth et al. [86] observed almost no twinning (<0.5% and 5.7% vol. fraction for rolling direction and transverse direction samples, respectively) and thus proposed that the work hardening plateau is related primarily to dislocation-based plasticity.

In this study, the deformation behavior of CP-Ti Grade 2 sheet is examined during in-plane uniaxial tensile loading. The evolution of the elastic lattice strains and peak shape is captured by *in situ* x-ray diffraction (XRD) to examine the development of intergranular stresses during loading and unloading. The twin volume and growth is quantified by quasi-*in situ* electron backscatter diffraction (EBSD) and *in situ* high resolution digital image correlation (HRDIC). It is demonstrated that the work hardening plateau is due to the sudden activation and multiplication of $\langle c + a \rangle$ slip and the subsequent redistribution of load among plastically deformed grain families. The springback can be attributed to a Bauschinger effect that is exacerbated by single-slip deformation and the development of compressive residual stresses along the tensile axis in many grain families.

6.2 Experimental Procedure

6.2.1 Material
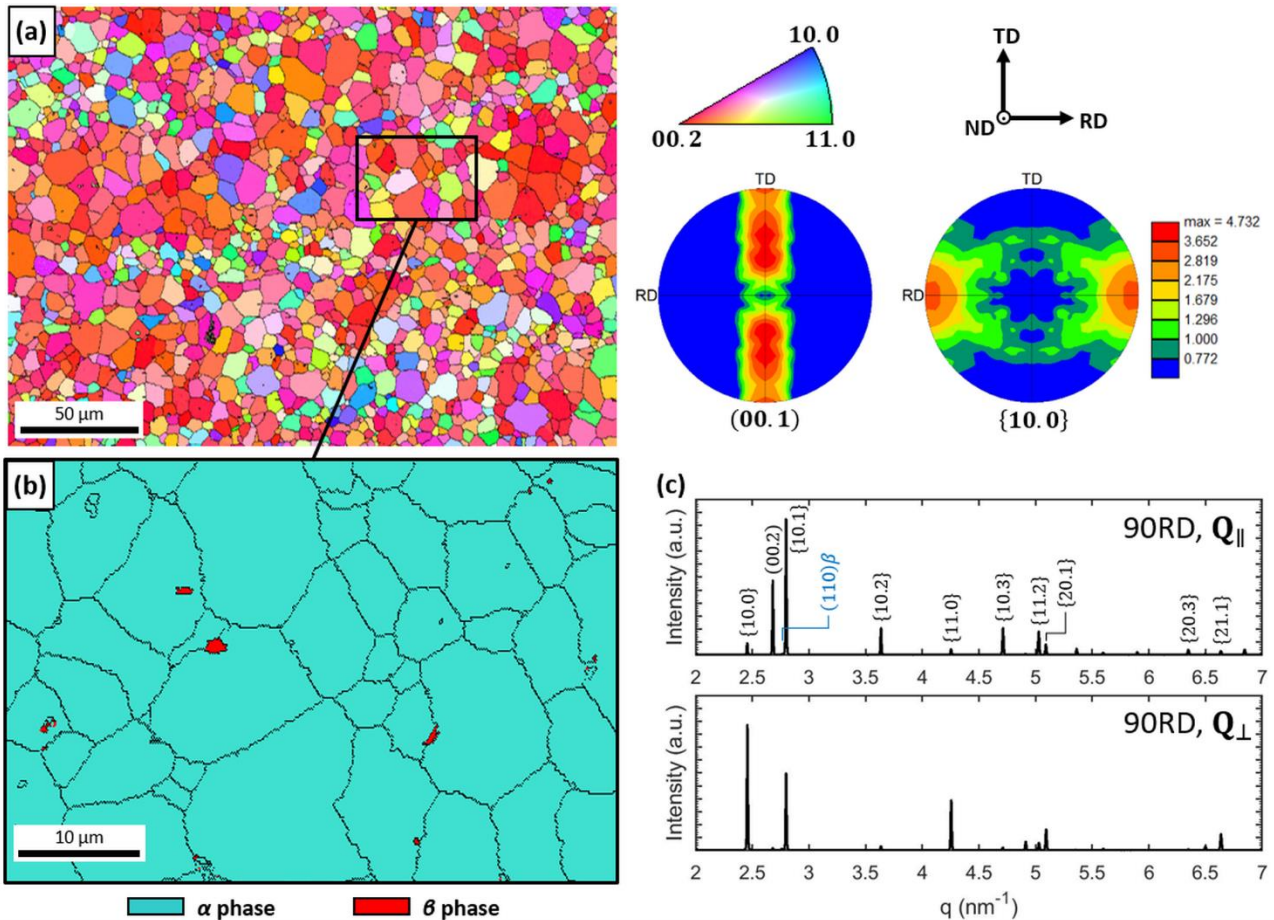
Figure 6-1 Initial microstructure of CP-Ti: (a) IPF grain orientation map with respect to TD (i.e. 90° to RD) with 0001 and $10\bar{1}0$ pole figures; (b) Magnified section of the corresponding phase map showing a few β grains in red; (c) Undeformed axial ($Q_\parallel$) and radial ($Q_\perp$) XRD patterns.

Sheets of commercially pure titanium (CP-Ti Grade 2) cold-rolled to 1.6 mm thick were supplied by TIMET. The initial microstructure is shown in Figure 6-1. The grain orientations are shown with respect to the loading direction, 90° to RD (Figure 6-1a). The material exhibits a slight basal texture perpendicular to RD typical of cold-rolled Ti. The CP-Ti is >99.8% α phase with small retained β grains dispersed throughout the material, as seen in the magnified section of the phase map in Figure 6-1b. The α grains are generally equiaxed with a grain size of 8.2 ± 3.4 µm while the β grains have a grain size of 0.7 ± 0.4 µm. The texture of the α grains is also visible in the axial ($Q_\parallel$) and radial ($Q_\perp$) diffraction patterns of the undeformed samples (Figure 6-1c).

6.2.2 *In situ* X-ray Diffraction

Flat, dogbone-shaped specimens were cut from the sheet using electrical discharge machining (EDM) at 0°, 45°, and 90° to the rolling direction (RD). The specimen design was based on the ASTM E8/EM8-11 test standard scaled so that the reduced section length was 32 mm. Interrupted uniaxial tensile tests were performed *in situ* using an INSTRON 100kN tensile test rig integrated into the XRD facilities. Samples were loaded using displacement control to 3.5%, 7%, and 10.5% total strain (3.5%, 5.25%, and 7% for the samples

at 90° to RD (90RD), due to the lower ductility along this direction) and unloaded to 20 MPa using force control. After each unloading step, the sample was held constant at 20 MPa for five minutes before reloading. The samples were loaded with an initial strain rate of $\dot{\varepsilon} = 0.0001$ s^{-1} and unloaded in force control at a rate of dF/dt = -4 N/s. The slow loading and unloading rates were chosen to give time to capture XRD spectra, as previous research on this material [8] suggests that the springback is largely independent of strain rate. Three samples were tested for each test type to ensure consistency in the measured results.

XRD spectra were collected *in situ* during the interrupted tensile tests at the JEEP I-12 beamline at Diamond Light Source, UK [161]. Samples were measured in transmission using a 53 keV beam with 300 × 300 µm^2 spot size. Diffraction patterns were recorded in 8 s intervals with a Pilatus 2M CdTe 2D area detector. The 2D images were radially binned using DAWN XRD processing software [266] at ± 3° parallel and perpendicular to the tensile axis ($Q_\parallel$ and $Q_\perp$, respectively).

The diffraction peaks were fit using a split Pearson VII function to extract the peak position $d_{hk.l}$, peak width (full-width at half-maximum – FWHM), and peak integrated intensity. The elastic lattice strains for a given grain family were calculated from the change in peak position of the corresponding $\{hk.l\}$ reflection ($\varepsilon_{hk.l} = \left(d_{hk.l} - d_{hk.l}^0\right)/d_{hk.l}^0$) and used to examine how the applied load is shared between different grain families (e.g. [4,33,152,267]). In the elastic regime, the elastic lattice strain evolves linearly with the applied stress. As grain families plastify, the load is transferred between the grains and $\varepsilon_{hk.l}$ deviates from linearity. For the $Q_\parallel$ (axial) reflections, an increase in $\varepsilon_{hk.l}$ means that the grain family goes in tension while a decrease means that it goes into compression along the tensile axis. For the $Q_\perp$ (radial) reflections, the change in $\varepsilon_{hk.l}$ is measured perpendicular to the loading direction, i.e. the Poisson contraction is measured. Thus an increase in $\varepsilon_{hk.l}$ implies that the grain family is in compression and vice versa.

The width of a $\{hk.l\}$ diffraction peak, FWHM$_{hk.l}$, can be affected by many sources. The most prominent are: (i) instrument resolution, (ii) the coherent scattering length (related to the average grain size), (iii) incoherent strain in the diffracting volume (e.g. from dislocations) and (iv) intergranular strains (i.e. different grains in the same grain family with different average strains). When considering the grain size and dislocations as many sources for peak broadening the FWHM can be described by [145,154]:

$$\text{FWHM}_{hk.l} = \frac{K_{Sch}}{D} + f_m g \sqrt{\rho_{\text{disl}} \overline{C_{hk.l}}} \tag{6-1}$$

where D is the crystallite size, K_{Sch} is the Scherrer constant, f_m is a function related to dislocation arrangement, g is a 1/$d_{hk.l}$, ρ_{disl} is the dislocation density, and $\overline{C_{hk.l}}$ is the contrast factor for the grain family. During deformation, an increase in the FWHM, "peak broadening," can be a signature of increasing dislocation density, decreasing average grain size (e.g. as grains are split by twinning), or the development of an inhomogeneous stress distribution between the grains of a given grain family [145,154,268]. Conversely, a decrease in FWHM can be a signature of decreasing dislocation density, e.g. by annihilation of dislocations, or the relaxation of local stress gradients.

Schmid Factor (SF) Analysis
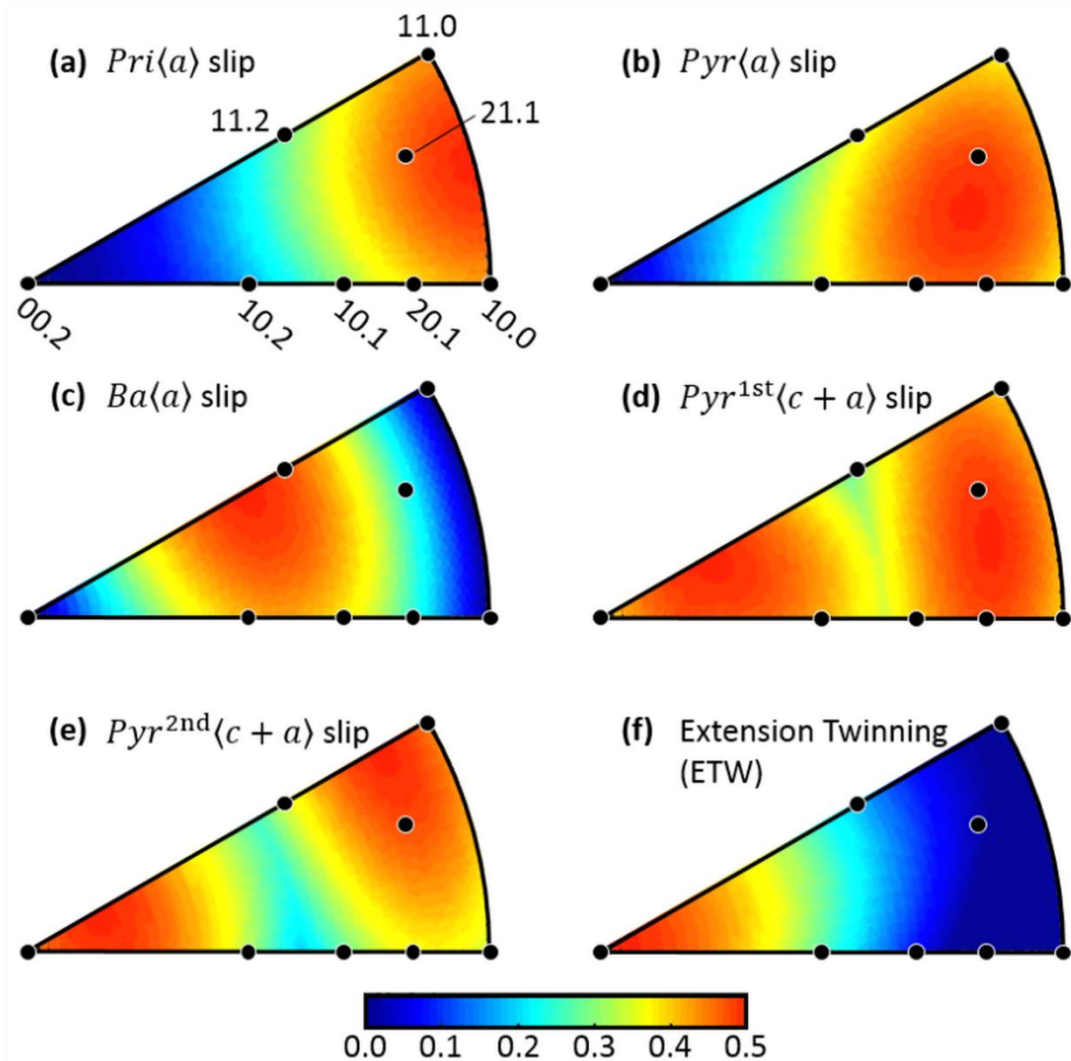
Figure 6-2 Axial ($Q_{\parallel}$) inverse pole figures of the maximum SF under uniaxial tension for all probable deformation mechanisms.

Schmid factors were calculated for all deformation mechanisms according to a generalized Schmid law proposed by Muránsky et al. [33]:

$$\mathrm{m} = \mathbf{b} \cdot \mathbf{g} \cdot \mathbf{S} \cdot \mathbf{g}^{\mathrm{T}} \cdot \mathbf{n}^{\mathrm{T}} \tag{6-2}$$

where **b** is the Burgers vector for slip, **S** is the 3-D stress tensor (in this case, the uniaxial stress), and **n** is the normal to the slip plane. For twinning, **b** and **n** are the twinning direction and normal to the twinning plane, respectively. The matrix **g** is a rotation matrix relating the stress tensor and grain orientation. Each axial grain family was converted to an orthonormal basis and the SFs for all possible slip systems were calculated using a c/a ratio of 1.588. The axial inverse pole figures (IPFs) of the maximum SF under uniaxial tension are shown in Figure 6-2. The IPFs are generated using the texture analysis toolbox MTEX developed in MATLAB™ [269].

	CRSS (MPa)	Relative CRSS (MPa)			
Model [Ref.]	$Pri\langle a \rangle$	$Ba\langle a \rangle$	$Pyr\langle a \rangle$	$Pyr^{1st}\langle c+a \rangle$	$Pyr^{2nd}\langle c+a \rangle$
TEM + Slip trace analysis [95]	120	1.5	1.2	2.0	--
CPFE single crystal [96]	181	1.2	--	2.6	--
CPFE single crystal [97]	150	2.3	--	7.4	--
Taylor-type modelling [98]	--	6.0	--	9.0	--
VPSC [99]	90	2.5	--	9.4	--
EPSC [100]	80	1.1	1.4	3.3	--
VPSC [101]	57	4.8	2.9	5.4	4.1
EPSC [102]	68	2.6	1.8	3.7	--
EVPSC [88]	141	1.8	1.4	2.4	2.5
EVPSC [103]	50	2.4	1.8	1.3	3.0

Table 6-1 Literature data for CRSS values relative to the CRSS of $Pri\langle a \rangle$ slip for CP-Ti at room temperature.

Critical resolved shear stress (CRSS) values from literature for commercially purity α-Ti at room temperature are shown in Table 6-1. In general, $\langle a \rangle$ slip on prismatic planes ($Pri\langle a \rangle$) is considered the easiest deformation mechanism, with pyramidal $\langle a \rangle$ slip ($Pyr\langle a \rangle$) second and basal $\langle a \rangle$ slip ($Ba\langle a \rangle$) third. Except for the recent work of Richeton et al. [103], $\langle c + a \rangle$ slip is generally regarded as more difficult than $\langle a \rangle$ slip mechanisms, which can result in twinning to accommodate strain along the c-axis. In combination with the CRSS, the SF can be used to identify the predominant active deformation mechanisms in a grain family at the onset of plasticity. This approach is not necessarily valid for individual grains in polycrystals or at high plastic strains, as it has been shown that the local stress tensor can differ significantly from the applied stress tensor (e.g. [22]). However, on a grain family scale, this approach has been shown to be a good predictor of active plasticity mechanisms at low strains [33,152].

6.2.3   Quasi-*In Situ* Electron Backscatter Diffraction

Flat, dogbone-shaped specimens were cut from the sheet by EDM at 0°, 45°, and 90° to the RD. The specimen shape was the same as the large dog bone design in [160] but with a thickness of 1.6 mm. The samples were mechanically ground using silicon carbide grinding paper to 2400 grit, then polished with 6, 3, and 1 µm diamond paste for three minutes each. Final polishing was done with 0.05 µm high purity OPS colloidal silica solution for two sessions of 30 minutes each. Samples were then vibration-polished for 12 hours to a mirror-finished condition for EBSD acquisition.

Interrupted uniaxial tensile tests were performed using an uniaxial tensile test rig (for details, see [160]). Samples were loaded using displacement control to 3.5% and 7% total strain and unloaded with a strain rate of $\dot{\varepsilon} = 0.0001$ s^{-1}. After each unload, the sample was removed and observed in a Zeiss ULTRA 55 field emission gun scanning electron microscope (FEG SEM) with an EDAX Hikari Camera. Images were captured at 20 kV in high current mode with an aperture of 120 µm. EBSD mapping was performed with 90 nm step size covering an area of 52 × 42 µm². The EBSD data was analyzed using OIM Analysis 7.3 software.

6.2.4   *In Situ* High Resolution Digital Image Correlation

Flat, dogbone-shaped specimens were prepared in the same manner as for the quasi-*in situ* EBSD. Additionally, a gold speckle pattern was applied to the surface by remodelling a thin layer of gold using the techniques described in [14,15]. Uniaxial tensile tests were performed using one axis of a miniaturized biaxial machine mounted inside of a FEG SEM Zeiss ULTRA 55 microscope. For more details about the machine,

please refer to [176]. Samples were loaded to ε = 9% at a strain rate of $\dot{\varepsilon}$ = 0.002 s^{-1}, an order of magnitude faster than the *in situ* XRD tests, to promote twinning. At the end of the loading the displacement of the machine was held constant for imaging.

High contrast images were taken using an in-lens detector to minimize the signal-to-noise ratio, as proposed by Yan et al. [13]. The SEM was operated at 3 kV with a 30 μm aperture at a working distance (WD) of 6 mm. A set of SEM images (3x3 grid) with a resolution of 3072 x 2304 pixels, covering an total area of 74 × 54 μm^2, were taken with a dwell time 25 μs. Strain maps were calculated from the SEM images using the open-source 2D DIC Matlab software Ncorr [234] using a subset radius of 10 pixels, subset spacing of 4 pixels, and strain radius of 5. These values were chosen as a good compromise between the strain resolution and noise caused by sample drift and lens distortions.

6.3   Results

6.3.1   Mechanical Response
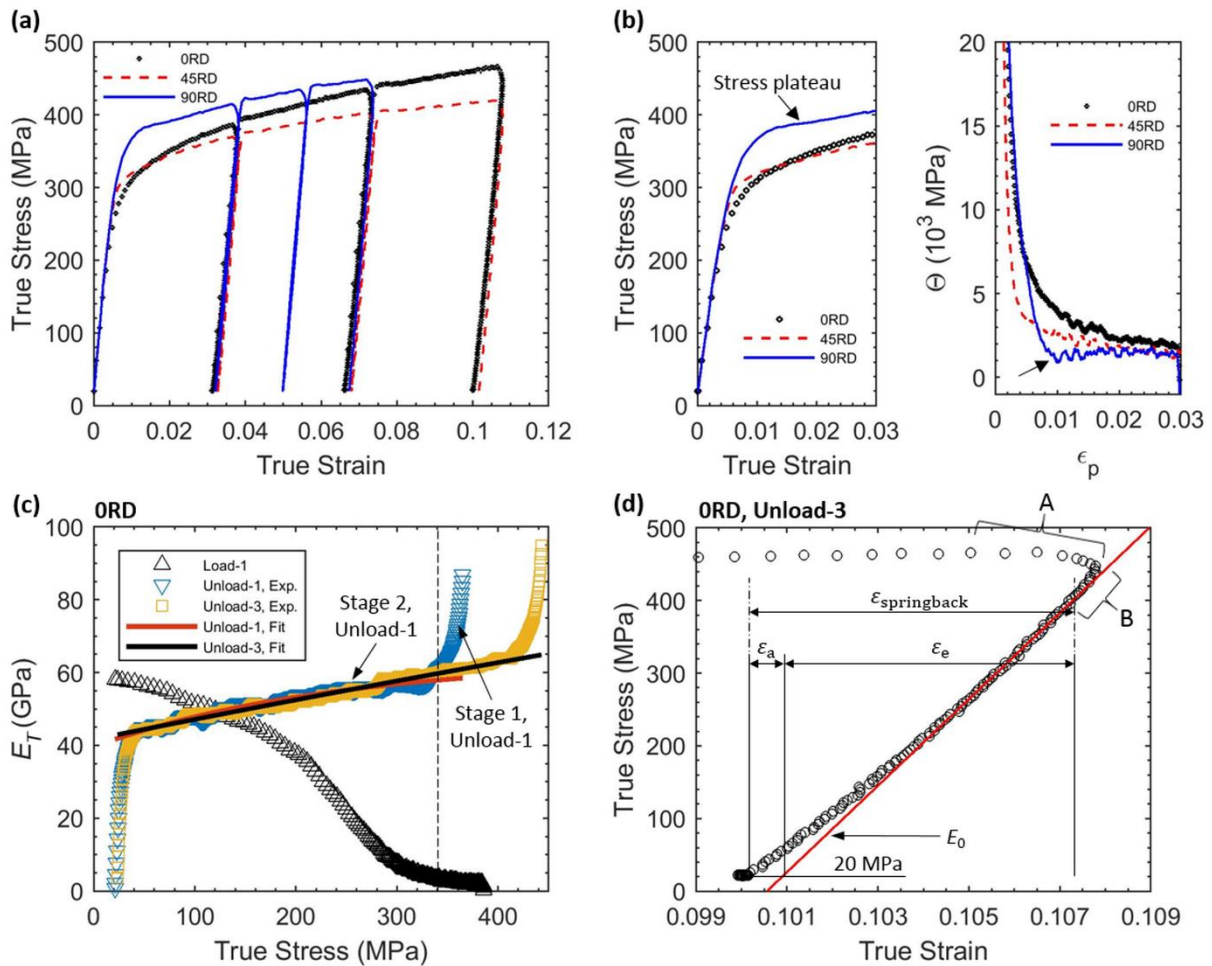
Figure 6-3 (a) True stress-true strain response for 0RD, 45RD, and 90RD; (b) Magnified view of the true stress-true strain curves for the first 3% of strain and the corresponding plastic work hardening Θ; (c) Instantaneous tangent modulus E_T versus true stress for the first load and first and last unload for the 0RD sample; (d) Magnified view of the final unload of the 0RD sample showing the springback and its components.

The macroscopic true stress-true strain response for test A for 0RD, 45RD, and 90RD are shown in Figure 6-3a. A stress plateau is visible in the first loading curve of the 90RD sample just after 0.2% yield ($R_{p0.2}$), highlighted in Figure 6-3b. The plastic work hardening rate $\Theta = d\sigma/d\varepsilon_\mathrm{p}$ is plotted next to it as a function of plastic strain ε_p. It is clear that the 90RD curve shows three distinct work hardening phases: a strong initial decrease, a slight increase, then a slow decrease parallel with the 0RD and 45RD samples. Mechanical tests of the same material by Khayatzadeh et al. [8] show that this concave stress-strain behavior is visible in 45RD and 0RD as well at higher strain rates. The magnitude of the stress drop increases with increasing angle from the rolling direction. The low strain rate used in this study ($\dot{\varepsilon} = 0.0001$ s^{-1} as opposed to 0.002, 0.01, or 0.1 s^{-1}) explains why such a plateau is not observed in the 0RD and 45RD samples.

For all samples, the true stress-true strain curves deviate substantially from linearity during both loading and unloading. Thus, to describe the loading and unloading behavior, the instantaneous tangent modulus E_T is calculated using a least squares fit over subsequent sets of 5,000 true stress-true strain data points. A similar procedure was used by Luo and Ghosh [250] to characterize the non-linear loading and unloading response of a DQSK steel. Figure 6-3c shows E_T as a function of true stress during initial loading and the first and last unloading stages for one of the 0RD samples. The consistent decrease in E_T during the loading and unloading shows that the curves are non-linear over the entire regime. However, it must be mentioned that the initial value of the modulus during loading is ~60 GPa, well below the reported modulus of 90-110 GPa [8]. This is a result of the compliance of the tensile test rig, as the displacement of the grips was used to calculate the strain. As the purpose of this study is to examine the relative springback with respect to loading direction and prestrain, the magnitude of the modulus is not critical, but the trends of the springback are. An assumption must be made that the response of the machine is consistent for all tests. This is a reasonable assumption considering that the tests never exceed 5 kN of applied load, an order of magnitude lower than the machine limit of 100 kN.

During the unloading stages, E_T initially drops sharply with applied stress before levelling off to a more steady decrease (Figure 6-3c). The initial drop is related to two behaviors. The first is the transition from displacement-controlled loading to force-controlled unloading. At the early stages of unloading the sample relaxes faster than the prescribed -4N/s unload rate. This is compensated by continuous forward motion of the crosshead until the desired unload rate is met. This regime is marked "A" in Figure 6-3d, which shows the unloading of a 0RD sample after 10.5% straining (i.e. third unloading stage). The continued forward motion results in the real true strain reaching 10.78% before the direction of the strain reverses. The second is a brief period of continued forward microplastic strain that delays how quickly the sample reaches the imposed unload rate. This has been previously described for DQSK steels [250]. In combination with the changing crosshead speed, this results in the non-linear E_T evolution, marked "B" in Figure 6-3d, before a steady unloading rate of -4 N/s is reached.

The evolution of E_T must therefore be divided into two stages: Stage 1, where the mechanical behavior is heavily influenced by the continuously changing crosshead speed, and Stage 2, where the degradation of E_T is primarily due to microstructural changes. The evolution of E_T in Stage 2 is non-linear and can be well-described by a function of the form $a\left(1 - e^{bx}\right)$, which has no physical meaning but describes well the slow degradation in E_T during unloading. The transition between these two stages can then be defined as the stress at which the measured E_T deviates more than 5% from the fit to Stage 2 (Figure 6-3c).

Due to the non-linear behavior of the unloading, it is inappropriate to define a linear "degraded elastic modulus," as is often done when calculating springback. Instead, the springback is split into an elastic and an

anelastic component, ε_e and ε_a, respectively. The anelastic component is taken as the difference between the unloaded strain (at 20 MPa) and the total springback minus the initial elastic modulus, and is related to all springback not associated with the elastic unload. Both components are shown graphically in Figure 6-3d. The total springback, ε_{sb}, is calculated as the difference between the true strain at the end of Stage 1 and the end of unloading.
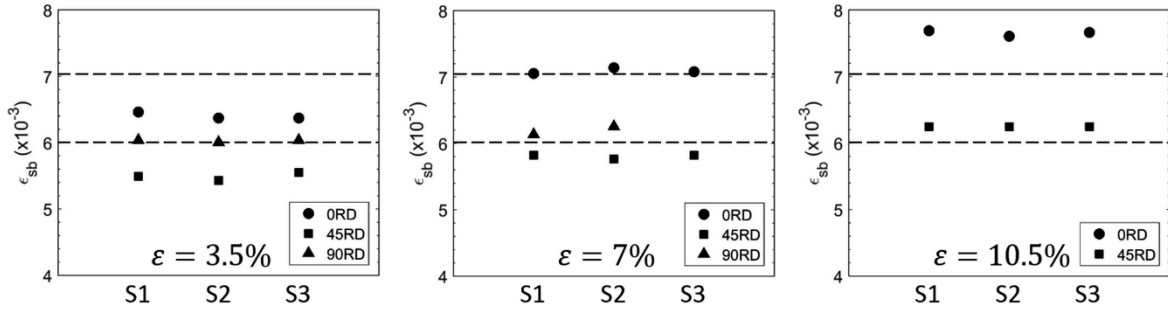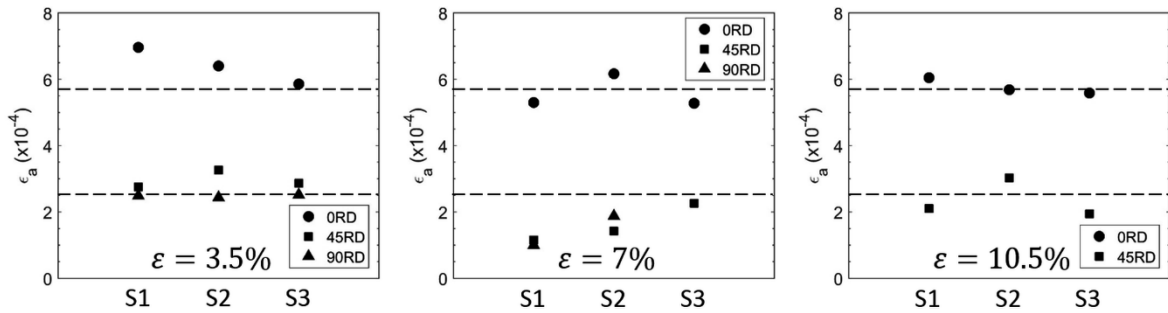
Figure 6-4 Magnitude of springback for each dogbone: (a) total springback ε_{sb} and (b) anelastic component ε_a of the springback. S1, S2, and S3 refer to the three samples for each loading direction. The dashed lines are guides for the eye.

The magnitude of ε_{sb} and ε_a are shown in Figure 6-4a and b, respectively, for each loading cycle. Three samples were measured for each loading direction, denoted S1, S2, and S3. One of the 90RD samples was loaded to different strain values for the second and third load and is therefore not shown. As expected, ε_{sb} increases with increasing applied strain for all loading directions. The springback for 0RD is consistently higher than 45RD and 90RD. As with ε_{sb}, the magnitude of the anelastic springback ε_a is highest in 0RD but does not show any trends with increasing prestrain. These trends are consistent with those observed by Khayatzadeh et al. [8] at higher strain rates.

6.3.2 Quasi-*In Situ* EBSD and HRDIC
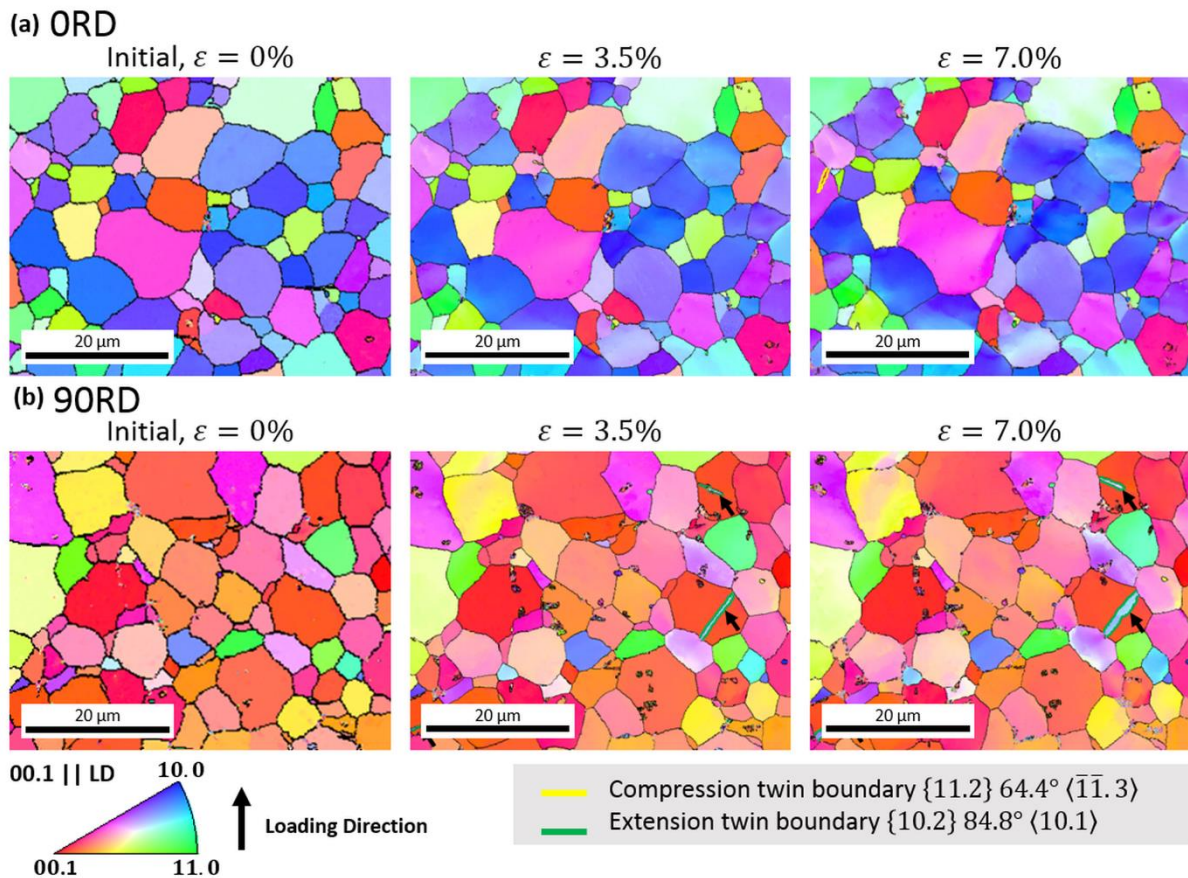
Figure 6-5 Evolution of IPF grain orientation maps w.r.t. the loading direction for (a) 0RD and (b) 90RD sample. Dark spots on the strained 90RD samples are due to low confidence index areas.

Quasi-*in situ* EBSD was performed to examine the role of deformation twinning. The microstructures of the 0RD and 90RD samples in the unloaded state and after straining to 3.5% and 7% are shown in Figure 6-5. In both samples, deformation twins are observed to form during the first loading cycle to ε = 3.5%. During the second loading cycle to ε = 7.0%, no new twins are formed, but existing twins tend to grow. In the 0RD sample, narrow $\{10.1\}\langle 10.2\rangle$ compression twins are observed, whereas in the 90RD sample the observed twins are $\{10.2\}\langle 10.1\rangle$ tension type. However, very little twinning is observed for both orientations. The area volume fraction of twins after 7% strain is 0.01% and 0.34% for 0RD and 90RD, respectively. By contrast, orientation gradients appear in many of the grains due to grain rotation caused by dislocation slip. The average grain size, however, does not appear to change significantly in this strain range.
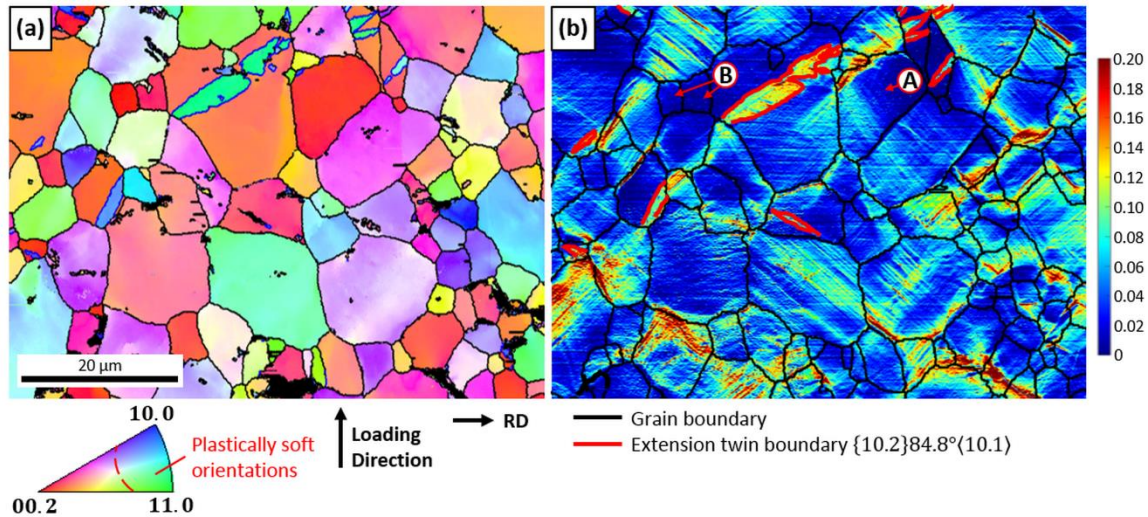
Figure 6-6 Microstructure of a 90RD dogbone loaded to ε = 9% at $\dot{\varepsilon}$ = 0.002 s^{-1}: (a) IPF grain orientation map and (b) strain distribution measured by HRDIC. Grain boundaries are drawn in black, and extension twin boundaries are highlighted in red.

Figure 6-6 shows the grain orientation map and strain distribution measured by HRDIC in a 90RD sample. The sample was loaded to ε = 9% at a strain rate of $\dot{\varepsilon}$ = 0.002 s^{-1}. Twin boundaries are highlighted in red. Even at the higher strain rate and strains, very little twinning is observed. $\{10.2\}\langle10.1\rangle$ extension twins are observed in grains with their c-axis oriented nearly parallel to the loading direction, which have a high SF for extension twinning (Figure 6-2). Interestingly, twinning is not observed in several $(00.2)_{\parallel}$ grains, which theoretically have the maximum SF of 0.5 for extension twinning. Instead, slip is observed as for instance in grain (A). There are also grains where no strain accommodation is observed, for instance in the two grains marked (B). HRDIC shows that strain is inhomogeneously accumulated in plastically "soft" grains such as $\{11.0\}_{\parallel}$, $\{10.0\}_{\parallel}$, and $\{21.1\}_{\parallel}$ (soft orientations indicated on the IPF color key in Figure 6-6a). These grains show large orientation gradients which have to be assigned to grain rotation due to dislocation slip.

6.3.3 *In Situ* XRD Results

Peak evolution during tensile loading
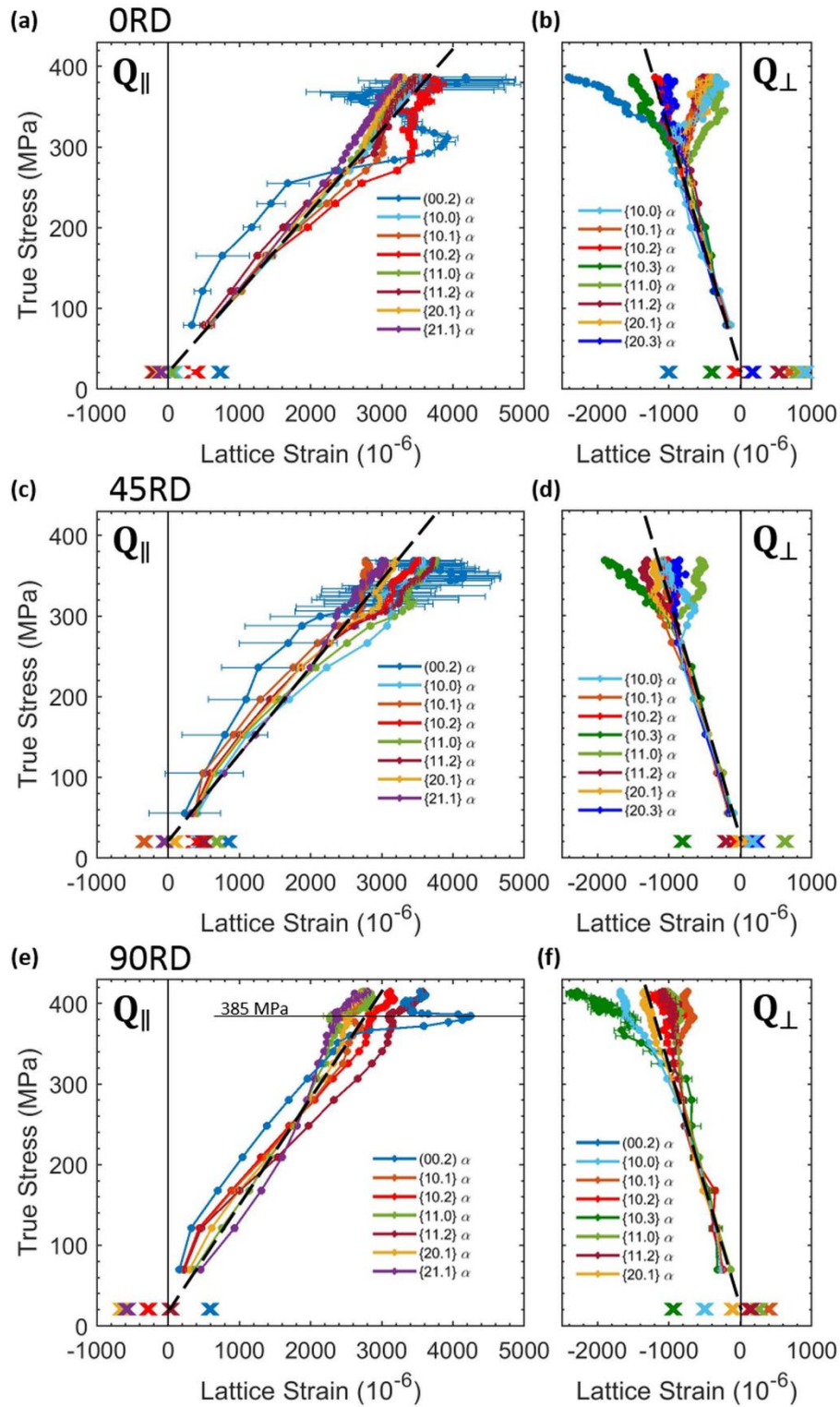
Figure 6-7 Lattice strain evolution versus applied stress for (a,b) 0RD, (c,d) 45RD, and (e,f) 90RD samples. Axial (Q$_\parallel$) and radial (Q$_\perp$) α grain families are shown on the right and left, respectively. The unload of the lattice strain is linear for all grain families and is not shown for clarity. The residual lattice strains after unload are marked by "x".
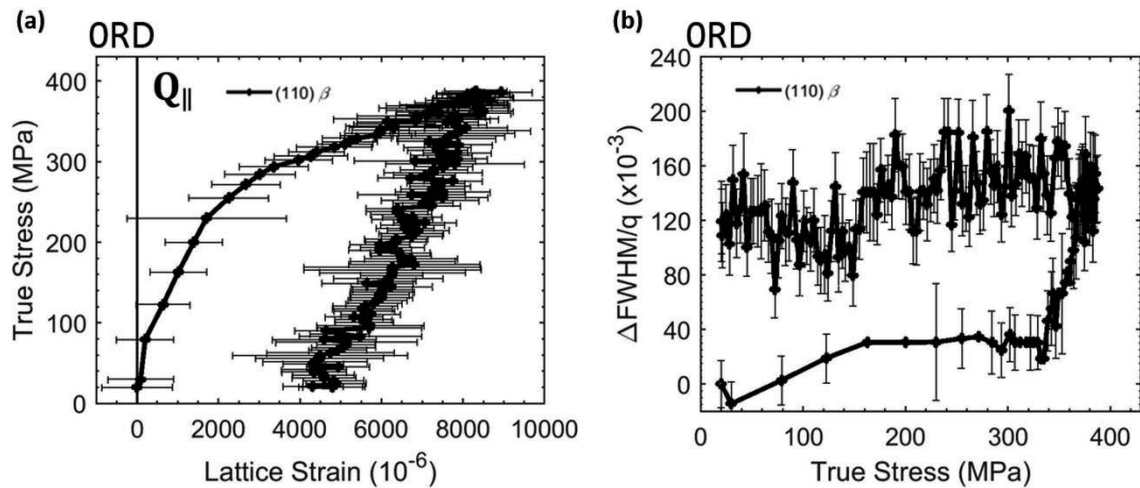
Figure 6-8 Peak behavior of the $(110)_{\parallel}$ β grain family in one of the 0RD samples: (a) lattice strain evolution and (b) peak broadening versus applied stress.

The evolution of the axial ($Q_{\parallel}$) and radial ($Q_{\perp}$) α elastic lattice strains during the first load-unload cycle (to 3.5% strain) is shown in Figure 6-7 as a function of the applied stress. The residual lattice strains after unloading are marked by "x". The initial lattice strain (at 20 MPa) of each grain family is not shown for clarity. For each grain family, a linear curve was fitted to the points in the elastic regime (under 180 MPa) and the lattice strains are shifted such that the fit passes through the initial point (20 MPa). A small but non-zero $(110)_{\parallel}$ β peak was observed in all samples. The lattice strain evolution and peak broadening of the $(110)_{\parallel}$ β grain family of the 0RD sample is shown separately in Figure 6-8 for clarity. The behavior of the $(110)_{\parallel}$ β peaks was consistent for all loading directions.

Each axial α grain family ($Q_{\parallel}$) consists of grains which all share the same orientation of the c-axis to the loading direction. Thus, the Schmid Factors (SFs) of the deformation mechanisms are the same for all of these grains. Conversely, each radial α grain family ($Q_{\perp}$) potentially consists of a wide range of grain orientations, i.e. contain plastically "soft" and "hard" grains. Therefore, the focus will primarily be on the lattice strain behavior of the axial grain families.
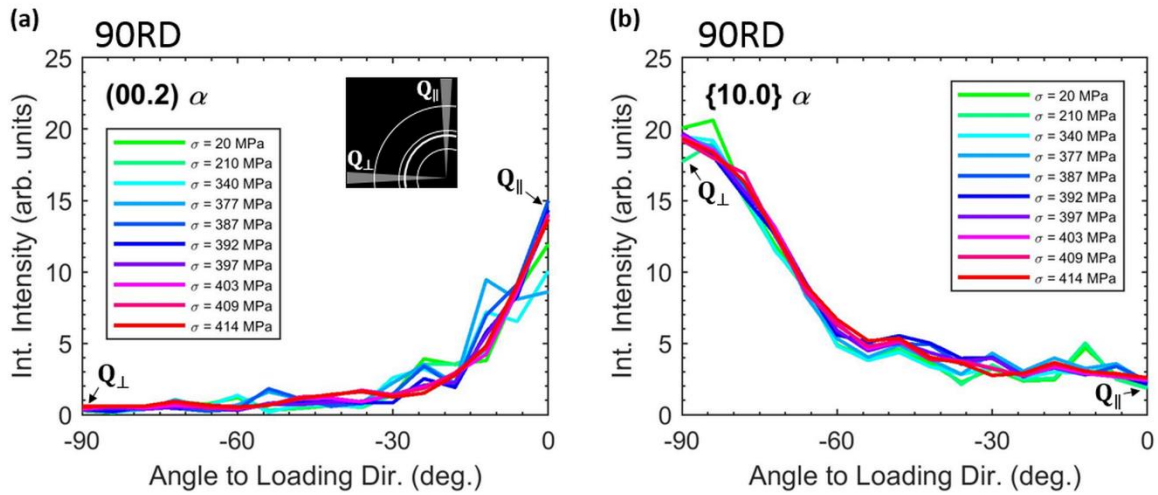
Figure 6-9 Radially integrated intensities of the (a) (00.2) α and (b) $\{10.0\}$ α grain families over the entire detector image. Radial bins are made in ±3° increments, e.g. shown schematically for $\mathbf{Q}_{\parallel}$ and $\mathbf{Q}_{\perp}$ in the inset in (a).

The radially integrated intensities of the (00.2) and $\{10.0\}$ peaks during loading are shown in Figure 6-9a and b, respectively. Radial bins are performed in ±3° increments as shown in the inset in Figure 6-9a, i.e. the intensity at -30° to the loading direction is radially integrated from -27° to -33°. The intensities of the (00.2) and $\{10.0\}$ grain families stay constant during loading suggesting that extension twinning does not play a significant role during deformation. This confirms the findings of the quasi-*in situ* EBSD. The following can be deduced from the behavior of the peaks during the first loading cycle:

The elastic behavior (<150 MPa) of the axial grains depends on the grain family, suggesting that this material is elastically anisotropic. Grain orientations with the *c*-axis aligned along the loading direction behave elastically stiffer. This is consistent with the behavior of single crystal Ti, which has elastic lattice constants $E_{(2\bar{1}\bar{1}0)} = E_{(01\bar{1}0)} = 104$ MPa and $E_{(0001)} = 146.2$ MPa [270]. The elastic anisotropy appears to increase at higher angles to the rolling direction (Figure 6-7).

For the 0RD samples (Figure 6-7a and b), the $\{21.1\}_{\parallel}$ α grain family sheds load around 150 MPa, implying that it plastifies well below the macroscopic yield stress. This can be explained by the activation of $Pri\langle a\rangle$ slip, with the lowest-CRSS mechanism, as this grain family has the highest SF among the measured grain families (Figure 6-2). There are only a small percentage of grains in this orientation, so the onset of microplasticity does not result in macroscopic yield. Instead, load is transferred to the plastically hard grain families: $(00.2)_{\parallel}$ α, $\{11.2\}_{\parallel}$ α, $\{10.1\}_{\parallel}$ α, and $\{10.2\}_{\parallel}$ α. The $\{20.1\}_{\parallel}$ α, $\{11.0\}_{\parallel}$ α, and $\{10.0\}_{\parallel}$ α shed load next, which can also be explained by the activation of $Pri\langle a\rangle$ slip. Due to the rolling texture, there are a large number of $\{11.0\}_{\parallel}$ α and $\{10.0\}_{\parallel}$ α grains (Figure 6-1a) and the initiation of plasticity results in macroscopic yield. The soft grain families continue to take load after yield.

At around 290 MPa, the $\{10.2\}_{\parallel}$ α, $\{10.1\}_{\parallel}$ α, and $\{11.2\}_{\parallel}$ α families shed load. The slope of the elastic lattice strain evolution for the $\{10.2\}_{\parallel}$ α and $\{10.1\}_{\parallel}$ α grain families becomes nearly vertical, implying that they behave nearly perfect plastic upon yielding. The load is redistributed back to the softer grain families and the $(00.2)_{\parallel}$ α grains. SF analysis suggests that this is due to the initiation of $Ba\langle a\rangle$ slip in the $\{10.2\}_{\parallel}$ α and $\{11.2\}_{\parallel}$ α grain families. On the other hand, plasticity in the $\{10.1\}_{\parallel}$ α grains more likely initiates due to $Pri\langle a\rangle$ or $Pyr\langle a\rangle$ slip as the CRSS for $Ba\langle a\rangle$ slip is relatively high compared to the other two modes (see

Table 6-1). The higher CRSS for $Pyr\langle a\rangle$ slip is (1.2-1.8× higher than $Pri\langle a\rangle$ slip) is offset by the 1.4× higher SF for $Pyr\langle a\rangle$ slip of the $\{10.1\}_{\parallel}$ α grain family.

At 310 MPa, the $(00.2)_{\parallel}$ α grain family begins to shed load due to the activation of $\langle c+a\rangle$ slip. At this point, all other grain families are taking load again. The elastic lattice strains in the $(00.2)_{\parallel}$ α family decrease, implying that the average stress on the grains must be decreasing. Since twinning only plays a small role in the deformation, the decrease must be related to instable plastic flow. However, as these grains are a minority due to the rolling texture, the lattice strain relaxation is not observed in the macroscopic mechanical response.

For the 45RD samples, the $\{21.1\}_{\parallel}$ α grain family behaves plastically soft, deforming well below macroplastic yield. Load is then redistributed to all of the other grain families as there is no strong texture along the loading axis. With the exception of the $(00.2)_{\parallel}$ α, all of the other grain families noticeably shed load at around 300 MPa, suggesting that plasticity initiates nearly simultaneously in many of the grains. All measured grain families behave nearly perfect plastic. This behavior explains the low plastic work hardening rate observed in Figure 6-3b. At around 335 MPa, the elastic lattice strains of the $(00.2)_{\parallel}$ α grain family suddenly drop. As in the 0RD sample, there is only a small percentage of grains in this orientation and the effect is not observed in the macroscopic response.

For the 90RD samples, the relative behavior of the grain families is similar to the 0RD samples. The plastically soft grain families ($\{21.1\}_{\parallel}$ α, $\{20.1\}_{\parallel}$ α, and $\{11.0\}_{\parallel}$ α) shed load early and the load is redistributed among the harder orientations. The $\{10.2\}_{\parallel}$ α, $\{10.1\}_{\parallel}$ α, and $\{11.2\}_{\parallel}$ α grain families behave nearly perfect plastic upon yield, and load is taken strongly by the $(00.2)_{\parallel}$ α grains. At this point, all of the measured grain families appear to be plastifying except the $(00.2)_{\parallel}$ α. Due to the rolling texture, there is a much larger percentage of plastically hard grain orientations in the 90RD samples, resulting in the highest yield stress. Between 380-390 MPa, the elastic lattice strains of the $(00.2)_{\parallel}$ α grain family drop sharply as the family plastifies. Load is redistributed to all of the other grain families. This stress range corresponds to the work hardening plateau highlighted in Figure 6-3b, where the plastic work hardening rate is lower than the other two directions. After 390 MPa, the $(00.2)_{\parallel}$ α grain family begins to take load again, implying that the grains have hardened.

For all loading directions, a small but non-zero $(110)_{\parallel}$ β peak is observed. This grain family takes load strongly, accompanied by a large peak broadening (Figure 6-8). The large, continuous increase in lattice strain of the (110) β peak implies that the retained β grains do not plastify, even though the β phase is typically softer than the α phase due to its BCC structure. This can be explained by a Hall-Petch hardening effect as the average β grain size is over an order of magnitude smaller than the α grains. Therefore, the large peak broadening is suspected to be a result of inhomogeneous stresses within the grain family, i.e. different β grains reaching different strains due to local stress variations. The same explanation was previously used to describe the similar peak behavior of small, hard cementite particles in a bainitic steel [249]. However, the fraction of β phase was measured by EBSD to be below 0.2%, so it is not expected to play a major role in the deformation.

The effect of the texture differences between 0RD, 45RD, and 90RD can be seen in the evolution of the radial $\{10.0\}_{\perp}$ α elastic lattice strains. The diffraction signal is integrated over a range of grain orientations with *c*-axis between 0° and 90° to the loading axis. Due to the rolling texture, the proportion of grains in each orientation is different with respect to the loading axis. In the 0RD samples (Figure 6-7b), the

majority of the $\{10.0\}_{\perp}$ α grains are perpendicular to the loading axis and have a soft orientation with SF > 0.37 for low-CRSS $Pri\langle a \rangle$ and $Pyr\langle a \rangle$ slip. The grain family sheds load strongly. In the 90RD samples (Figure 6-7f), the majority of the grains have their c-axis nearly parallel to the loading direction, a hard orientation which deforms by high-CRSS $\langle c + a \rangle$ slip. Consequently, the grain family behaves plastically hard and takes load. At 380 MPa, the $\{10.0\}_{\perp}$ α also sheds load along with the $(00.2)_{\parallel}$ α grain family. The 45RD samples (Figure 6-7d) are in between the other two loading directions.

Peak profile evolution during tensile loading
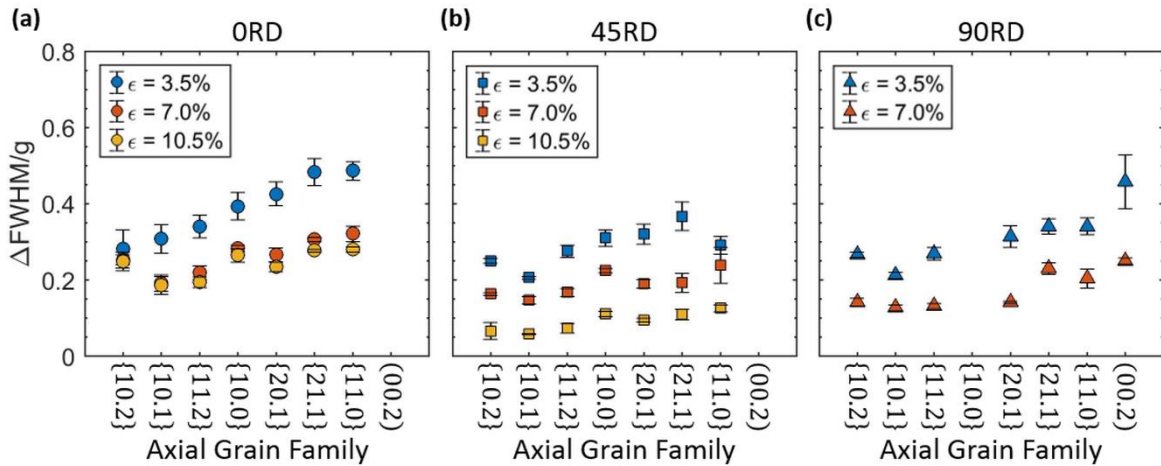
Figure 6-10 Average magnitude of ΔFWHM/g when fully loaded for the (a) 0RD, (b) 45RD, and (c) 90RD samples. The peaks are arranged by increasing peak broadening during the first load of the 0RD sample.

The average magnitude of the peak broadening during each loading step is shown for the three loading directions in Figure 6-10. The values are normalized to $g = 1/d_{hk.l}$ to remove the broadening contribution due to the peak d-spacing. The $(00.2)_{\parallel}$ α grain family for the 0RD and 45RD samples and the $\{10.0\}_{\parallel}$ α grain family for the 90RD sample are not shown due to low grain statistics. The peak broadening progressively decreases for each subsequent 3.5% strain increment for all loading directions. However, the 0RD samples exhibit consistently higher peak broadening for a given grain family than the other loading directions.
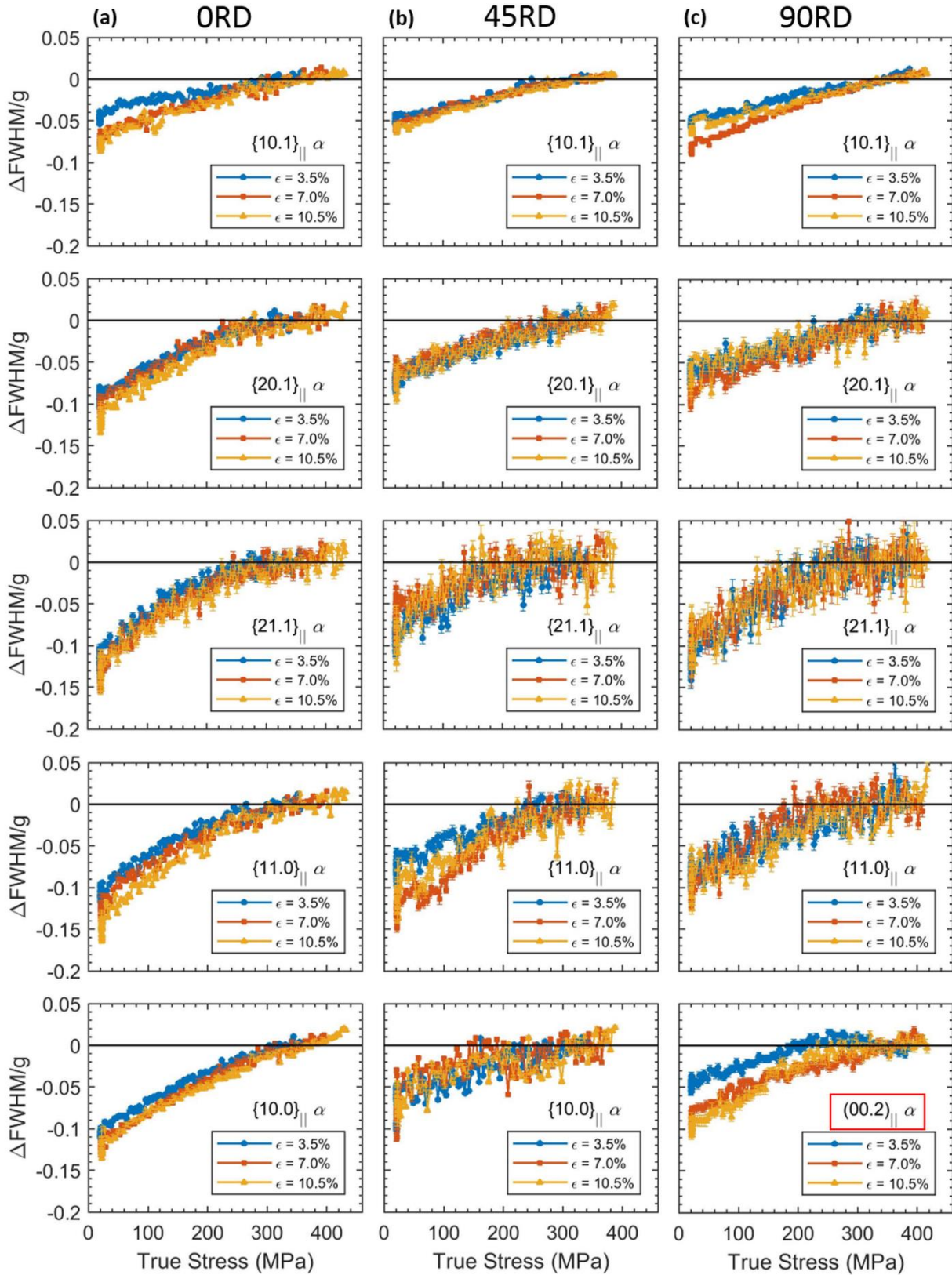
Figure 6-11 ΔFWHM/g of (a) 0RD, (b) 45RD, and (c) 90RD sample during each unload. The change in peak width is normalized to the average value of the measurements above 300 MPa. The $(00.2)_{\parallel} \alpha$ is shown for 90RD, highlighted in red, instead of the $\{10.0\}_{\parallel} \alpha$ due to grain statistics.

The change in peak width of several α grain families during the unloads is shown in Figure 6-11. The curves have been normalized to the average of the points above 300 MPa. The $\{10.0\}_\parallel \alpha$ grain family is shown for 0RD and 45RD while the $(00.2)_\parallel \alpha$ family is shown for 90RD due to grain statistics. The magnitude of ΔFWHM/g is directly comparable for a given grain family between different loading directions. However, comparing peak broadening between different grain families is less trivial. FWHM is directly related to the square root of the contrast factor $\sqrt{C_{hk.l}}$ and a function f_m which depend on the relative activity and arrangement of different slip mechanisms in a given grain family for HCP materials [155]. Thus, only the relative trends of the peak broadening are considered when comparing between different grain families.

The peak width decrease is non-linear for all grain families. The decrease in FWHM changes noticeably between 250 and 300 MPa, the same stress range where the macroscopic unload begins to deviate noticeably from the elastic component of the unload (Figure 6-3d). After each unload, the samples were held constant at 20 MPa for 5 minutes. The peak width continues to decrease during the hold.

6.4   Discussion

6.4.1   Three-stage Work Hardening

A work hardening plateau is observed during loading along 90RD (Figure 6-3b). This behavior is often described during compression for CP-Ti [89–93] and other HCP materials [262–265] as the result of $\{10.2\}\langle10.1\rangle$ extension twinning and the subsequent hardening in which dislocation glide is hindered by the new twin boundaries. More recently, the three-stage work hardening has been reported for tensile tests in CP-Ti [86–88]. Becker et al. [87] reported that the three stages correspond to easy dislocation slip, the activation of $\{11.2\}\langle\overline{11}.3\rangle$ compression twinning, and the saturation of this twinning system and subsequent activation of $\{10.2\}\langle10.1\rangle$ extension twinning. On the other hand, both Roth et al. [86] and Amouzou et al. [88] observed almost no twinning (<0.5% and 5.7% vol. fraction for rolling direction and transverse direction samples, respectively) and thus proposed that the work hardening plateau is the result of multi-slip work hardening after an initial period of easy single glide.

The small fraction of twinning observed for the samples in this study supports the idea that the three-stage work hardening is predominantly governed by dislocation-based mechanisms. A minimum is observed in the plastic work hardening rate of the 90RD samples at around $\varepsilon_\mathrm{p} = 0.0099$ (an applied stress of 386 MPa). This corresponds to a sudden lattice strain relaxation in the $(00.2)_\parallel \alpha$ grain family that can be rationalized by the activation and rapid multiplication of $Pyr^{1st}\langle c + a \rangle$ slip. In fact, this behavior is observed for all loading directions but only noticeably affects the macroscopic response of the 90RD sample due to the large percentage of $(00.2)_\parallel \alpha$ grains. As the $(00.2)_\parallel \alpha$ grain family plastifies, load is redistributed to the other grain families. These observations are supported by the EVPSC model of Richeton et al. [103], which predicts that the low initial work hardening rate can be explained by a reduction in intergranular stresses and the fast multiplication of mobile $Pyr^{1st}\langle c + a \rangle$ dislocations. The easy generation and glide of dislocations in the $(00.2)_\parallel \alpha$ grains is rapidly exhausted and the grains begin to harden. The plastic work hardening rate increases. Once the $(00.2)_\parallel \alpha$ grains harden sufficiently they again behave plastically hard. Plastic flow increases in the other grain families and the work hardening rate begins to decrease in parallel with the 0RD and 45RD samples.

The elastic lattice strain drop of the $(00.2)_\parallel \alpha$ grain family also gives direct evidence that the grain-resolved stress along the loading direction decreases in grains during continuous loading. This was recently

reported for the first time in CP Ti by Abdolvand et al. [22], who observed the phenomenon in several grains with 3D-XRD. They also performed crystal plasticity finite element simulations which suggest that the stress drop is largest in plastically hard grains surrounded by hard grain neighbours. This is consistent with the much quicker lattice strain relaxation observed in the 90RD samples, as this type of hard grain "cluster" should be more prevalent due to the rolling texture. However, the presence of the lattice strain drop in all samples suggests that this effect is active regardless of loading direction.

6.4.2   Non-Linear Anelastic Strain Recovery

A non-linear springback is observed during unloading for all loading directions. Khayatzadeh et al. [8,94] previously described the springback in the same material as the cumulative effect of three components: the elastic recovery, a degradation in the elastic modulus, and an anelastic strain recovery. No degradation in the elastic modulus was observed in our results, although the initial springback behavior was likely affected by the slow reversal of the machine crosshead. However, an anelastic strain recovery was observed to occur for all loading directions. Consistent with the findings of Khayatzadeh et al., the anelastic strain recovery is larger along 0RD than in 45RD and 90RD and appears to stay constant regardless of pre-strain (Figure 6-4).

The unloading can be explained in terms of the competition between external applied forces and internal repulsive inter- and intragranular forces. As the applied stress is decreased, mobile dislocations begin to move backward. Backstresses from dislocation pile-ups accumulated at barriers act as the driving force. The FWHM begins to decrease, suggesting that dislocations are either annihilating or rearranging to reduce the strain. Between 250 and 300 MPa (depending on the grain family), the peak width for all grain families starts to decrease more quickly. Consequently, the anelastic strain recovery begins to increase exponentially. Cleveland and Ghosh [254] describe this regime as the release of dislocations that were initially pinned in the forward direction. As the forward applied stress is reduced, progressively more dislocations reach the critical stress for backwards motion. A higher number of dislocations increases the likelihood of annihilation events, resulting in the exponential decrease in FWHM. The presence of strong backstresses is confirmed by the continued decrease in FWHM even as the sample is held constant in the "unloaded" state (20 MPa).

The observed springback anisotropy implies that the internal stress does not develop equally along the different loading directions. A couple of observations from the *in situ* XRD results support this idea. Firstly, each 3.5% strain increment results in higher peak broadening in the 0RD samples than in the 45RD and 90RD samples. The similar behavior of the 45RD and 90RD samples suggest that this is not simply an effect of the macroscopic texture. Secondly, the elastic lattice strains after the first loading-unloading cycle show that the residual stress state varies with loading direction. In the 0RD sample, the majority of grains lie with their c-axis oriented near perpendicular to the loading direction. The behavior of the $\{10.0\}_{\parallel} \alpha$, $\{11.0\}_{\parallel} \alpha$, and $\{21.1\}_{\parallel} \alpha$ grain families suggest that these grains will end with approximately no residual stress. By parallel logic, the behavior of the $(00.2)_{\parallel} \alpha$ grain family suggest that majority of grains in the 90RD sample will end up with a tensile residual stress along the loading direction. These effects are indicative of an anisotropic plastic behavior during unloading. However, the further interpretation of this data requires the use of crystal plasticity simulations.

6.5   Conclusion

The deformation behavior of cold rolled CP Ti sheet was examined by *in situ* XRD, quasi-*in situ* EBSD, and HRDIC. The material exhibits a three-stage work hardening during tensile loading despite the lack of

significant twin activity. The work hardening plateau is shown to be the result of the sudden activation and multiplication of $\langle c + a \rangle$ slip in plastically hard grains which results in redistribution of load among other grain families. A non-linear anelastic springback is observed during unloading that can be attributed to the annihilation/rearrangement of dislocations. XRD measurements imply the development of higher internal stresses during loading in the rolling direction, resulting in a significant springback anisotropy. These findings can be used to significantly improve crystal plasticity simulations for the prediction of tensile deformation and springback behavior in Ti.

6.6 Acknowledgements

Chapter 7   Conclusions

7.1   Achieved results

In this thesis, various *in situ* mechanical testing techniques were harnessed to address specific plastic deformation behaviors in polycrystalline Mg and Ti alloys. The main conclusions, presented in detail in each chapter, are summarized below:

Mg AZ31B

The plastic behavior of cold-rolled Mg AZ31B alloy under tensile multiaxial loading and strain path changes was examined with *in situ* neutron diffraction, acoustic emission, and EBSD. The evolution of the elastic lattice strains shows that the plastic response depends strongly on the rolling texture and loading mode. During uniaxial loading, the initial deformation is dominated by basal $\langle a \rangle$ slip and $\{10\bar{1}2\}$-type extension twinning, with an increasing role of non-basal slip as the deformation proceeds. This is consistent with literature on the deformation mechanisms of Mg alloys. Multiaxial tensile loading, on the other hand, exhibits very little twinning, implying that the deformation is instead dominated by basal $\langle a \rangle$ and $\langle c + a \rangle$ slip on 2nd order pyramidal planes.

Strain path change experiments were also performed which show that the plastic response depends strongly on the loading history of the material. A uniaxial prestrain results in 1) the hardening of soft grain families by dislocation slip and 2) a texture change due to grain rotation by twinning. The prestrain either beneficially or adversely affects the plastic response depending on the angle of the strain during reloading. For a strain path change angle greater than 170 degrees, the plastic response is softened. Tensile twins formed during the prestrain can either detwin or form secondary tensile twins, two low-CRSS deformation mechanisms which accomodate strain without increasing the dislocation density. Primary extension twinning and the backwards motion of dislocations due to the nearly reversed strain direction provide other easy sources of strain accomodation. By contrast, a strain path change angle less than 135 degrees results in a hardened plastic response. The tensile twins formed during the prestrain act as high-angle barriers to dislocation slip. The absence of significant primary extension twinning results in increased slip activity which is hindered by dislocation networks built up during prestrain. The results of the study can be used to validate crystal plasticity models of deformation in this alloy.

Chapter 4 also presents a method for interpreting diffraction data in samples under multiaxial stress, the Normalized Resolved Shear Stress. This extends the idea of Schmid's Law to systems under multiaxial stresses, and can take into account both tensile-tensile and tensile-compressive stress states.

Ti-6Al-4V

The high work-hardening behavior of a Ti-6Al-4V alloy produced by electron-beam melting and a novel post-treatment was examined with *in situ* x-ray diffraction and high resolution digital image correlation. The high-energy diffraction results revealed the presence of a third phase in the material, which was previously believed to have a dual-phase $\alpha + \alpha'$ microstructure. The high work hardening is found to be the result of load-sharing between the three phases. The α' martensite, traditionally regarded as a strong, brittle phase, behaves plastically soft and plastifies well below macroplastic yield. The third phase behaves mechanically hard, taking load throughout the entire deformation. The presence of an additional hard phase allows the α and α' phases to deform to higher strains than they would reach in a traditional dual-phase system.

Unfortunately, due to the similar crystallographic structure and location within the martensite, the third phase could not be uniquely identified using the techniques presented in Chapter 5. Its location among the α' martensite suggests that it could be orthorhombic (OR) α'' martensite. Selected area electron diffraction of several small laths within the martensite regions shows strong indexing confidence (3% error) when fitting with the OR parameters calculated from the XRD peaks. However, α'' is traditionally reported to be a soft phase. The hard mechanical behavior suggests that it could be an HCP phase, such as a secondary α phase, which behaves plastically hard due to the small lath size. However, there is no clear explanation in existing literature for how this phase could have formed. The identification of this third phase and its volume fraction should be the primary focus of further research into this material.

Commercial purity Grade 2 Ti

The work hardening and springback behavior of a cold-rolled commercially pure Ti sheet was investigated with *in situ* x-ray diffraction and quasi-*in situ* EBSD. The evolution of the elastic lattice strains shows that the cold-rolling texture has a strong effect on the plastic behavior during tensile loading. Along the rolling direction, a large percentage of grains are well-oriented for low-CRSS prismatic $\langle a \rangle$ slip result in plasticity in many grains at low applied stresses. The rolling direction samples consistently have a lower yield stress and higher work hardening as a result. By contrast, there are a large percentage of grains with their *c*-axis oriented along the transverse direction (90 degrees to the rolling direction). These grains have very low SFs for all $\langle a \rangle$-type slip mechanisms, instead deforming preferentially by high-CRSS $\langle c + a \rangle$ slip. This results in a high yield stress and low work hardening during tensile loading.

A plastic work hardening rate plateau is observed for samples loaded in the transverse direction shortly after yield. The elastic lattice strain evolution provides direct evidence that this is the result of a sudden load-shedding in the hard grain orientations as they begin to plastify. The redistribution of load to hardened grain families results in a brief period of increased plastic work hardening. Twinning was not found to play a signifcant role in the deformation. The diffraction results show that this phenomenon is active during loading in all directions, but is only observed in the macroscopic mechanical response of the transverse direction because of the large percentage of these hard grains. The EBSD results confirm that very little twinning is observed during deformation up to strains greater than 7%.

A permanent, non-linear strain recovery, "springback", was observed during unloading. Diffraction peak profile analysis suggests that the anelastic springback behavior during unloading is the effect of backwards motion of dislocations due to backstresses in the materials. Dislocations annihilate or rearrange, resulting in a permanent strain recovery. The anelastic springback is consistently higher along the rolling direction, and rolling direction samples consistently show higher peak broadening for all grain families for the same amount of strain. It is anticipated that the results of these experiments could be used to improve crystal plasticity models for predicting plasticity and springback in Ti.

Composite cruciform design for multiaxial loading

A novel bottom-up approach to cruciform design was proposed in Chapter 3 in which a flat cruciform is reinforced with a mechanically dissimilar material. This technique allows for a reduced gauge section without introducing mechanical damage, e.g. by machining the test section. The technique was able to effectively increase the plastic strain at the center of an Al cruciform under uniaxial and equibiaxial loading. A parametric study of theoretical reinforcement materials indicates that the ideal reinforcement material is stronger than the base material and has a high work hardening. The work hardening of the reinforcement is more important

than its elastic modulus or yield strength. This technique can be applied to any cruciform shape or base material.

7.2   Future development

The Mg and Ti alloys explored in this thesis are widely used for structural components in the transportation and biomedical industries. Thus, the proper understanding of their plastic behavior is of practical importance for improving manufacturing procedures. The results also link the mechanical behavior to specific microstructural properties that can guide the development of new alloys or techniques. Further experiments that could improve the interpretation of the results presented in this thesis are discussed below with respect to each material.

Mg AZ31B

- Crystal plasticity finite-element (CPFE) modelling: To fully interpret the *in situ* mechanical tets, the neutron diffraction results should be modeled within a crystal plasticity framework. NRSS analysis only provides an initial interpretation of the behavior at the beginning of plasticity. Additionally, the diffraction signal is integrated over the coherent scattering volume of entire grain families, so information at a single grain level is lost. The CPFE method can be used to gain information about mechanical phenomena at a grain level, including local stress inhomogeneity, lattice rotations, and shape changes [1]. One should keep in mind that the models should be validated against experimental data, as improper constitutive modelling inputs can lead to inaccurate conclusions.

- Triangulated acoustic emission (AE): Repeating the strain paths with triangulated AE could provide additional information about the dynamics of active deformation processes in the gauge section of the cruciform samples. AE was performed for all of the *in situ* experiments reported in Chapter 4 but using a single sensor, so the signal was convoluted with the plasticity from the intersection of the arms. Adaptive sequential k-means analysis of AE can identify twinning mechanisms and distinguish between different types of dislocation slip events.

Ti-6Al-4V

- Identification of the third phase: The primary focus of further research on this material should be identifying the third phase. Atom probe tomography (APT) could potentially identify small differences in solute distribution within the martensite regions that could not be captured by the transmission kikuchi diffraction. For example, recent APT observations of in SLM-printed Ti-6Al-4V by Haubrich et al. [271] was able to identify phases and chemical compositions at the nanometer scale.

- Expanding the applications of the post-treatment: It would be interesting to see if the post-treatment procedure could be applied to other additive manufacturing techniques, such as selective laser melting. The current post-treatment also limits two of the dimensions of the final part to below 15 mm, which severely limits the applications of the material. It would be of practical use to determine if the post-treatment process could be scaled up and what the ultimate size limits would be for homogeneous quenching of the material.

- Additional heat treatments: There is significant interest in creating multi-phase, multi-scale microstructures to enhance the mechanical properties of this alloy. Traditionally, additional heat

treatments are applied to decompose the metastable martensite into β and a secondary α phase with a smaller grain size than the primary α lamellae. The *in situ* mechanical test techniques applied in this study could further elucidate the role of microstructure in determining macroscopic mechanical properties of this alloy.

Commercial Purity Grade 2 Ti

- Dislocation density-based CPFE modelling for springback: The premise that the anelastic springback is a result of dislocation annihilation should be examined with CPFE modelling. Constitutive models have been developed for various materials that capture dislocation generation, motion, and annihilation [272–274]. Such models could be useful for interpreting the peak broadening behavior observed with *in situ* x-ray diffraction.

- *In situ* mechanical tests at elevated temperatures: It has been shown that springback in CP Ti is reduced during deformation at elevated temperatures [275]. High temperatures are known to enhance dislocation mobility. By examining the influence of temperature on deformation behavior, one could further understand the deformation mechanisms responsible for springback.

- *In situ* strain path change tests: As was shown with the Mg AZ31B, the relative activity of different deformation mechanisms in HCP metals varies with loading direction. Different prestrains could be used to activate different dislocation mechanisms and change the initial dislocation structure. The influence of different types of prestrain on springback could provide additional information on dislocation-dislocation interactions during unloading.

References

[1] F. Roters, P. Eisenlohr, L. Hantcherli, D.D. Tjahjanto, T.R. Bieler, D. Raabe, Overview of constitutive laws, kinematics, homogenization and multiscale methods in crystal plasticity finite-element modeling: Theory, experiments, applications, Acta Materialia. 58 (2010) 1152–1211. doi:10.1016/j.actamat.2009.10.058.

[2] K. Máthis, G. Csiszár, J. Čapek, J. Gubicza, B. Clausen, P. Lukáš, A. Vinogradov, S.R. Agnew, Effect of the loading mode on the evolution of the deformation mechanisms in randomly textured magnesium polycrystals – Comparison of experimental and modeling results, International Journal of Plasticity. 72 (2015) 127–150. doi:10.1016/j.ijplas.2015.05.009.

[3] J. Čapek, K. Máthis, B. Clausen, J. Stráská, P. Beran, P. Lukáš, Study of the loading mode dependence of the twinning in random textured cast magnesium by acoustic emission and neutron diffraction methods, Materials Science and Engineering: A. 602 (2014) 25–32. doi:10.1016/j.msea.2014.02.051.

[4] K. Sofinowski, T. Panzner, M. Kubenova, J. Čapek, S. Van Petegem, H. Van Swygenhoven, In situ tension-tension strain path changes of cold-rolled Mg AZ31B, Acta Materialia. 164 (2019) 135–152. doi:10.1016/j.actamat.2018.10.033.

[5] T. Hama, Y. Tanaka, M. Uratani, H. Takuda, Deformation behavior upon two-step loading in a magnesium alloy sheet, International Journal of Plasticity. 82 (2016) 283–304. doi:10.1016/j.ijplas.2016.03.009.

[6] C. Ma, A. Chapuis, X. Guo, L. Zhao, P. Wu, Q. Liu, X. Mao, Modeling the deformation behavior of a rolled Mg alloy with the EVPSC-TDT model, Materials Science and Engineering: A. 682 (2017) 332–340. doi:10.1016/j.msea.2016.11.027.

[7] L. Zhao, A. Chapuis, Y. Xin, Q. Liu, VPSC-TDT modeling and texture characterization of the deformation of a Mg-3Al-1Zn plate, Journal of Alloys and Compounds. 710 (2017) 159–165. doi:10.1016/j.jallcom.2017.03.243.

[8] S. Khayatzadeh, M.J. Thomas, Y. Millet, S. Rahimi, Characterisation and modelling of in-plane springback in a commercially pure titanium (CP-Ti), J Mater Sci. 53 (2018) 6872–6892. doi:10.1007/s10853-017-1983-8.

[9] T. Hama, T. Sakai, Y.P. Korkolis, H. Takuda, Crystal-plasticity finite-element simulation of time-dependent springback in a commercially-pure titanium sheet, J. Phys.: Conf. Ser. 1063 (2018) 012122. doi:10.1088/1742-6596/1063/1/012122.

[10] A.M. Minor, G. Dehm, Advances in in situ nanomechanical testing, MRS Bulletin. 44 (2019) 438–442. doi:10.1557/mrs.2019.127.

[11] S. Van Petegem, J. Wagner, T. Panzner, M.V. Upadhyay, T.T.T. Trang, H. Van Swygenhoven, In-situ neutron diffraction during biaxial deformation, Acta Materialia. 105 (2016) 404–416. doi:10.1016/j.actamat.2015.12.015.

[12] H. Van Swygenhoven, S. Van Petegem, In-situ mechanical testing during X-ray diffraction, Materials Characterization. 78 (2013) 47–59. doi:10.1016/j.matchar.2012.12.010.

[13] D. Yan, C.C. Tasan, D. Raabe, High resolution in situ mapping of microstrain and microstructure evolution reveals damage resistance criteria in dual phase steels, Acta Materialia. 96 (2015) 399–409. doi:10.1016/j.actamat.2015.05.038.

[14] F. Di Gioacchino, J. Quinta da Fonseca, Plastic Strain Mapping with Sub-micron Resolution Using Digital Image Correlation, Exp Mech. 53 (2013) 743–754. doi:10.1007/s11340-012-9685-2.

[15] W.-N. Hsu, E. Polatidis, M. Šmíd, N. Casati, S. Van Petegem, H. Van Swygenhoven, Load path change on superelastic NiTi alloys: In situ synchrotron XRD and SEM DIC, Acta Materialia. 144 (2018) 874–883. doi:10.1016/j.actamat.2017.11.035.

[16] A. Ghaderi, M.R. Barnett, Sensitivity of deformation twinning to grain size in titanium and magnesium, Acta Materialia. 59 (2011) 7824–7839. doi:10.1016/j.actamat.2011.09.018.

[17] H. Fan, J.A. El-Awady, Molecular Dynamics Simulations of Orientation Effects During Tension, Compression, and Bending Deformations of Magnesium Nanocrystals, J. Appl. Mech. 82 (2015) 101006. doi:10.1115/1.4030930.

[18] W.Y. Wang, S.L. Shang, Y. Wang, Z.-G. Mei, K.A. Darling, L.J. Kecskes, S.N. Mathaudhu, X.D. Hui, Z.-K. Liu, Effects of Alloying Elements on Stacking Fault Energies and Electronic Structures of Binary Mg Alloys: A First-Principles Study, Materials Research Letters. 2 (2014) 29–36. doi:10.1080/21663831.2013.858085.

[19] P. Kwasniak, H. Garbacz, K.J. Kurzydlowski, Solid solution strengthening of hexagonal titanium alloys: Restoring forces and stacking faults calculated from first principles, Acta Materialia. 102 (2016) 304–314. doi:10.1016/j.actamat.2015.09.041.

[20] G.I. Taylor, Plastic Strain in Metals, Journal of the Institute of Metals. 62 (1938) 307–324.

[21] M.O. Pekguleryuz, 1 - Current developments in wrought magnesium alloys, in: C. Bettles, M. Barnett (Eds.), Advances in Wrought Magnesium Alloys, Woodhead Publishing, 2012: pp. 3–62. doi:10.1533/9780857093844.1.3.

[22] H. Abdolvand, J. Wright, A.J. Wilkinson, Strong grain neighbour effects in polycrystals, Nature Communications. 9 (2018) 171. doi:10.1038/s41467-017-02213-9.

[23] A. Akhtar, E. Teghtsoonian, Solid solution strengthening of magnesium single crystals—I alloying behaviour in basal slip, Acta Metallurgica. 17 (1969) 1339–1349. doi:10.1016/0001-6160(69)90151-5.

[24] A. Akhtar, E. Teghtsoonian, Solid solution strengthening of magnesium single crystals—ii the effect of solute on the ease of prismatic slip, Acta Metallurgica. 17 (1969) 1351–1356. doi:10.1016/0001-6160(69)90152-7.

[25] N. Stanford, M.R. Barnett, Solute strengthening of prismatic slip, basal slip and {101̄2} twinning in Mg and Mg–Zn binary alloys, International Journal of Plasticity. 47 (2013) 165–181. doi:10.1016/j.ijplas.2013.01.012.

[26] J.A. Yasi, L.G. Hector, D.R. Trinkle, Prediction of thermal cross-slip stress in magnesium alloys from direct first-principles data, Acta Materialia. 59 (2011) 5652–5660. doi:10.1016/j.actamat.2011.05.040.

[27] J.A. Yasi, L.G. Hector, D.R. Trinkle, Prediction of thermal cross-slip stress in magnesium alloys from a geometric interaction model, Acta Materialia. 60 (2012) 2350–2358. doi:10.1016/j.actamat.2012.01.004.

[28] J.S. Park, Y.W. Chang, The Effect of Alloying Elements on the c/a Ratio of Magnesium Binary Alloys, Advanced Materials Research. (2007). doi:10.4028/www.scientific.net/AMR.26-28.95.

[29] S.R. Agnew, Ö. Duygulu, Plastic anisotropy and the role of non-basal slip in magnesium alloy AZ31B, International Journal of Plasticity. 21 (2005) 1161–1193. doi:10.1016/j.ijplas.2004.05.018.

[30] S.R. Agnew, C.N. Tomé, D.W. Brown, T.M. Holden, S.C. Vogel, Study of slip mechanisms in a magnesium alloy by neutron diffraction and modeling, Scripta Materialia. 48 (2003) 1003–1008. doi:10.1016/S1359-6462(02)00591-2.

[31] A. Jain, S.R. Agnew, Modeling the temperature dependent effect of twinning on the behavior of magnesium alloy AZ31B sheet, Materials Science and Engineering: A. 462 (2007) 29–36. doi:10.1016/j.msea.2006.03.160.

[32] B. Clausen, C.N. Tomé, D.W. Brown, S.R. Agnew, Reorientation and stress relaxation due to twinning: Modeling and experimental characterization for Mg, Acta Materialia. 56 (2008) 2456–2468. doi:10.1016/j.actamat.2008.01.057.

[33] O. Muránsky, D.G. Carr, M.R. Barnett, E.C. Oliver, P. Šittner, Investigation of deformation mechanisms involved in the plasticity of AZ31 Mg alloy: In situ neutron diffraction and EPSC modelling, Materials Science and Engineering: A. 496 (2008) 14–24. doi:10.1016/j.msea.2008.07.031.

[34] G. Proust, C.N. Tomé, A. Jain, S.R. Agnew, Modeling the effect of twinning and detwinning during strain-path changes of magnesium alloy AZ31, International Journal of Plasticity. 25 (2009) 861–880. doi:10.1016/j.ijplas.2008.05.005.

[35] I. Chelladurai, D. Adams, D.T. Fullwood, M.P. Miles, S. Niezgoda, I.J. Beyerlein, M. Knezevic, Modeling of trans-grain twin transmission in AZ31 via a neighborhood-based viscoplastic self-consistent model, International Journal of Plasticity. (2018). doi:10.1016/j.ijplas.2018.03.012.

[36] D. Steglich, Y. Jeong, M.O. Andar, T. Kuwabara, Biaxial deformation behaviour of AZ31 magnesium alloy: Crystal-plasticity-based prediction and experimental validation, International Journal of Solids and Structures. 49 (2012) 3551–3561. doi:10.1016/j.ijsolstr.2012.06.017.

[37] H. Wang, P.D. Wu, C.N. Tomé, J. Wang, Study of lattice strains in magnesium alloy AZ31 based on a large strain elastic-viscoplastic self-consistent polycrystal model, International Journal of Solids and Structures. 49 (2012) 2155–2167. doi:10.1016/j.ijsolstr.2012.04.026.

[38] W. Wu, H. Qiao, K. An, X. Guo, P. Wu, P.K. Liaw, Investigation of deformation dynamics in a wrought magnesium alloy, International Journal of Plasticity. 62 (2014) 105–120. doi:10.1016/j.ijplas.2014.07.005.

[39] M. Zecevic, M. Knezevic, I.J. Beyerlein, C.N. Tomé, An elasto-plastic self-consistent model with hardening based on dislocation density, twinning and de-twinning: Application to strain path changes in HCP metals, Materials Science and Engineering: A. 638 (2015) 262–274. doi:10.1016/j.msea.2015.04.066.

[40] H. Wang, B. Clausen, L. Capolungo, I.J. Beyerlein, J. Wang, C.N. Tomé, Stress and strain relaxation in magnesium AZ31 rolled plate: In-situ neutron measurement and elastic viscoplastic polycrystal modeling, International Journal of Plasticity. 79 (2016) 275–292. doi:10.1016/j.ijplas.2015.07.004.

[41] par J.F. Stohr, J.P. Poirier, Etude en microscopie electronique du glissement pyramidal 1122 ⟨1123⟩ dans le magnesium, Philosophical Magazine. 25 (1972) 1313–1329. doi:10.1080/14786437208223856.

[42] S.R. Agnew, J.A. Horton, M.H. Yoo, Transmission electron microscopy investigation of ⟨c+a⟩ dislocations in Mg and α-solid solution Mg-Li alloys, Metall and Mat Trans A. 33 (2002) 851–858. doi:10.1007/s11661-002-0154-x.

[43] K. Máthis, K. Nyilas, A. Axt, I. Dragomir-Cernatescu, T. Ungár, P. Lukáč, The evolution of non-basal dislocations as a function of deformation temperature in pure magnesium determined by X-ray diffraction, Acta Materialia. 52 (2004) 2889–2894. doi:10.1016/j.actamat.2004.02.034.

[44] H. Zhang, G. Huang, J. Fan, H.J. Roven, B. Xu, H. Dong, Deep drawability and drawing behaviour of AZ31 alloy sheets with different initial texture, Journal of Alloys and Compounds. 615 (2014) 302–310. doi:10.1016/j.jallcom.2014.06.199.

[45] W. Wen, M. Borodachenkova, C.N. Tomé, G. Vincze, E.F. Rauch, F. Barlat, J.J. Grácio, Mechanical behavior of Mg subjected to strain path changes: Experiments and modeling, International Journal of Plasticity. 73 (2015) 171–183. doi:10.1016/j.ijplas.2014.10.009.

[46] A. Serra, D.J. Bacon, A new model for 1012 twin growth in hcp metals, Philosophical Magazine A. 73 (1996) 333–343. doi:10.1080/01418619608244386.

[47] A. Serra, D.J. Bacon, Computer simulation of twin boundaries in the h.c.p. metals, Philosophical Magazine A. 54 (1986) 793–804. doi:10.1080/01418618608244438.

[48] A. Serra, D.J. Bacon, R.C. Pond, Twins as barriers to basal slip in hexagonal-close-packed metals, Metall and Mat Trans A. 33 (2002) 809–812. doi:10.1007/s11661-002-0149-7.

[49] A. Serra, R.C. Pond, D.J. Bacon, Computer simulation of the structure and mobility of twinning disclocations in H.C.P. Metals, Acta Metallurgica et Materialia. 39 (1991) 1469–1480. doi:10.1016/0956-7151(91)90232-P.

[50] F. Wang, S.R. Agnew, Dislocation transmutation by tension twinning in magnesium alloy AZ31, International Journal of Plasticity. 81 (2016) 63–86. doi:10.1016/j.ijplas.2016.01.012.

[51] A.L. Oppedal, H. El Kadiri, C.N. Tomé, G.C. Kaschner, S.C. Vogel, J.C. Baird, M.F. Horstemeyer, Effect of dislocation transmutation on modeling hardening mechanisms by twinning in magnesium, International Journal of Plasticity. 30–31 (2012) 41–61. doi:10.1016/j.ijplas.2011.09.002.

[52] H. El Kadiri, A.L. Oppedal, A crystal plasticity theory for latent hardening by glide twinning through dislocation transmutation and twin accommodation effects, Journal of the Mechanics and Physics of Solids. 58 (2010) 613–624. doi:10.1016/j.jmps.2009.12.004.

[53] P. Chen, F. Wang, B. Li, Dislocation absorption and transmutation at {101$\bar{}$2} twin boundaries in deformation of magnesium, Acta Materialia. 164 (2019) 440–453. doi:10.1016/j.actamat.2018.10.064.

[54] M. Gong, G. Liu, J. Wang, L. Capolungo, C.N. Tomé, Atomistic simulations of interaction between basal dislocations and three-dimensional twins in magnesium, Acta Materialia. 155 (2018) 187–198. doi:10.1016/j.actamat.2018.05.066.

[55] H. Wang, P.D. Wu, J. Wang, C.N. Tomé, A crystal plasticity model for hexagonal close packed (HCP) crystals including twinning and de-twinning mechanisms, International Journal of Plasticity. 49 (2013) 36–52. doi:10.1016/j.ijplas.2013.02.016.

[56] H. Wang, P.D. Wu, C.N. Tomé, J. Wang, A constitutive model of twinning and detwinning for hexagonal close packed polycrystals, Materials Science and Engineering: A. 555 (2012) 93–98. doi:10.1016/j.msea.2012.06.038.

[57] H. Zhang, A. Jérusalem, E. Salvati, C. Papadaki, K.S. Fong, X. Song, A.M. Korsunsky, Multi-scale mechanisms of twinning-detwinning in magnesium alloy AZ31B simulated by crystal plasticity modeling and validated via in situ synchrotron XRD and in situ SEM-EBSD, International Journal of Plasticity. (2019). doi:10.1016/j.ijplas.2019.02.018.

[58] D.W. Brown, A. Jain, S.R. Agnew, B. Clausen, Twinning and Detwinning during Cyclic Deformation of Mg Alloy AZ31B, Materials Science Forum. 539–543 (2007) 3407–3413. doi:10.4028/www.scientific.net/MSF.539-543.3407.

[59] J. Čapek, K. Máthis, T. Krajšák, The Use of Acoustic Emission and Neutron Diffraction to Reveal the Active Deformation Mechanisms in Polycrystalline Magnesium and Comparison to Theoretical Modeling, in: A. Singh, K. Solanki, M. V.nuel, N.R. Neelameggham (Eds.), Magnesium Technology 2016, John Wiley & Sons, Inc., 2016: pp. 213–216. doi:10.1002/9781119274803.ch43.

[60] C.J. Geng, B.L. Wu, X.H. Du, Y.D. Wang, Y.D. Zhang, F. Wagner, C. Esling, Low cycle fatigue behavior of the textured AZ31B magnesium alloy under the asymmetrical loading, Materials Science and Engineering: A. 560 (2013) 618–626. doi:10.1016/j.msea.2012.10.004.

[61] I.J. Beyerlein, L. Capolungo, P.E. Marshall, R.J. McCabe, C.N. Tomé, Statistical analyses of deformation twinning in magnesium, Philosophical Magazine. 90 (2010) 2161–2190. doi:10.1080/14786431003630835.

[62] I.J. Beyerlein, R.J. McCabe, C.N. Tomé, Effect of microstructure on the nucleation of deformation twins in polycrystalline high-purity magnesium: A multi-scale modeling study, Journal of the Mechanics and Physics of Solids. 59 (2011) 988–1003. doi:10.1016/j.jmps.2011.02.007.

[63] J.J. Jonas, S. Mu, T. Al-Samman, G. Gottstein, L. Jiang, É. Martin, The role of strain accommodation during the variant selection of primary twins in magnesium, Acta Materialia. 59 (2011) 2046–2056. doi:10.1016/j.actamat.2010.12.005.

[64] G. Liu, R. Xin, X. Shu, C. Wang, Q. Liu, The mechanism of twinning activation and variant selection in magnesium alloys dominated by slip deformation, Journal of Alloys and Compounds. 687 (2016) 352–359. doi:10.1016/j.jallcom.2016.06.136.

[65] S. Mu, J.J. Jonas, G. Gottstein, Variant selection of primary, secondary and tertiary twins in a deformed Mg alloy, Acta Materialia. 60 (2012) 2043–2053. doi:10.1016/j.actamat.2012.01.014.

[66] H. Yoshinaga, T. Obara, S. Morozumi, Twinning deformation in magnesium compressed along the C-axis, Materials Science and Engineering. 12 (1973) 255–264. doi:10.1016/0025-5416(73)90036-0.

[67] S.L. Couling, C.S. Roberts, New twinning systems in magnesium, Acta Cryst. 9 (1956) 972–973. doi:10.1107/S0365110X56002758.

[68] I.J. Beyerlein, J. Wang, M.R. Barnett, C.N. Tomé, Double twinning mechanisms in magnesium alloys via dissociation of lattice dislocations, Proc. R. Soc. A. 468 (2012) 1496–1520. doi:10.1098/rspa.2011.0731.

[69] É. Martin, L. Capolungo, L. Jiang, J.J. Jonas, Variant selection during secondary twinning in Mg–3%Al, Acta Materialia. 58 (2010) 3970–3983. doi:10.1016/j.actamat.2010.03.027.

[70] M.R. Barnett, Z. Keshavarz, A.G. Beer, X. Ma, Non-Schmid behaviour during secondary twinning in a polycrystalline magnesium alloy, Acta Materialia. 56 (2008) 5–15. doi:10.1016/j.actamat.2007.08.034.

[71] M. Lentz, M. Risse, N. Schaefer, W. Reimers, I.J. Beyerlein, Strength and ductility with {$10\bar{1}1$} — {$10\bar{1}2$} double twinning in a magnesium alloy, Nature Communications. 7 (2016) 11068. doi:10.1038/ncomms11068.

[72] M.K. McQuillan, Phase transformations in titanium and its alloys, Metallurgical Reviews. 8 (1963) 41–104. doi:10.1179/mtlr.1963.8.1.41.

[73] G. Ter Haar, T. Becker, G.M. Ter Haar, T.H. Becker, Selective Laser Melting Produced Ti-6Al-4V: Post-Process Heat Treatments to Achieve Superior Tensile Properties, Materials. 11 (2018) 146. doi:10.3390/ma11010146.

[74] B. Vrancken, L. Thijs, J.-P. Kruth, J. Van Humbeeck, Heat treatment of Ti6Al4V produced by Selective Laser Melting: Microstructure and mechanical properties, Journal of Alloys and Compounds. 541 (2012) 177–185. doi:10.1016/j.jallcom.2012.07.022.

[75] G. Kasperovich, J. Hausmann, Improvement of fatigue resistance and ductility of TiAl6V4 processed by selective laser melting, Journal of Materials Processing Technology. 220 (2015) 202–214. doi:10.1016/j.jmatprotec.2015.01.025.

[76] H.K. Rafi, N.V. Karthik, H. Gong, T.L. Starr, B.E. Stucker, Microstructures and Mechanical Properties of Ti6Al4V Parts Fabricated by Selective Laser Melting and Electron Beam Melting, J. of Materi Eng and Perform. 22 (2013) 3872–3883. doi:10.1007/s11665-013-0658-0.

[77] K. Wissenbach, S. Höges, P. Robotti, A. Molinari, L. Facchini, E. Magalini, Ductility of a Ti-6Al-4V alloy produced by selective laser melting of prealloyed powders, Rapid Prototyping Journal. 16 (2010) 450–459. doi:10.1108/13552541011083371.

[78] H. Matsumoto, H. Yoneda, K. Sato, S. Kurosu, E. Maire, D. Fabregue, T.J. Konno, A. Chiba, Room-temperature ductility of Ti–6Al–4V alloy with α′ martensite microstructure, Materials Science and Engineering: A. 528 (2011) 1512–1520. doi:10.1016/j.msea.2010.10.070.

[79] H. Matsumoto, K. Kodaira, K. Sato, T.J. Konno, A. Chiba, Microstructure and Mechanical Properties of α′ Martensite Type Ti Alloys Deformed under the α′ Processing, MATERIALS TRANSACTIONS. 50 (2009) 2744–2750. doi:10.2320/matertrans.MA200912.

[80] A. Zafari, K. Xia, High Ductility in a fully martensitic microstructure: a paradox in a Ti alloy produced by selective laser melting, Materials Research Letters. 6 (2018) 627–633. doi:10.1080/21663831.2018.1525773.

[81] C. de Formanoir, A. Brulard, S. Vivès, G. Martin, F. Prima, S. Michotte, E. Rivière, A. Dolimont, S. Godet, A strategy to improve the work-hardening behavior of Ti–6Al–4V parts produced by additive manufacturing, Materials Research Letters. 5 (2017) 201–208. doi:10.1080/21663831.2016.1245681.

[82] C. de Formanoir, G. Martin, F. Prima, S.Y.P. Allain, T. Dessolier, F. Sun, S. Vivès, B. Hary, Y. Bréchet, S. Godet, Micromechanical behavior and thermal stability of a dual-phase α+α′ titanium alloy produced by additive manufacturing, Acta Materialia. 162 (2019) 149–162. doi:10.1016/j.actamat.2018.09.050.

[83] X. Tan, Y. Kok, W.Q. Toh, Y.J. Tan, M. Descoins, D. Mangelinck, S.B. Tor, K.F. Leong, C.K. Chua, Revealing martensitic transformation and α/β interface evolution in electron beam melting three-dimensional-printed Ti-6Al-4V, Scientific Reports. 6 (2016) 26039. doi:10.1038/srep26039.

[84] G. Welsch, R. Boyer, E.W. Collings, Materials Properties Handbook: Titanium Alloys, ASM International, 1993.

[85] O.M. Ivasishin, R.V. Teliovich, Transformation plasticity in titanium alpha double prime martensite, J. Phys. IV France. 11 (2001) Pr4-165-Pr4-172. doi:10.1051/jp4:2001421.

[86] A. Roth, M.A. Lebyodkin, T.A. Lebedkina, J.-S. Lecomte, T. Richeton, K.E.K. Amouzou, Mechanisms of anisotropy of mechanical properties of α-titanium in tension conditions, Materials Science and Engineering: A. 596 (2014) 236–243. doi:10.1016/j.msea.2013.12.061.

[87] H. Becker, W. Pantleon, Work-hardening stages and deformation mechanism maps during tensile deformation of commercially pure titanium, Computational Materials Science. 76 (2013) 52–59. doi:10.1016/j.commatsci.2013.03.028.

[88] K.E.K. Amouzou, T. Richeton, A. Roth, M.A. Lebyodkin, T.A. Lebedkina, Micromechanical modeling of hardening mechanisms in commercially pure α-titanium in tensile condition, International Journal of Plasticity. 80 (2016) 222–240. doi:10.1016/j.ijplas.2015.09.008.

[89] S. Nemat-Nasser, W.G. Guo, J.Y. Cheng, Mechanical properties and deformation mechanisms of a commercially pure titanium, Acta Materialia. 47 (1999) 3705–3720. doi:10.1016/S1359-6454(99)00203-7.

[90] A.A. Salem, S.R. Kalidindi, R.D. Doherty, Strain hardening regimes and microstructure evolution during large strain compression of high purity titanium, Scripta Materialia. 46 (2002) 419–423. doi:10.1016/S1359-6462(02)00005-2.

[91] A.A. Salem, S.R. Kalidindi, R.D. Doherty, Strain hardening of titanium: role of deformation twinning, Acta Materialia. 51 (2003) 4225–4237. doi:10.1016/S1359-6454(03)00239-8.

[92] A.A. Salem, S.R. Kalidindi, R.D. Doherty, S.L. Semiatin, Strain hardening due to deformation twinning in α-titanium: Mechanisms, Metall and Mat Trans A. 37 (2006) 259–268. doi:10.1007/s11661-006-0171-2.

[93] F. Coghe, W. Tirry, L. Rabet, D. Schryvers, P. Van Houtte, Importance of twinning in static and dynamic compression of a Ti–6Al–4V titanium alloy with an equiaxed microstructure, Materials Science and Engineering: A. 537 (2012) 1–10. doi:10.1016/j.msea.2011.12.047.

[94] S. Khayatzadeh, S. Rahimi, P. Blackwell, Effect of Plastic Deformation on Elastic and Plastic Recovery in CP-Titanium, Key Engineering Materials. 716 (2016) 891–896. doi:10.4028/www.scientific.net/KEM.716.891.

[95] B. Barkia, V. Doquet, J.P. Couzinié, I. Guillot, E. Héripré, In situ monitoring of the deformation mechanisms in titanium with different oxygen contents, Materials Science and Engineering: A. 636 (2015) 91–102. doi:10.1016/j.msea.2015.03.044.

[96] J. Gong, A.J. Wilkinson, Anisotropy in the plastic flow properties of single-crystal α titanium determined from micro-cantilever beams, Acta Materialia. 57 (2009) 5693–5705. doi:10.1016/j.actamat.2009.07.064.

[97] C. Zambaldi, Y. Yang, T.R. Bieler, D. Raabe, Orientation informed nanoindentation of α-titanium: Indentation pileup in hexagonal metals deforming by prismatic slip, Journal of Materials Research. 27 (2012) 356–367. doi:10.1557/jmr.2011.334.

[98] M.J. Philippe, M. Serghat, P. Van Houtte, C. Esling, Modelling of texture evolution for materials of hexagonal symmetry—II. application to zirconium and titanium α or near α alloys, Acta Metallurgica et Materialia. 43 (1995) 1619–1630. doi:10.1016/0956-7151(94)00329-G.

[99] N.P. Gurao, R. Kapoor, S. Suwas, Deformation behaviour of commercially pure titanium at extreme strain rates, Acta Materialia. 59 (2011) 3431–3446. doi:10.1016/j.actamat.2011.02.018.

[100] J.L.W. Warwick, N.G. Jones, K.M. Rahman, D. Dye, Lattice strain evolution during tensile and compressive loading of CP Ti, Acta Materialia. 60 (2012) 6720–6731. doi:10.1016/j.actamat.2012.08.042.

[101] N. Benmhenni, S. Bouvier, R. Brenner, T. Chauveau, B. Bacroix, Micromechanical modelling of monotonic loading of CP α-Ti: Correlation between macroscopic and microscopic behaviour, Materials Science and Engineering: A. 573 (2013) 222–233. doi:10.1016/j.msea.2013.02.022.

[102] D. Gloaguen, G. Oum, V. Legrand, J. Fajoui, S. Branchu, Experimental and theoretical studies of intergranular strain in an alpha titanium alloy during plastic deformation, Acta Materialia. 61 (2013) 5779–5790. doi:10.1016/j.actamat.2013.06.022.

[103] T. Richeton, F. Wagner, C. Chen, L.S. Toth, Combined Effects of Texture and Grain Size Distribution on the Tensile Behavior of α-Titanium, Materials (Basel). 11 (2018). doi:10.3390/ma11071088.

[104] J.L.W. Warwick, N.G. Jones, K.M. Rahman, D. Dye, Lattice strain evolution during tensile and compressive loading of CP Ti, Acta Materialia. 60 (2012) 6720–6731. doi:10.1016/j.actamat.2012.08.042.

[105] H. Seto, H. Takebe, K. Takahashi, H. Fujii, K. Mori, Effects of Oxygen Concentration and Grain Size on Twinning Deformation Behavior in Commercially Pure Titanium, in: Proceedings of the 13th World Conference on Titanium, John Wiley & Sons, Ltd, 2016: pp. 1167–1170. doi:10.1002/9781119296126.ch198.

[106] S. Han, P. Eisenlohr, M.A. Crimp, ECCI based characterization of dislocation shear in polycrystalline arrays during heterogeneous deformation of commercially pure titanium, Materials Characterization. 142 (2018) 504–514. doi:10.1016/j.matchar.2018.06.003.

[107] N. Deng, T. Kuwabara, Y.P. Korkolis, Cruciform Specimen Design and Verification for Constitutive Identification of Anisotropic Sheets, Exp Mech. 55 (2015) 1005–1022. doi:10.1007/s11340-015-9999-y.

[108] R. v Mises, Mechanik der festen Körper im plastisch- deformablen Zustand, Nachrichten von der Gesellschaft der Wissenschaften zu Göttingen, Mathematisch-Physikalische Klasse. 1913 (1913) 582–592.

[109] V. Bonnand, J.L. Chaboche, P. Gomez, P. Kanouté, D. Pacou, Investigation of multiaxial fatigue in the context of turboengine disc applications, International Journal of Fatigue. 33 (2011) 1006–1016. doi:10.1016/j.ijfatigue.2010.12.018.

[110] R.A. Cláudio, L. Reis, M. Freitas, Biaxial high-cycle fatigue life assessment of ductile aluminium cruciform specimens, Theoretical and Applied Fracture Mechanics. 73 (2014) 82–90. doi:10.1016/j.tafmec.2014.08.007.

[111] M.V. Upadhyay, T. Panzner, S.V. Petegem, H.V. Swygenhoven, Stresses and Strains in Cruciform Samples Deformed in Tension, Exp Mech. 57 (2017) 905–920. doi:10.1007/s11340-017-0270-6.

[112] D.A. Kelly, Problems in creep testing under biaxial stress systems, The Journal of Strain Analysis for Engineering Design. 11 (1976) 1–6. doi:10.1243/03093247V111001.

[113] W. Müller, K. Pöhlandt, New experiments for determining yield loci of sheet metal, Journal of Materials Processing Technology. 60 (1996) 643–648. doi:10.1016/0924-0136(96)02399-0.

[114] ISO 16842:2014 - Metallic materials -- Sheet and strip -- Biaxial tensile testing method using a cruciform test piece, ISO. (n.d.). http://www.iso.org/iso/home/store/catalogue_ics/catalogue_detail_ics.htm?ics1=77&ics2=040&ics3= 10&csnumber=57812 (accessed May 25, 2016).

[115] T. Kuwabara, S. Ikeda, K. Kuroda, Measurement and analysis of differential work hardening in cold-rolled steel sheet under biaxial tension, Journal of Materials Processing Technology. 80–81 (1998) 517–523. doi:10.1016/S0924-0136(98)00155-1.

[116] J. Huh, H. Huh, C.S. Lee, Effect of strain rate on plastic anisotropy of advanced high strength steel sheets, International Journal of Plasticity. 44 (2013) 23–46. doi:10.1016/j.ijplas.2012.11.012.

[117] R. Baptista, R.A. Claudio, L. Reis, J.F.A. Madeira, I. Guelho, M. Freitas, Optimization of cruciform specimens for biaxial fatigue loading with direct multi search, Theoretical and Applied Fracture Mechanics. 80 (2015) 65–72. doi:10.1016/j.tafmec.2015.06.009.

[118] I.H. Wilson, D.J. White, Cruciform specimens for biaxial fatigue tests: An investigation using finite-element analysis and photoelastic-coating techniques, Journal of Strain Analysis. 6 (1971) 27–37. doi:10.1243/03093247V061027.

[119] S. Zhang, M. Sakane, Multiaxial creep–fatigue life prediction for cruciform specimen, International Journal of Fatigue. 29 (2007) 2191–2199. doi:10.1016/j.ijfatigue.2006.12.012.

[120] Y. Yu, M. Wan, X.-D. Wu, X.-B. Zhou, Design of a cruciform biaxial tensile specimen for limit strain analysis by FEM, Journal of Materials Processing Technology. 123 (2002) 67–70. doi:10.1016/S0924-0136(02)00062-6.

[121] W. Liu, D. Guines, L. Leotoing, E. Ragneau, Identification of sheet metal hardening for large strains with an in-plane biaxial tensile test and a dedicated cross specimen, International Journal of Mechanical Sciences. 101–102 (2015) 387–398. doi:10.1016/j.ijmecsci.2015.08.022.

[122] D.R. Hayhurst, A biaxial-tension creep-rupture testing machine, Journal of Strain Analysis. 8 (1973) 119–123. doi:10.1243/03093247V082119.

[123] A. Makinde, L. Thibodeau, K.W. Neale, Development of an apparatus for biaxial testing using cruciform specimens, Experimental Mechanics. 32 (1992) 138–144. doi:10.1007/BF02324725.

[124] I. Zidane, D. Guines, L. Léotoing, E. Ragneau, Development of an in-plane biaxial test for forming limit curve (FLC) characterization of metallic sheets, Meas. Sci. Technol. 21 (2010) 055701. doi:10.1088/0957-0233/21/5/055701.

[125] E. Hoferlin, A. Van Bael, P. Van Houtte, G. Steyaert, C. De Maré, Biaxial tests on cruciform specimens for the validation of crystallographic yield loci, Journal of Materials Processing Technology. 80 (1998) 545–550. doi:10.1016/S0924-0136(98)00123-X.

[126] V. Bonnand, J.L. Chaboche, P. Gomez, P. Kanouté, D. Pacou, Investigation of multiaxial fatigue in the context of turboengine disc applications, International Journal of Fatigue. 33 (2011) 1006–1016. doi:10.1016/j.ijfatigue.2010.12.018.

[127] E. Gentili, L. Tabaglio, F. Aggogeri, Review on Micromachining Techniques, in: E. Kuljanic (Ed.), AMST'05 Advanced Manufacturing Systems and Technology, Springer Vienna, 2005: pp. 387–396.

[128] D. Bäuerle, Nanosecond-Laser Ablation, in: D. Bäuerle (Ed.), Laser Processing and Chemistry, Springer Berlin Heidelberg, Berlin, Heidelberg, 2011: pp. 237–278. doi:10.1007/978-3-642-17613-5_12.

[129] M.S. Brown, C.B. Arnold, Fundamentals of Laser-Material Interaction and Application to Multiscale Surface Modification, in: K. Sugioka, M. Meunier, A. Piqué (Eds.), Laser Precision Microfabrication, Springer Berlin Heidelberg, Berlin, Heidelberg, 2010: pp. 91–120. doi:10.1007/978-3-642-10523-4_4.

[130] S. Nolte, C. Momma, H. Jacobs, A. Tünnermann, B.N. Chichkov, B. Wellegehausen, H. Welling, Ablation of metals by ultrashort laser pulses, J. Opt. Soc. Am. B, JOSAB. 14 (1997) 2716–2722. doi:10.1364/JOSAB.14.002716.

[131] B. Jaeggi, B. Neuenschwander, M. Schmid, M. Muralt, J. Zuercher, U. Hunziker, Influence of the Pulse Duration in the ps-Regime on the Ablation Efficiency of Metals, Physics Procedia. 12 (2011) 164–171. doi:10.1016/j.phpro.2011.03.118.

[132] I.N. Zavestovskaya, A.P. Kanavin, Laser Ablation of Metals by Low-Density Picosecond Pulses, Bull. Lebedev Phys. Inst. 45 (2018) 6–9. doi:10.3103/S1068335618010025.

[133] M.P. Echlin, M. Straw, S. Randolph, J. Filevich, T.M. Pollock, The TriBeam system: Femtosecond laser ablation in situ SEM, Materials Characterization. 100 (2015) 1–12. doi:10.1016/j.matchar.2014.10.023.

[134] A. Kumar, T.M. Pollock, Mapping of femtosecond laser-induced collateral damage by electron backscatter diffraction, Journal of Applied Physics. 110 (2011) 083114. doi:10.1063/1.3653839.

[135] Q. Feng, Y.N. Picard, H. Liu, S.M. Yalisove, G. Mourou, T.M. Pollock, Femtosecond laser micromachining of a single-crystal superalloy, Scripta Materialia. 53 (2005) 511–516. doi:10.1016/j.scriptamat.2005.05.006.

[136] D. Bouilly, D. Perez, L.J. Lewis, Damage in materials following ablation by ultrashort laser pulses: A molecular-dynamics study, Phys. Rev. B. 76 (2007) 184119. doi:10.1103/PhysRevB.76.184119.

[137] A. Guitton, A. Irastorza-Landa, R. Broennimann, D. Grolimund, S. Van Petegem, H. Van Swygenhoven, Picosecond pulsed laser for microscale sample preparation, Materials Letters. 160 (2015) 589–591. doi:10.1016/j.matlet.2015.06.119.

[138] G.C. Sneddon, P.W. Trimby, J.M. Cairney, Transmission Kikuchi diffraction in a scanning electron microscope: A review, Materials Science and Engineering: R: Reports. 110 (2016) 1–12. doi:10.1016/j.mser.2016.10.001.

[139] T.H. de Keijser, J.I. Langford, E.J. Mittemeijer, A.B.P. Vogels, Use of the Voigt function in a single-line method for the analysis of X-ray diffraction line broadening, J Appl Cryst. 15 (1982) 308–314. doi:10.1107/S0021889882012035.

[140] R.K. Nandi, S.P.S. Gupta, The analysis of X-ray diffraction profiles from imperfect solids by an application of convolution relations, Journal of Applied Crystallography. 11 (1978) 6–9. doi:10.1107/S0021889878012595.

[141] N.C. Halder, C.N.J. Wagner, Analysis of the Broadening of Powder Pattern Peaks Using Variance, Integral Breadth, and Fourier Coefficients of the Line Profile, in: G.R. Mallett, M.J. Fay, W.M. Mueller (Eds.), Advances in X-Ray Analysis, Springer US, 1966: pp. 91–102.

[142] B.E. Warren, X-ray studies of deformed metals, Progress in Metal Physics. 8 (1959) 147–202. doi:10.1016/0502-8205(59)90015-2.

[143] W. Voigt, Über das Gesetz der Intensitätsverteilung Innerhald der Linien eines Gasspektrums, in: Sitzungsberichte Der Mathematisch-Physikalischen Klasse Der K. B. Akademie Der Wissenschaften, Königlich Bayerischen Akademie der Wissenschaften, 1912: pp. 603–620.

[144] T.D. Keijser, E.J. Mittemeijer, H.C.F. Rozendaal, The determination of crystallite-size and lattice-strain parameters in conjunction with the profile-refinement method for the determination of crystal structures, Journal of Applied Crystallography. 16 (1983) 309–316. doi:10.1107/S0021889883010493.

[145] P. Scardi, M. Leoni, R. Delhez, Line broadening analysis using integral breadth methods: a critical review, J Appl Cryst. 37 (2004) 381–390. doi:10.1107/S0021889804004583.

[146] P. Scardi, M. Leoni, Line profile analysis: pattern modelling versus profile fitting, J Appl Cryst. 39 (2006) 24–31. doi:10.1107/S0021889805032978.

[147] H. Mughrabi, Dislocation wall and cell structures and long-range internal stresses in deformed metal crystals, Acta Metallurgica. 31 (1983) 1367–1379. doi:10.1016/0001-6160(83)90007-X.

[148] V. Vidal, L. Thilly, S. Van Petegem, U. Stuhr, F. Lecouturier, P.-O. Renault, H. Van Swygenhoven, Plasticity of nanostructured Cu–Nb-based wires: Strengthening mechanisms revealed by in situ

deformation under neutrons, Scripta Materialia. 60 (2009) 171–174. doi:10.1016/j.scriptamat.2008.09.032.

[149]   B.E. Warren, X-ray Diffraction, Courier Corporation, 1990.

[150]   J.B. Cohen, C.N.J. Wagner, Determination of Twin Fault Probabilities from the Diffraction Patterns of fcc Metals and Alloys, Journal of Applied Physics. 33 (1962) 2073–2077. doi:10.1063/1.1728897.

[151]   L. Balogh, G. Ribárik, T. Ungár, Stacking faults and twin boundaries in fcc crystals determined by x-ray diffraction profile analysis, Journal of Applied Physics. 100 (2006) 023512. doi:10.1063/1.2216195.

[152]   S.R. Agnew, D.W. Brown, C.N. Tomé, Validating a polycrystal model for the elastoplastic response of magnesium alloy AZ31 using in situ neutron diffraction, Acta Materialia. 54 (2006) 4841–4852. doi:10.1016/j.actamat.2006.06.020.

[153]   T.H. Simm, P.J. Withers, J. Quinta da Fonseca, An evaluation of diffraction peak profile analysis (DPPA) methods to study plastically deformed metals, Materials & Design. 111 (2016) 331–343. doi:10.1016/j.matdes.2016.08.091.

[154]   T.H. Simm, Peak Broadening Anisotropy and the Contrast Factor in Metal Alloys, Crystals. 8 (2018) 212. doi:10.3390/cryst8050212.

[155]   I.C. Dragomir, T. Ungár, Contrast factors of dislocations in the hexagonal crystal system, J Appl Cryst. 35 (2002) 556–564. doi:10.1107/S0021889802009536.

[156]   R. Pynn, Neutron Scattering—A Non-destructive Microscope for Seeing Inside Matter, in: L. Liang, R. Rinaldi, H. Schober (Eds.), Neutron Applications in Earth, Energy and Environmental Sciences, Springer US, Boston, MA, 2009: pp. 15–36. doi:10.1007/978-0-387-09416-8_2.

[157]   U. Stuhr, H. Spitzer, J. Egger, A. Hofer, P. Rasmussen, D. Graf, A. Bollhalder, M. Schild, G. Bauer, W. Wagner, Time-of-flight diffraction with multiple frame overlap Part II: The strain scanner POLDI at PSI, Nuclear Instruments and Methods in Physics Research Section A: Accelerators, Spectrometers, Detectors and Associated Equipment. 545 (2005) 330–338. doi:10.1016/j.nima.2005.01.321.

[158]   U. Stuhr, M. Grosse, W. Wagner, The TOF-strain scanner POLDI with multiple frame overlap—concept and performance, Materials Science and Engineering: A. 437 (2006) 134–138. doi:10.1016/j.msea.2006.04.069.

[159]   P.R. Willmott, D. Meister, S.J. Leake, M. Lange, A. Bergamaschi, M. Böge, M. Calvi, C. Cancellieri, N. Casati, A. Cervellino, Q. Chen, C. David, U. Flechsig, F. Gozzo, B. Henrich, S. Jäggi-Spielmann, B. Jakob, I. Kalichava, P. Karvinen, J. Krempasky, A. Lüdeke, R. Lüscher, S. Maag, C. Quitmann, M.L. Reinle-Schmitt, T. Schmidt, B. Schmitt, A. Streun, I. Vartiainen, M. Vitins, X. Wang, R. Wullschleger, The Materials Science beamline upgrade at the Swiss Light Source, J Synchrotron Radiat. 20 (2013) 667–682. doi:10.1107/S0909049513018475.

[160]   H. Van Swygenhoven, B. Schmitt, P.M. Derlet, S. Van Petegem, A. Cervellino, Z. Budrovic, S. Brandstetter, A. Bollhalder, M. Schild, Following peak profiles during elastic and plastic deformation: A synchrotron-based technique, Review of Scientific Instruments. 77 (2006) 013902. doi:10.1063/1.2162453.

[161]   M. Drakopoulos, T. Connolley, C. Reinhard, R. Atwood, O. Magdysyuk, N. Vo, M. Hart, L. Connor, B. Humphreys, G. Howell, S. Davies, T. Hill, G. Wilkin, U. Pedersen, A. Foster, N. De Maio, M. Basham, F. Yuan, K. Wanelik, I12: the Joint Engineering, Environment and Processing (JEEP) beamline at Diamond Light Source, J Synchrotron Rad. 22 (2015) 828–838. doi:10.1107/S1600577515003513.

[162]   C.R. Heiple, S.H. Carpenter, Acoustic emission produced by deformation of metals and alloys - A review., Journal of Acoustic Emission. 6 (1987) 177–204.

[163]   C.R. Heiple, S.H. Carpenter, Acoustic emission produced by deformation of metals and alloys - A review: Part II, J. Acoust. Emission. 6 (1987) 215–237.

[164]   C. Scruby, H. Wadley, J.E. Sinclair, The origin of acoustic emission during deformation of aluminium and an aluminium–magnesium alloy, Philosophical Magazine A. 44 (1981) 249–274. doi:10.1080/01418618108239532.

[165]   J. Čapek, Investigation of basic deformation mechanisms of magnesium alloys by means of advanced in-situ methods and theoretical modeling, Charles University, 2017.

[166] E. Shiratori, K. Ikegami, Experimental study of the subsequent yield surface by using cross-shaped specimens, Journal of the Mechanics and Physics of Solids. 16 (1968) 373–394. doi:10.1016/0022-5096(68)90002-1.

[167] D.E. Green, K.W. Neale, S.R. MacEwen, A. Makinde, R. Perrin, Experimental investigation of the biaxial behaviour of an aluminum sheet, International Journal of Plasticity. 20 (2004) 1677–1706. doi:10.1016/j.ijplas.2003.11.012.

[168] P.E. Dyer, R.J. Farley, Dynamics of laser-induced periodic surface structures in excimer laser ablation of polymers, Journal of Applied Physics. 74 (1993) 1442–1444. doi:10.1063/1.354906.

[169] C. Guo, G. Rodriguez, A. Lobad, A.J. Taylor, Breaking Metals with Ultrafast Optical Excitation, Optics & Photonics News, OPN. 11 (2000) 47–47. doi:10.1364/OPN.11.12.000047.

[170] R.L. Harzic, D. Breitling, M. Weikert, S. Sommer, C. Föhl, F. Dausinger, S. Valette, C. Donnet, E. Audouard, Ablation comparison with low and high energy densities for Cu and Al with ultra-short laser pulses, Appl. Phys. A. 80 (2005) 1589–1593. doi:10.1007/s00339-005-3206-4.

[171] J. König, S. Nolte, A. Tünnermann, Plasma evolution during metal ablation with ultrashort laser pulses, Opt. Express, OE. 13 (2005) 10597–10607. doi:10.1364/OPEX.13.010597.

[172] G.M. Hommer, J.S. Park, P.C. Collins, A.L. Pilchak, A.P. Stebner, A New In Situ Planar Biaxial Far-Field High Energy Diffraction Microscopy Experiment, in: Advancement of Optical Methods in Experimental Mechanics, Volume 3, Springer, Cham, 2017: pp. 61–70. doi:10.1007/978-3-319-41600-7_7.

[173] Abaqus 6.14 Documentation, (n.d.). http://abaqus.software.polimi.it/v6.14/index.html (accessed July 25, 2017).

[174] M.V. Upadhyay, T. Panzner, S.V. Petegem, H.V. Swygenhoven, Stresses and Strains in Cruciform Samples Deformed in Tension, Exp Mech. (2017) 1–16. doi:10.1007/s11340-017-0270-6.

[175] Hill, A Theory of the Yielding and Plastic Flow of Anisotropic Metals | Proceedings of the Royal Society of London A: Mathematical, Physical and Engineering Sciences, (n.d.). http://rspa.royalsocietypublishing.org/content/193/1033/281 (accessed July 6, 2017).

[176] S.V. Petegem, A. Guitton, M. Dupraz, A. Bollhalder, K. Sofinowski, M.V. Upadhyay, H.V. Swygenhoven, A Miniaturized Biaxial Deformation Rig for in Situ Mechanical Testing, Exp Mech. 57 (2017) 569–580. doi:10.1007/s11340-016-0244-0.

[177] R.W. Klein, B.W. Williams, J. McKinley, J.R. Einhorn, S.R. Agnew, Exploration of Thin-Walled Magnesium Alloy Tube Extrusion for Improved Crash Performance, in: A. Singh, K. Solanki, M. V.nuel, N.R. Neelameggham (Eds.), Magnesium Technology 2016, John Wiley & Sons, Inc., 2016: pp. 223–228. doi:10.1002/9781119274803.ch45.

[178] J. Bohlen, M.R. Nürnberg, J.W. Senn, D. Letzig, S.R. Agnew, The texture and anisotropy of magnesium–zinc–rare earth alloy sheets, Acta Materialia. 55 (2007) 2101–2112. doi:10.1016/j.actamat.2006.11.013.

[179] J. Hirsch, T. Al-Samman, Superior light metals by texture engineering: Optimized aluminum and magnesium alloys for automotive applications, Acta Materialia. 61 (2013) 818–843. doi:10.1016/j.actamat.2012.10.044.

[180] D.W. Brown, S.R. Agnew, S.P. Abeln, W.R. Blumenthal, M.A.M. Bourke, M.C. Mataya, C. Tomé, S.C. Vogel, The Role of Texture, Temperature and Strain Rate in the Activity of Deformation Twinning, Materials Science Forum. (2005). doi:10.4028/www.scientific.net/MSF.495-497.1037.

[181] D.W. Brown, S.R. Agnew, M.A.M. Bourke, T.M. Holden, S.C. Vogel, C.N. Tomé, Internal strain and texture evolution during deformation twinning in magnesium, Materials Science and Engineering: A. 399 (2005) 1–12. doi:10.1016/j.msea.2005.02.016.

[182] S.R. Agnew, D.W. Brown, S.C. Vogel, T. Holden, In-Situ Measurement of Internal Strain Evolution during Deformation Dominated by Mechanical Twinning, Materials Science Forum. 404–407 (2002) 747–754. doi:10.4028/www.scientific.net/MSF.404-407.747.

[183] A. Jain, O. Duygulu, D.W. Brown, C.N. Tomé, S.R. Agnew, Grain size effects on the tensile properties and deformation mechanisms of a magnesium alloy, AZ31B, sheet, Materials Science and Engineering: A. 486 (2008) 545–555. doi:10.1016/j.msea.2007.09.069.

[184] M.A. Gharghouri, G.C. Weatherly, J.D. Embury, J. Root, Study of the mechanical properties of Mg-7.7at.% Al by in-situ neutron diffraction, Philosophical Magazine A. 79 (1999) 1671–1695. doi:10.1080/01418619908210386.

[185] X. Hong, A. Godfrey, W. Liu, A. Orozco-Caballero, J.Q. da Fonseca, Effect of pre-existing twinning on strain localization during deformation of a magnesium alloy, Materials Letters. 209 (2017) 94–96. doi:10.1016/j.matlet.2017.07.077.

[186] H. Qiao, S.R. Agnew, P.D. Wu, Modeling twinning and detwinning behavior of Mg alloy ZK60A during monotonic and cyclic loading, International Journal of Plasticity. 65 (2015) 61–84. doi:10.1016/j.ijplas.2014.08.010.

[187] H. Wang, S.Y. Lee, M.A. Gharghouri, P.D. Wu, S.G. Yoon, Deformation behavior of Mg-8.5wt.%Al alloy under reverse loading investigated by in-situ neutron diffraction and elastic viscoplastic self-consistent modeling, Acta Materialia. 107 (2016) 404–414. doi:10.1016/j.actamat.2016.01.066.

[188] J. Čapek, K. Máthis, B. Clausen, M. Barnett, Dependence of twinned volume fraction on loading mode and Schmid factor in randomly textured magnesium, Acta Materialia. 130 (2017) 319–328. doi:10.1016/j.actamat.2017.03.017.

[189] K. Máthis, P. Beran, J. Čapek, P. Lukáš, In-situ neutron diffraction and acoustic emission investigation of twinning activity in magnesium, J. Phys.: Conf. Ser. 340 (2012) 012096. doi:10.1088/1742-6596/340/1/012096.

[190] B. Song, G. Huang, H. Li, L. Zhang, G. Huang, F. Pan, Texture evolution and mechanical properties of AZ31B magnesium alloy sheets processed by repeated unidirectional bending, Journal of Alloys and Compounds. 489 (2010) 475–481. doi:10.1016/j.jallcom.2009.09.090.

[191] M. Knezevic, A. Levinson, R. Harris, R.K. Mishra, R.D. Doherty, S.R. Kalidindi, Deformation twinning in AZ31: Influence on strain hardening and texture evolution, Acta Materialia. 58 (2010) 6230–6242. doi:10.1016/j.actamat.2010.07.041.

[192] H. El Kadiri, J. Kapil, A.L. Oppedal, L.G. Hector, S.R. Agnew, M. Cherkaoui, S.C. Vogel, The effect of twin–twin interactions on the nucleation and propagation of {101̄2} twinning in magnesium, Acta Materialia. 61 (2013) 3549–3563. doi:10.1016/j.actamat.2013.02.030.

[193] P. Chen, B. Li, D. Culbertson, Y. Jiang, Contribution of extension twinning to plastic strain at low stress stage deformation of a Mg-3Al-1Zn alloy, Materials Science and Engineering: A. 709 (2018) 40–45. doi:10.1016/j.msea.2017.10.038.

[194] L. Lv, Y. Xin, H. Yu, R. Hong, Q. Liu, The role of dislocations in strain hardening of an extension twinning predominant deformation, Materials Science and Engineering: A. 636 (2015). doi:10.1016/j.msea.2015.04.007.

[195] S.R. Agnew, O. Duygulu, Tem investigation of dislocation mechanisms in Mg alloy AZ31B sheet, Magnesium Technology 2004. (2004).

[196] A.L. Oppedal, H.E. Kadiri, C.N. Tomé, S.C. Vogel, M.F. Horstemeyer, Anisotropy in hexagonal close-packed structures: improvements to crystal plasticity approaches applied to magnesium alloy, Philosophical Magazine. 93 (2013) 4311–4330. doi:10.1080/14786435.2013.827802.

[197] F. Wang, S. Agnew, Dislocation-Twin Interactions in Magnesium Alloy AZ31, in: Magnesium Technology 2015, Springer, Cham, 2015: pp. 139–144. doi:10.1007/978-3-319-48185-2_27.

[198] H. Qiao, X.Q. Guo, A.L. Oppedal, H. El Kadiri, P.D. Wu, S.R. Agnew, Twin-induced hardening in extruded Mg alloy AM30, Materials Science and Engineering: A. 687 (2017) 17–27. doi:10.1016/j.msea.2016.12.123.

[199] X.Y. Lou, M. Li, R.K. Boger, S.R. Agnew, R.H. Wagoner, Hardening evolution of AZ31B Mg sheet, International Journal of Plasticity. 23 (2007) 44–86. doi:10.1016/j.ijplas.2006.03.005.

[200] R.H. Wagoner, X.Y. Lou, M. Li, S.R. Agnew, Forming behavior of magnesium sheet, Journal of Materials Processing Technology. 177 (2006) 483–485. doi:10.1016/j.jmatprotec.2006.04.121.

[201] Y. Chino, K. Kimura, M. Mabuchi, Deformation characteristics at room temperature under biaxial tensile stress in textured AZ31 Mg alloy sheets, Acta Materialia. 57 (2009) 1476–1485. doi:10.1016/j.actamat.2008.11.033.

[202]   R.A. Lebensohn, C.N. Tomé, A self-consistent anisotropic approach for the simulation of plastic deformation and texture development of polycrystals: Application to zirconium alloys, Acta Metallurgica et Materialia. 41 (1993) 2611–2624. doi:10.1016/0956-7151(93)90130-K.

[203]   R.A. Lebensohn, C.N. Tomé, P.P. CastaÑeda, Self-consistent modelling of the mechanical behaviour of viscoplastic polycrystals incorporating intragranular field fluctuations, Philosophical Magazine. 87 (2007) 4287–4322. doi:10.1080/14786430701432619.

[204]   O. Arnold, J.C. Bilheux, J.M. Borreguero, A. Buts, S.I. Campbell, L. Chapon, M. Doucet, N. Draper, R. Ferraz Leal, M.A. Gigg, V.E. Lynch, A. Markvardsen, D.J. Mikkelson, R.L. Mikkelson, R. Miller, K. Palmen, P. Parker, G. Passos, T.G. Perring, P.F. Peterson, S. Ren, M.A. Reuter, A.T. Savici, J.W. Taylor, R.J. Taylor, R. Tolchenov, W. Zhou, J. Zikovsky, Mantid—Data analysis and visualization package for neutron scattering and SR experiments, Nuclear Instruments and Methods in Physics Research Section A: Accelerators, Spectrometers, Detectors and Associated Equipment. 764 (2014) 156–166. doi:10.1016/j.nima.2014.07.029.

[205]   E. Pomponi, A. Vinogradov, A real-time approach to acoustic emission clustering, Mechanical Systems and Signal Processing. 40 (2013) 791–804. doi:10.1016/j.ymssp.2013.03.017.

[206]   M. Ardeljan, I.J. Beyerlein, B.A. McWilliams, M. Knezevic, Strain rate and temperature sensitive multi-level crystal plasticity model for large plastic deformation behavior: Application to AZ31 magnesium alloy, International Journal of Plasticity. 83 (2016) 90–109. doi:10.1016/j.ijplas.2016.04.005.

[207]   H. Wang, B. Raeisinia, P.D. Wu, S.R. Agnew, C.N. Tomé, Evaluation of self-consistent polycrystal plasticity models for magnesium alloy AZ31B sheet, International Journal of Solids and Structures. 47 (2010) 2905–2917. doi:10.1016/j.ijsolstr.2010.06.016.

[208]   P.D. Wu, X.Q. Guo, H. Qiao, S.R. Agnew, D.J. Lloyd, J.D. Embury, On the rapid hardening and exhaustion of twinning in magnesium alloy, Acta Materialia. 122 (2017) 369–377. doi:10.1016/j.actamat.2016.10.016.

[209]   S. Mu, T. Al-Samman, V. Mohles, G. Gottstein, Cluster type grain interaction model including twinning for texture prediction: Application to magnesium alloys, Acta Materialia. 59 (2011) 6938–6948. doi:10.1016/j.actamat.2011.07.045.

[210]   M.A. Kumar, I.J. Beyerlein, R.J. McCabe, C.N. Tomé, Grain neighbour effects on twin transmission in hexagonal close-packed materials, Nature Communications. 7 (2016) 13826. doi:10.1038/ncomms13826.

[211]   L. Wu, S.R. Agnew, D.W. Brown, G.M. Stoica, B. Clausen, A. Jain, D.E. Fielden, P.K. Liaw, Internal stress relaxation and load redistribution during the twinning–detwinning-dominated cyclic deformation of a wrought magnesium alloy, ZK60A, Acta Materialia. 56 (2008) 3699–3707. doi:10.1016/j.actamat.2008.04.006.

[212]   L. Wu, S.R. Agnew, Y. Ren, D.W. Brown, B. Clausen, G.M. Stoica, H.R. Wenk, P.K. Liaw, The effects of texture and extension twinning on the low-cycle fatigue behavior of a rolled magnesium alloy, AZ31B, Materials Science and Engineering: A. 527 (2010) 7057–7067. doi:10.1016/j.msea.2010.07.047.

[213]   M. Arul Kumar, I.J. Beyerlein, C.N. Tomé, Grain size constraints on twin expansion in hexagonal close packed crystals, Journal of Applied Physics. 120 (2016) 155105. doi:10.1063/1.4965719.

[214]   S.-G. Hong, S.H. Park, C.S. Lee, Strain path dependence of {10−12} twinning activity in a polycrystalline magnesium alloy, Scripta Materialia. 64 (2011) 145–148. doi:10.1016/j.scriptamat.2010.09.030.

[215]   L. Capolungo, I.J. Beyerlein, C.N. Tomé, Slip-assisted twin growth in hexagonal close-packed metals, Scripta Materialia. 60 (2009) 32–35. doi:10.1016/j.scriptamat.2008.08.044.

[216]   A. Khosravani, D.T. Fullwood, B.L. Adams, T.M. Rampton, M.P. Miles, R.K. Mishra, Nucleation and propagation of {101−2} twins in AZ31 magnesium alloy, Acta Materialia. 100 (2015) 202–214. doi:10.1016/j.actamat.2015.08.024.

[217]   M.H. Yoo, Slip, twinning, and fracture in hexagonal close-packed metals, MTA. 12 (1981) 409–418. doi:10.1007/BF02648537.

[218]   O.L.A. Harrysson, O. Cansizoglu, D.J. Marcellin-Little, D.R. Cormier, H.A. West, Direct metal fabrication of titanium implants with tailored materials and mechanical properties using electron beam melting technology, Materials Science and Engineering: C. 28 (2008) 366–373. doi:10.1016/j.msec.2007.04.022.

[219]   L.E. Murr, S.A. Quinones, S.M. Gaytan, M.I. Lopez, A. Rodela, E.Y. Martinez, D.H. Hernandez, E. Martinez, F. Medina, R.B. Wicker, Microstructure and mechanical behavior of Ti–6Al–4V produced by rapid-layer manufacturing, for biomedical applications, Journal of the Mechanical Behavior of Biomedical Materials. 2 (2009) 20–32. doi:10.1016/j.jmbbm.2008.05.004.

[220]   D. Banerjee, J.C. Williams, Perspectives on Titanium Science and Technology, Acta Materialia. 61 (2013) 844–879. doi:10.1016/j.actamat.2012.10.043.

[221]   M. Qian, W. Xu, M. Brandt, H.P. Tang, Additive manufacturing and postprocessing of Ti-6Al-4V for superior mechanical properties, MRS Bulletin. 41 (2016) 775–784. doi:10.1557/mrs.2016.215.

[222]   M. Peters, J. Kumpfert, C.H. Ward, C. Leyens, Titanium Alloys for Aerospace Applications, Advanced Engineering Materials. 5 (2003) 419–427. doi:10.1002/adem.200310095.

[223]   S. Ford, Additive Manufacturing Technology: Potential Implications for U.S. Manufacturing Competitiveness, Social Science Research Network, Rochester, NY, 2014. https://papers.ssrn.com/abstract=2501065 (accessed November 13, 2018).

[224]   K. Wang, The use of titanium for medical applications in the USA, Materials Science and Engineering: A. 213 (1996) 134–137. doi:10.1016/0921-5093(96)10243-4.

[225]   M. Niinomi, Mechanical properties of biomedical titanium alloys, Materials Science and Engineering: A. 243 (1998) 231–236. doi:10.1016/S0921-5093(97)00806-X.

[226]   G. Lütjering, Influence of processing on microstructure and mechanical properties of (α+β) titanium alloys, Materials Science and Engineering: A. 243 (1998) 32–45. doi:10.1016/S0921-5093(97)00778-8.

[227]   S. Bruschi, S. Poggio, F. Quadrini, M.E. Tata, Workability of Ti–6Al–4V alloy at high temperatures and strain rates, Materials Letters. 58 (2004) 3622–3629. doi:10.1016/j.matlet.2004.06.058.

[228]   Y. Long, T. Wang, H.Y. Zhang, X.L. Huang, Enhanced ductility in a bimodal ultrafine-grained Ti–6Al–4V alloy fabricated by high energy ball milling and spark plasma sintering, Materials Science and Engineering: A. 608 (2014) 82–89. doi:10.1016/j.msea.2014.04.057.

[229]   S. Zherebtsov, E. Kudryavtsev, S. Kostjuchenko, S. Malysheva, G. Salishchev, Strength and ductility-related properties of ultrafine grained two-phase titanium alloy produced by warm multiaxial forging, Materials Science and Engineering: A. 536 (2012) 190–196. doi:10.1016/j.msea.2011.12.102.

[230]   Y. Chong, T. Bhattacharjee, M.-H. Park, A. Shibata, N. Tsuji, Factors determining room temperature mechanical properties of bimodal microstructures in Ti-6Al-4V alloy, Materials Science and Engineering: A. 730 (2018) 217–222. doi:10.1016/j.msea.2018.06.019.

[231]   S. Hémery, V.T. Dang, L. Signor, P. Villechaise, Influence of Microtexture on Early Plastic Slip Activity in Ti-6Al-4V Polycrystals, Metall and Mat Trans A. 49 (2018) 2048–2056. doi:10.1007/s11661-018-4569-4.

[232]   H. Galarraga, R.J. Warren, D.A. Lados, R.R. Dehoff, M.M. Kirka, P. Nandwana, Effects of heat treatments on microstructure and properties of Ti-6Al-4V ELI alloy fabricated by electron beam melting (EBM), Materials Science and Engineering: A. 685 (2017) 417–428. doi:10.1016/j.msea.2017.01.019.

[233]   J. Yao, T. Suo, S. Zhang, F. Zhao, H. Wang, J. Liu, Y. Chen, Y. Li, Influence of heat-treatment on the dynamic behavior of 3D laser-deposited Ti–6Al–4V alloy, Materials Science and Engineering: A. 677 (2016) 153–162. doi:10.1016/j.msea.2016.09.036.

[234]   J. Blaber, B. Adair, A. Antoniou, Ncorr: Open-Source 2D Digital Image Correlation Matlab Software, Exp Mech. 55 (2015) 1105–1122. doi:10.1007/s11340-015-0009-1.

[235]   S.S. Al-Bermani, M.L. Blackmore, W. Zhang, I. Todd, The Origin of Microstructural Diversity, Texture, and Mechanical Properties in Electron Beam Melted Ti-6Al-4V, Metall and Mat Trans A. 41 (2010) 3422–3434. doi:10.1007/s11661-010-0397-x.

[236]   A. Safdar, L.-Y. Wei, A. Snis, Z. Lai, Evaluation of microstructural development in electron beam melted Ti-6Al-4V, Materials Characterization. 65 (2012) 8–15. doi:10.1016/j.matchar.2011.12.008.

[237]   M. Simonelli, Y.Y. Tse, C. Tuck, On the Texture Formation of Selective Laser Melted Ti-6Al-4V, Metall and Mat Trans A. 45 (2014) 2863–2872. doi:10.1007/s11661-014-2218-0.

[238]   T. Ahmed, H.J. Rack, Phase transformations during cooling in α+β titanium alloys, Materials Science and Engineering: A. 243 (1998) 206–211. doi:10.1016/S0921-5093(97)00802-2.

[239]   D. Raabe, S. Sandlöbes, J. Millán, D. Ponge, H. Assadi, M. Herbig, P.-P. Choi, Segregation engineering enables nanoscale martensite to austenite phase transformation at grain boundaries: A pathway to ductile martensite, Acta Materialia. 61 (2013) 6132–6152. doi:10.1016/j.actamat.2013.06.055.

[240]   D. Raabe, M. Herbig, S. Sandlöbes, Y. Li, D. Tytko, M. Kuzmina, D. Ponge, P.-P. Choi, Grain boundary segregation engineering in metallic alloys: A pathway to the design of interfaces, Current Opinion in Solid State and Materials Science. 18 (2014) 253–261. doi:10.1016/j.cossms.2014.06.002.

[241]   M. Kuzmina, M. Herbig, D. Ponge, S. Sandlöbes, D. Raabe, Linear complexions: Confined chemical and structural states at dislocations, Science. 349 (2015) 1080–1083. doi:10.1126/science.aab2633.

[242]   F. Bridier, D.L. McDowell, P. Villechaise, J. Mendez, Crystal plasticity modeling of slip activity in Ti–6Al–4V under high cycle fatigue loading, International Journal of Plasticity. 25 (2009) 1066–1082. doi:10.1016/j.ijplas.2008.08.004.

[243]   J. Galan-Lopez, S. Naghdy, P. Verleysen, L.A.I. Kestens, F. Coghe, L. Rabet, J. Degrieck, Mechanical behavior and texture prediction of Ti-6Al-4V based on elastic viscoplastic self-consistent modelling, IOP Conf. Ser.: Mater. Sci. Eng. 82 (2015) 012027. doi:10.1088/1757-899X/82/1/012027.

[244]   F. Bridier, P. Villechaise, J. Mendez, Analysis of the different slip systems activated by tension in a α/β titanium alloy in relation with local crystallographic orientation, Acta Materialia. 53 (2005) 555–567. doi:10.1016/j.actamat.2004.09.040.

[245]   J.C. Williams, R.G. Baggerly, N.E. Paton, Deformation behavior of HCP Ti-Al alloy single crystals, Metall and Mat Trans A. 33 (2002) 837–850. doi:10.1007/s11661-002-0153-y.

[246]   S. Zaefferer, A study of active deformation systems in titanium alloys: dependence on alloy composition and correlation with deformation texture, Materials Science and Engineering: A. 344 (2003) 20–30. doi:10.1016/S0921-5093(02)00421-5.

[247]   R. Castro, L. Séraphin, Contribution à l'étude métallographique et structurale de l'alliage de titane TA6V, Les Mémoires Scientifiques de La Revue de Métallurgie. 63 (1966) 1025–1058.

[248]   G. Lütjering, J.C. Williams, Titanium, 2nd ed., Springer-Verlag, Berlin Heidelberg, 2007. //www.springer.com/de/book/9783540713975 (accessed November 12, 2018).

[249]   M.A. Weisser, A.D. Evans, S. Van Petegem, S.R. Holdsworth, H. Van Swygenhoven, In situ room temperature tensile deformation of a 1% CrMoV bainitic steel using synchrotron and neutron diffraction, Acta Materialia. 59 (2011) 4448–4457. doi:10.1016/j.actamat.2011.03.068.

[250]   L. Luo, A.K. Ghosh, Elastic and Inelastic Recovery After Plastic Deformation of DQSK Steel Sheet, J. Eng. Mater. Technol. 125 (2003) 237–246. doi:10.1115/1.1491574.

[251]   J. Mendiguren, F. Cortés, X. Gómez, L. Galdos, Elastic behaviour characterisation of TRIP 700 steel by means of loading–unloading tests, Materials Science and Engineering: A. 634 (2015) 147–152. doi:10.1016/j.msea.2015.03.050.

[252]   Z. Chen, U. Gandhi, J. Lee, R.H. Wagoner, Variation and consistency of Young's modulus in steel, Journal of Materials Processing Technology. 227 (2016) 227–243. doi:10.1016/j.jmatprotec.2015.08.024.

[253]   J.A. Benito, J. Jorba, J.M. Manero, A. Roca, Change of Young's modulus of cold-deformed pure iron in a tensile test, Metall and Mat Trans A. 36 (2005) 3317–3324. doi:10.1007/s11661-005-0006-6.

[254]   R.M. Cleveland, A.K. Ghosh, Inelastic effects on springback in metals, International Journal of Plasticity. 18 (2002) 769–785. doi:10.1016/S0749-6419(01)00054-7.

[255]   F. Morestin, M. Boivin, On the necessity of taking into account the variation in the Young modulus with plastic strain in elastic-plastic software, Nuclear Engineering and Design. 162 (1996) 107–116. doi:10.1016/0029-5493(95)01123-4.

[256]   M. Yang, Y. Akiyama, T. Sasaki, Evaluation of change in material properties due to plastic deformation, Journal of Materials Processing Technology. 151 (2004) 232–236. doi:10.1016/j.jmatprotec.2004.04.114.

[257]   R. Pérez, J.A. Benito, J.M. Prado, Study of the Inelastic Response of TRIP Steels after Plastic Deformation, ISIJ Int. 45 (2005) 1925–1933. doi:10.2355/isijinternational.45.1925.

[258]   H.Y. Yu, Variation of elastic modulus during plastic deformation and its influence on springback, Materials & Design. 30 (2009) 846–850. doi:10.1016/j.matdes.2008.05.064.

[259]   L. Sun, R.H. Wagoner, Complex unloading behavior: Nature of the deformation and its consistent constitutive representation, International Journal of Plasticity. 27 (2011) 1126–1144. doi:10.1016/j.ijplas.2010.12.003.

[260]   D. Shechtman, D.G. Brandon, Orientation dependent slip in polycrystalline titanium, J Mater Sci. 8 (1973) 1233–1237. doi:10.1007/BF00549337.

[261]   C.H. Cáceres, T. Sumitomo, M. Veidt, Pseudoelastic behaviour of cast magnesium AZ91 alloy under cyclic loading–unloading, Acta Materialia. 51 (2003) 6211–6218. doi:10.1016/S1359-6454(03)00444-0.

[262]   L. Jiang, J.J. Jonas, R.K. Mishra, A.A. Luo, A.K. Sachdev, S. Godet, Twinning and texture development in two Mg alloys subjected to loading along three different strain paths, Acta Materialia. 55 (2007) 3899–3910. doi:10.1016/j.actamat.2007.03.006.

[263]   M.R. Barnett, Z. Keshavarz, A.G. Beer, D. Atwell, Influence of grain size on the compressive deformation of wrought Mg–3Al–1Zn, Acta Materialia. 52 (2004) 5093–5103. doi:10.1016/j.actamat.2004.07.015.

[264]   D. Sarker, D.L. Chen, Detwinning and strain hardening of an extruded magnesium alloy during compression, Scripta Materialia. 67 (2012) 165–168. doi:10.1016/j.scriptamat.2012.04.007.

[265]   B. Wang, R. Xin, G. Huang, Q. Liu, Effect of crystal orientation on the mechanical properties and strain hardening behavior of magnesium alloy AZ31 during uniaxial compression, Materials Science and Engineering: A. 534 (2012) 588–593. doi:10.1016/j.msea.2011.12.013.

[266]   J. Filik, A.W. Ashton, P.C.Y. Chang, P.A. Chater, S.J. Day, M. Drakopoulos, M.W. Gerring, M.L. Hart, O.V. Magdysyuk, S. Michalik, A. Smith, C.C. Tang, N.J. Terrill, M.T. Wharmby, H. Wilhelm, Processing two-dimensional X-ray diffraction and small-angle scattering data in DAWN 2, J Appl Cryst. 50 (2017) 959–966. doi:10.1107/S1600576717004708.

[267]   B. Clausen, T. Lorentzen, T. Leffers, Self-consistent modelling of the plastic deformation of f.c.c. polycrystals and its implications for diffraction measurements of internal stresses, Acta Materialia. 46 (1998) 3087–3098. doi:10.1016/S1359-6454(98)00014-7.

[268]   Z. Sun, S. Van Petegem, A. Cervellino, K. Durst, W. Blum, H. Van Swygenhoven, Dynamic recovery in nanocrystalline Ni, Acta Materialia. 91 (2015) 91–100. doi:10.1016/j.actamat.2015.03.033.

[269]   F. Bachmann, R. Hielscher, H. Schaeben, Texture Analysis with MTEX − Free and Open Source Software Toolbox, Solid State Phenomena. 160 (2010) 63–68. doi:10.4028/www.scientific.net/SSP.160.63.

[270]   D. Tromans, Elastic Anisotropy of HCP Metal Crystals and Polycrystals, International Journal of Recent Research and Applied Studies. (2011). https://www.researchgate.net/publication/267371648_Elastic_Anisotropy_of_HCP_Metal_Crystals_and_Polycrystals (accessed March 25, 2019).

[271]   J. Haubrich, J. Gussone, P. Barriobero-Vila, P. Kürnsteiner, E.A. Jägle, D. Raabe, N. Schell, G. Requena, The role of lattice defects, element partitioning and intrinsic heat effects on the microstructure in selective laser melted Ti-6Al-4V, Acta Materialia. 167 (2019) 136–148. doi:10.1016/j.actamat.2019.01.039.

[272]   A. Alankar, P. Eisenlohr, D. Raabe, A dislocation density-based crystal plasticity constitutive model for prismatic slip in α-titanium, Acta Materialia. 59 (2011) 7003–7009. doi:10.1016/j.actamat.2011.07.053.

[273]   A. Alankar, I.N. Mastorakos, D.P. Field, A dislocation-density-based 3D crystal plasticity model for pure aluminum, Acta Materialia. 57 (2009) 5936–5946. doi:10.1016/j.actamat.2009.08.028.

[274]   M. Ardeljan, I.J. Beyerlein, M. Knezevic, A dislocation density based crystal plasticity finite element model: Application to a two-phase polycrystalline HCP/BCC composites, Journal of the Mechanics and Physics of Solids. 66 (2014) 16–31. doi:10.1016/j.jmps.2014.01.006.

[275]   F. Ozturk, R.E. Ece, N. Polat, A. Koksal, Effect of Warm Temperature on Springback Compensation of Titanium Sheet, Materials and Manufacturing Processes. 25 (2010) 1021–1024. doi:10.1080/10426914.2010.492056.

Curriculum Vitae

KARL SOFINOWSKI

Rosenweg 9, 5210 Windisch   USA citizen, born in 1992
CH-Schweiz
karl.sofinowski@gmail.com
https://www.linkedin.com/in/karl-sofinowski-81a90272

EMPLOYMENT HISTORY

Kimberly Clark Corporation, Fullerton, CA, USA   *Jan – May 2015*
   Machine Failure Analysis and Lubrication Engineer Co-op

National Science Foundation REU Grant, Atlanta, United States   *June - Aug 2012*
   Undergraduate research assistant under Dr. Aubrey Dyer

nGimat Co., Norcross, GA, USA   *June - Dec 2011*
   Nanocoatings and Nanofilms Product Analysis Intern

Naval Research Laboratory, Washington, D.C., USA   *June – Aug 2009*
   Science and Engineering Apprenticeship Program Intern

EDUCATION

PhD Materials Science and Engineering   *2015 – 2019*
NXMM group, École Polytechnique Fédérale de Lausanne**,** Switzerland
PEM group, Paul Scherrer Institute, Switzerland

B.S. Mechanical Engineering   *2010 – 2014*
Georgia Institute of Technology, Atlanta, GA
Concentration: Mechanics of Materials
GPA: 3.97/4.0, graduate with Highest Honors

- Capstone Design Project: Optimized design of axial flow pump impellers for irrigation in Bangladesh
- MEMS device undergraduate researcher under Dr. Olivier Pierron

High School   *2006 – 2010*
Thomas Jefferson High School for Science and Technology

PUBLICATIONS

K. Sofinowski, T. Panzner, M. Kubenova, J. Čapek, S. Van Petegem, H. Van Swygenhoven, *In situ* tension-tension strain path changes of cold-rolled Mg AZ31B, Acta Materialia. 164 (2019) 135–152.

K. Sofinowski, M. Šmíd, I. Kuběna, S. Vivés, N. Casati, S. Godet, H. Van Swygenhoven, *In situ* characterization of a high work hardening Ti-6Al-4V prepared by electron beam melting. Acta Materialia: *Under Review*

K. Sofinowski, M. Šmíd, S. Van Petegem, S. Rahimi, T. Connoley, H. Van Swygenhoven, *In situ* characterization of work hardening and springback in grade 2 α-titanium under tensile load. Acta Materialia: *Under Review*

E. Polatidis, K. Sofinowski, W-N. Hsu, H. Van Swygenhoven, Following Microstructures During Deformation: In Situ X-Ray/Neutron Diffraction and HRDIC, IOP Science Conference Series. I*n press*

J. Čapek, T. Panzner, K. Sofinowski, D. Drozdenko, K. Máthis, In situ Neutron Diffraction and Acoustic Emission During the Biaxial Loading of AZ31 Alloy, in: D. Orlov, V. Joshi, K.N. Solanki, N.R. Neelameggham (Eds.), Magnesium Technology 2018, Springer International Publishing, 2018: pp. 199–202.

J. Čapek, T. Panzner, K. Sofinowski, D. Drozdenko, K. Máthis, Twinning Evolution in Magnesium Alloys under Biaxial Loading, Acta Physica Polonica A. 134 (2018) 853–856.

S. Van Petegem, A. Guitton, M. Dupraz, A. Bollhalder, K. Sofinowski, M. V. Upadhyay, H. Van Swygenhoven. A Miniaturized Biaxial Deformation Rig for In Situ Mechanical Testing, Exp. Mech. (2017), 1-12.

CONFERENCE PRESENTATIONS

Oral Presentations

TMS 2019 Annual Meeting and Exhibition, USA	03/2019
MSE 2018, Germany	09/2018
18th International Conference on the Strength of Materials, USA	07/2018
2017 MRS Fall Meeting & Exhibit, USA	12/2017
Euromat 2017, Greece	09/2017
2016 MRS Fall Meeting & Exhibit, USA	12/2016

LANGUAGES

English (native), French (C1), German (B1)